TRACKING OPTIMISATION AND THE MEASUREMENT OF $K^+ \to \pi^+\mu^+\mu^-$ AT NA62

Andrew Sturgess

Thesis submitted to the University of Birmingham
for the degree of Doctor of Philosophy

Supervisors:
Prof. Cristina Lazzeroni
Dr. Chris Parkinson

Particle Physics Group
School of Physics and Astronomy
University of Birmingham
Birmingham, B15 2TT

August 29, 2018

Abstract

The NA62 experiment at CERN is designed to perform a precision measurement of the ultra-rare $K^+ \to \pi^+ \nu\bar{\nu}$ branching fraction. The experiment relies on a kinematic background rejection using the missing mass-squared signatures of the contributing background components. As the signal is of the $\mathcal{O}(10^{-10})$ smaller than that of the most common kaon decays, the tracking performance of the detector must be exceptional in order to achieve a large signal to background ratio of $S/B \approx 10$. In this thesis, two tools to aid with the tracking procedure have been developed. Firstly, a field map which describes the fringe field of the spectrometer magnet has been created, tested and implemented in the NA62 Monte-Carlo software. Additionally, an analysis procedure to improve the precision and accuracy of track momentum in data was developed.

Such tools are essential, not only for the $K^+ \to \pi^+ \nu\bar{\nu}$ decay, but also for all decays containing tracks. In particular, they have been used to aid the measurement of the branching fraction and form factor for the Standard Model decay $K^+ \to \pi^+ \mu^+ \mu^-$ which is described here. The measurement has been performed using the data collected by the NA62 experiment in 2016 and 2017. The event selection, trigger efficiency determination and the analysis techniques used for the measurement are presented. The analyses of the two data sets are provided separately to demonstrate the progressing sensitivity of the detector. The final results are compatible with previous measurements in literature, demonstrating the future potential of NA62 for when a larger data set is available.

Declaration of author's contribution

The design, construction and operation of the NA62 experiment at the Super Proton Synchrotron is the result of the hard work and collaboration of hundreds of people and institutes around the world. Without this effort, the study of fundamental high-energy phenomena would not be possible. In this thesis, the analyzed data sample was collected by the NA62 experiment in 2016 and 2017. This data was used to measure the $K^+ \to \pi^+\mu^+\mu^-$ branching fraction and form factor which is described in Chapters 6 to 9. The analysis is the result of my own work. The theoretical motivation and descriptions of the detectors provided in Chapter 2 and 3 are included to provide a complete picture of the analysis. Whilst I was not involved in the design or construction of the experiment, I took part in the data-taking operation between 2015 and 2017.

Except for the measurements used to build the simulation, the development of the fringe-field map described in Chapter 4, and the spectrometer calibration tool explained in Chapter 5, are both the result of my own work except where explicitly stated. No other qualifications have been achieved with the work reported in this thesis.

Acknowledgements

I would like to express my appreciation to my supervisors Cristina Lazzeroni and Chris Parkinson, as without their expertise, guidance and suggestions, the research presented in this thesis would not have been possible. I would also like to thank John Fry for his exceptionally useful critiques of this thesis. I am also grateful to L'uboš Bičian for the hours of discussions and meetings we shared. Furthermore, I wish to express gratitude to the University of Birmingham for providing me with funding and a place to develop my skills as a researcher, programmer and teacher.

To the NA62 group, I thank you for the enlightening experience and for all of the good times. A special mention goes to the inhabitants of W313 and W327 with whom I spent a vast deal of time with over the last four years; thanks for being my own personal Stack Exchange. To all of my friends outside of physics, cheers for pretending to be interested in my work! Furthermore, thanks goes to Ado and the rest of the BB for all of the San Marino challenges over the years, and to Kyle Lafferty for ending the dream of World Cup glory prematurely every time. I wish to thank my parents for their unwavering support, cups of tea and unbelievable sense of humour, and to my siblings for reminding me that they are still the intelligent ones. And finally, this thesis is dedicated to Milly, as without her unbelievable excellence, I would have given in a long time ago.

Contents

List of Figures

List of Tables

Acronyms

$\mathcal{CP}$ Charge-Parity. 23, 24, 26, 29, 39

AGS Alternating Gradient Synchrotron. 39

BNL Brookhaven National Laboratory. 28, 30, 31, 38, 39

C.L Confidence Level. 27, 30, 32, 165

CDA Closest-Distance of Approach. 121, 126, 137

CEDAR Cherenkov Differential counter. 47, 52, 53

CHOD NA48 Charged Hodoscope. 55–57, 63, 97, 127

CKM Cabibbo-Kobayashi-Maskawa. 23, 24, 26, 27

CREAM Calorimeter Readout Module. 58, 64

FCNC Flavour-Changing Neutral Current. 23, 28, 32–35

GIM Glashow, Iliopoulis and Maiani. 23, 28, 29, 34, 35

GTK GigaTracker. 50, 69, 119, 122, 155, 161

J-PARC Japan Proton Accelerator Research Complex. 30

KOTO K^0 at Tokai. 30

KTAG Kaon Tagger. 52, 53, 63, 65, 116, 117, 134, 135, 137

L0TP Level 0 Trigger Processor. 62, 64

LAV Large Angle Veto. 57, 58, 63, 65, 157–162, 165, 166

LECs Low-Energy Constants. 36–38, 42, 114, 118, 141, 168–170, 179–181, 184, 187, 194, 196, 197

LFU Lepton Flavour Universality. 22, 34

LFUV Lepton Flavour Universality Violation. 32, 33, 37

LFV Lepton Flavour Violating. 39

LKr Liquid Krypton Calorimeter. 48, 49, 58–60, 63, 126, 127, 136, 137

LNV Lepton Number Violating. 127

MC Monte Carlo. 6, 66, 67, 82, 83, 93, 97, 98, 104, 109, 111, 115, 118, 120, 122–125, 128, 130–133, 139, 143, 146, 159

MC Monte Carlo. 109

MCA Monte Carlo + Accidentals. 12, 143, 155–157, 159–162, 182, 192

MFV Minimal Flavour Violation. 37

MUV Muon Veto. 5, 7, 47–49, 60–63, 65, 118, 120, 121, 125–127, 129, 133–135, 137, 138, 162, 163, 178, 179, 183

NA62FW NA62 Framework. 104

NA62MC NA62 Monte Carlo. 66, 68, 69, 71, 72, 82, 92, 109, 119

NewCHOD New Charged Hodoscope. 7, 56, 61, 63, 64, 97, 120, 121, 124, 126, 127, 137, 150–155, 163, 178, 179

NP New Physics. 22, 29, 30, 33–35, 37, 38, 41–43

PDF Probability Density Function. 171–173, 179, 180, 188, 193

PMT Photomultiplier Tubes. 53–57, 60, 61, 63, 64, 145

RICH Ring Imaging Cherenkov. 4, 49, 53, 54, 63, 64, 116, 145

SAV Small Angle Veto. 59

SES Single Event Sensitivity. 32

SLAC Stanford Linear Accelerator Centre. 28

SM Standard Model. 22–24, 26–28, 30, 32–35, 37, 43

SPS Super Proton-Synchrotron. 46

SR Signal Region. 31, 41, 45, 92, 97, 98, 115, 125, 128–130, 163, 171, 173

TDAQ Trigger and Data Acquisition. 61–63, 116, 117, 122, 141, 142, 152, 186, 190, 193

TDC Time to Digital Converter. 53, 64

UT Unitarity Triangle. 25–27, 32

1

Introduction

For the last half-century, the Standard Model (SM) of particle physics has developed into one of the most accomplished theories in history. The most recent verification is the discovery of the Higgs-like resonance at the LHC by both the ATLAS and CMS experiments. The resonance, with mass $M_H = (125.18 \pm 0.16)$ GeV/c^2, has solved the puzzle of the last unconfirmed particle in the SM [1][2]. The unprecedented success of the theory demands extreme scrutiny. If the SM is the principle description of the fundamental interactions in the universe, then it is the responsibility of humanity to truly understand its implications. As an approximate theory, there are a large number of open questions that are yet to be understood: why are there so many arbitrary parameters, and why are there three generations of fundamental particles? It is through the tireless collaboration of thousands of physicists around the world that a plethora of wide-ranging experiments are attempting to answer these questions. While LHC physics continues to probe higher and higher energy scales, intensity-frontier experiments are concentrating on measuring large statistics of rare decays in the chance of observing deviations from SM predictions. Both approaches are complimentary and are necessary to truly test the validity of the SM.

The topic of this thesis is an analysis performed by the intensity-frontier experiment NA62. The design, construction and operation of the experiment represents the efforts of over two hundred physicists, without whom this thesis would not be possible. Situated at the CERN Super Proton Synchrotron (SPS), NA62 is a kaon fac-

tory. The kaon has always played a pivotal role in experimental flavour physics. For example, the large discrepancy between the kaon production and decay time-scale lead to the postulation of the strangeness quantum number and the expansion to a second generation of the quark family. With the strange and charm quark came the explanation to why $K_L \to \mu^+\mu^-$ is highly suppressed with respect to $K^+ \to \mu^+\nu_\mu$. The neutral kaon sector also provided the first evidence of both direct and indirect Charge-Parity ($\mathcal{CP}$) violation [3][4], which relates to one of the big questions in physics: why is there such a large asymmetry between matter and antimatter in the universe?

NA62 is optimised to measure the ultra-rare $K^+ \to \pi^+\nu\bar{\nu}$ decay, which is yet another probe of the SM. With a branching fraction of $\approx 10^{-10}$, the decay is considered a golden-channel because of a precise SM prediction; any deviation from expectation by an experimental measurement could hint to New Physics (NP). After only one year of data acquisition, NA62 has reached the SM sensitivity for the process, and the paper is soon-to-be submitted to Physics Letters B. Furthermore, the demanding nature of the $K^+ \to \pi^+\nu\bar{\nu}$ measurement means that NA62 is ideal for the measurement of other rare processes. Decays of the form $K^+ \to \pi^+\ell^+\ell^-$ offer a kaon-physics approach to measure observables which have analogous counterparts in other flavour sectors; it is some of these observables which have displayed tantalising hints of NP being a preferable solution over the SM prediction. In this thesis, the less accurately measured $K^+ \to \pi^+\mu^+\mu^-$ channel is investigated. Whilst the branching fraction is large ($\approx 10^{-8}$) in comparison to the flagship measurement, it can be used to test Lepton Flavour Universality (LFU) in a way which is complimentary to current B-physics analyses.

The first chapter outlines the theoretical motivation for these rare kaon measurements. Importantly, the experimental technique to observe and measure both processes requires incredibly high-precision tracking. In Chapter 3, the beam and subdetector systems of NA62 are described, while Chapters 4 and 5 provides the development of the MNP33 fringe-field map and a procedure to calibrate the spectrometer momentum determination, both vital for precision analyses involving charged

tracks. Using 2016 NA62 data, a selection for the rare decay $K^+ \to \pi^+\mu^+\mu^-$ is developed in Chapter 6, whilst the understanding of the trigger efficiency, a highly important aspect of the data analysis, is provided in Chapter 7. Both the branching fraction and form factor for the decay are extracted in Chapter 8, including a study in to the relative systematic errors. Notably, the work in this chapter suggests that the 2016 data set suffers from a series of complicated systematic issues; in Chapter 9, the 2017 data set is studied to learn about the future prospects of the measurement. A paper on the $K^+ \to \pi^+\mu^+\mu^-$ analysis presented in this thesis is in preparation for submission in the near future.

2

Theoretical motivation

In the last century, the kaon has played a pivotal role in developing the understanding of electroweak interactions in the Standard Model (SM). The NA62 experiment is the next in a long line of fixed target kaon experiments at CERN. The primary aim is to perform a precise measurement of the ultra-rare $K^+ \to \pi^+ \nu\bar{\nu}$ branching fraction in order to search for New Physics (NP). Whilst NA62 is optimised for this measurement, the experiment is well equipped to study other rare K^+ processes because of the demanding nature of the principle decay. An example is the $K^+ \to \pi^+\mu^+\mu^-$ channel which is the subject of the analysis in Chapter 8, and can be used to test Lepton Flavour Universality (LFU). In this chapter, the theoretical motivation to study both of these decays is explored, including the current experimental status.

2.1 The $K^+ \to \pi^+ \nu\bar{\nu}$ decay

2.1.1 CKM framework

In the SM, kaons are the lightest mesons to exhibit 'strangeness', a historical term first used in the early 1950's to describe a new set of particles with peculiar features. One unusual property is the relative discrepancy in the timescales of production and decay; particles are produced in $\approx 10^{-23}$ s but survive for a substantially longer time of up to $\approx 10^{-10}$ s [5][6]. Additionally, strange particles are only ever produced in even numbers, suggesting the conservation of some unknown property. In 1953, and in an effort to adequately describe these processes, Gell-Mann and Nishijima

introduced the strangeness quantum number [7][8]. Strangeness was postulated to be conserved by all interactions *apart* from the nuclear weak force, in an effort to explain the large difference in the observed timescales. Strangeness $S = -(n_s - n_{\bar{s}})$ is the difference in the number of strange n_s and anti-strange $n_{\bar{s}}$ particles in a process.

In the modern day SM, strangeness enters because of the strange quark, a constituent component of the kaon and all strange hadrons. The strange quark is a member of the second generation of the three quark families described by the Cabibbo-Kobayashi-Maskawa (CKM) unitary matrix:

$$\begin{pmatrix} d' \\ s' \\ b' \end{pmatrix} = V_{CKM} \begin{pmatrix} d \\ s \\ b \end{pmatrix} = \begin{pmatrix} V_{ud} & V_{us} & V_{ub} \\ V_{cd} & V_{cs} & V_{cb} \\ V_{td} & V_{ts} & V_{tb} \end{pmatrix} \begin{pmatrix} d \\ s \\ b \end{pmatrix}. \tag{2.1}$$

The CKM matrix V_{CKM} relates the flavour eigenstates d, s, b to the weak interaction eigenstates d', s', b' which couple with the u, c, t quarks. The magnitude of each element V_{iq} ($i = u, c, t,\ q = d, s, b$) contains the strength of the flavour-changing charged current interaction between generations, where $i \rightarrow q$ describes the quark transition; a Flavour-Changing Neutral Current (FCNC) is forbidden at tree-level by the Glashow, Iliopoulis and Maiani (GIM) mechanism (see Section 2.1.3). For a unitary $n \times n$ matrix (such as V_{CKM}), there are $N = n^2$ free parameters. With the addition of the invariance of the CKM matrix under reparameterisation, the number of parameters is reduced to just $N = (n-1)^2$. The presence of only three quark families in the SM leads to four parameters, of which three are real and free and one is a complex phase; the presence of the complex phase is responsible for Charge-Parity ($\mathcal{CP}$) violation. To display the parameters more clearly, the CKM matrix can be decomposed using the Wolfenstein parameterisation [9]:

$$|V_{CKM}| = \begin{pmatrix} 1 - \frac{1}{2}\lambda^2 - \frac{1}{8}\lambda^4 & \lambda & A\lambda(\bar{\rho} - i\bar{\eta}) \\ -\lambda + \frac{1}{2}A^2\lambda^5[1 - 2(\bar{\rho} + i\bar{\eta})] & 1 - \frac{1}{2}\lambda^2 - \frac{1}{8}\lambda^4(1 + 4A^2) & A\lambda^2 \\ A\lambda^3[1 - (\bar{\rho} + i\bar{\eta})] & -A\lambda^2 + \frac{1}{2}A\lambda^4[1 - 2(\bar{\rho} + i\bar{\eta})] & 1 - \frac{1}{2}A^2\lambda^4 \end{pmatrix}, \tag{2.2}$$

which is a power-series expansion of parameter λ up to the $\mathcal{O}(\lambda^6)$, where A, λ, $\bar{\rho}$ are the real parameters and the imaginary quantity $i\bar{\eta}$ represents the complex phase. The parameters are related by [10],

$$\lambda^2 = \frac{|V_{us}|^2}{|V_{ud}|^2 + |V_{us}|^2}, \tag{2.3}$$

$$A^2\lambda^2 = \frac{|V_{cb}|^2}{|V_{ud}|^2 + |V_{us}|^2}, \tag{2.4}$$

$$\bar{\rho} + i\bar{\eta} = -\frac{V_{ud}V_{ub}^*}{V_{cd}V_{cb}^*}. \tag{2.5}$$

The location of the phase $i\bar{\eta}$ is not significant physically, as any number of different parameterisations will lead to the same result provided that there is a single complex phase that cannot be transformed away. This is verified by the Jarlskog invariant, which measures $\mathcal{CP}$ violation,

$$J_{\mathcal{CP}} \equiv |\mathrm{Im}(V_{ij}V_{kl}V_{il}^*V_{kj}^*)| = A^2\lambda^6\bar{\eta}, \quad (i \neq k, j \neq l). \tag{2.6}$$

without any sum over i, j, k, l [11]. As long as $\bar{\eta}$ is non-zero, $\mathcal{CP}$ violation will be present in the SM and directly proportional to $J_{\mathcal{CP}}$.

2.1.2 Unitarity

Possibly the most natural representation of the four CKM parameters can be extracted by exploiting the unitarity of the CKM matrix,

$$\left(V_{CKM}^\dagger V_{CKM}\right)_{i,j} = \sum_q V_{qi}^* V_{qj} = \delta_{ij}. \tag{2.7}$$

In general, the diagonal elements ($i = j$) are real, whereas the off-diagonal elements ($i \neq j$) are complex, making them suitable for measuring $\mathcal{CP}$ violation. Of the eighteen possible relations, the six off-diagonal terms can be represented in the complex plane as triangles. The most common representations are the triangles where each 'side' is the same order of magnitude $\mathcal{O}(\lambda^3)$,

$$V_{ud}V_{ub}^* + V_{cd}V_{cb}^* + V_{td}V_{tb}^* = 0, \tag{2.8}$$

$$V_{ud}V_{td}^* + V_{us}V_{ts}^* + V_{ub}V_{tb}^* = 0, \tag{2.9}$$

which is displayed in the complex plane as seen in Figure 2.1. The first triangle

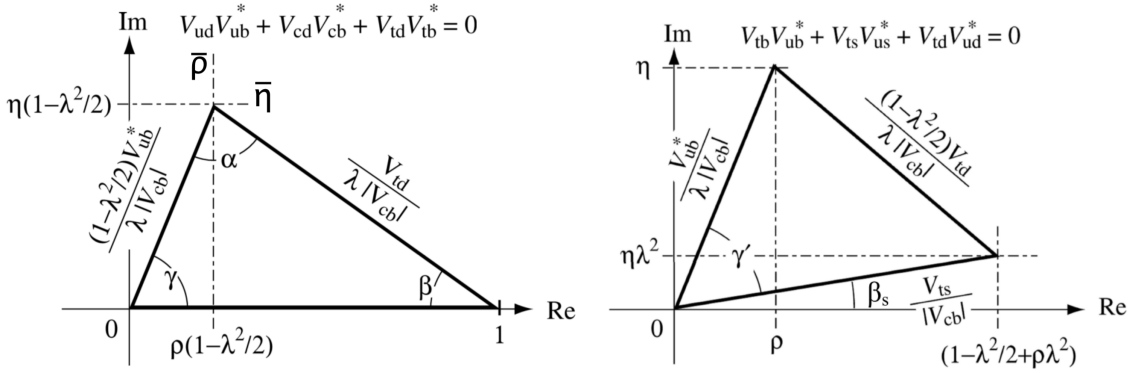

Figure 2.1: The two same-order complex triangles obtained using Equations 2.8 and 2.9, with the sides re-scaled by $V_{cd}V_{cb}^*$ in the first instance and $V_{us}V_{cb}^*$ in the second. The area of both triangles is equivalent to $J_{\mathcal{CP}}/2$ [10].

is often referred to as the Unitarity Triangle (UT). The coordinates of the vertex in the complex plane are ($\bar{\rho}$, $\bar{\eta}$), while the two remaining vertices occupy only the real dimension with coordinates (0, 0) and (1, 0). The magnitude of the sides S_u and S_t, corresponding to (0, 0)→($\bar{\rho}$, $\bar{\eta}$) and ($\bar{\rho}$, $\bar{\eta}$)→(0, 1), are given in Ref. [10] as,

$$S_u \equiv \left|\frac{V_{ud}V_{ub}^*}{V_{cd}V_{cb}^*}\right| \equiv \frac{(1-\frac{\lambda^2}{2})V_{ub}^*}{\lambda\,|V_{cb}|} = \sqrt{\bar{\rho}^2+\bar{\eta}^2}, \tag{2.10}$$

$$S_t \equiv \left|\frac{V_{td}V_{tb}^*}{V_{cd}V_{cb}^*}\right| \equiv \frac{V_{td}}{\lambda\,|V_{cb}|} = \sqrt{(1-\bar{\rho}^2)+\bar{\eta}^2}. \tag{2.11}$$

and the angles α, β and γ:

$$\alpha \equiv \arg\left(-\frac{V_{td}V_{tb}^*}{V_{ud}V_{ub}^*}\right) = \arg\left(-\frac{1-\bar{\rho}-i\bar{\eta}}{\bar{\rho}+i\bar{\eta}}\right), \tag{2.12}$$

$$\beta \equiv \arg\left(-\frac{V_{cd}V_{cb}^*}{V_{td}V_{tb}^*}\right) = \arg\left(\frac{1}{1-\bar{\rho}-i\bar{\eta}}\right), \tag{2.13}$$

$$\gamma \equiv \arg\left(-\frac{V_{ud}V_{ub}^*}{V_{cd}V_{cb}^*}\right) = \arg\left(\bar{\rho}+i\bar{\eta}\right). \tag{2.14}$$

The second triangle is tilted from the horizontal axis by the angle β_s defined as,

$$\beta_s \equiv \left(-\frac{V_{ts}V_{tb}^*}{V_{cs}V_{cb}^*}\right) = \lambda^2\bar{\eta} + \mathcal{O}(\lambda^4), \tag{2.15}$$

which is extracted from B_s^0 measurements such as $B_s^0 \to J/\psi K^+K^-$ [10][12]. A considerable effort is placed in measuring the sides and angles of the UT in modern day

experimental flavour physics. Examples of direct constraints are the measurements of the CKM matrix elements [13]:

$$|V_{CKM}| = \begin{pmatrix} 0.97434^{+0.00011}_{-0.00012} & 0.22506 \pm 0.00500 & 0.00357 \pm 0.00015 \\ 0.22492 \pm 0.00050 & 0.97351 \pm 0.00013 & 0.04110 \pm 0.00130 \\ 0.00875^{+0.00032}_{-0.00033} & 0.04030 \pm 0.00130 & 0.99915 \pm 0.00005 \end{pmatrix}. \quad (2.16)$$

The most precise value of $|V_{ud}|$ is extracted from nuclear physics experiments via super-allowed β decays [14]. For the elements $|V_{ui}|$ and $|V_{ci}|$ $(i = d, s, b)$, most measurements are constrained via leptonic and semileptonic K, D or B decays. For example, $|V_{us}|$ can be extracted using the semi-leptonic $K^+ \to \pi^0 \ell^+ \nu_\ell (K_{\ell 3})$ decays, processes which are common at NA62. Parameters involving the top-quark ($|V_{ti}|$) are typically more difficult to constrain due to the energy scale of $m_t \approx 175\,\mathrm{GeV/c^2}$. The parameter $|V_{tb}|$ can be extracted based on single-top production cross-sections, but the determination is much less accurate compared to limits imposed by the constraint of unitarity. The matrix elements $|V_{td}|$ and $|V_{ts}|$ are most accurately obtained from rare loop-mediated B or K decays. Combining the measurements from the matrix elements with the determination of the CKM parameters leads to the unitarity triangle in $(\bar{\rho}, \bar{\eta})$ space, displayed in Figure 2.2. The globally preferred fit parameters and corresponding UT angles are determined to be [13]:

$$A = 0.8110 \pm 0.026, \quad (2.17)$$

$$\lambda = 0.22506 \pm 0.00050, \quad (2.18)$$

$$\bar{\rho} = 0.124^{+0.019}_{-0.018}, \quad (2.19)$$

$$\bar{\eta} = 0.356 \pm 0.011, \quad (2.20)$$

$$\alpha = (87.6^{+3.5}_{-3.3})^\circ, \quad (2.21)$$

$$\beta = (21.9^{+0.7}_{-0.7})^\circ, \quad (2.22)$$

$$\gamma = (73.2^{+6.3}_{-7.0})^\circ. \quad (2.23)$$

The Jarlskog invariant $J_{\mathcal{CP}}$ is therefore $(3.04^{+0.31}_{-0.20}) \times 10^{-5}$, corresponding to twice the area of the UT and equivalent to the amount of $\mathcal{CP}$ violation in the SM [13].

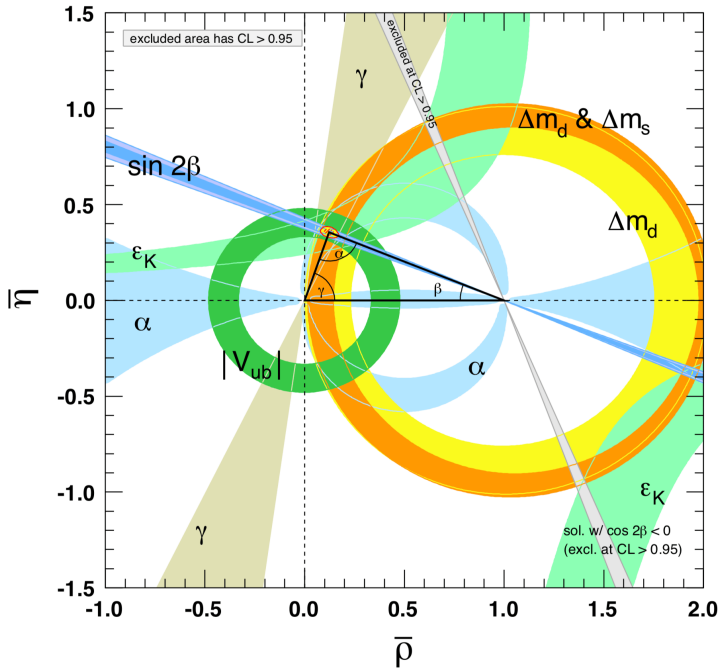

Figure 2.2: Constrains on the unitarity triangle in the $(\bar{\rho}, \bar{\eta})$ plane, where shaded areas have a 95% Confidence Level (C.L) [13].

Importantly, the current measurements are in agreement with unitarity:

$$|V_{ud}|^2 + |V_{us}|^2 + |V_{ub}|^2 = 0.9996 \pm 0.0005, \tag{2.24}$$

$$|V_{cd}|^2 + |V_{cs}|^2 + |V_{cb}|^2 = 1.0400 \pm 0.0320, \tag{2.25}$$

$$\alpha + \beta + \gamma = (183^{+7}_{-8})^{\circ}, \tag{2.26}$$

where the Equation 2.24 and 2.25 correspond to the first and second rows of the CKM matrix and Equation 2.26 refers to the UT angles [13]. As the sensitivity and precision of experimental measurement improves, if there is a deviation from unitarity or the parameters disagree significantly for different processes, the validity of the SM can be questioned and modifications due to NP could be considered.

2.1.3 Theoretical prediction of $K \to \pi\nu\bar{\nu}$

The kaon sector has the potential to play an even more vital role in experimental flavour physics. The decays $K^+ \to \pi^+\nu\bar{\nu}$ and $K_L \to \pi^0\nu\bar{\nu}$ are ultra-rare and considered as golden channels because of their clean theoretical prediction. By simply measuring the branching fraction of the processes, the validity of the SM can be

tested. The decays are ultra-rare because of the GIM mechanism. Unlike the charged weak current, changing quark flavour via the neutral current is forbidden at the tree-level in the SM. This is a consequence of the existence of the charm quark, which was postulated by Glashow, Iliopoulis and Maiani in 1970, before it was discovered later via the J/ψ meson at both the Stanford Linear Accelerator Centre (SLAC) and the Brookhaven National Laboratory (BNL) [15][16]. In their work to unify both the electromagnetic and weak interaction, it was discovered that the existence of a fourth new "charm" quark was needed, in addition to u, d, s, to explain the rarity of the FCNC process $K_L \rightarrow \mu^+\mu^-$ with respect to the common leptonic $K^+ \rightarrow \mu^+\nu_\mu$ decay. The GIM mechanism leads to two distinct features: FCNC processes are forbidden at tree-level by the structure of the third component of the weak isospin; but can proceed at higher order loops which are subsequently suppressed based on ratio of the quark mass to the $W^\pm$ boson [17]. Figure 2.3 contains the dominant short-distance Feynman diagrams for the $K^+ \rightarrow \pi^+\nu\bar{\nu}$ decay, Here, three diagrams

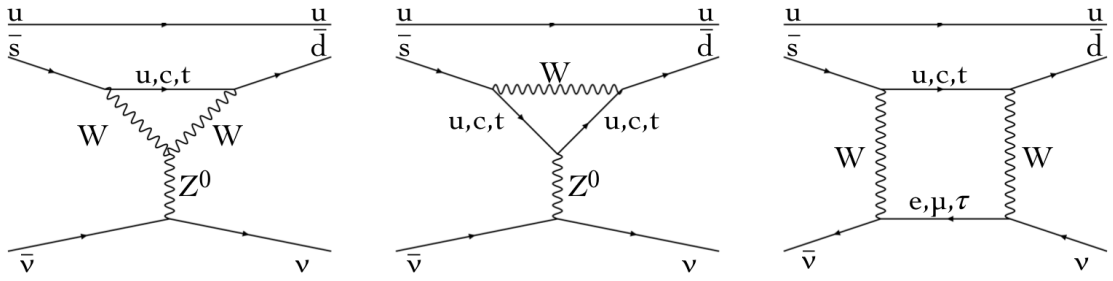

Figure 2.3: The dominant Feynman diagrams for $K^+ \rightarrow \pi^+\nu\bar{\nu}$ decay; Z-penguin and box loop diagrams. Each diagram is an example of the short-distance contribution, where the $|V_{td}|$ dependence enters in the loop.

contribute to the process, with two Z-penguins and a box loop. The amplitude of the decay is of the form [18],

$$A\left(s \rightarrow d\nu\bar{\nu}\right) \approx \sum_{q=u,c,t} \lambda_q X_{SM}\left(x_q\right), \tag{2.27}$$

$$\approx \frac{m_t^2}{M_W^2}\lambda_t + \frac{m_c^2}{M_W^2}\ln\left(\frac{M_W}{m_c}\right)\lambda_c + \frac{\Lambda_{\mathrm{QCD}}^2}{M_W^2}\lambda_u, \tag{2.28}$$

where $\lambda_q = V_{qd}V_{qs}^*$ $(q = u, c, t)$, $x_q = m_q^2/M_W^2$ (where m_q is the quark mass and M_W is the W$^\pm$ mass), $X(x_q)$ is a loop function for the quark-contributions and $\Lambda_{\mathrm{QCD}} \approx 1$ GeV is a constant corresponding to the energy-scale where non-perturbative QCD is

dominant. This is a power-like (hard) GIM mechanism, dominated by the first term involving the top-quark mass. As a result, the decay is suitable to measure matrix element $|V_{td}|$ (assuming no NP contributions) and is dominated by only short-distance QCD effects, reducing the systematic uncertainties in the theoretical prediction. The SM branching fraction for the two $K \to \pi\nu\bar{\nu}$ decays is,

$$\mathcal{B}\left(K_L \to \pi^0\nu\bar{\nu}\right) = \kappa_L \left(\frac{\mathrm{Im}\ \lambda_t}{\lambda^5} X\right)^2 (1 - \delta_\epsilon)\,, \tag{2.29}$$

$$\mathcal{B}\left(K^+ \to \pi^+\nu\bar{\nu}\right) = \kappa_+ (1 + \Delta_{\mathrm{EM}}) \left\{ \left(\frac{\mathrm{Im}\ \lambda_t}{\lambda^5} X\right)^2 + \left(\frac{\mathrm{Re}\ \lambda_t}{\lambda^5} X + \frac{\mathrm{Re}\lambda_c}{\lambda} \left(P_c + \delta P_{c,u}\right)\right)^2 \right\}, \tag{2.30}$$

where $\delta_\epsilon = \sqrt{2}|\epsilon|[1 + P_c/(A^2\lambda)]/\eta$, $P_{c,u}(X)$ is the loop-function for the c, u quarks ($\delta P_{c,u}$ is the difference between the two) and Δ_{EM} includes the electromagnetic corrections [19]. The largest theoretical uncertainty originates in the $\kappa_{+,L}$ terms, which correspond to the long-distance effects. Ultimately, both terms depend on the hadronic matrix elements which are constrained by experiment,

$$\kappa_L = (2.231 \pm 0.013) \times 10^{-10} (\lambda/0.225)^8, \tag{2.31}$$

$$\kappa_+ = (5.173 \pm 0.025) \times 10^{-11} (\lambda/0.225)^8, \tag{2.32}$$

and are extracted via semi-leptonic $K_{\ell 3}$ decays [20]. The K^+ process has a $\mathcal{CP}$ conserving real and a $\mathcal{CP}$ violating imaginary component, whilst the K_L decay is purely imaginary and therefore is maximally $\mathcal{CP}$ violating. The numerical prediction is:

$$\mathcal{B}(K_L \to \pi^0\nu\bar{\nu}) = (3.00 \pm 0.30) \times 10^{-11}, \tag{2.33}$$

$$\mathcal{B}(K^+ \to \pi^+\nu\bar{\nu}) = (8.40 \pm 1.00) \times 10^{-11}, \tag{2.34}$$

corresponding to a precision to within 10% [21]. Of this, only ≈4% is due to the true theoretical uncertainty; the largest component is the parametric error entering from the κ terms (Equations 2.31 and 2.32) due to the CKM elements. The channels are seen as golden because of this small theoretical uncertainty; if an experimental measurement is similarly as precise and there is a notable deviation between the values,

it can be expected that NP is contributing within the loop at a similar magnitude to the SM.

2.1.4 Experimental status

The NA62 and K^0 at Tokai (KOTO) experiments aim to measure the $K^+ \to \pi^+\nu\bar{\nu}$ and $K_L \to \pi^0\nu\bar{\nu}$ branching fractions to a precision better than 10% in order to test the SM. The current experimental limits on the measurements are,

$$\mathcal{B}(K^+ \to \pi^+\nu\bar{\nu}) = (17.3^{+11.5}_{-10.5}) \times 10^{-11}, \tag{2.35}$$

$$\mathcal{B}(K_L \to \pi^0\nu\bar{\nu}) < 3.0 \times 10^{-9} \ \ (90\% \ \mathrm{C.L}). \tag{2.36}$$

The K_L channel has not yet been observed. The best upper limit has been set by first-stage of the KOTO experiment at the Japan Proton Accelerator Research Complex (J-PARC) Proton Synchrotron [22]. At KOTO, protons with central momentum 30 GeV/c are directed onto a 66 mm long gold target to produce a secondary neutral K_L beam which is offset by 16° with respect to the primary beam axis. The detector is a hermetic particle veto, with the Caesium-Iodide electromagnetic calorimeter (CsI) used to detect the secondary $\pi^0 \to \gamma\gamma$ decay in the absence of any other signals [23]. Equation 2.36 was achieved using data from 2015, and is expected to improve using the full 2015-2018 data set.

The K^+ channel was measured with the E787/E949 experiments at the BNL [24]. Both experiments were performed using stopped kaon decays, where E949 was the final upgraded stage of the experiment. A secondary K^+ beam with momentum centred at 710 MeV/c was slowed using an active scintillator fibre target, and the decay products measured using the apparatus displayed in Figure 2.4. The detector was immersed in a 1T solenoidal magnetic field, with the hermetic argon-ethane drift chamber occupying the radial regions around the target. A range-stack followed the drift-chamber, and was designed to measure the position and energy of the secondary charged particles. The stack contained multiple layers of plastic scintillators coupled to multi-wire proportional chambers for accurate position determination. The outer-layer of the detector is the photon-veto barrel, useful for

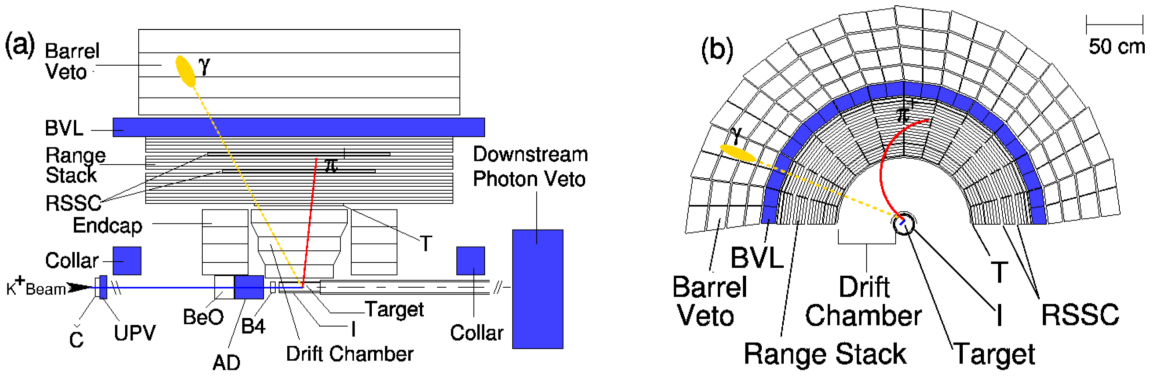

Figure 2.4: The E949 detector, the final form of E787 experiment at BNL [25].

suppressing the background decays containing π^0 such as $K^+ \to \pi^+\pi^0$. The total number of $K^+ \to \pi^+\nu\bar{\nu}$ candidates recorded by both collaborations was 5+2 (E787 + E949), as displayed in Figure 2.5. Two types of Signal Region (SR) were necessary

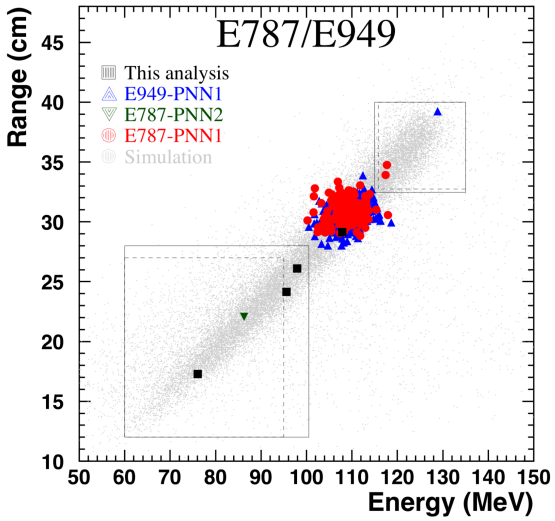

Figure 2.5: The seven observed $K^+ \to \pi^+\nu\bar{\nu}$ candidates at the two BNL experiments. Two Signal Regions (SRs) were used which divide the phase-space, as the irreducible $K^+ \to \pi^+\pi^0$ background enters at the centre of the region. The range refers to the radial distance from the beam-pipe and measured with the range-stack [24].

due to the irreducible $K^+ \to \pi^+\pi^0$ background at the centre of the $K \to \pi^+\nu\bar{\nu}$ phase-space.

The NA62 experiment uses an alternative decay in-flight technique, which greatly improves photon-detection efficiency in order to suppress backgrounds such as $K^+ \to$

$\pi^+\pi^0$. After a year of data-taking and the observation of a single $K \to \pi^+\nu\bar{\nu}$ candidate, NA62 has already reached the SM Single Event Sensitivity (SES) [26]:

$$SES = (3.15 \pm 0.01_{\text{stat}} \pm 0.2_{\text{syst}}) \times 10^{-10}, \tag{2.37}$$

which corresponds to a limit on the branching fraction of,

$$\mathcal{B}(K^+ \to \pi^+\nu\bar{\nu}) < 11 \times 10^{-10} \ (90\% \text{ C.L.}). \tag{2.38}$$

NA62 aims to improve the precision in the K^+ channel by collecting of the $\mathcal{O}(100)$ candidates over the lifetime of the experiment.

2.2 The $K^+ \to \pi^+\mu^+\mu^-$ decay

2.2.1 Anomalies in flavour physics

Despite the success of the SM especially in terms of the UT and the discovery of the Higgs-like resonance, there have been a notable number of high-profile anomalies appearing indirectly after Run 1 at the LHC. The LHCb experiment in particular has observed three notable examples relating to the B-physics sector [27]:

- **$P_5^{'}$ deviation:** The observable $P_5^{'}$ is one of five angular variables used to describe four-body FCNC B-decays [28]. A tension has been discovered with respect to the SM for the $B \to K^*\mu^+\mu^-$ decay for this variable of between 2-3σ [29] [30].

- **$B_s \to \phi\mu^+\mu^-$:** The LHCb and CDF combined differential branching fraction of the $B_s \to \phi\mu^+\mu^-$ decay deviates by 3.5σ from the lattice QCD prediction in the region between 14.0 $< q^2 <$ 19.0 GeV^2/c^4 [31] [32] [33] .

- **Lepton flavour universality:** LHCb has observed a tension suggesting Lepton Flavour Universality Violation (LFUV) for $b \to s$ transitions. The most prominent example is for the $B \to K\ell^+\ell^-$ decays ($\ell = e, \mu$) in the phase-space region

between $1 < m^2_{\ell\ell} < 6$ GeV^2/c^4. The ratio,

$$R(K\ell\ell) = \frac{\mathcal{B}(B \to K\mu^+\mu^-)}{\mathcal{B}(B \to Ke^+e^-)} = 0.745^{+0.090}_{-0.074} \pm 0.036, \tag{2.39}$$

deviates by 2.6σ from the theoretically clean SM prediction of $R_{SM}(K) = 1.0003 \pm 0.0001$ [34] [35]. The first observation of a LFUV discrepancy came from BaBar, which has subsequently been remeasured by LHCb [36], for the ratio of the tree-level processes,

$$R(D^*) = \frac{\mathcal{B}(B \to D^*\tau\nu_\tau)}{\mathcal{B}(B \to D^*\ell\nu_\ell)} = 0.322 \pm 0.018 \pm 0.012. \tag{2.40}$$

However, the prediction is $R_{SM}(D^*) = 0.252 \pm 0.003$, a discrepancy of over 3σ [37] [38].

By combining the discrepancies for the loop mediated $b \to s$ transitions, the global fits find that the (NP + SM) solution is preferred to the SM by close to 5σ [39] [40]. The effective Hamiltonian for FCNC $b \to s$ ($|\Delta B| = 1$) transitions is,

$$\mathcal{H}_{eff} = -\frac{4G_F}{\sqrt{2}} V_{tb}V^*_{ts} \sum_i C^B_i(\mu) Q^B_i(\mu) + (h.c), \tag{2.41}$$

where G_F is the Fermi coupling constant, and $\left\{Q^B_i\right\}$ is a set of local composite operators with Wilson coefficients C^B_i [27]. As all FCNC decays are forbidden at tree-level, only the loop semi-leptonic operators with non-zero Wilson terms contribute in the form of penguin or box diagrams. The two of specific interest are,

$$Q^B_9 = \frac{e^2}{32\pi^2} \left[\bar{s}\gamma^\mu(1-\gamma_5)b\right] \sum_{\ell=e,\mu} \left[\bar{\ell}\gamma_\mu\ell\right], \tag{2.42}$$

$$Q^B_{10} = \frac{e^2}{32\pi^2} \left[\bar{s}\gamma^\mu(1-\gamma_5)b\right] \sum_{\ell=e,\mu} \left[\bar{\ell}\gamma_\mu\gamma_5\ell\right]. \tag{2.43}$$

It is through these processes that NP is expected to enter, which can be interpreted as a contribution on top of the SM component to $C^B_{9,10}$ [27].

2.2.2 Lepton flavour universality

Although some of the most interesting discrepancies currently originate in B-physics, K-physics can play a highly complimentary role to NP searches. The most obvious examples are the $K \to \pi\nu\bar{\nu}$ decays, explained previously in Section 2.1. Aside from the measurement of the golden channels, one of the most directly accessible phenomena to study is LFU. In the SM, the coupling of leptons to the electroweak gauge bosons is independent of flavour; the difference in the branching fractions for weak processes involving different generations of leptons depends only on the mass difference between them. However, as with lepton and baryon number, lepton flavour universality is not a fundamental symmetry but is inferred through precise experimentation. The evidence provided by the $R(K\ell\ell)$ and $R(D^*)$ measurements hint that the SM might not be the complete picture.

The rare FCNC processes $K^+ \to \pi^+\ell^+\ell^-$ ($\ell = e, \mu$) are directly analogous to the decays used to measure $R(K\ell\ell)$, as they both yield related observables. In a similar fashion to $b \to s$ transitions, $s \to d$ ($|\Delta S| = 1$) processes are described using the effective Lagrangian,

$$\mathcal{L}_{eff}^{|\Delta S|=1} = -\frac{G_F}{\sqrt{2}} V_{ud} V_{us}^* \sum_i C_i(\mu) Q_i(\mu) + (h.c), \tag{2.44}$$

where again, $\{Q_i\}$ are a set of local composite operators with corresponding Wilson coefficients C_i [27]. Figure 2.6 contains the contributing Feynman diagrams to the process; the $K^+ \to \pi^+\ell^+\ell^-$ amplitude depends on the logarithm-like (soft) GIM mechanism, as the γ-penguin also contributes. Therefore, these decays are only rare, unlike the ultra-rare $K \to \pi\nu\bar{\nu}$ [41], and the related theoretical uncertainties are larger. Like with B decays, only the loop diagrams contribute because they generate the only non-zero Wilson coefficients for the semileptonic operators Q_{7V} and Q_{7A},

$$Q_{7V} \equiv Q_{11} = [\bar{s}\gamma^\mu(1-\gamma_5)d] \sum_{\ell=e,\mu} \left[\bar{\ell}\gamma_\mu \ell\right], \tag{2.45}$$

$$Q_{7A} \equiv Q_{12} = [\bar{s}\gamma^\mu(1-\gamma_5)d] \sum_{\ell=e,\mu} \left[\bar{\ell}\gamma_\mu\gamma_5 \ell\right]. \tag{2.46}$$

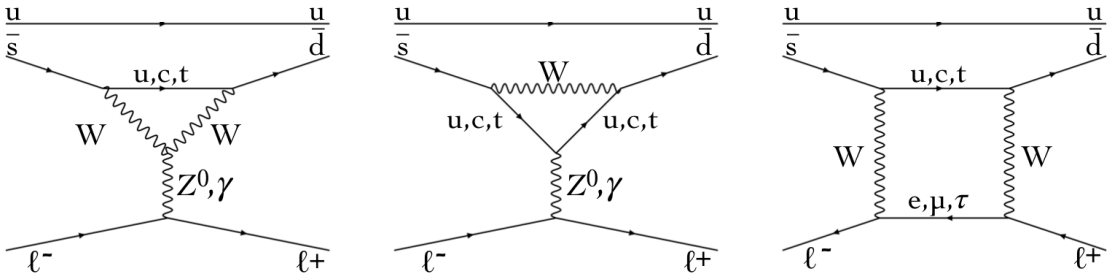

Figure 2.6: Z, γ-penguin and box contributions to the $K^+ \to \pi^+\ell^+\ell^-$ decay, with an amplitude governed by the logarithm-like (soft) GIM mechanism.

Again, NP processes can be interpreted as deviations from the SM Wilson coefficients $C_{7V,7A}$ [27].

2.2.3 The form factor

The semi-leptonic FCNC processes $K^+ \to \pi^+\ell^+\ell^-$ ($\ell = e, \mu$) are described by single-photon exchange at low energies (i.e $K \to \pi\gamma^* \to \pi\ell^+\ell^-$) [42]. The amplitude for the process is determined using an electroweak transition form factor $W(z)$, such that the differential decay rate is given by,

$$\frac{d\Gamma_{\pi\ell\ell}}{dz} = \frac{\Omega_C \alpha^2 M_K}{12\pi(4\pi)^4} \lambda^{3/2}(1, z, r_\pi^2) \sqrt{1 - 4\frac{r_\ell^2}{z}} \left(1 + 2\frac{r_\ell^2}{z}\right) |W(z)|^2, \tag{2.47}$$

where α is the fine structure constant, and,

$$r_{\pi,\ell} = M_{\pi,\ell}/M_K, \tag{2.48}$$

$$z = (q/M_K)^2 \equiv (m_{\ell\ell}/M_K)^2, \tag{2.49}$$

$$\lambda(a, b, c) = a^2 + b^2 + c^2 - 2ab - 2ac - 2bc. \tag{2.50}$$

The term Ω_C contains the Coulomb interaction, described by,

$$\Omega_C\left(\beta_{ij}\right) = \prod_{i,j=1,2,3;i<j} \frac{2\pi\alpha Q_i Q_j}{\beta_{ij}} \left(e^{\frac{2\pi\alpha Q_i Q_j}{\beta_{ij}}} - 1\right)^{-1}, \tag{2.51}$$

where $\beta_{i,j}$ is the relative velocity of any two daughters in the decay and $Q_i = \pm 1$ are the associated charges [43]. The decay is constrained to the phase-space between $4r_\ell^2 \leqslant z \leqslant (1 - r_\pi^2)$. The form factor $W(z)$ is an analytical function to describe

the single-photon exchange. The form factor also has a non-zero contribution from intermediate dispersion states. At small dilepton invariant masses, a $\pi^+\pi^-$ loop enters into the transition and is the dominant dispersion relation, whereas the higher masses can be approximated with a high degree of accuracy by a low-order polynomial with respect to z [42][44]. The form factor therefore contains two terms,

$$W(z) = G_F M_{K^+}^2 W^{pol}(z) + W^{\pi\pi}(z), \tag{2.52}$$

where $W^{\pi\pi}(z)$ is the contribution from the two-pion state and $W^{pol}(z)$ describes the low-order polynomial. The $W^{\pi\pi}(z)$ term can be calculated via Figure 2.7, by ex-

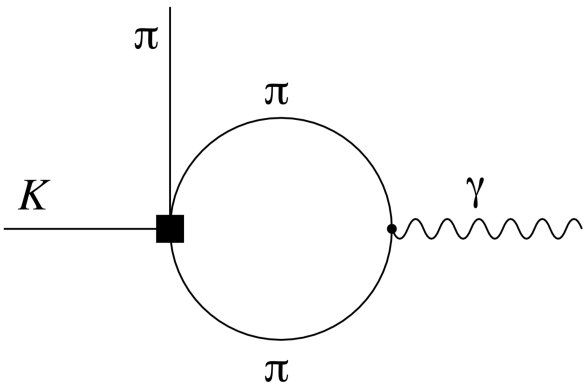

Figure 2.7: The two-pion loop contribution to the χPT form factor, the dominant dispersion relation at low $m_{\ell\ell}$. Other dispersion states can occur at high $m_{\ell\ell}$, such as the K-loop [42][44].

panding the $K \to 3\pi$ amplitude up to $\mathcal{O}(p^4)$. The $W^{pol}(z)$ term takes the simplest form [45],

$$W^{pol}(z) = (a_+ + b_+ z), \tag{2.53}$$

where a_+ and b_+ are free Low-Energy Constants (LECs), used to describe the non-perturbative QCD effects in the chiral expansion, with the main assumption that this polynomial describes all contributions from intermediate states except the two-pion loop. Figure 2.8 contains the theoretical $d\Gamma/dz$ shape for the $\mu\mu$ channel, which is the subject of the thesis, with each component of the form factor $W(z)$ displayed. The LECs have been taken from the current best measurements (Table 2.1). The $W^{\pi\pi}(z)$ term is small in comparison to $W^{pol}(z)$ for the current-best LECs . However, the overall $d\Gamma/dz$ magnitude is larger than for just $W(z) = W^{pol}(z)$ due to the cross term

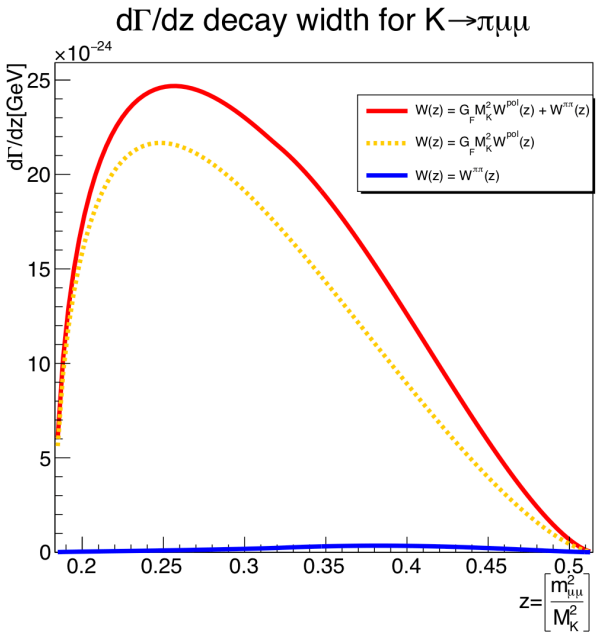

Figure 2.8: Predicted $d\Gamma/dz \sim |W(z)|^2$ spectrum with respect to z for several versions of the form factor $W(z)$. The overall spectrum is dominated by $W^{pol}(z)$.

between the two components. Importantly, for LFU to hold true, the LECs must be identical for both $\mu\mu$ and ee channels of $K^+ \to \pi^+\ell^+\ell^-$; any deviation between the parameters $a_+^{\mu\mu} - a_+^{ee}$ would be a sign of short distance NP [40]. As shown in Ref. [27], the difference in the parameters $a_+^{\rm NP}$ can be represented as a dependence on the Wilson coefficient C_{7V}, by projecting the $SU(3)_L$ chiral current onto the $\Delta S = 1$ sector [46], leading to,

$$a_+^{\rm NP} = \frac{2\pi\sqrt{2}}{\alpha} V_{ud}V_{us}^* C_{7V}^{\rm NP}, \tag{2.54}$$

and therefore, NP will enter as a difference in the Wilson coefficients of the two channels [40],

$$C_{7V}^{\mu\mu} - C_{7V}^{\rm ee} = \alpha \frac{a_+^{\mu\mu} - a_+^{ee}}{2\pi\sqrt{2}V_{ud}V_{us}^*}. \tag{2.55}$$

The crucial aspect of this measurement is that it is an entirely complimentary technique to the B-physics searches, but with different systematics. If LFUV is observed, the simplest extension to the SM is Minimal Flavour Violation (MFV), which if assumed can directly relate the Wilson coefficients of loop processes in K-physics to

B-physics, specifically C_{7V} to C_9^B,

$$C_9^{B,\mu\mu} - C_9^{B,ee} = -\frac{a_+^{\mu\mu} - a_+^{ee}}{\sqrt{2}V_{td}V_{ts}^*}, \tag{2.56}$$

as the coefficients of the two-sectors are correlated in the presence of NP. The quality of the bounds is therefore restricted by only the experimental determination of the LECs for both ee and $\mu\mu$ channels.

In order to obtain both the LECs and the corresponding branching fraction, the differential decay rate $d\Gamma/dz$ spectrum must be reconstructed using experimental data. In this thesis, NA62 data is used to perform this task. By integrating the spectrum and normalising to the K^+ decay-width, the branching fraction can be measured in a model-independent fashion. By fitting the spectrum with the theoretical prediction of $d\Gamma/dz$ (Equation 2.47), the LECs can be extracted.

2.2.4 Experimental Status

The current and most precise determinations of the $K \to \pi^+\ell^+\ell^-$ branching fractions are,

$$\mathcal{B}(K^+ \to \pi^+ e^+ e^-) = (3.11 \pm 0.04_{\text{stat}} \pm 0.12_{\text{syst}}) \times 10^{-7}, \tag{2.57}$$

$$\mathcal{B}(K^+ \to \pi^+ \mu^+ \mu^-) = (9.62 \pm 0.21_{\text{stat}} \pm 0.13_{\text{syst}}) \times 10^{-8}. \tag{2.58}$$

performed by the NA48/2 experiment [47][48]. The LECs were also extracted, contained in Table 2.1. There have been two measurements of the ee channel LECs, firstly by the E865 experimental at BNL and secondly by the NA48/2 experiment at CERN. Only NA48/2 has measured the LECs for the $\mu\mu$ channel. Notably, the existing literature misses the measurement of the second minima in the positive (a_+, b_+) space.

Table 2.1: Current experimental measurements of the LECs for both ee and $\mu\mu$ channels.

Channel	a_+	b_+	Experiment
ee	-0.587$\pm$0.010	-0.655 $\pm$ 0.044	E865 [49]
ee	-0.578$\pm$0.016	-0.779 $\pm$ 0.066	NA48/2 [47]
$\mu\mu$	-0.575$\pm$0.039	-0.813 $\pm$ 0.145	NA48/2 [48]

The E865 experiment was performed at the BNL Alternating Gradient Synchrotron (AGS), constructed specifically to search for the Lepton Flavour Violating (LFV) decay of $K^+ \to \pi^+\mu^+e^-$ [50]. Figure 2.9 contains the schematic of the apparatus, where an unseparated 6 GeV/c beam with a 2.5% K^+ component is allowed to decay upstream of a series of sub-detectors. The kaons decay in an evacuated volume 5 m

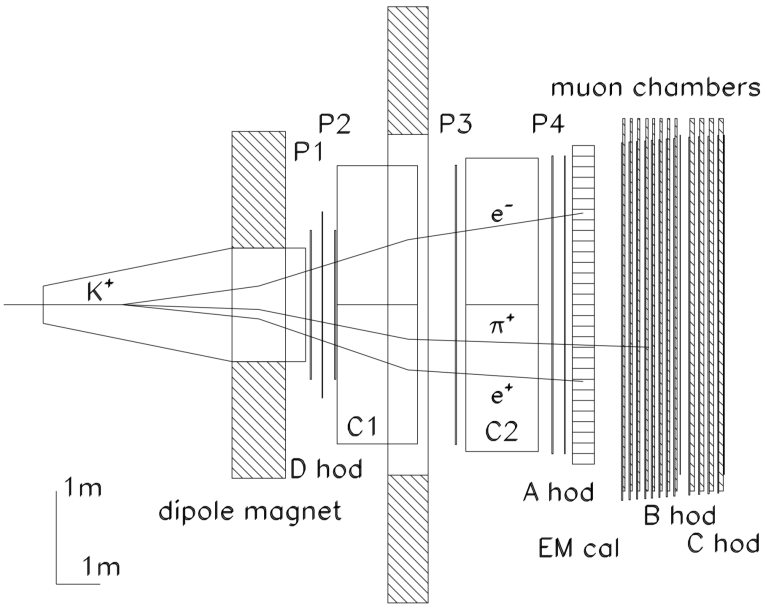

Figure 2.9: The E865 experiment; K^+ decay in-flight, steered by two sets of dipole magnets to separate pions and electrons [49].

upstream of a charge-separating dipole magnet. Tracking was performed in the four $P1\to4$ proportional chambers, interspaced by a spectrometer dipole magnet with a 0.833 Tm field integral. Two Cherenkov counters $C_{1,2}$ filled with H_2/CH_4 were used for particle-identification, while a Shashlik electromagnetic calorimeter was installed for energy measurements, containing 600 11.4 $\times$ 11.4 cm^2 modules equivalent to 15 radiation lengths in depth. The final detector system is the muon range stack, corresponding to iron-planes segmented between 24 regions of proportional tubes.

The NA48/2 experiment at CERN was proposed to search for direct $\mathcal{CP}$ violation in $K^\pm$ decays, redesigned from the neutral kaon experiment NA48 which occupied the same experimental cavern [51]. Figure 2.10 displays the drawing of the NA48/2 beam-line and detector. NA48/2 also used an unseparated beam, but con-

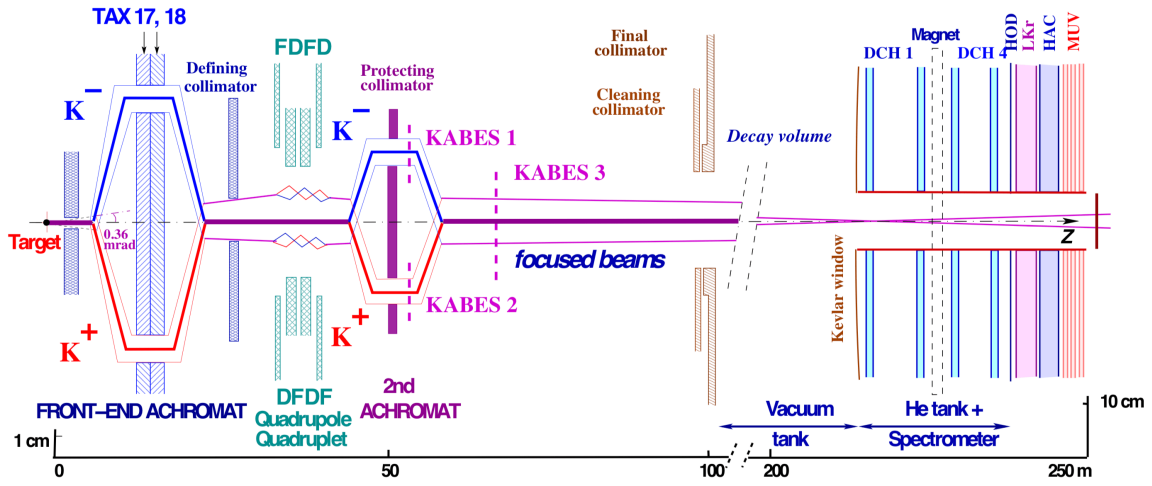

Figure 2.10: The NA48/2 beam-line and detector. Two kaon beams $K^{\pm}$ were propagated to the decay volume [47].

tained both $K^{\pm}$ which followed similar paths due to symmetric beam-optics. The secondary beam was tuned to have momentum (60 $\pm$ 3) GeV/c, and only 5.7% of particles in the beam were $K^{\pm}$. The evacuated decay-volume is followed by four $DCH1{\rightarrow}4$ drift-chambers, housed in a helium tank, where the spectrometer magnetic with field integral $\approx$0.4 Tm was sandwiched by the second and third chamber. The spectrometer was followed by the Charged Hodoscope (CHOD), consisting two planes (one vertical and horizontal) of plastic scintillator strips, used for fast triggering. The Liquid Krypton Calorimeter (LKr) is homogeneous electromagnetic calorimeter, using a 7 m^3 active volume of liquid krypton and 13248 transversely segmented cells, corresponding to a depth of 27 radiation lengths. Finally, the muon detector (MUV) was located furthest downstream, comprised of three planes of 2.7 m long plastic scintillator strips. The ends of each strip were coupled to PMTs, which were aligned horizontally in the first and third planes and vertically in the middle plane.

The invariant mass spectra for the three measurements are shown in Figure 2.11. Here, (a) corresponds to the two-dimensional reconstructed $K_{\pi ee}$ invariant mass versus dielectron mass for E865, with the top-left plot displaying the MC agreement in one-dimension. Both (b) and (c) are from NA48/2, corresponding to the $K_{\pi\ell\ell}$

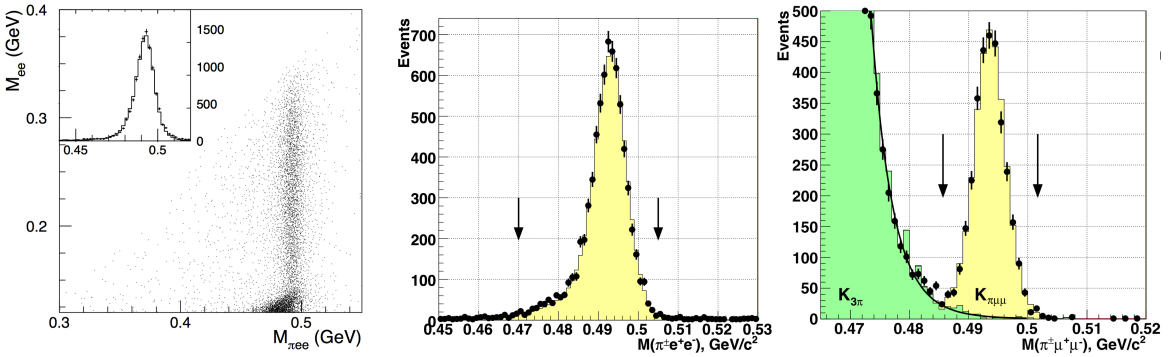

(a) E865 ee (b) NA48/2 ee (c) NA48/2 $\mu\mu$

Figure 2.11: The three invariant mass spectra where (a) is the ee channel from E865, (b) and (c) are the ee and $\mu\mu$ channels from NA48/2 experiments. The SR's are denoted by the arrows [49][47][48].

invariant mass including MC agreement for the ee and $\mu\mu$ channels respectively. In all analyses, the selection signature was the identification of a single pion track and opposite sign lepton pair originating from a three-track vertex in the decay volume. The E865 sample contains 10300 candidates with background contamination of 1.2%, mostly due to $K^+ \to \pi^+ e^+ e^- \gamma$ decays where the photon was missed. The SR was defined using the dielectron invariant mass of > 150 MeV/c^2. The sample of 7235 $K_{\pi ee}$ candidates from NA48/2 was collected using a SR defined as 470 $<$ $M_{\pi ee}$ $<$ 505 MeV/c^2 (slightly asymmetric with respect to M_K due to the radiative tail) with a background contamination of $(1.0 \pm 0.1_{\text{stat}})$%. The 3120 $K_{\pi\mu\mu}$ candidates were collected in SR $|M_{\pi\mu\mu}\text{-}M_K| < 8$ MeV/c^2. The sample suffers from a relatively large background contamination at $(3.3 \pm 0.5_{\text{stat}} \pm 0.5_{\text{syst}})$%, where the tail-end of secondary $\pi \to \mu\nu_\mu$ decays of the common $K^\pm \to \pi^\pm\pi^\pm\pi^\mp$ process enters directly into the SR. Due to the kinematic similarity of the signal and background decays, the separation between the two samples is small and can only be increased with improved tracking and a larger dipole field-integral. At NA62 both larger and significantly cleaner samples of the ee and $\mu\mu$ channels are expected to be collected over the lifetime of the experiment because of vast increases in instantaneous rate, improved tracking and larger field-integrals (see Chapters 3 and 4).

Using the current available measurements, the constraint on the NP contribution to

the Wilson coefficient C_9^B from the perspective of K-physics is,

$$C_9^{B,\mu\mu} - C_9^{B,ee} = -\frac{a_+^{\mu\mu} - a_+^{ee}}{\sqrt{2}V_{td}V_{ts}^*} = 19 \pm 79, \tag{2.59}$$

where a_+^{ee} is the average of the two results in Table 2.1 [40]. The determination of this value is consistent with zero, but the test is limited by the large error present in the $\mu\mu$ channel. The required improvement in precision is of the $\mathcal{O}(10)$ to probe NP, which requires samples of the $\mathcal{O}(100)$ larger. In this thesis, an analysis is performed to extract the LECs for the $K^+ \to \pi^+\mu^+\mu^-$ decay, using the 2016 and 2017 NA62 data (Chapters 6 to 9). This is a proof of concept to perform the most precise $K^+ \to \pi^+\mu^+\mu^-$ measurement at the newest K experiment at CERN.

3

The NA62 experiment

The NA62 experiment is designed to collect ≈ 100 ultra-rare $K^+ \to \pi^+\nu\bar{\nu}$ ($K_{\pi\nu\nu}$) decays in a time period of three years [52][53]. By performing a precise measurement of the branching fraction, a comparison with the SM prediction can be made in order to search for any discrepancy that could be attributed to NP. In this chapter, the main experimental strategy is discussed and a description of the full NA62 detecting apparatus is provided. As the $K_{\pi\nu\nu}$ decay is experimentally challenging, NA62 is well suited to perform other rare analyses such as the $K^+ \to \pi^+\mu^+\mu^-$ decay, which is the subject of this thesis. Special emphasis is placed on systems critical to the tracking optimisation and analysis performed in the following chapters.

3.1 Experimental strategy

The ultra-rare $K_{\pi\nu\nu}$ decay is an experimentally challenging process to measure. In principle, the characteristic signature is simple: A positively charged kaon, tagged in the beam, and a single charged pion track in the absence of any other signals in the downstream of the experiment. However, in an extreme high-intensity environment like the one at NA62, any decay or process that leads to this same experimental signature can contribute directly as background.

At NA62, there are multiple considerations to make with regards to reducing the possible backgrounds. One of the main sources are the other decay modes of the

K^+, described in Table 3.1. Here, a strategy to suppress these backgrounds is in-

Table 3.1: The main K^+ decay processes and the methods to suppress their signatures, followed by the two rare decays discussed in this thesis and their selection strategies [54][55].

Decay Channel	Label	Branching Fraction(%)	Reduction (Selection) Strategy
$K^+ \to \mu^+\nu_\mu$	$K_{\mu 2}$	63.56 ± 0.11	μ veto, two-body kinematics
$K^+ \to \pi^+\pi^0$	$K_{2\pi}$	20.67 ± 0.08	γ veto,two-body kinematics
$K^+ \to \pi^+\pi^+\pi^-$	$K_{3\pi}$	5.58 ± 0.02	Track multiplicity, three-body kinematics
$K^+ \to \pi^0 e^+\nu_e$	K_{e3}	5.07 ± 0.04	γ veto,E/p
$K^+ \to \pi^0\mu^+\nu_\mu$	$K_{\mu 3}$	3.34 ± 0.03	γ,μ veto
$K^+ \to \pi^+\pi^0\pi^0$	$K^0_{3\pi}$	1.76 ± 0.02	γ veto, three-body kinematics
$K^+ \to \pi^+\mu^+\mu^-$	$K_{\pi\mu\mu}$	$(9.4 \pm 0.6) \times 10^{-8}$	Three-track vertex, two μ veto signals
$K^+ \to \pi^+\nu\bar{\nu}$	$K_{\pi\nu\nu}$	$(1.7 \pm 1.1) \times 10^{-10}$	One π^+ track only

cluded, highlighting the variety of different methods that are required. Notably, the current experimental determination of $K_{\pi\nu\nu}$ suggests that the branching fraction of the more common modes is of the $\mathcal{O}(10^{10})$ larger, requiring a background suppression of the $\mathcal{O}(10^{11})$ to achieve a reasonable signal to background ratio $S/B \approx 10$.

The NA62 experiment uses a 75 GeV/c high-momentum K^+ secondary beam-line, allowing K^+ to decay in-flight. The $K_{\pi\nu\nu}$ kinematics are displayed in Figure 3.1: As

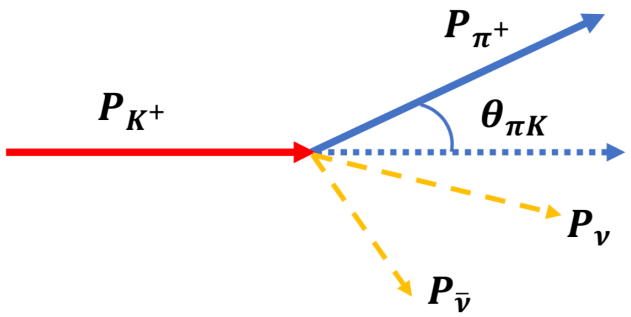

Figure 3.1: The $K_{\pi\nu\nu}$ kinematics; only the K^+ and π^+ are observable.

the $\nu\bar{\nu}$ pair is invisible to the experiment, the only measurable observables are the K^+ and π^+ momenta and the angle $\theta_{\pi K}$ between the two. As a fraction of the energy is 'missing', the most suitable description of the kinematics is the squared missing

invariant-mass m^2_{miss}, on the assumption that the observed charged track is a pion:

$$m^2_{miss} = (P_K - P_\pi)^2, \tag{3.1}$$

$$= M_K^2 + M_\pi^2 - 2E_K E_\pi + 2|P_K||P_\pi| \cos\theta_{\pi K}, \tag{3.2}$$

where $E_{K,\pi} = \sqrt{M^2_{K,\pi} + P^2_{K,\pi}}$. The unconstrained missing mass distribution is displayed in Figure 3.2, normalised to the total decay width. The signal decay is multiplied by a factor of 10^{10}. As $K_{\pi\nu\nu}$ is a three-body decay, the m^2_{miss} distribution is

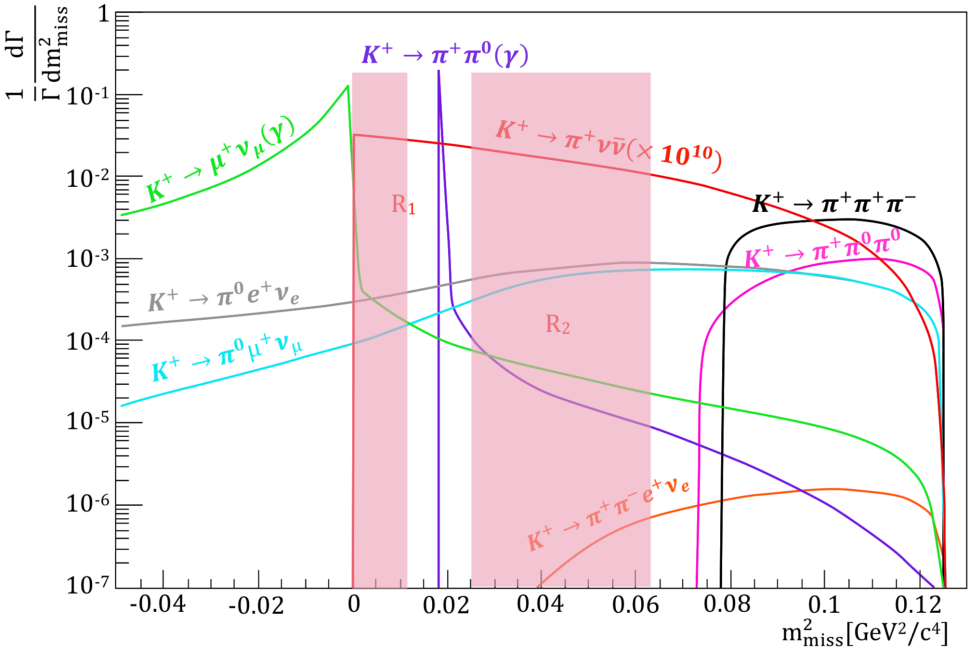

Figure 3.2: The missing mass^2 distribution for the main decay modes of the K^+, including the decay $K_{\pi\nu\nu}$ multiplied by a factor of 10^{10}. The $K_{2\pi}$ peak leads to the natural choice of two signal regions on either side, R_1 and R_2 [54].

continuous with upper and lower limits. The two-body $K^+ \to \pi^+\pi^0$ peaks sharply inside of the $K_{\pi\nu\nu}$ spectrum because a pion is correctly assigned, but has a radiative tail due to $K^+ \to \pi^+\pi^0\gamma$ decays. The most common decay $K^+ \to \mu^+\nu_\mu$ is always negative as $m_\pi > m_\mu$. Similar to the signal, the $K^+ \to \pi^+\pi^+\pi^-$ distribution is a constrained continuous distribution, but as two pions are undetected, the distribution is situated at large positive values of m^2_{miss}.

Two Signal Regions (SRs) are defined as follows:

- **Region I:** Between 0 and the sharp peak from $K^+ \to \pi^+\pi^0$

- **Region II:** Between the sharp $K^+ \to \pi^+\pi^0$ peak and before the low $K_{3\pi 0}$ threshold.

which reject the backgrounds for the majority of K^+ decays. A notable feature of Figure 3.2 is that both signal regions still have non-zero contributions from background decays which feature a π^0 or γ (for example, $K^+ \to \pi^0\ell^+\nu_\ell$ and $K^+ \to \pi^+\pi^0\gamma$). Powerful hermetic photon rejection of the $\mathcal{O}(10^8)$ is required to reject either the primary photons or the secondary $\pi^0 \to \gamma\gamma$ decays. A major motivation to use a high-momentum K^+ beam is the huge gain in photon detection efficiency, a feature that was a large limiting factor for background suppression in previous stopped kaon experiments such as E787 and E949 [24] [25] [52].

3.2 NA62 Beam-line

The NA62 experiment is situated in the ECN3 cavern in the North Area of CERN. The primary 400 GeV/c proton beam is delivered by the Super Proton-Synchrotron (SPS) in 30 s super-cycles with two five-second flat-top spills (also known as bursts). The extracted proton beam is directed onto the 400 mm long 4 mm radius T10 beryllium target at the start of the experimental cavern (Z = 0 m), from which the K12 high-intensity secondary hadron beam is derived. Before the decay volume at Z = 102.4 m, a series of magnet and collimator systems are used to shape and steer the K12 beam. Figure 3.3 contains a schematic of the vertical optics of the beam-steering in this region. A fraction of the secondary beam at an angle to maximise the kaon component passes through a 15 mm bore collimator towards the small aperture quadrupole triplet (Q1, Q2, Q3) which focus the secondary beam to a central momentum of roughly 75 GeV/c. Next the A1 front-end achromat, which consists of four dipole magnets, is used to remove off-momentum protons. The first two dipoles steer the beam vertically in order to sweep muons away and then traverse TAX1, a narrow bore collimator to absorb protons and other beam-halo particles. Before TAX2, a $1.3X_0$ tungsten radiator is placed, specifically chosen to cause positrons to lose energy via bremsstrahlung, while leaving the rest of the beam relatively untouched. Following A1, a series of quadrupoles (Q4, Q5, Q6) and collimators (C1, C2) are used to refocus the beam and remove unwanted beam parti-

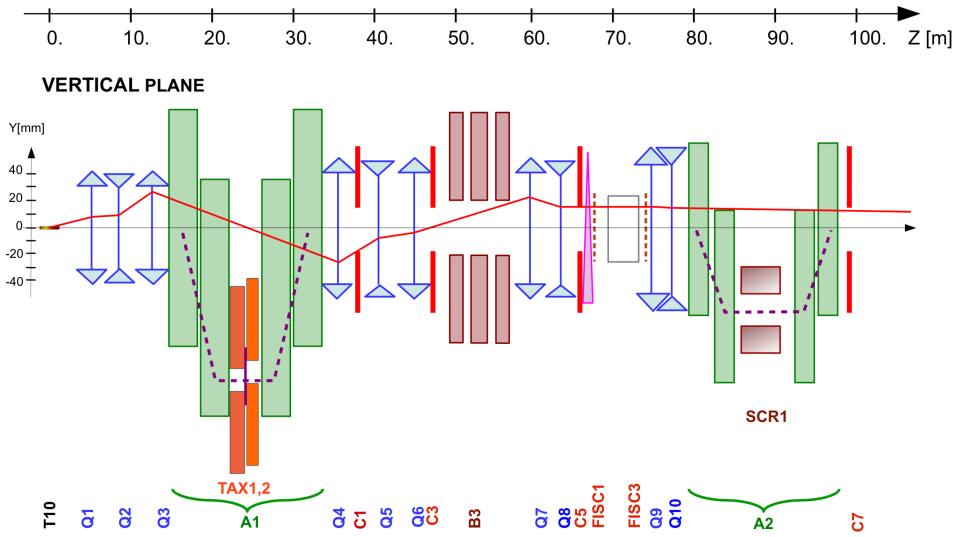

Figure 3.3: Optics and layout of the K12 beam in the vertical view. The solid line is the nominal trajectory of K^+ particle at 75 GeV/c from the target [53].

cles; at this stage, the degraded positrons from the radiator and particles outside of the (75 $\pm$ 0.8) GeV/c range are swept away by the C3 collimator, while surviving muons are removed by three 2 m long B3 dipoles The Cherenkov Differential counter (CEDAR) tank is situated at Z = 69 m. For high-efficiency kaon tagging, the beam must be reshaped to be parallel and aligned with the beam-axis, performed by two quadrupoles (Q7, Q8) and cleaning collimators (C4, C5) which absorb the beam tail-ends. The beam is steered up to the GTK tracking-system, which contains three silicon micro-pixel stations. The second A2 achromat is placed between GTK1 and GTK3, which has four vertically deflecting C-shaped dipoles. The achromat defocuses any remaining muons using the scraper magnets whilst shaping the secondary beam, with the final collimators absorbing any deflected particles. At the end of GTK3 at 102 m, the TRIM5 dipole magnet is used to deflect the beam by an angle of 1.2 mrad in the positive X-dimension. Figure 3.4 displays the X-direction of the beam with respect to Z. The TRIM5 deflection is corrected by -3.6 mrad at the MNP33 large-aperture dipole magnet which is situated inside of the STRAW spectrometer, as to match with the central aperture of the Liquid Krypton Calorimeter (LKr) calorimeter whose face is aligned with the central axis. The final stage is to dump the beam, which is deflected by -13.2 mrad just after the MUV3 detector. Table 3.2 contains the overall properties of the K12 beam as it enters the decay-volume.

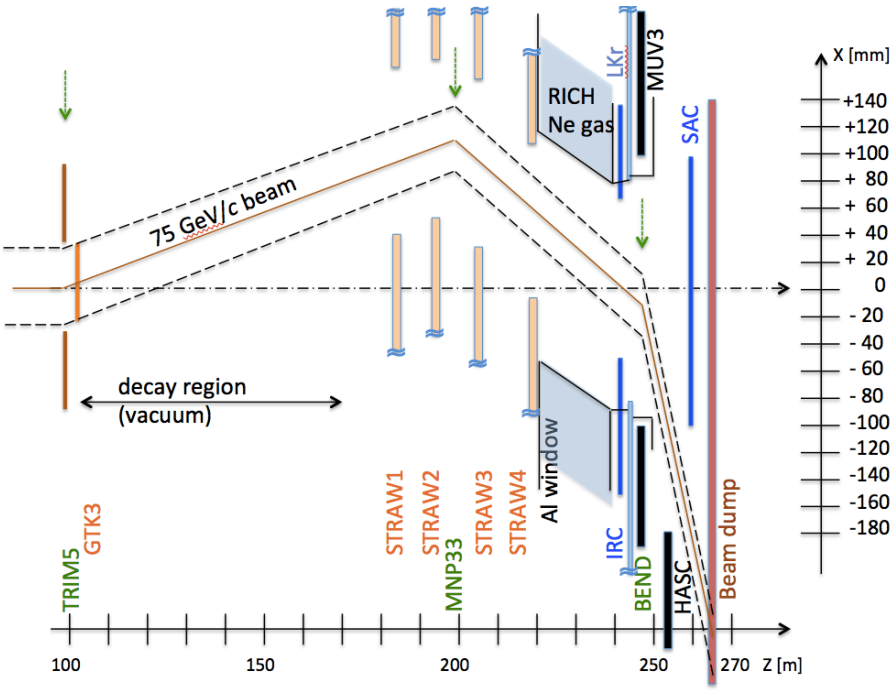

Figure 3.4: Downstream beam-line layout post TRIM5. The TRIM5 steers the beam by 1.2 mrad in the X-dimension up to the MNP33 dipole which then deflects the beam back by -3.6 mrad to match with the central aperture of the LKr which is on the central axis. The beam dump is placed after the SAC, and the beam is deflected by -13.2 mrad just after the MUV3 [53].

Notably, only 6% of the 75 GeV/c beam are kaons. As all downstream sub-detectors

Table 3.2: The nominal properties of the K12 secondary beam, including the instantaneous rates of the various beam components.

Momentum	Mean Value $\Delta P/P$ (RMS)	75 GeV/c 1.0%
Instantaneous Rate	p	173 MHz (23%)
	K^+	45 MHz (6%)
	π^+	525 MHz (70%)
	μ^+	$\approx$ 5 MHz (<1%)
	Total	750 MHz

have a central beam-hole, the vast majority of the K12 beam particles continue along the beam-axis without being observed downstream.

3.3 Detectors at NA62

3.3.1 Detector overview

A schematic drawing of the NA62 experiment is displayed in Figure 3.5. Here, K^+ decays from the K12 beam which occur in the fiducial volume between 102.4 m $<$ Z $<$ 180.0 m will be fully reconstructed. As the beam is at high-momentum, the sub-detector architecture is hermetic for particles up to 50 mrad with respect to the Z-axis. A short summary of the sub-detectors systems is provided in Table 3.3.

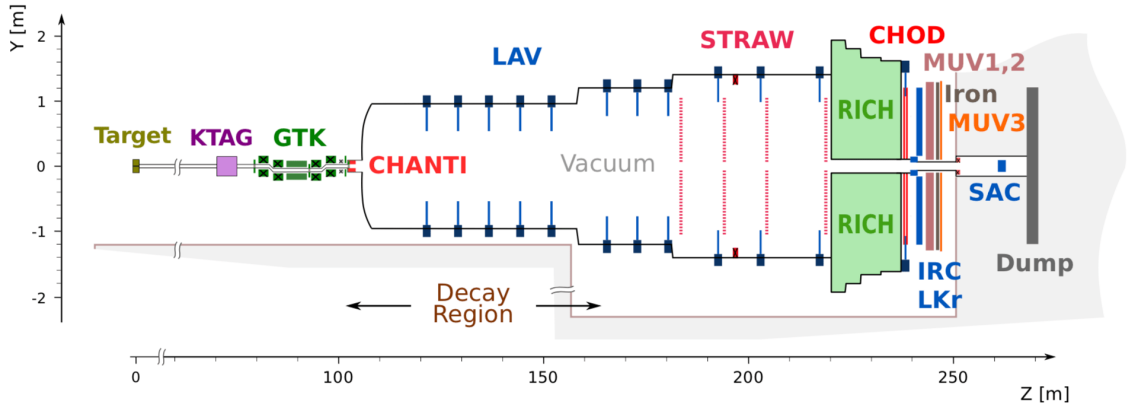

Figure 3.5: The NA62 beam-line and detector. The length is approximately 270 m, with K^+ decays occurring in the fiducial decay region [53].

The sub-detectors denoted as 'Other' are small systems crucial for the $K^+ \to \pi^+\nu\bar{\nu}$

Table 3.3: A short summary of the NA62 detector systems and their purposes.

System	Detector	Purpose
Tracking	GigaTracker	Precise K^+ momentum, time and position measurement
	STRAW	Reconstruct charged tracks from K^+ decays
Particle ID	KTAG	Uses Cherenkov light to time-stamp K^+
	RICH	Cherenkov detector to provide π and μ separation
Hodoscopes	NA48 CHOD	Fast minimum bias triggers for charged tracks
	NewCHOD	More complex kinematic triggers for charged tracks
Photon Veto	LAV	Large angle photon veto 8.5 mrad $< \theta <$ 50 mrad
	LKr	Intermediate photon veto between 1.5 mrad $< \theta <$ 8.5 mrad
	SAV	IRC and SAC, reject photons parallel to beam 1.5 mrad $< \theta$.
Muon Veto	MUV1,2	Hadronic calorimeters for π and μ separation
	MUV3	Behind an iron wall to detect μ only
Other	CHANTI	Rejects inelastic beam interactions from the GTK stations
	MUV0	Rejects large angle π^- from $K_{3\pi}$ downstream of RICH
	HASC	Rejects beam-parallel π^+ from $K_{3\pi}$ at the beam-dump

measurement only; the CHANTI is used to veto events containing inelastic K^+ interactions, whereas both the MUV0 and HASC are used to detect specific topologies of $K^+ \to \pi^+\pi^+\pi^-$ decays which contribute specifically as single track background. Below, only the most crucial detector systems to the analyses presented in the following chapters are described in detail.

3.3.2 Tracking

3.3.2.1 GigaTracker (GTK)

The GigaTracker (GTK) is designed to provide precision measurements of the K^+ momentum, time and position within the K12 beam. The GTK is situated upstream of the fiducial decay volume and consists of three hybrid silicon micro-pixel stations, offset vertically around the A2 achromat. Figure 3.6 contains a schematic drawing of the GTK system. The momentum measurements are extracted via the vertical

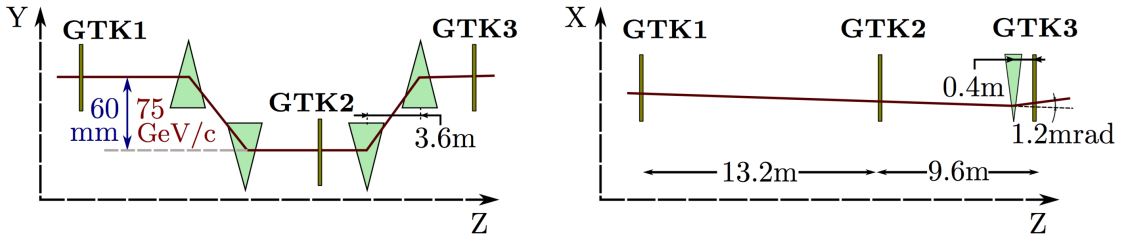

Figure 3.6: Left: the YZ view and right: the XZ view of the GTK. The red-line denotes the optimal path of a 75 GeV/c K^+ beam particle [53].

displacement of the kaon path between GTK1 and 2. The momentum precision is $\sigma(P) = 1.5$ MeV/c, whilst the angular resolution on the beam-slope determination $(dX/dZ, dY/dZ)$ is 16 μrad. As the GTK is subjected to an instantaneous rate of up to 750 MHz, the time resolution of the detector is of the $\mathcal{O}$(200 ps) in order to differentiate between the pile-up of kaons. Each station receives approximately 4×10^{14} neutrons per cm^2 in a year of data taking. The stations must be radiation hard as to last a year of data acquisition, while only corresponding to a small amount of material ($0.005X_0$). Each micro-pixel detector consists of 1.8×10^4 pixels of 300×300 μm^2 area, arranged in an array of 200×90 elements. Ten application-specific integrated circuits (ASIC) chips are used per station, used to read out 40×45 pixels

each.

3.3.2.2 Straw spectrometer (STRAW)

The Straw spectrometer (STRAW) is used to measure the momentum and trajectory of the K^+ decay products after the fiducial decay volume. Figure 3.7 contains a drawing of the end of the vacuum region where the STRAW is located. The spec-

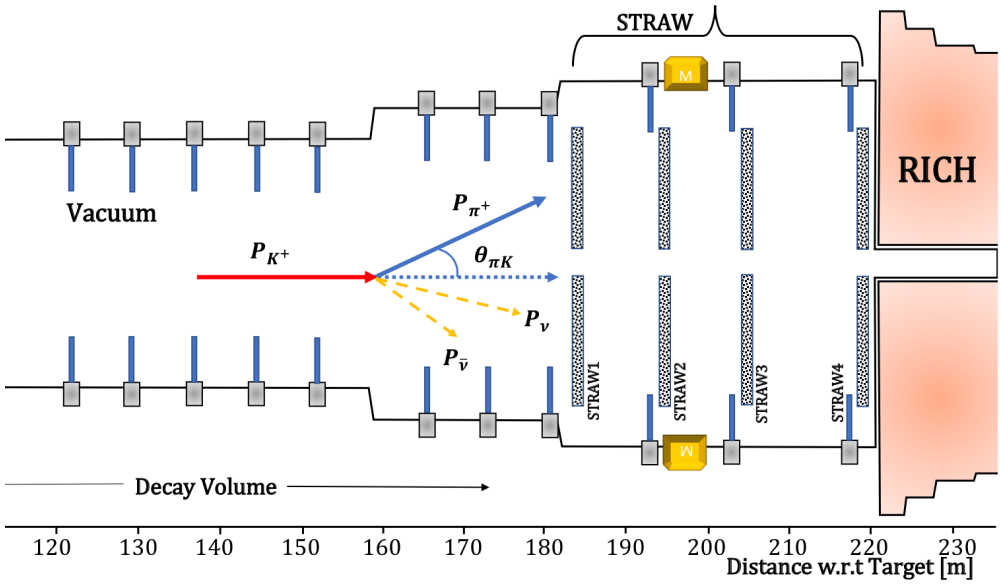

Figure 3.7: The STRAW; four chambers, separated by 10 m (15 m for chamber four), interspaced by the MNP33 dipole magnet.

trometer consists of four straw chambers and the MNP33 large-aperture dipole magnet. The magnet is positioned between the second and third chambers, and delivers a field integral of ≈ 0.9 Tm in the positive X-dimension (equivalent to a +270 MeV/c kick). The chambers are built using two modules, each containing two views. The first module contains the $(X, Y) = (0°, 90°)$ views, and the second is rotated by $-45°$ relatively, such that $(U, V) = (-45°, 45°)$. Each view consists of 448 straw tubes, divided into four layers and staggered to guarantee at least two hits per view. Figure 3.8 contains a schematic of the module orientation in the chambers, including the straw tube staggering. Each chamber has a diameter of 2.1 m and a 12 cm gap in each view at the centre for the beam-pipe. The straw tubes are constructed out of 36 μm thick polyethylene terephthalate (PET), and are 9.82 mm in diameter and 2160 mm in length. The tubes are gas-filled with a combination of 70% Ar and 30% CO_2

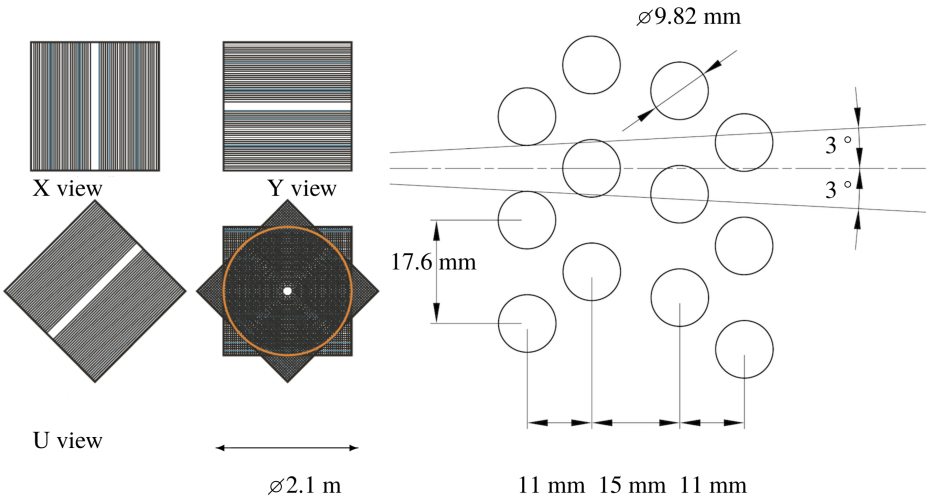

Figure 3.8: Left: how a full STRAW chamber is constructed using four (U, V, X, Y) views and right: the staggering of the four-layers of straw tubes to guarantee at least two hits for a track per view [53][56].

operated at atmospheric pressure. The straws are coated with 50 nm copper, and lined with 20 nm of gold, containing a tensioned gold-plated tungsten wire which are 30 μm in diameter. The combined material budget for the entire STRAW is ultimately very low, at $0.02X_0$, in order to reduce multiple-scattering. Each STRAW chamber uses custom front-end electronics to read-out data, where sets of 16 straw tubes are controlled by a FPGA served by two CARIOCA chips, developed for the LHCb muon read-out [57]. After evaluation, the track momentum resolution is consistent with design at $\sigma(P)/P = 0.3\% \bigoplus 0.005\%P$, whilst the angular resolution is $\sigma(\theta) = 60$ μrad for tracks with momentum P = 10 GeV/c and only 20 μrad at P = 50 GeV/c [53].

3.3.3 Particle Identification

3.3.3.1 Kaon Tagger (KTAG)

The role of the Kaon Tagger (KTAG) is to identify (i.e time-stamp) the 6% component of the K12 hadron beam which are K^+. The kaon tagging system comprises of two components; a differential CEDAR and a photomultiplier octagon (KTAG). The CEDAR is a nitrogen (N_2) 0.94 m^3 filled tank which is placed directly in the beamline at $Z = 69$ m after the T10 target. Figure 3.9 contains a schematic diagram of the

CEDAR, including the Cherenkov light-path of a K^+ candidate. By controlling the

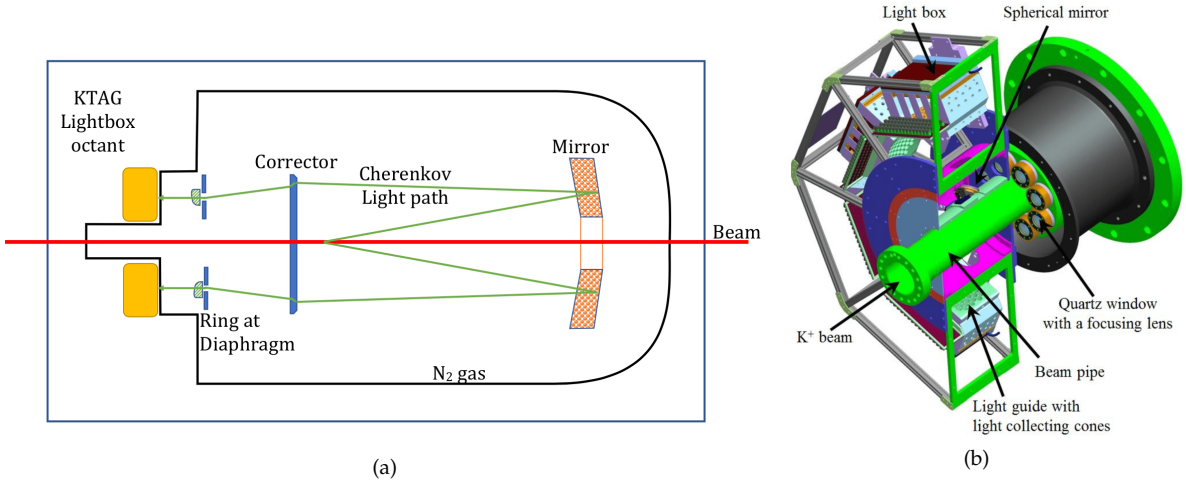

Figure 3.9: Schematic drawing of the CEDAR and KTAG. The tank is shown in (a), including the tracing of the K^+ Cherenkov light, whereas (b) displays the KTAG photo-multiplier octant which directs the Cherenkov light to eight light boxes [53][58].

pressure in the tank (1.7 bar for K^+ operation), the opening angle of the Cherenkov light-cone can be controlled such that only K^+ candidates generate rings which can pass through the narrow slit diaphragm and into the KTAG. Therefore, the KTAG is tuned with both a pressure and alignment scan to maximise detection efficiency. The light exits the diaphragm through eight quartz windows into an octagon of spherical mirrors which reflect the light radially towards the photo-multiplier 'light' boxes. Each light box (also known as a sector) contains 48 Photomultiplier Tubes (PMT), which are read-out using 128-channel Time to Digital Converter (TDC) boards. The coincidence of signals in multiple sectors is used to time-stamp each beam kaon with a time-resolution $\sigma(t)$ = 70 ps, as the photons generated from both protons and pions will not register coincidental signals in more than five light boxes due to the diaphragm. Naturally, the KTAG system is highly sensitive to beam conditions, and so the beam must be shaped to be flat and parallel with the beam-axis as it traverses the CEDAR tank.

3.3.3.2 RICH

The RICH is the downstream particle identification detector situated at $Z = 223$ m, used primarily to separate pions, muons and electrons in the momentum range be-

tween 15 GeV/c $<$ P $<$ 35 GeV/c. The RICH is an 17.5 m long ferro-pearlitic steel cylinder filled with neon-gas at atmospheric pressure, corresponding to a refractive index $(n-1) = 62 \times 10^{-6}$. Figure 3.10 contains a schematic drawing of the RICH. The tank gradually reduces in diameter, with the upstream section the largest at 4.2

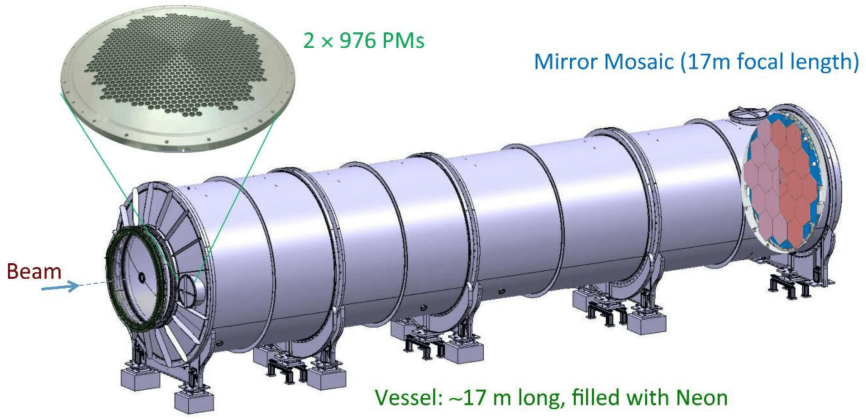

Figure 3.10: Schematic drawing of the RICH; the beam traverses the centre of the detector, with particles above threshold producing Cherenkov light which is reflected by the two halves of theRICH mirror (denoted by different colours) back to the two PMT arrays [53].

m to house the two honeycomb structured photo-multiplier matrices, each containing 976 PMTs residing either side of the beam-pipe. Any particle with mass m and momentum P above the threshold $P_{\text{threshold}} = m/\sqrt{n^2-1}$ will produce Cherenkov light. The light travels towards the RICH mirror, a mosaic constructed using 20 hexagonally-shaped spherical mirrors. The two vertical halves of mosaic have different centres of curvature, in order to reflect the Cherenkov light to either the left or right PMT matrix. This is to avoid light intercepting the beam-pipe. The Cherenkov cone with angle,

$$\cos(\theta_c) = \frac{1}{n\beta} = \frac{1}{n}\sqrt{1+\frac{m^2}{P^2}} \tag{3.3}$$

will form a ring on the PMT matrix with radius $r = f\tan(\theta_c)$, where f = 17 m is the focal length. By approximation that $n-1 \ll 1$ and that the mass m is far smaller than momentum P, the radius can be collapsed using the small angle approximation to

be,

$$r = f \tan\theta_c \approx f\sqrt{\frac{2(n-1)}{n} - \frac{m^2}{nP^2}}. \tag{3.4}$$

Therefore, the RICH can be used in combination with the spectrometer; the momentum measurement can assign the particle type of a track based on the radius.

3.3.4 Hodoscopes

3.3.4.1 NA48 Hodoscope (CHOD)

The NA48 Charged Hodoscope (CHOD) is a device used to obtain a fast response to the charged products of K^+ decays. Figure 3.11 displays a schematic drawing of the detector.

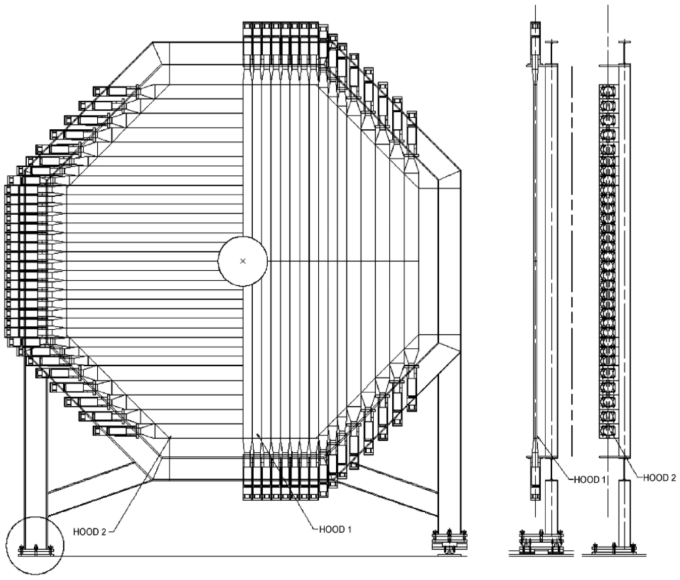

Figure 3.11: Schematic drawing of the NA48 CHOD. The first plane is built using vertical slabs whilst the second contains horizontal slabs [53].

The CHOD is comprised of two consecutive octagonal planes separated by 40 cm, situated at $Z = 239$ m downstream of the T10 target. Each plane consists of 64 plastic scintillator slabs, with the first aligned vertically and the second horizontally. Each slab is 20 mm thick, corresponding to $0.1X_0$, but vary in length (between 600 mm for outer counters to 1210 mm for the inner) depending on their position relative to the beam-hole. The slabs are read-out at one end by fast PMTs; for a charged particle

traversing the detector, two time measurements are performed corresponding to a single vertical and horizontal slab measurement. The time resolution of the CHOD is $\sigma(t)$ = 400 ps, compatible with the NA48 experiment despite the far higher instantaneous rate, providing a suitable source for fast minimum bias triggers for decays with at least a single charged track.

3.3.4.2 NewCHOD

The NewCHOD is a charged hodoscope designed specifically for NA62, situated just before the NA48 CHOD at $Z = 238$ m. Figure 3.12 contains a schematic diagram of the face of the NewCHOD, including the positioning of the 152 plastic scintillator tiles.

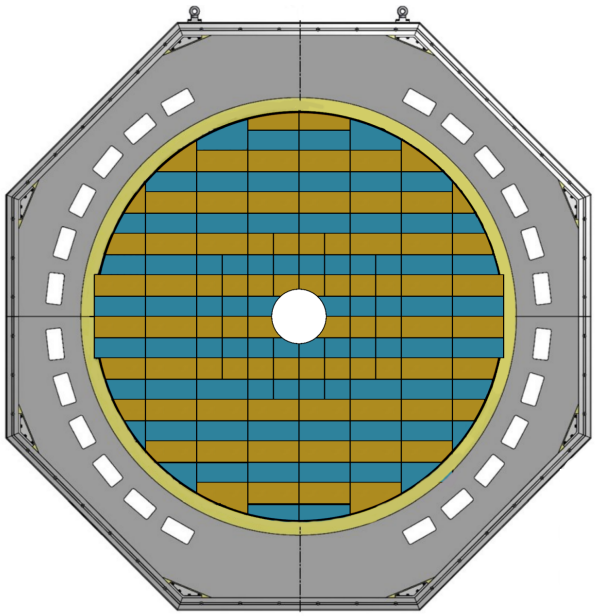

Figure 3.12: Schematic drawing of the NewCHOD. The single plane structure uses 152 tiles, with unique sizes and shapes at the edges and at the beam-hole of the detector [59].

Each tile is 30 mm thick, covering a region between 140 mm $<$ R < 1070 mm. The tile centres are spaced by 107 mm such that they overlap by 1 mm in the Y-dimension; this was achieved by staggering the tiles longitudinally around a 3 mm central support foil. Each tile is 108 mm in height, and are either 134 or 286 mm wide depending on the position relative to the beam-pipe. Only the tiles on the outside edge of the detector are unique sizes. The resulting material thickness of the detector is $0.13X_0$. The scintillation light from each tile is collected by wavelength-shifting fibres and

detected by a pair of Silicon PMTs (SiPM). The 304 SiPM pairs are read out by a single 512-channel TEL62 board [60]. The time resolution is slightly larger than for the NA48 CHOD, at $\sigma(t)$ = 1 ns. The NewCHOD is used to define more complicated geometrically based firmware algorithms for use in the low-level trigger. Most of the criteria use NewCHOD quadrants, defined by dividing the face of the detector into four quarters of equal size. These quadrant triggers are used for decays containing either single or multiple charged tracks (see Section 3.4).

3.3.5 Photon Veto

3.3.5.1 Large Angle Veto (LAV)

The Large Angle Veto (LAV) is a system of twelve independent ring-shaped detectors placed at longitudinal positions beginning at the start of the decay volume and finishing just before the CHOD (Figure 3.5). As the LAV spans a large longitudinal range, the inner and outer ring radii increases with Z as the vacuum tank size increases. The LAV covers the angular region between 8.5 mrad $< \theta_\gamma <$ 50 mrad with respect to the Z-dimension, designed to detect wide-angle photon emission originating from the $\pi^0 \to \gamma\gamma$ in the $K_{2\pi}$ decay. Figure 3.13 displays a single LAV station, most of which contain either four or five layers of lead-glass crystal blocks. The rings are staggered with respect to the first layer so that the gaps between the crystals are covered, with each block corresponding to 10 $\times$ 37 cm^2 of surface area relative to the Z-axis. High-energy photons which interact with the glass blocks generate electromagnetic showers which produce Cherenkov light in the material; the resulting photons are detected by the PMTs coupled to the base of each block. To ensure a 10^8 rejection power for the photon veto overall, the LAV has achieved the design inefficiency better than 10^{-4}. This level is due to low-energy $E_\gamma \leqslant 200$ MeV photons which are difficult to distinguish from noise in the detector.

3.3.5.2 Liquid Krypton calorimeter (LKr)

The Liquid Krypton calorimeter (LKr) is the same detector used in the NA48 experiment. Placed at Z = 241 m downstream of the target, the LKr is an electromagnetic, quasi-homogeneous calorimeter which uses 7 m^3 of liquid krypton housed inside

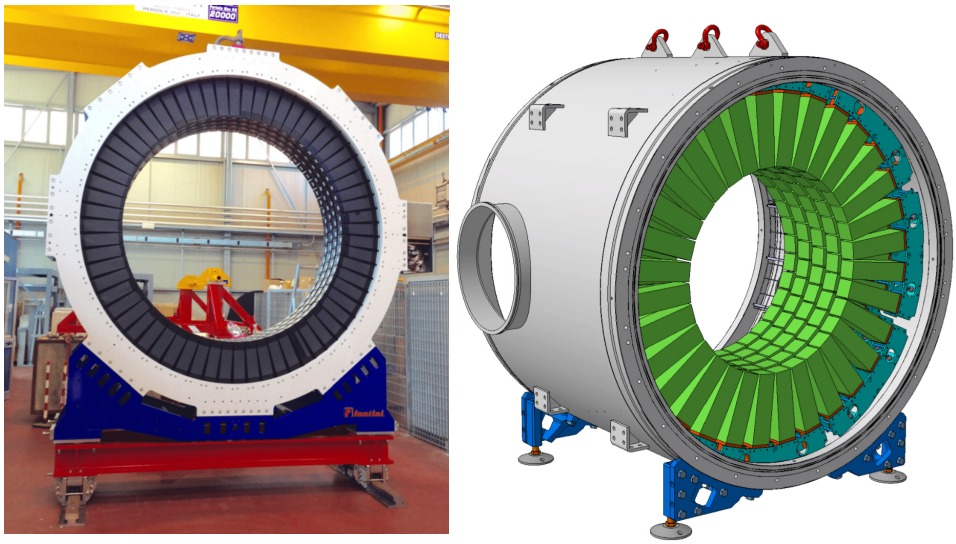

(a) (b)

Figure 3.13: A LAV station, where (a) is a photograph of LAV12 before insertion into the beam and (b) is a schematic drawing with five lead-glass layers [53][61].

cryostat at 120 K. At NA62, its principle purpose is to veto photons in the angular region between 1.0 mrad $< \theta_\gamma <$ 8.5 mrad with respect to the Z-dimension. The face of the calorimeter is octagonal, covering a region between 80 mm $<$ R $<$ 1280 mm, and is 1270 mm in depth which corresponds to $27X_0$. Figure 3.14 displays a quadrant of the LKr including the 2×2 cm^2 Cu-Be electrode cells. In total, 13248 cells cover the transverse face of the detector and the each span the full depth. To handle the increased rates relative to NA48, a brand-new Calorimeter Readout Module (CREAM) was developed. The energy resolution of the LKr as measured by NA62 was estimated based on simulated data,

$$\frac{\sigma(E)}{E} = \frac{4.8\%}{\sqrt{E}} \bigoplus \frac{11\%}{E} \bigoplus 0.9\%, \tag{3.5}$$

which is in agreement with the NA48/2 resolution [53]. With the energy measured in GeV, the first term is shower-dependent, the second due to noise and the final due to residual cell miscalibration.

3.3.5.3 Small Angle Veto (SAV)

The Small Angle Veto (SAV) consists of two systems, the Intermediate Ring Calorimeter (IRC) and the Small Angle Calorimeter (SAC). The IRC sits just before the LKr

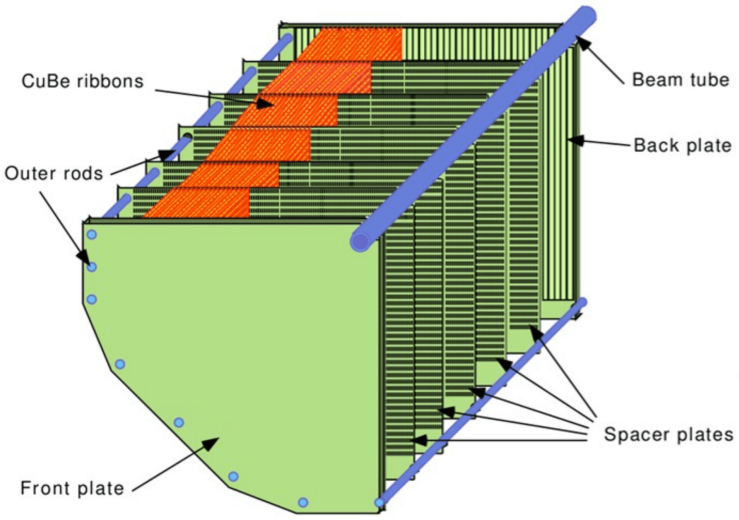

Figure 3.14: Schematic drawing of a quadrant of the LKr. The Cu-Be cells traverse the depth of the detector, kept separate by spacer panels [53].

and wraps directly around the beam-pipe. The SAC is placed at $Z = 261$ m directly in the beam-line, after the K12 beam has been deflected to the dump. Both are used to detect photons which are emitted parallel to the beam with angles below 1.5 mrad. Figure 3.15 contains a photograph of both detectors. Both the IRC and SAC are Shashlik calorimeters, using plastic scintillator as the active volume and lead as the absorber. The IRC covers the transverse region between 120 mm $<$ R $<$ 290 mm, slightly offset in positive X. The IRC contains two separate modules, with the first containing 25 layers and the second 45, where each layer is 3 mm thick corresponding to lead absorber and plastic scintillator. The depth is equivalent to $19X_0$. The SAC is similarly designed but is contained to a single volume, consisting of 70 layers with dimensions 205×205 mm^2 and also corresponds to $19X_0$. Four PMTs are used to read-out the scintillation light.

3.3.6 Muon Veto

3.3.6.1 MUV1,2

The MUV1,2 are both iron and scintillator hadronic sampling calorimeters. The purpose of these calorimeters is to provide energy-based separation for pions and muons. In conjunction with the LKr, pions are expected to have deposited their energy in at least one of the detectors such that the value $E_{\mathrm{Tot}} = E_{\mathrm{LKr}} + E_{\mathrm{MUV1}} + E_{\mathrm{MUV2}}$

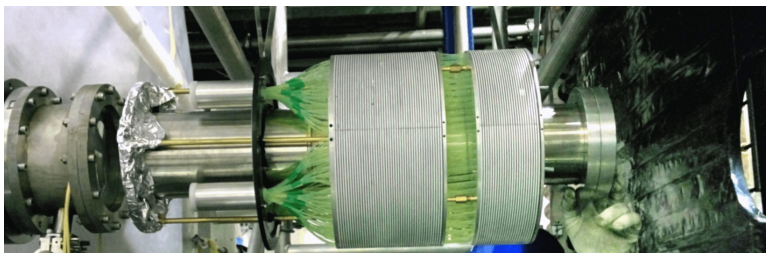

(a)

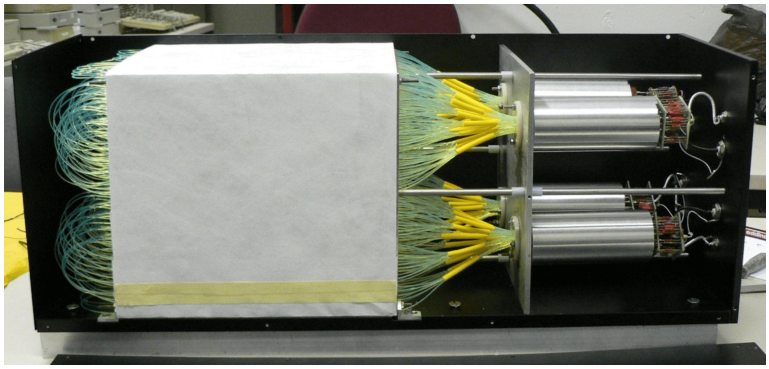

(b)

Figure 3.15: Photograph of (a) the IRC and (b) the SAC. The IRC wraps around the beam-line, whereas the SAC is inserted directly into the beam-line [53].

can be used as a particle identification discriminant. Figure 3.16 contains a schematic of the full MUV system. The MUV1(2) has 24(22) layers, equivalent to 4.1(3.7) interaction lengths. For the MUV1, 22 of the 24 layers cover a transverse region of 2700 $\times$ 2600 mm^2, whilst the first and last layers extend to slightly larger dimensions to cover the electronics. Each iron plates is separated by 9 mm thick, 60 mm wide scintillator strips, which are arranged in both the horizontal and vertical direction and span the full transverse size of the detector. Strips in the same consecutive position are read out to a pair of PMTs (one for each end of the strip) by wavelength-shifting fibres; this leads to $22 \cdot 2$ vertical and horizontal channels, equivalent to 176 channels overall. The MUV2 is the refurbished front module of the NA48 hadron calorimeter (HAC) but with reversed longitudinal orientation. Each MUV2 scintillator plane contains 22 strips, with each spanning 1300 mm, equivalent to half of the transverse size of the detector. The same read-out strategy is used as MUV1, with $11 \cdot 2$ vertical and horizontal channels, resulting in 88 channels overall.

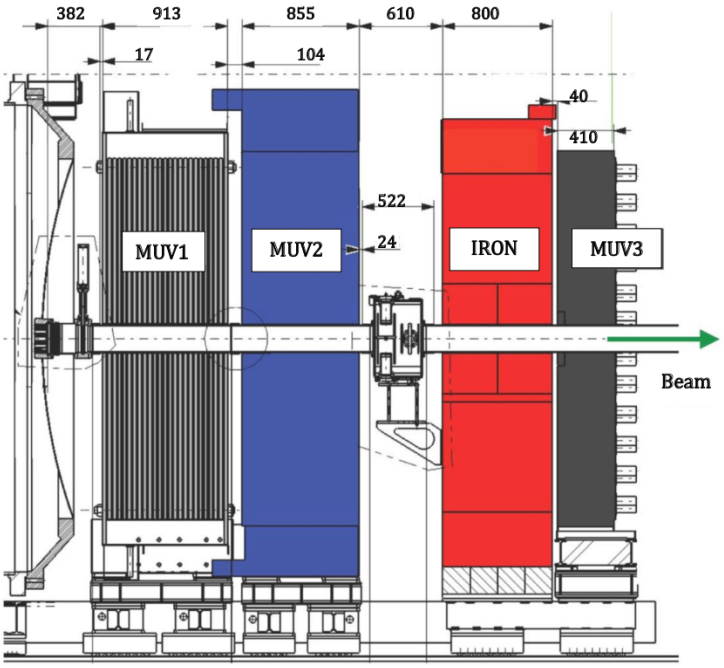

Figure 3.16: A schematic of the full MUV system. MUV1 and MUV2 are both sampling hadronic calorimeters used to separate pions from muons, whereas the MUV3 is used to detect/veto muons which traverse the iron wall [54][53].

3.3.6.2 MUV3

The MUV3 detector is designed to be a fast muon veto. It is located behind an 80 cm deep iron-wall at the end of the MUV system, where the wall is used to stop any surviving hadrons (Figure 3.16). The MUV3 is a large square-faced detector with transverse size 2640 $\times$ 2640 mm^2. Like the NewCHOD, the MUV3 consists of plastic scintillator tiles, with 140 regular 220 $\times$ 220 mm^2 tiles which cover the majority of the face, and eight smaller tiles (4/9 of the regular area) which are placed around the beam-hole as the rate in that region is substantially higher. Figure 3.17 contains the expected srates for the MUV3 tiles for nominal beam conditions. Notably, the rate increases as the tiles approach the beam-pipe, with one 'hot-tile' which counts at 3.2 MHz. This is due to the decay of beam pions to muons. Two PMTs are used to read-out each tile, placed directly behind the scintillator. The signals are fed to a constant-fraction discriminator (CFD) which are then sent to a TEL62. In total, the MUV3 has 296 read-out channels. The time-resolution on the individual MUV3 channels is $\sigma(t) \approx 600$ ps. With the average reconstruction efficiency above 99% (see

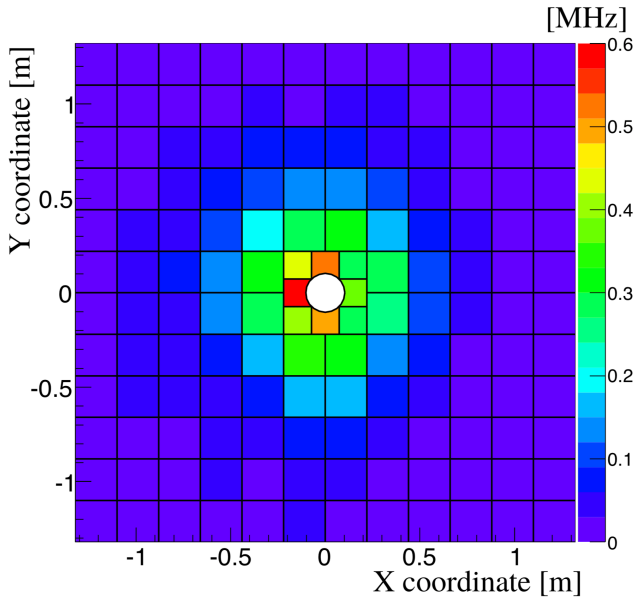

Figure 3.17: The MUV3 tile rate for nominal beam conditions. A single 'hot-tile' is present in the inner tiles, with rate 3.2 MHz which is higher than the colour-scale [53].

Figure 6.3), the MUV3 is the primary muon identification system at NA62.

3.4 Trigger and data acquisition (TDAQ)

One of the most important aspects of the experiment is the Trigger and Data Acquisition (TDAQ) system. The TDAQ refers to the series of processes which collect data and record it to disk for further analysis. In this section, an overview of the NA62 TDAQ is provided, including greater emphasis on the aspects that are heavily involved in the $K^+ \to \pi^+\mu^+\mu^-$ analysis described between Chapters 6 to 9.

3.4.1 The trigger logic

The NA62 experiment adopts a multi-level triggering strategy to ultimately reduce the downstream particle flux (10 MHz) to a rate limited by the available bandwidth for storing the data to tape (≈100 KHz). A minimum bias approach is not feasible at this instantaneous rate, requiring a complicated TDAQ strategy to achieve stable data-acquisition [62]. The trigger levels are as follows:

- $\mathbf{L_0}$: A hardware-based trigger, evaluating sub-detector digitised signals before passing the decision to the Level 0 Trigger Processor (L0TP). Each trigger 'prim-

itive' can then be used to build a trigger 'mask', where the L0TP returns a decision based on the timing coincidence of multiple primitives. The maximum L0 hardware trigger rate is 1 MHz.

- **L_1**: A trigger implemented in software, requiring loose selection criteria for specific sub-detectors based upon the signal decay of interest. Each 'algorithm' is applied sequentially, aiming to reduce the trigger rate to below 100 KHz.

The first two stages of the trigger were in operation for both 2016 and 2017. Figure 3.18 displays the flow of the TDAQ for each NA62 sub-detector. Only five TEL62

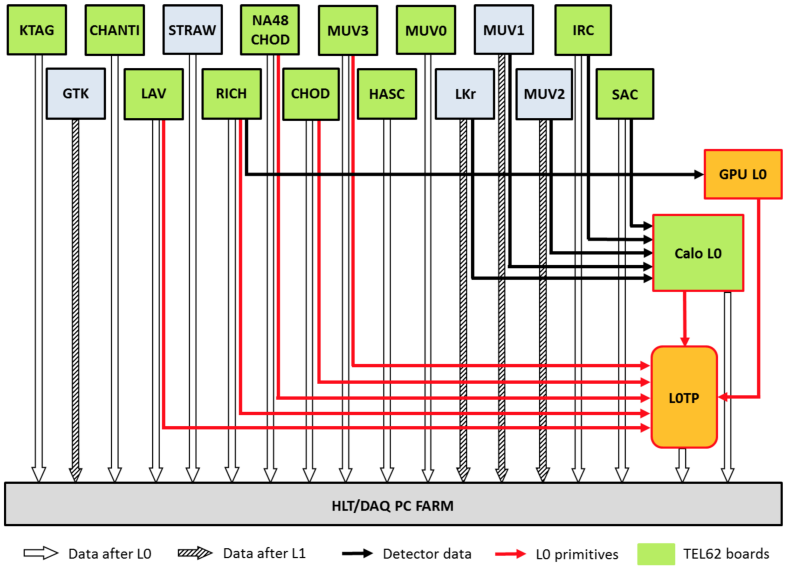

Figure 3.18: The general flow of the TDAQ for every sub-detector. The red arrows denote detectors which generate L_0 primitives, whilst the black contribute to the L_0 Calo initially. Detectors in green use TEL62 boards [63].

detectors contribute to the L_0, whilst all calorimeters (LKr , MUV1, MUV2) pass through the L_0 Calo. As the L_1 trigger is applied at the software level, it is possible to utilise any of the detectors. A brief description of the detectors used in the trigger in 2016 and 2017 is provided in Table 3.4.

3.4.2 L_0 primitives

The L_0 hardware trigger is designed to use a small set of the fastest sub-detector signals to reduce the input rate from 10 MHz to below 1 MHz. Each sub-detector generates primitives, a time-stamped data-packet containing information on whether

Table 3.4: Brief description of the detectors which contribute to the L_0 and L_1, including the type of criteria implemented.

Trigger Level	Detector	Type of Criteria
L_0	RICH	Loose PMT multiplicity for charged tracks
	NewCHOD	Geometric and tile based multiplicity for charged tracks
	CHOD	Minimum bias multiplicity for charged tracks
	LAV	Fast γ veto using LAV12
	Calorimeters	Total energy using LKr and MUV1,2
L_1	KTAG	Loose K^+ time-stamping
	LAV	γ veto using all LAV stations
	STRAW	Partial reconstruction of charged tracks

specific criteria were met according to the trigger firmware for each sub-detector. The majority of the detectors involved in the L_0 generate primitives using TEL62 boards equipped with TDCs, whilst the calorimeter primitives are produced using the CREAM readout system (Figure 3.18) [60]. Only the TEL62-generated primitives are important for the analysis presented in Chapter 8. Each TDC primitive consists of a 64-bit data block, which is segmented into 12.5(6.25) ns time slots in 2016(2017). If multiple primitives are generated at times within the resolution of the sub-detector, the primitives are merged. As all TDC triggers are based on hit multiplicity in the same event, hits must be sorted to build the time-clusters which produce the primitives. This is a feature which has become important when interpreting specific inefficiencies (see Chapter 7).

In order to build a L_0 'mask', the L0TP identifies which primitives were simultaneously true within a 10 ns time-window, which is the reason for the time-sorting. If any of the primitive coincidences match with any of user-requested trigger masks, the L_0 trigger is fired and the event is passed to the L_1 software stage. Two masks were important for this thesis, defined as the following combination of primitives:

- **Multi-track trigger:** RICH$\cdot$ Q_X,
- **Dimuon trigger:** RICH$\cdot$ Q_X $\cdot$ MO_2.

The primitives are described below,

- **RICH**: Low threshold-multiplicity requirement of at least two or more RICH PMT supercells (defined as 8-adjacent PMTs) fired within a 12.5(10) ns coinci-

dence for 2016(2017). Expected to be efficient for events containing positively charged tracks.

- $\mathbf{Q_X}$: Hits in at least two diagonally-opposite NewCHOD quadrants, within a 10 ns coincidence. This primitive is designed to collect three-track decays.
- $\mathbf{MO_2}$: Hits in at least two or more outer MUV3 pads within a 10 ns coincidence, designed to collect dimuon final states.

To perform rare three-track decay measurements, one must collect a normalisation sample of an abundant, well-understood decay with three-track topology, i.e $K^+ \to \pi^+\pi^+\pi^-$ ($K_{3\pi}$) through the Multi-track mask. The Dimuon mask is used to collect a sample of rare $K^+ \to \pi^+\mu^+\mu^-$ ($K_{\pi\mu\mu}$) decays, using the same logic apart from the additional MO_2 condition. By using close to the same logic, most systematic effects can be vastly reduced by normalisation.

3.4.3 L_1 algorithms

After an event has passed the L_0 stage, the L_1 software trigger is put into effect on the PC farm. The algorithms are applied sequentially, meaning the rate is subsequently reduced at each stage. Again, there are three relevant algorithms which are applied at the L_1 stage for both Multi-track and Dimuon triggers. All of the possible L_1 algorithms in 2016 and 2017 data are described below,

- **KTAG:** Searches for at least five out of eight KTAG sectors to be in time-coincidence and within 10 ns of the L_0 trigger time. This is to positively identify a beam kaon candidate consistent with the event time.
- **!LAV**: Used as a veto, the algorithm searches for at least two hits with leading and trailing signal edges within the full LAV detector; the time of the leading signal edge of the hit must also be within 10 ns of the L_0 trigger time. The motivation is to suppress the abundant $K^+ \to \pi^+\pi^0$ background by detecting at least one photon from $\pi^0 \to \gamma\gamma$.
- **STRAW$_e$:** Denoted 'e' for 'exotic', this algorithm uses a fast two-dimensional Hough transform and simple momentum evaluation to perform a crude track-reconstruction [64]. The trigger accepts events containing a negative-track.

Negative tracks appear only in three-track decays and are typically a signature in exotic decay searches.

For the analysis described between Chapters 6 to 9, either all or at least a combination of the above L_1 algorithms were implemented.

4

Simulation of the MNP33 fringe field

In this chapter, the simulation of the MNP33 magnetic fringe field is described. Using a database of field measurements recorded in 2013, a three-dimensional map was created by fitting measurement planes with smooth two-dimensional polynomial surfaces. By extrapolating the parameters of the surfaces longitudinally, a map covering the full three-dimensional geometric acceptance of the vacuum tank was created. The accuracy of the map was calculated by direct comparison with raw measurements, and the systematic errors estimated to ensure that the map performs to within the same tolerances set by the tracking system for precision momentum measurements.

4.1 Motivation for mapping fields

The implementation of a highly accurate three-dimensional field map for NA62 Monte Carlo (NA62MC) is mutually beneficial to all aspects of data-analysis at NA62. If the simulation provided only a simplistic representation of the field present in the detector (for example, a fixed momentum kick at the spectrometer magnet), the accuracy of the MC productions would be severely comprised with respect to the raw data in the following categories:

- Track/vertex trajectory and quality.
- Sub-detector illuminations downstream.

- Accuracy of signal and background acceptances.

If the tracking trajectory is inherently different between data and simulation, the illumination of the sub-detector systems downstream of the spectrometer will differ between MC and reality. As simulated samples are used to estimate signal acceptance, the discrepancy renders the calculation completely unreliable. This is especially detrimental for the precision measurement of rare or ultra-rare processes such as $K^+ \to \pi^+\mu^+\mu^-$ or $K^+ \to \pi^+\nu\bar{\nu}$. To avoid this, the simulated map must be three-dimensional to cover every possible trajectory through the field.

Three-distinct regions based upon the longitudinal Z coordinate are displayed in Figure 4.1. The regions are designated based on the nature of the field approaching

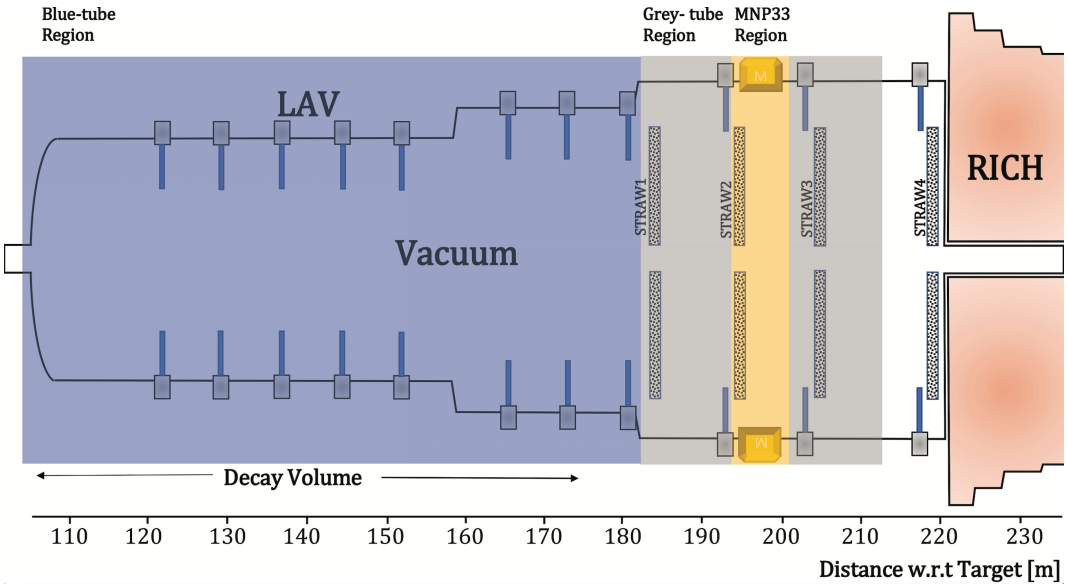

Figure 4.1: The NA62 decay volume, divided into the three natural field-map regions. The blue-tube region makes up the majority of the vacuum tank and contains LAV1-8. The grey-tube region sits symmetrically around the MNP33 magnet region, and houses the spectrometer stations.

before and after the MNP33 magnet, as explained below:

- **The blue-tube**: The region between $104.458 \leqslant Z[\text{m}] < 181.175$ contains the majority of the vacuum tank, consisting of the first eight LAV stations interspaced by twelve 6 m long steel 'blue' tubes. The blue-tube is the first region that charged tracks traverse before reaching the spectrometer. The field is typically small in this region of $\mathcal{O}(10\ \mu\text{T})$ and is due a combination of two independent

sources. Firstly, the steel tubes are reworked from the NA48/2 experiment, where residual magnetisation occurs as a result of work-hardening. A contribution of similar size is also expected due to the non-zero earth field, known to be $\approx 40\ \mu$T at the geographic location of the experiment [65].

- **The grey-tube**: The regions between $181.175 \leqslant Z$[m] < 193.363 and $200.907 < Z$[m] $\leqslant 212.200$ contain the grey-tube segments, situated either side of the MNP33 magnet. In this region, the fringe field of the MNP33 magnet is dominant. The field increases rapidly to values approaching ≈ 1 mT, and is maximal for Z-positions which are closest to the magnet.

- **MNP33 Dipole Magnet**: The region between $193.363 \leqslant Z$[m] $\leqslant 200.907$ contains the MNP33 large aperture dipole magnet. The magnet is situated in between the two central spectrometer chambers, and was substantially rebuilt since the NA48/2 experiment. The magnet has a large rectangular cross-section of 4.4 wide by 4 m high. The physical dipole is 1.3 m long, centred at 196.995 m, and the iron yokes open by 2.4 m vertically and 3.2 m horizontally. The primary field points in the negative Y-dimension, and is substantially larger than the other components. Over the MNP33 volume, the integrated vertical field delivers $I_{B_Y} = \int B_Y.dZ \approx$ 0.9 Tm, corresponding to a transverse momentum kick in the X-dimension by ≈270 MeV/c. The field strength at the centre of the magnet is 0.38 T.

At the time of this analysis, both the blue-tube and MNP33 field maps were developed and implemented into NA62MC[66]. The missing component is the fringe field of the grey-tubes, which is developed here. The strategy to develop the field map is to use a large sample of field measurements at different (X, Y, Z) coordinates to build a three-dimensional field map, as follows:

- Fit each (X, Y) measurement Z-plane with a smooth two-dimensional curve which accurately describes the surface for each field orientation.

- Develop a criteria for identifying and removing rogue measurements, to improve the quality of the fit.

- Extract the parameters in each plane, and then fit the longitudinal dependence of each parameter with a suitable function.
- Link the map to the blue-tube and MNP33 field-maps already in place for NA62MC, ensuring a slow and physical transition at the cross-over boundary.

The fringe field integral must be known to within the following precision:

$$\sigma_{I_B} = \Delta \int B \cdot dZ \; < \; 3 \times 10^{-4} \, \mathrm{Tm}, \tag{4.1}$$

as outlined in Ref [67], in order to have a negligible effect on the measurement of kinematic variables by the spectrometer. Notably, processes containing charged tracks are insensitive to the B_Z component of the magnetic field, as the NA62 beam-direction is roughly parallel to the Z-axis [68]. Additionally, the MNP33 is anti-symmetric about the centre of the magnet resulting in the complete cancellation of the upstream and downstream B_Z components.

A description of the measurement procedure for the vacuum tubes is found in Section 4.2, followed by the construction of the field map in Section 4.3, where the surface fits, point deletion and map-linking is performed. Finally, the systematic errors of the map are estimated in Section 4.4.

4.2 Measurement sample

The field measurements were performed in September 2013. A sensor comprised of three orthogonal Siemens KSY44 Hall probes was used to measure the field strength in each dimension, explained fully in Ref [67]. In the vacuum tubes, measurements were performed to cover the forward decay 'cone' with half-angle of 20 mrad, ensuring complete coverage of the secondary K^+ decay products between the GTK3 and STRAW2. This was implemented using the grid structure displayed in Figure 4.2. The sensor was placed at each (X,Y) position in the grid-mount and a full set of measurements were recorded at specific values of Z in order to create a series of measurement planes. For the blue-tube, the spacing was typically 2 m between planes, with fifteen planes before 120 m recorded using only the inner grid mount

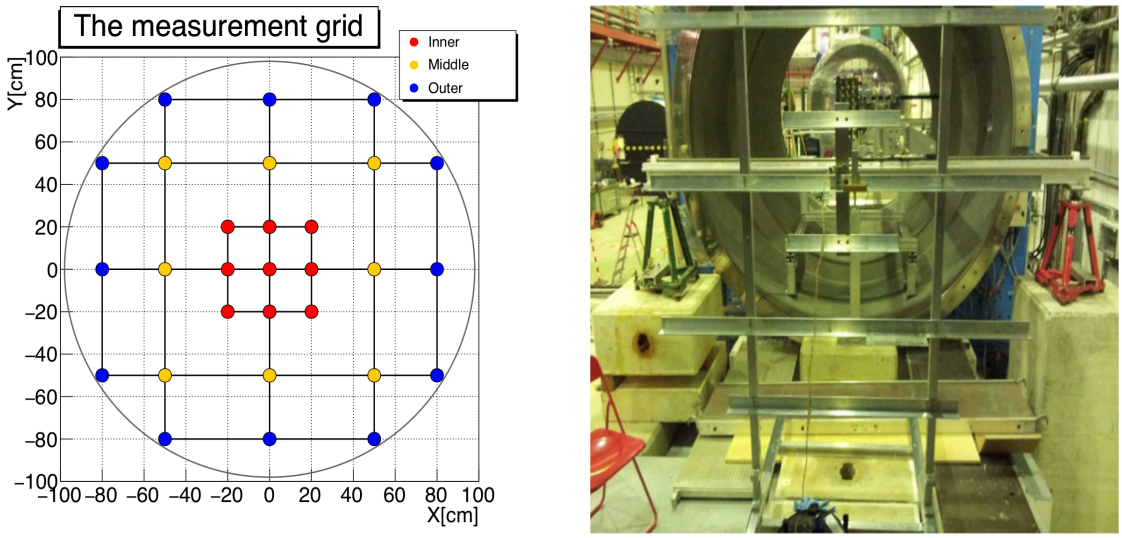

(a) (b)

Figure 4.2: Magnetic Field measurement grids. (a) is a schematic of the grid used for the vacuum tube measurements where each coloured marker corresponds to a sensor measurement position. (b) is a photograph of the real mount [67].

and twenty-five planes using both inner and middle grids for the Z-values after. Therefore, the number of blue-tube measurements (if a single set is recorded per plane), corresponds to $N = 15 \cdot 9 + 25 \cdot (9 + 8) = 135 + 425 = 560$ B_i components in total. The grey-tube region is measured similarly, creating measurement planes spaced by 30 cm and using the full grid structure. The smaller separation is to account for rapidly increasing field components. With fifteen additional Z-planes, the grey-tube consists of $N = 15 \cdot (9+8+12) = 435$ B_i components. The error associated to each measurement is 5.6 μT, based on the precision of the hall-probes. Only the region upstream of the MNP33 is measured, due to technical limitations, with the intention that the field can be reflected symmetrically around the magnet centre for the downstream region.

4.2.1 Blue-tube planes

As the blue-tubes use the same measurement strategy, understanding the field composition in this region is beneficial for the fringe field map development. Figure 4.3 displays the Z-dependence of the B_X and B_Y components for the central grid position (0 cm, 0 cm) for the blue-tube, including the field-map evaluation. The most

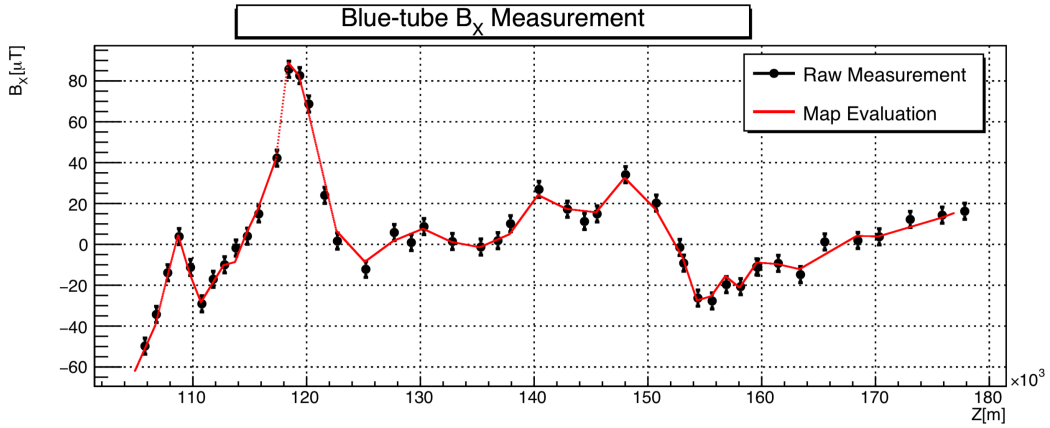

(a)

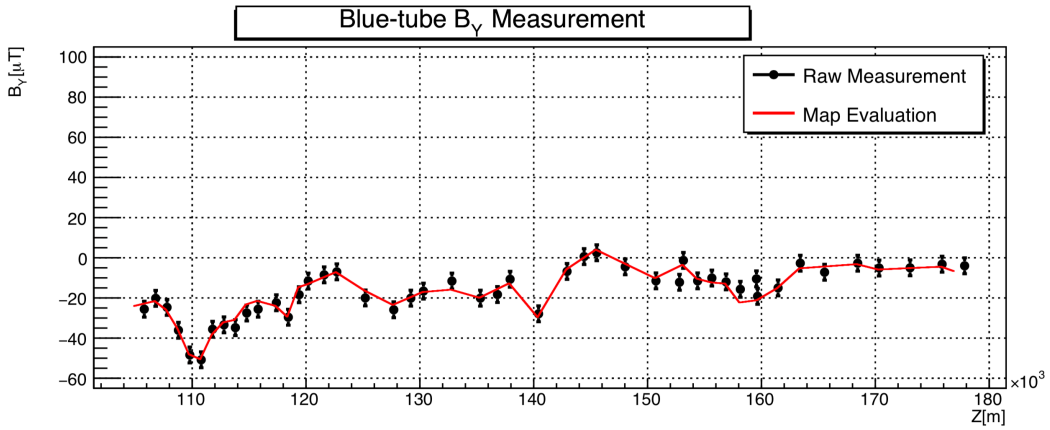

(b)

Figure 4.3: Z-dependence of the blue-tube field for central grid position (0 cm, 0 cm) with respect to (a) B_X and (b) B_Y. The red-line displays the blue-tube field-map evaluation of the field [67].

notable features are for B_X, where the field is extremely complex. B_X increases to $\approx$ 80 μT at Z = 120 m, as the residual field is affected by the presence of man-hole covers and flanges where work-hardening significantly alters the magnetisation of dense material. Despite the low magnitude of the field components with respect to the MNP33, the considerable length of the tank leads to significant trajectory modification for charged tracks. For example, the central position raw field-integrals are $\int B_X \cdot dZ \approx$ 411 μTm and $\int B_Y \cdot dZ \approx$ -1057 μTm, which result in certain kinematic properties as displayed in Figure 4.4. The resolution on the observable invariant mass for $K^+ \to \pi^+\pi^+\pi^-$ ($K_{3\pi}$) is altered significantly when including the field map into NA62MC compared to the corrected case, equivalent to the map being turned off. A tool was developed as described in Ref. [69] to correct for the field modification. The corrections applied improve the resolution and the azimuthal angle

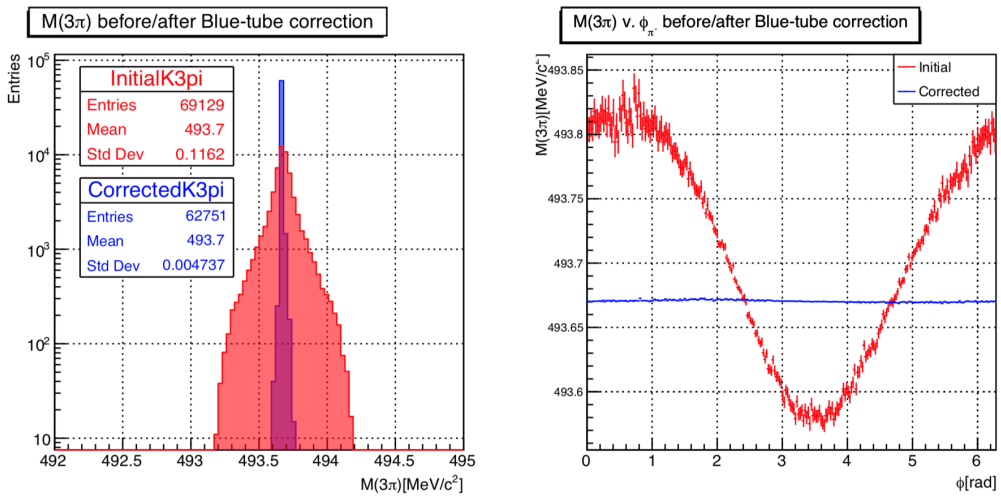

Figure 4.4: Left: The $(K_{3\pi})$ invariant mass simulated in NA62MC in the presence of the blue-tube field. Right: the variation in the invariant mass with respect to the azimuthal angle $\phi = P_X/P_Y$ of the π^-. The distributions seen in red correspond to the effect from the blue-tube field, whereas blue is after correcting the field using the tool.

variation of the mass to far below the experimental requirements.

4.2.2 Grey-tube planes

Figure 4.5 displays the Z-dependence of the B_X and B_Y components for a few specifically chosen grid-positions in the grey-tube region. As expected, most grid-positions display a rapid increase in field magnitude with Z. As B_Y is the primary field-component of the MNP33, all grid-positions increase up to $\approx$ 5000 μT with the largest increase for positions at the centre of the grid. The B_X component is a second-order field, where central grid-positions do not increase rapidly unlike those on the edge of the grid. Measurements for B_X are within $\pm$ 800 μT at the final $Z-$plane where (X, Y) = (+,+) and (-,-) grid-positions have negative magnitudes and (X, Y) = (+,-), (-,+) positive. For comparison with the blue-tube, the raw field integrals in the grey-tube for the central position are $\int B_X \cdot dZ \approx 224$ μTm and $\int B_Y \cdot dZ \approx 5438$ μTm, noting that the maximal contribution for B_X occurs at the corners of the grid.

The Z-dependence in Figure 4.5 show many interesting features. In B_Y, one grid measurement at Z = 190.863 m is a clear anomaly. In B_X, several grid positions

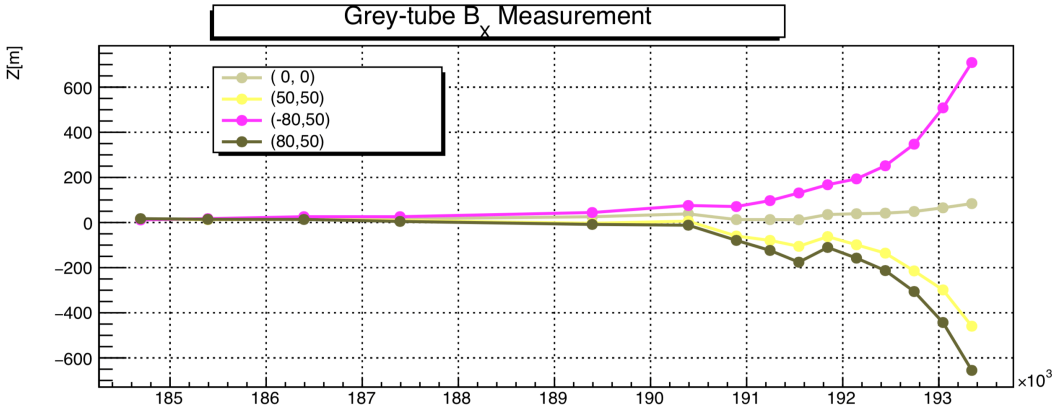

(a)

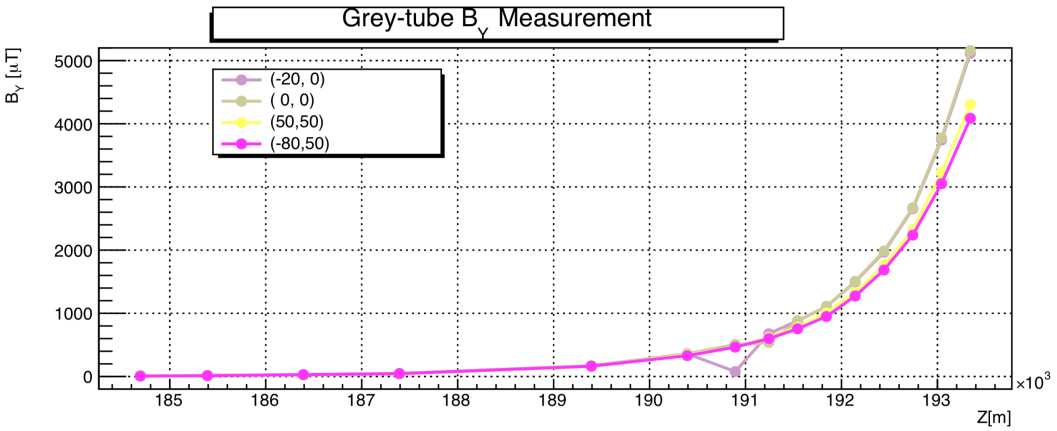

(b)

Figure 4.5: Z-dependence of the grey-tube field for multiple grid positions (X[cm],Y[cm]) with respect to (a) B_X and (b) B_Y.

show a distinct non-uniformity in the region between $191 < Z[\text{m}] < 192$ m of ≈ 50 μT. There are three possibilities for these effects,

- **Hysteresis**: Several MNP33 trips occurred during the measurement procedure. If the MNP33 magnet trips, the current supplied to the coils must be ramped slowly to approach back to the design field-strength. This can cause the magnet to realign and become magnetised differently to the previous conditions and the field to lag as the current reaches the nominal value. Hysteresis such as this is expected to be at the level of $1/1000$, meaning the effect is of the $\mathcal{O}(1\ \mu\text{T})$ for the fringe field.

- **Magnetisation**: In the blue-tube region, the magnetisation of reworked material lead to clear non-uniformities in the field map at certain positions in Z. The

regions which were observed to be contributing values of the $\mathcal{O}(100\ \mu\text{T})$, a similar magnitude to the distortion in Figure 4.5. This suggests that magnetisation due to reworking is also a major contribution for the grey-tubes.

- **Human error**: The single anomaly observed in B_Y is expected to be due to human error, as the magnitude is factor ≈ 10 smaller than measurements for close-grid positions at the same Z.

The issues highlight the need for some quality control when constructing the field map. The measurement plane surfaces can also be plotted, as displayed in Figure 4.6. Here, both B_X and B_Y are displayed for three out of the fifteen planes

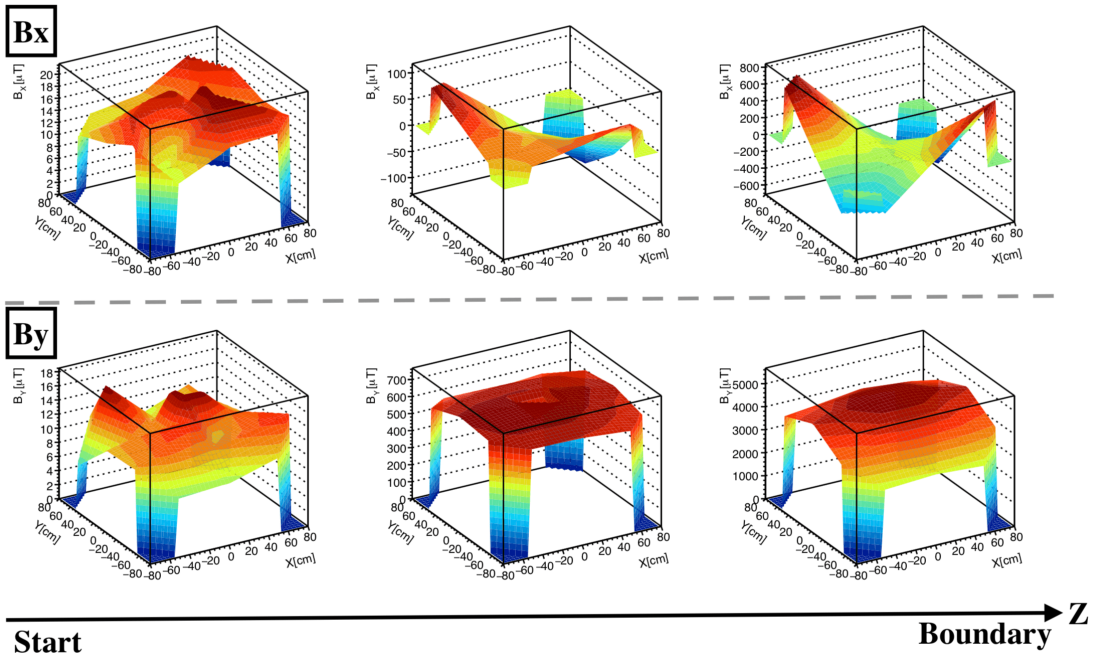

Figure 4.6: The field surfaces for planes at the start, middle and end of the grey-tube region. The top row is for B_X and bottom for B_Y. The shape in both cases transitions to physical shapes at high Z from the blue-tube-like fluctuations observed at low Z.

corresponding to the start, middle and end of the grey-tube measurement region. The typical magnitudes at the beginning are low and blue-tube-like, but as the field increases rapidly with Z, the shape transforms into more pure mathematical shapes. By the end of the grey-tube, B_X is distinctly saddle-shaped and B_Y is appears to be a two-dimensional elliptical paraboloid, as the stray fringe field is now completely dominant with respect to the residual field.

4.3 Building the field-map

The measurements are now used to build the three-dimensional fringe field map. Each plane is fitted with the following two-dimensional polynomial,

$$B(X,Y) = B_0 + \alpha_x X + \alpha_y Y + \alpha_{xx} X^2 + \alpha_{yy} Y^2 + \alpha_{xy} XY, \tag{4.2}$$

where $B(X,Y)$ is the evaluated field at a given (X,Y) position, B_0 is the constant term of the field fit, and the α parameters correspond to the constants of the linear or quadratic terms with respect to the coordinate space. The lowest-order polynomial which returned a reasonable description was chosen, by fitting each $z-$plane with polynomials of increasing order to find the best agreement overall. The shapes displayed in Figure 4.6 display paraboloidal surfaces which can be described mathematically with two-dimensional polynomials. As a set of parameters is obtained per measurement plane, the plane-parameter dependence with Z can be modelled. The three-dimensional field is therefore,

$$B(X,Y,Z) = B_0(Z) + \alpha_x(Z) X + \alpha_y(Z) Y + \alpha_{xx}(Z) X^2 + \alpha_{yy}(Z) Y^2 + \alpha_{xy}(Z) XY, \tag{4.3}$$

where each of parameters of Equation 4.2 is replaced by a Z-dependent smooth curve extracted by fitting. With this, the field can be known anywhere and the map becomes three-dimensional. To improve the accuracy of the map, care must be taken to handle points which are statistically rogue; i.e a systematically shifted from expectation. The field must also then be linked to the blue-tube and MNP33 maps. This is easier for the blue-tube which uses the same measurement technique, whereas the MNP33 uses a factor ≈ 10 more measurements and an entirely different grid structure.

4.3.1 Measurement deletion

Using Equation 4.2, each of the fifteen measurement planes is fitted to create a smooth surface to describe the field-shape which can then be used for interpolation. Figure 4.7 displays the two-dimensional (X,Y) data-fit residual for three specifically

chosen planes.

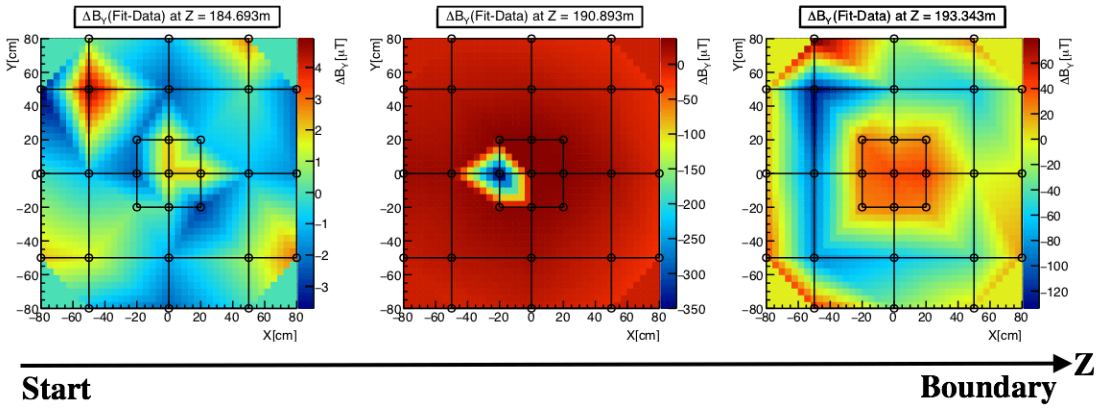

Figure 4.7: B_Y data-fit residuals for Z-planes at the start, middle and end of the grey-tube. The measurement grid structure has been drawn for perspective. The central plot is the B_Y plane where a clear anomaly was observed in Figure 4.5.

At the start of the grey-tube, ΔB_Y is small across the grid, well within the error assigned to each measurement point (5.6 μT). By the end, the magnitude of the field increases by a factor $\approx$ 100 and so the differences are far greater than the measurement error. The central case of Figure 4.7 corresponds to the anomaly observed in Figure 4.5, suspected to be due to human error. The point pulls the fit and worsens the agreement for the other points in the grid. An algorithm was designed to handle systematically suspicious points as follows:

- Fit measurement plane with Equation 4.2.
- Delete any grid-position where the data-fit residual ΔB_i deviates by more than $\pm$100 μT, and re-perform the fit.

The algorithm uses residuals instead of pull distributions because the error assigned to each point is identical. The value of 100 μT is chosen close to double the magnitude of the deviation observed due to magnetisation in the blue-tubes. The algorithm is limited to delete only one-point per plane to keep the measurement sample as large as possible. Regardless, point deletion does not drastically affect the overall fit. Figure 4.8 displays the difference between the Z-plane fit before and after the deletion of the rogue measurement (denoted by an 'X') from the central plane displayed in Figure 4.7. The maximal change of the fit occurred closest to the point that

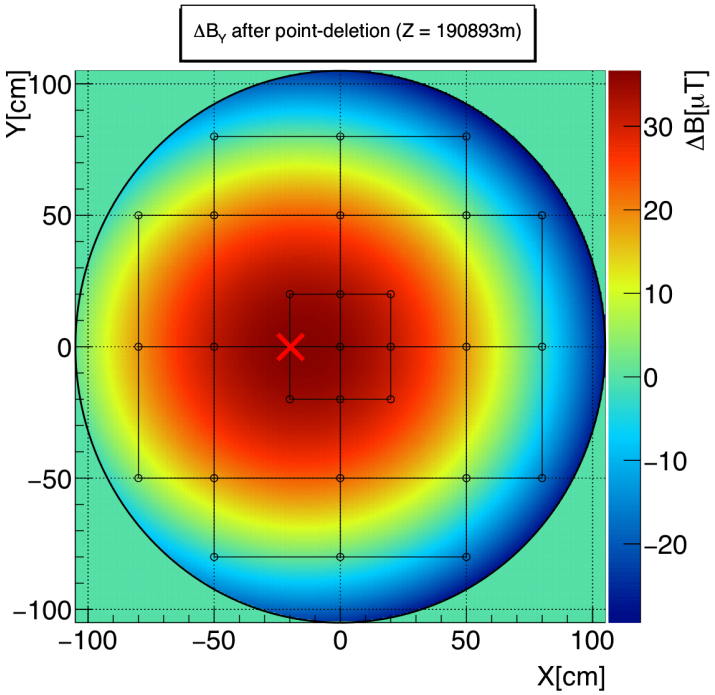

Figure 4.8: Difference in the 2D B_Y fit before and after deletion of measurement point (-20 cm, 0 cm) for Z-plane 190.843 m. The outline of the plot corresponds to the grey-tube inner radius.

was deleted, but even in this extreme case (the largest deviation by any point in the sample), the typical $\Delta B \approx 30$ μT is small with respect to the average field magnitude of the plane (500 μT). Table 4.1 displays the four measurements which were deleted by the procedure, including one at the final measurement plane for both B_X and B_Y.

Table 4.1: Summary of the measurement-deletion algorithm. Four points were deleted in total.

Field	Z-Plane[m]	Coordinate (X[cm],Y[cm]	Fit-Data δB[μT]
B_X	193.343	(-50,50)	103.2
B_Y	190.893	(-20,0)	392.7
B_Y	191.243	(0,0)	121.9
B_Y	193.343	(-50,50)	133.6

Additionally, each measurement plane as a whole was investigated for systematic effects. As observed in Figure 4.5 of Section 4.2, several grid-positions show a distortion in B_X between 191 $<$ Z[m] $<$ 192. The cause is suspected to be due to magnetisation and creates a kink in the otherwise smooth Z-dependence. To observe the effect of this kink with respect to a smooth curve, the raw field-integrals for B_X were calculated for the entire fringe field region with and without the two planes

for each grid position. The difference between the grid-position integrals is calculated and the residual fitted with a Gaussian curve in Figure 4.9. In general, the

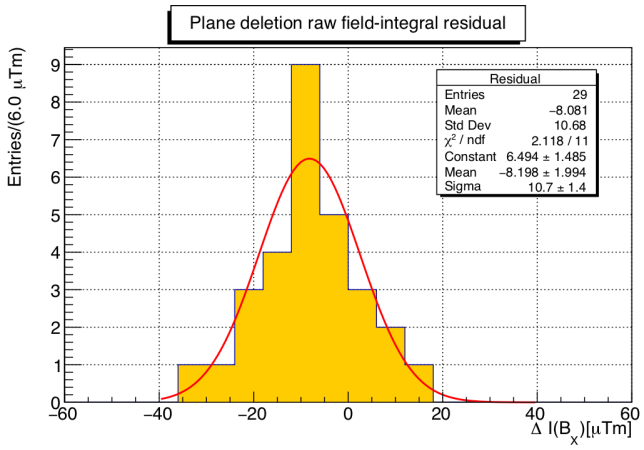

Figure 4.9: The residual of the field integral for B_X at each grid-position before and after deleting two planes, fitted with a Gaussian distribution. The impact of the deletion is relatively small.

larger deviations come from positions furthest from the centre. The deletion of the two planes has a small effect on the raw B_X field-integral, shifting the value by $\approx$ -8 μTm on average for all grid positions. This corresponds to less than 3% of the total field-integral for B_X at the central-grid where the field magnitude is smallest. The shift is small because the first plane 191.123 m and second 191.153 m deviate in opposite directions, leading to a partial cancellation. For simplicity, the two planes were permanently removed for B_X as the impact on the field-integral is minuscule with respect to the performance requirements.

4.3.2 Plane interpolation

After the quality-control measures in the previous section, each B_i measurement plane is fitted for the final time with the two-dimensional polynomial described by Equation 4.2. In order to have a three-dimensional field-map, the Z-dependence of each of the six parameters must be modelled, performed using polynomial fits of the form,

$$f_z = p_0 + \sum_{n=1}^{b} p_n (z - z_0)^n \tag{4.4}$$

where p_0 is a constant parameter of the polynomial, z_0 is the Z-plane value at the end of the blue-tube region (183.331 m), and b is the smallest number required to obtain an adequate fit, in order to keep the number of terms as small as possible. Due the rapidly-increasing nature of the fringe field, in some circumstances it was necessary to modify Equation 4.4 to include an exponential term,

$$f_z = p_0 + \gamma(z - z_0)e^{\delta(z_E - z)} + \sum_{n=1}^{b} p_n(z - z_0)^n \tag{4.5}$$

where γ, δ are additional fit parameters, and z_E = 193.343 m is the Z-plane at the end of the grey-tube. By multiplying non-constant terms by $(z - z_0)$, the fringe field map can be easily matched to the blue-tube. The blue-tube map is implemented with a similar method, by fitting measurement planes with two-dimensional polynomial and interpolating the parameters. Simply, the constant terms in Equation 4.4 and 4.5 can be fixed to match those from the blue-tube map p_0^{BT}, leading to a seamless transition at the boundary z_0.

Figure 4.10 and 4.11 displays the six α surface parameter distributions with respect to Z for the B_X and B_Y field. The lower magnitude of the B_X field with respect to the 5.6 μT measurement error leads to a better fit performance than for B_Y, and clearly the parameter dependence with Z is not always smooth. The region around 191 m, which was the focus of measurement quality previously, displays some features that are hard to describe fully with polynomial curves. However, the regions of rapid increase are well described by the exponential-polynomial fits in all parameters, such that the field evaluation is expected to be reliable. Figure 4.12 contains the Z-dependence of a multiple grid-positions displayed earlier but now containing the fringe field simulation. The agreement with the data is excellent. The field integrals at the central grid position (0 cm, 0 cm) for the simulation are $\int B_X \cdot dZ \approx 220$ μTm and $\int B_Y \cdot dZ \approx 5448$ μTm, which is different by less than 2%(1%) for $B_X(B_Y)$ to the raw field measurements. The comparison can be made for all grid positions with the average deviation calculated to be about the same value.

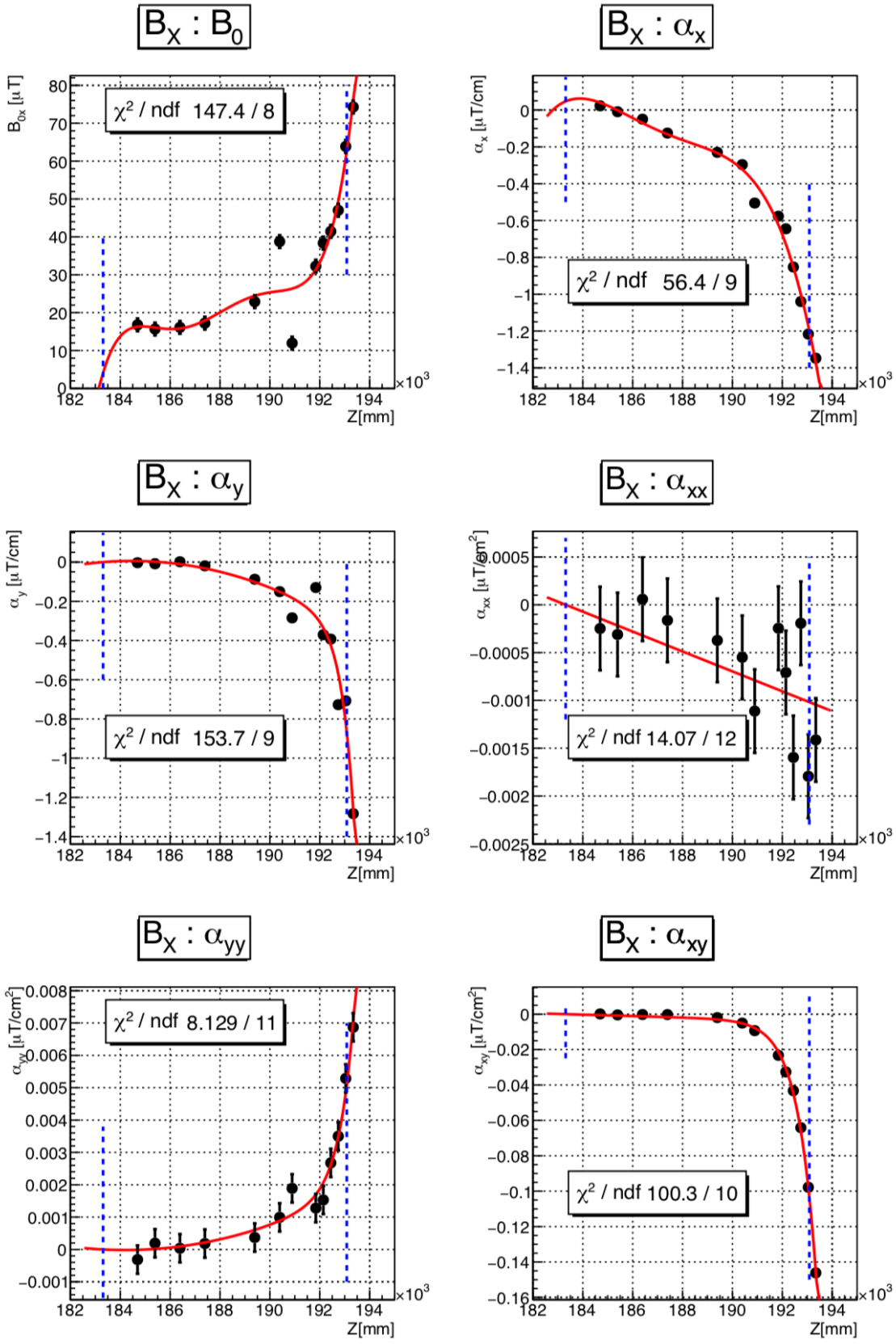

Figure 4.10: The six surface-parameter Z-dependence fits for B_X. The blue-lines denote the start and end of the fringe field regions.

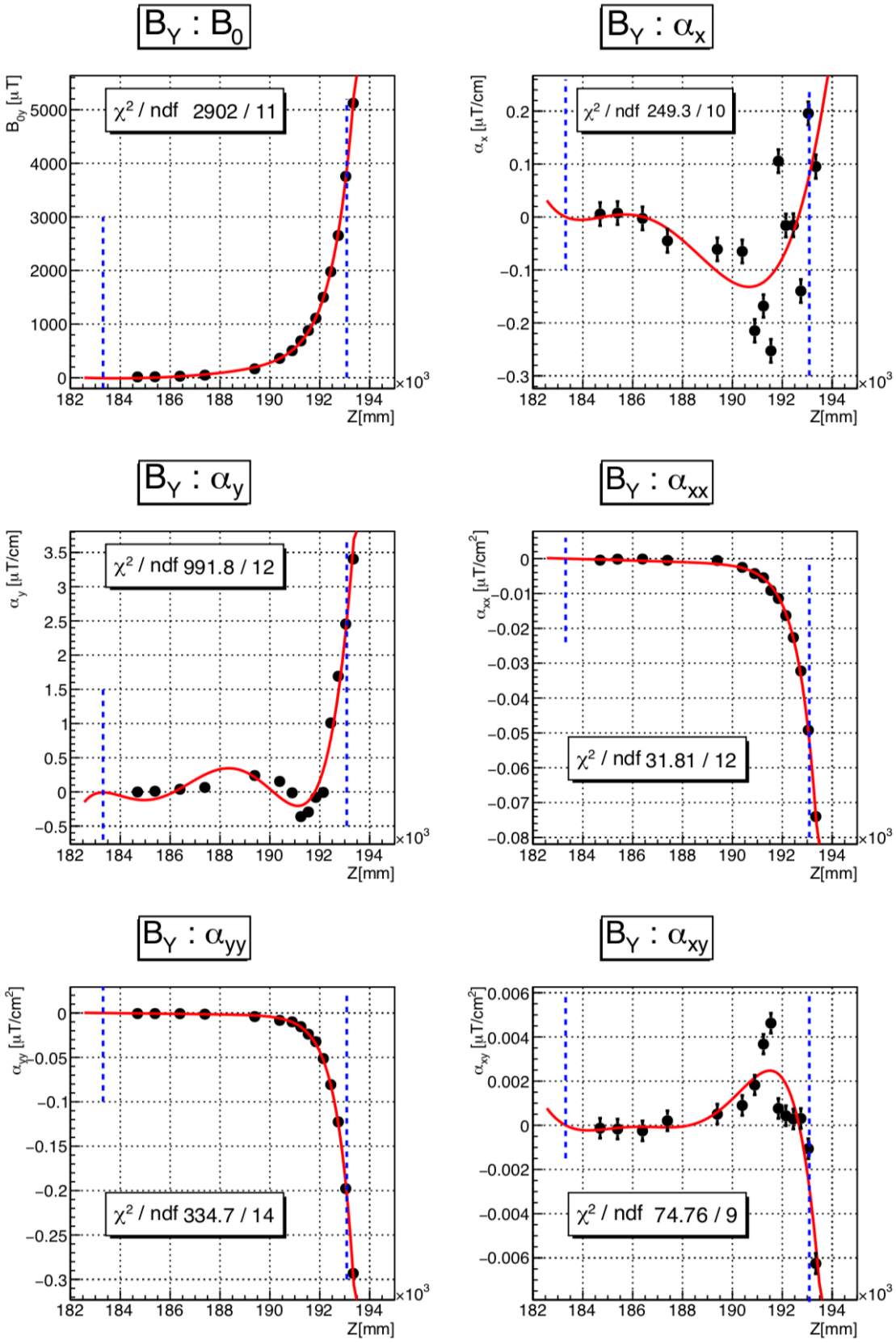

Figure 4.11: The six surface-parameter Z-dependence fits for B_Y. The blue-lines denote the start and end of the fringe field regions.

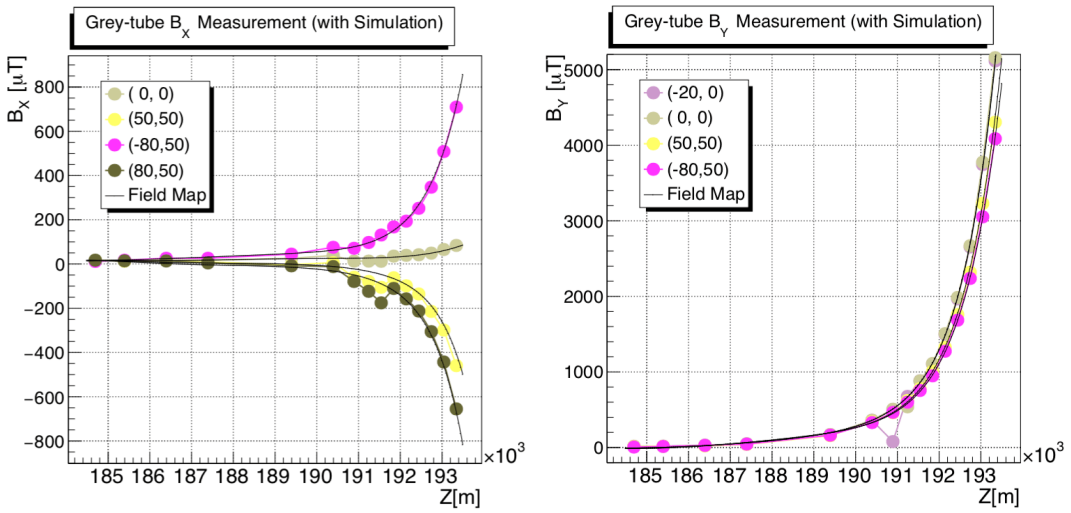

(a) (b)

Figure 4.12: Z-dependence of the grey-tube field now including the field-map simulation for multiple grid positions (X[cm],Y[cm]) with respect to (a) B_X and (b) B_Y.

4.3.3 Linking the fringe map with MNP33

As described by Ref. [70], the MNP33 field was measured using a far more granular grid-structure with respect to the vacuum tubes, with ultra-fine 80 mm steps in Z to build up over 3000 measurements. The map implemented in NA62MC is also constructed differently, using a direct trilinear interpolation approach on the measurement sample instead of any smooth fitting techniques. The high-accuracy of this approach comes at the cost of CPU performance, with the MNP33 map being by far the slowest component to evaluate in MC generation [71].

Though there is no simple method to connect the maps, the final blue-line marked at Z = 193.083 m in the parameter fits of Figure 4.10 and 4.11 corresponds to the start of the MNP33 field-map region; this occurs within the grey-tube volume. In this region, measurements were performed using both the vacuum tube and MNP33 grid structures. Figure 4.13 contains the residual difference between the fringe field and MNP33 maps at the boundary for both B_X and B_Y. There is a clear discrepancy for the B_Y component between the two field maps, where the fringe field is drastically larger by up to 500 μT at the boundary. As the MNP33 measurement procedure was far more extensive than for the grey-tube, the MNP33 map is considered to be more

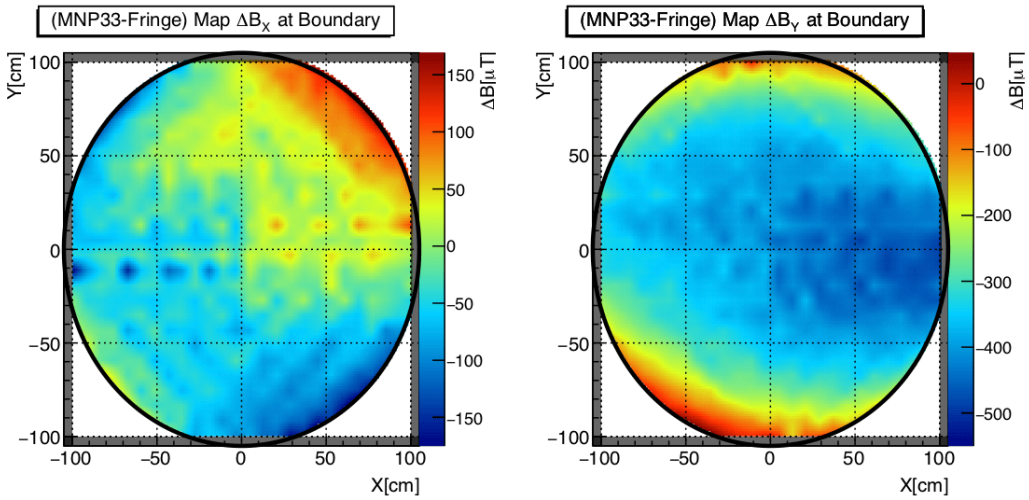

Figure 4.13: Difference in fringe field and MNP33 maps at the cross-over boundary for left, B_X and right, B_Y. The grey-border corresponds to the MNP33 (X, Y) region, simulated between ($\pm$100 cm, $\pm$100 cm), and the black-line the inner radius of the grey-tube. A clear discrepancy can be observed in B_Y, with a difference in the central region up to -500 μT.

reliable, and so the decision was taken to re-scale the fringe field map in order to match with the MNP33. To determine the optimal scale fraction f_{FF}, the difference between the fringe field and MNP33 field maps was evaluated at all MNP33 grid positions. By multiplying the fringe field evaluation by f_{FF} and performing a fine-scan, the ideal scale-fraction was found when the mean of the residual difference was equivalent to zero for B_Y. Figure 4.14 displays the result of the fine-scan in f_{FF}. The scaling constant is therefore,

$$f_{FF} = 0.897. \tag{4.6}$$

which will shrink the field integrals by 10%. To apply the scale-factor, a simple modification is made to the fits described by Equations 4.4 and 4.5. All terms are multiplied by f_{FF}, except for the constant term as to preserve the blue-tube matching. The scaling feature is desirable, as the MNP33 magnet can change current, such that the magnitude (but not shape) of the field can alter depending on the data-taking configuration of NA62. The MC scale-factor applied to the field is therefore made in factors of f_{FF}. Figure 4.15 shows the differences between the two maps at the boundary post-scaling. While the agreement improves and residual difference in B_Y more symmetric, a smooth transition across the entire face is impossible with

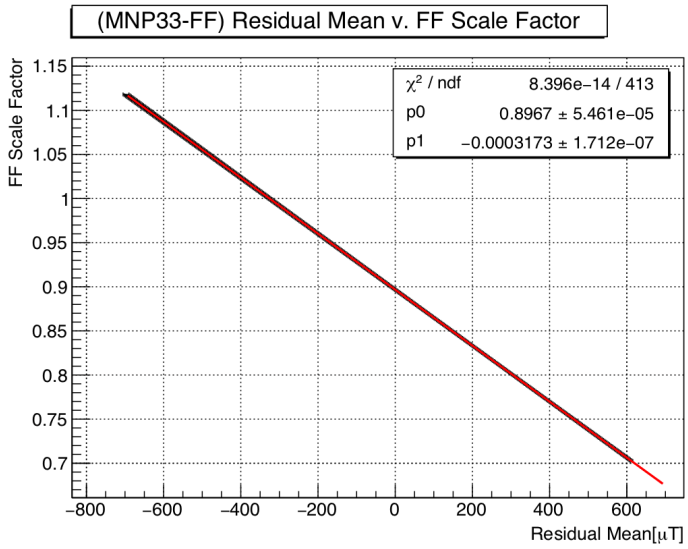

Figure 4.14: The fringe field scale-factor fine-scan plotted against the residual mean of the MNP33/Fringe field. The ideal scale-fraction is situated at zero on the X-axis

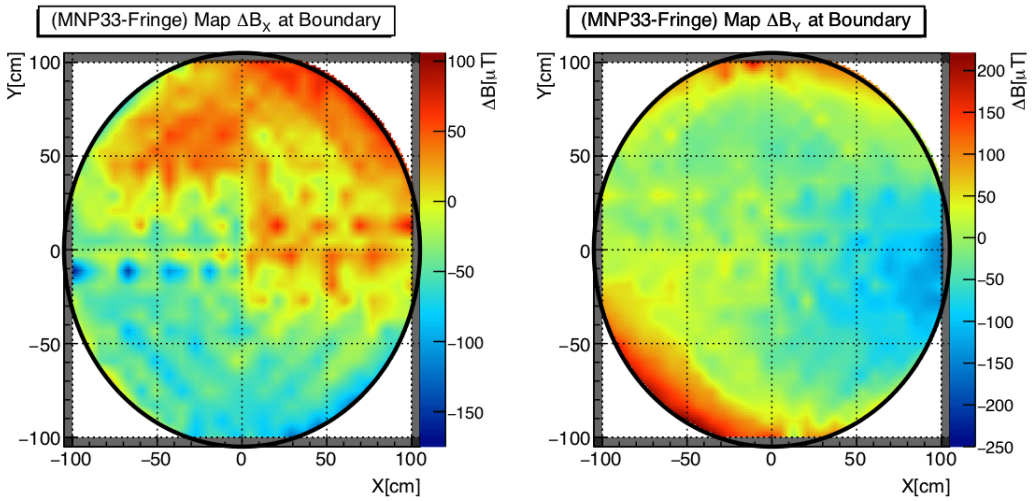

Figure 4.15: Difference in fringe field and MNP33 maps at the cross-over boundary for left, B_X and right, B_Y after scaling by Equation 4.6. The difference is now more symmetrical, but is not smooth or exact.

only a re-scaling. In order to avoid field discontinuities at the boundary, a buffer region was introduced to slowly interpolate between the maps. The region is implemented in the following fashion,

- Define the start of the buffer region Z_B = 192.683 m, 0.4 m before the MNP33 map begins. This is motivated by the typical gap between measurements planes in the grey-tube region.
- The field evaluated at $Z \leqslant Z_B$ uses the standard fringe field map.
- In the region $Z_B < Z < Z_{\mathrm{MNP33}}$, the field values are interpolated linearly between the fringe field map at Z_B and the MNP33 map at Z_{MNP33}.
- The field evaluated at $Z > Z_{\mathrm{MNP33}}$ uses the standard MNP33 field map.

The justification for the buffer region is contained in Figure 4.16, using the ($\pm$20 cm, $\pm$20 cm) grid positions that are common to both the vacuum tube and MNP33 measurement approaches. The disagreement between the fringe field and MNP33 raw measurements can be seen most clearly for B_X where the magnitudes are small. If a buffer region was not used, the field would be discontinuous at the boundary. To understand the impact of the buffer region on the field integral, the calculation must be modified slightly. As the MNP33 map starts at 193.083 m, the final grey-tube measurement plane at 193.383 m is bypassed and is transferred to the MNP33 field integral instead, leading to a 25% decrease overall for central B_Y values. The scaling of the measurements and map by f_{FF} also decreases the overall field-integral by 10%. Table 4.2 compares the raw measurement integral to the field map integrals with and without the buffer zone for central grid position (0 cm, 0 cm). The level of

Table 4.2: Comparing the raw and field map integrals for central grid position (0 cm, 0 cm) for the final fringe-field map.

Integral Type	$\int B_X \cdot dZ$ [μTm]	$\int B_Y \cdot dZ$ [μTm]
Raw Measurements	181	3676
Field Map	182	3691
Field Map (Buffer)	184	3695

difference between the field map integral with and without the buffer zone is similar for all grid positions, with the buffer case 2(3) μTm larger for $B_X(B_Y)$ on average.

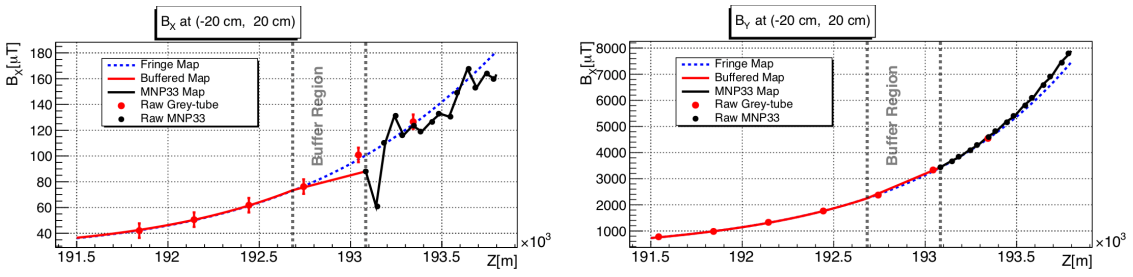

(a) B_X (-20 cm, 20 cm)

(b) B_Y (-20 cm, 20 cm)

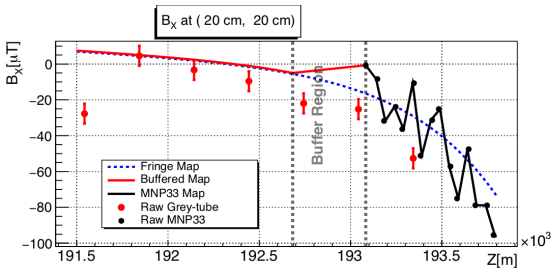

(c) B_X (20 cm, 20 cm)

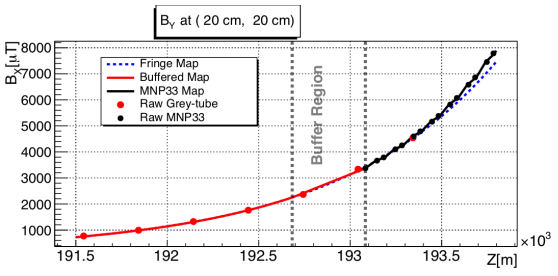

(d) B_Y (20 cm, 20 cm)

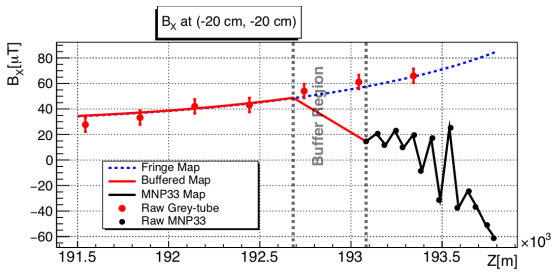

(e) B_X (-20 cm, -20 cm)

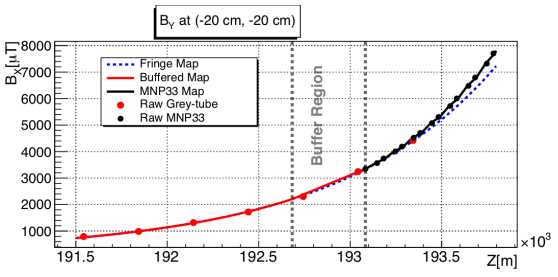

(f) B_Y (-20 cm, -20 cm)

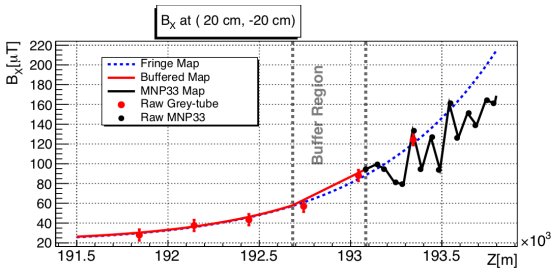

(g) B_X (20 cm, -20 cm)

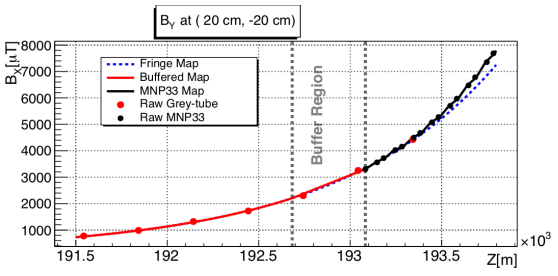

(h) B_Y (20 cm, -20 cm)

Figure 4.16: Displaying the buffer region by comparing both fringe field and MNP33 maps to the raw measurements for four grid positions. The left column contains B_X and right B_Y. The red line is the buffered fringe field map, including blue-line which is the version without the buffer. The black line is the MNP33 map, whilst the black points are the raw MNP33 measurements. The agreement with the raw data is excellent after scaling by f_{FF} for all fringe field cases. The buffer region is most clearly seen for the low magnitude B_X fields, where the boundary would be discontinuous if using the blue-line.

4.3.4 Fringe field downstream of MNP33

The fringe field data set was only produced upstream of the MNP33, relying on the observation that the field is highly symmetric around the centre of the magnet in the Z-axis. In addition, it was not technically possible to install the measurement grid downstream after the magnet had been commissioned. Therefore, the fringe field map had to be reflected about the centre of the MNP33 magnet at Z_m = 196.995 m and matched to the MNP33 field. The only real difference for the downstream fringe field is the introduction of a final buffer-zone at Z= 210.679 m to slowly reduce the field components to zero over 1.4 m. The choice of zero instead of the earth field, for example, is entirely arbitrary and the difference between choosing either approach to the magnitude of the downstream field integral is ≈ 5 μTm, less than 1% of the downstream fringe-field for both B_X and B_Y.

4.4 Overall Performance

4.4.1 Fringe field systematics

To estimate the systematic errors of the field map, we can first consider the measurement errors provided by the authors of Ref. [67]. Here, the systematics are calculated for measurement and sampling errors, where they note that the largest systematic uncertainty for the fringe field is due to the mixing of the B_Y component of the field into B_X via sensor miscalibration. By considering all sources for the important transverse components only, the total data measurement systematic is given as

$$\sigma^{\mathrm{Data}}_{I_{B_X}} = 120\ \mu\mathrm{Tm}, \tag{4.7}$$

$$\sigma^{\mathrm{Data}}_{I_{B_Y}} = 40\ \mu\mathrm{Tm}. \tag{4.8}$$

For the simulated map developed here, the contribution to the field integrals due to the difference between the field map and the measured data must be considered. This is estimated by computing the difference between the raw measurements and the field map evaluation for each Z-plane, with a single value per grid position. Figure 4.17 displays the mean deviation for B_X and B_Y in the fringe field region, ex-

tracted by fitting the residual for each plane with a log-likelihood Gaussian fit and noting that the data values were scaled by f_{FF} to account for the overall disagreement between the fringe field and MNP33 maps.

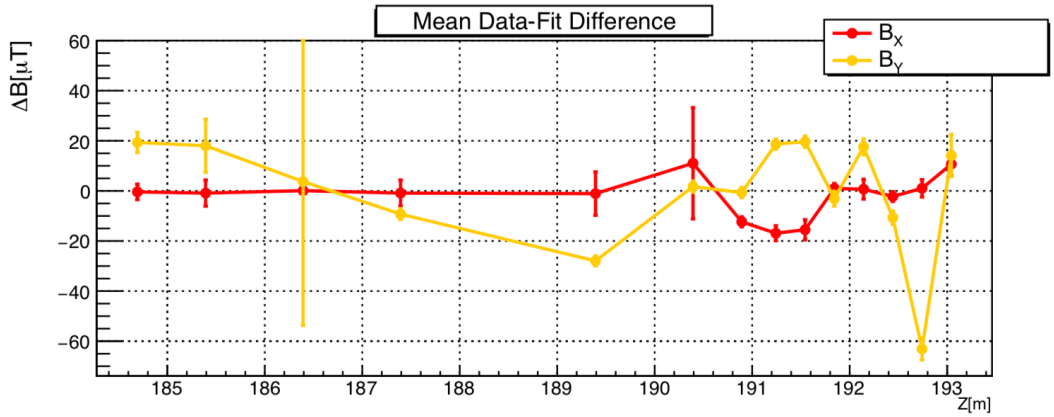

Figure 4.17: The average field deviation between the final field map and the measurements at each Z-plane. The larger magnitude of B_Y on average leads to larger deviations overall.

The total error in the field map components is estimated as the sum in quadrature of each plane deviation, ignoring the final fringe field measurement plane at 193.331 m which was not used in the map. This leads to the overall field systematic for the fringe map,

$$\sigma_{B_X}^{\mathrm{FF}} = 30\ \mu\mathrm{T}, \tag{4.9}$$

$$\sigma_{B_Y}^{\mathrm{FF}} = 83\ \mu\mathrm{T}, \tag{4.10}$$

To translate these errors into an overall field integral systematic, the following method was adopted:

- Create a modified field evaluation: sum the average field deviation and the field-map evaluation for all grid-positions at each Z-plane (extracted from Figure 4.17).
- In order estimate the systematic using a trapezium rule integration, define the following interval:

$$I_{\mathrm{interval}} = \left(\frac{B_{P_s} + B_{P_e}}{2}\right)\Delta_{Z_{se}}. \tag{4.11}$$

  Here $B_{P_{s,e}}$ is the evaluated field for the start and end planes of the interval

and $\Delta_{Z_{se}}$ is the distance in Z between the two interval planes. For fourteen grey-tube planes, there are thirteen intervals that must be computed in order to calculate the total field integral.

- Evaluate the difference in the interval integral for the modified and standard fields. The systematic error is the sum in quadrature of this difference for all thirteen intervals.

The overall error is multiplied by a factor of two as the fringe field has an upstream and downstream component,

$$\sigma^{\mathrm{FF}}_{I_{B_X}} = 16\ \mu\mathrm{Tm}, \tag{4.12}$$

$$\sigma^{\mathrm{FF}}_{I_{B_Y}} = 70\ \mu\mathrm{Tm}. \tag{4.13}$$

As a sanity check, the difference between the raw field and field map integrals were instead estimated for each grid-position for the whole grey-tube. The result is displayed for both B_X and B_Y in Figure 4.18. The average field integral deviation

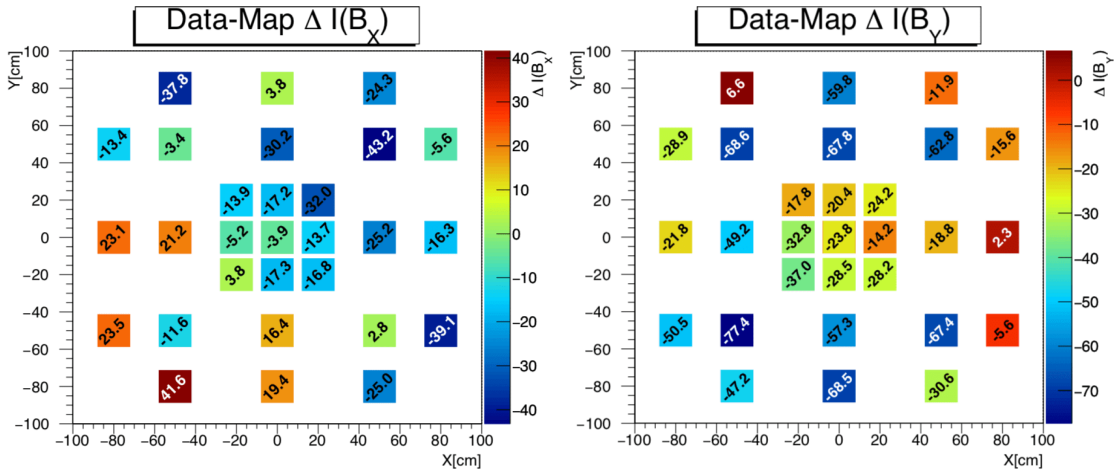

(a) B_X (b) B_Y

Figure 4.18: Difference between raw field and fringe map integral for the full grey-tube at each measurement position. A cross-check for the systematic calculation can be used by taking the average deviation across the surface for both B_X and B_Y.

across the surfaces is in agreement with the artificial modification approach, with the raw measurement being slightly lower on average in both cases at ≈ -8 μTm for B_X and ≈ -35 μTm for B_Y. The systematics for the field map are different in nature to the measurement systematics where σ_{B_X} is larger than σ_{B_Y}. The B_Y systematic

is dominated by the large deviation at plane 192.743 m, but this region sits inside the buffer region and so the agreement depends on accuracy of the MNP33 field map. Combining the errors in quadrature with the remainder of the decay-region systematics leads to only a small modification to Equations 4.7 and 4.8,

$$\sigma_{I_{B_X}}^{\mathrm{FF-Total}} = 121\ \mu\mathrm{Tm}, \tag{4.14}$$

$$\sigma_{I_{B_Y}}^{\mathrm{FF-Total}} = 81\ \mu\mathrm{Tm}, \tag{4.15}$$

remaining well within the performance requirements of $3 < 10^{-4}$ Tm.

4.4.2 Contribution to field integral

The final field integrals for B_X and B_Y are displayed in Figure 4.19, containing both fringe field and MNP33 maps in (X, Y) space. The fringe field is typically contributes less than 1% of the full field integral for both B_X and B_Y components. The fringe field integrals for (0 cm, 0 cm) are,

$$I_{B_X} = \int B_X \cdot dZ = (368 \pm 121)\ \mu\mathrm{Tm}, \tag{4.16}$$

$$I_{B_Y} = \int B_Y \cdot dZ = (7390 \pm 81)\ \mu\mathrm{Tm}, \tag{4.17}$$

which is roughly the average value across (X, Y) for B_X and close to the maximal contribution for B_Y. The B_X field is fairly asymmetric, contributing negatively in the (+,+) corner and positively in the (+,-) and (+,-) regions, with (-,-) close to the average value. The B_Y field is much less varied and changes by only ≈10% across the full (X, Y) space.

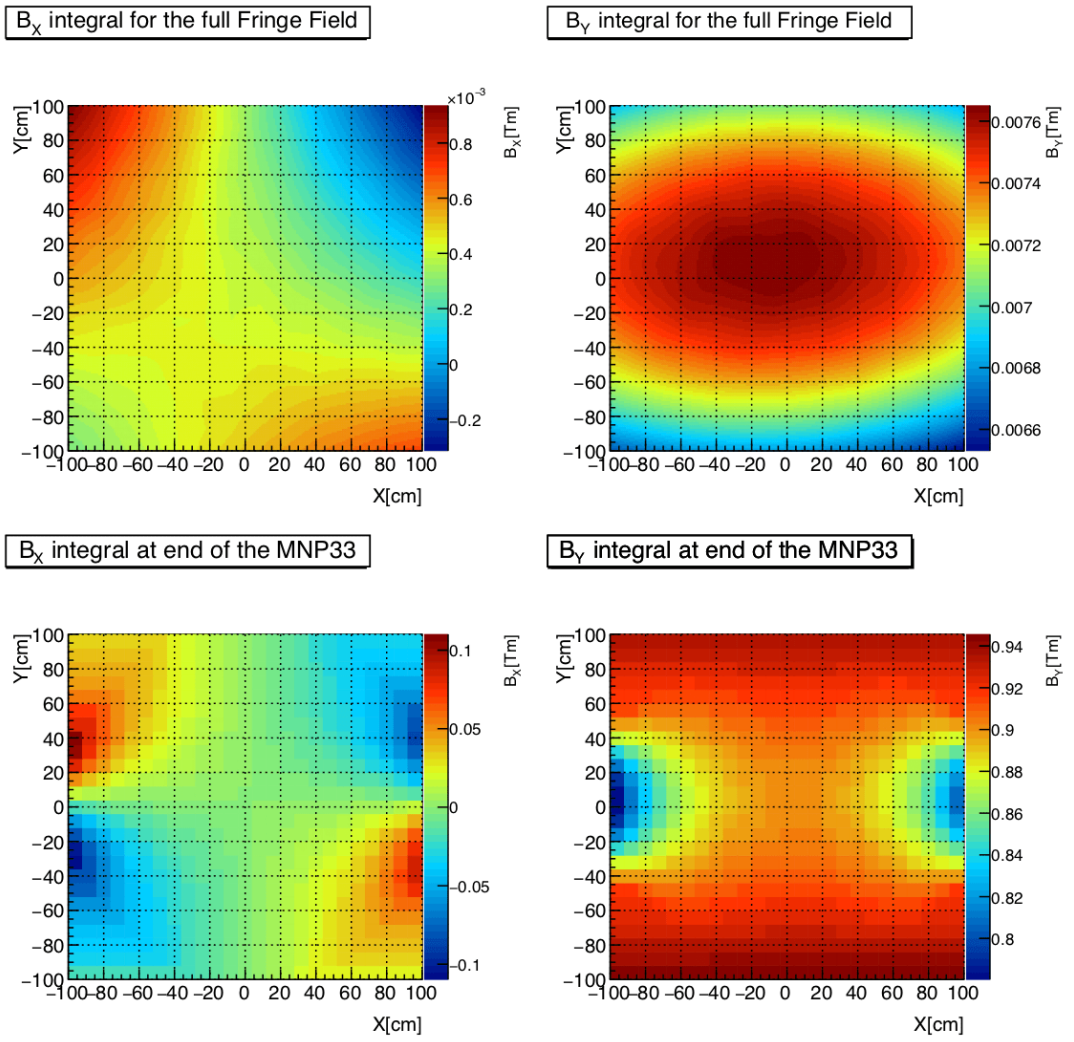

Figure 4.19: The total field integrals in Tm for the fringe (top row) and MNP33 (bottom row) field maps. B_X is contained in the first column and B_Y the second, with the upstream and downstream fringe fields summed together.

5

Development of a spectrometer calibration procedure

In this chapter, the development of a spectrometer momentum calibration procedure is presented. The correction model is explained, and the implementation of an algorithm is provided after a data-driven tuning strategy. Additionally, the time-dependence of the calibration parameters is interpreted in both 2016 and 2017 NA62 data, including the effect of the correction on the reconstructed kaon mass. Finally, the performance is verified further, using simulated samples after deliberate alteration of NA62MC and NA62Reconstruction to mimic the effects that the procedure is designed to correct for.

5.1 Motivation

For the measurement of the ultra-rare $K^+ \to \pi^+\nu\bar{\nu}$ decay, the most fundamentally important sub-detector system is the spectrometer. As described in Section 3.1, the $K^+ \to \pi^+\nu\bar{\nu}$ analysis relies on kinematic background rejection, using the missing-mass signatures of the main K^+ decay modes; a systematically wrong momentum determination can result in decay misidentification, diminishing the precision of the analysis. The same is true for other analyses, such as the $K^+ \to \pi^+\mu^+\mu^-$ decay (Chapter 8) where both the mean value and resolution of the invariant mass defines the Signal Region (SR).

There are two aspects to consider for ensuring high track quality:

- a high performance track reconstruction, including spacial alignment.
- a complete and accurate description of the magnetic fields in the decay volume and spectrometer.

The latter case of these criteria is described in great detail in Chapter 4, whilst the former is beyond the scope of this thesis. The purpose of this chapter is, however, to describe the development of an analysis tool which improves the determination of track momentum without any prior knowledge of field accuracy or reconstruction performance. A tool is required that uses a data-driven method to correct for any residual miscalibrations in the tracking system, regardless of their origin or magnitude.

Section 5.2 contains the correction model used, including a prediction of the calibration constants, whilst Section 5.3 and 5.4 describe the procedure developed to accurately extract the constants from data. Finally, the performance of the calibration is measured for both 2016 and 2017 data sets and verified further using MC samples in Section 5.5.

5.2 Correction Model

The adopted momentum correction model was implemented previously for NA48/2 data analysis [72]. The tracking system was similar, with four spectrometer drift chambers interspaced by the same MNP33 magnet in operation at NA62, but with a smaller field integral [73]. The model is simple, as displayed in Equation 5.1,

$$P_{nom} = P_{obs}(1 + \beta)(1 + \alpha q P_{obs}), \tag{5.1}$$

where P_{nom} is the nominal (corrected) momenta, P_{obs} is the reconstructed momenta and q is sign of the track charge [74]. Here, parameters α and β are calibration constants used to address either field miscalibration or spectrometer misalignment, with the definition (or derivation) of each provided in this section. Whilst the model itself is over-simplified, the possibility of using a more complicated approach is lim-

ited by the requirements of the data-processing; the model must be simple, make sense physically and use only a small amount of CPU time for each event.

5.2.1 The α parameter

The α parameter, in principle, can correct for any residual spectrometer chamber misalignment. The effect of a chamber misalignment can be understood using the example provided by Figure 5.1. Here, it is assumed that only the final spectrometer chamber is offset in the X-direction by some unknown size ΔX.

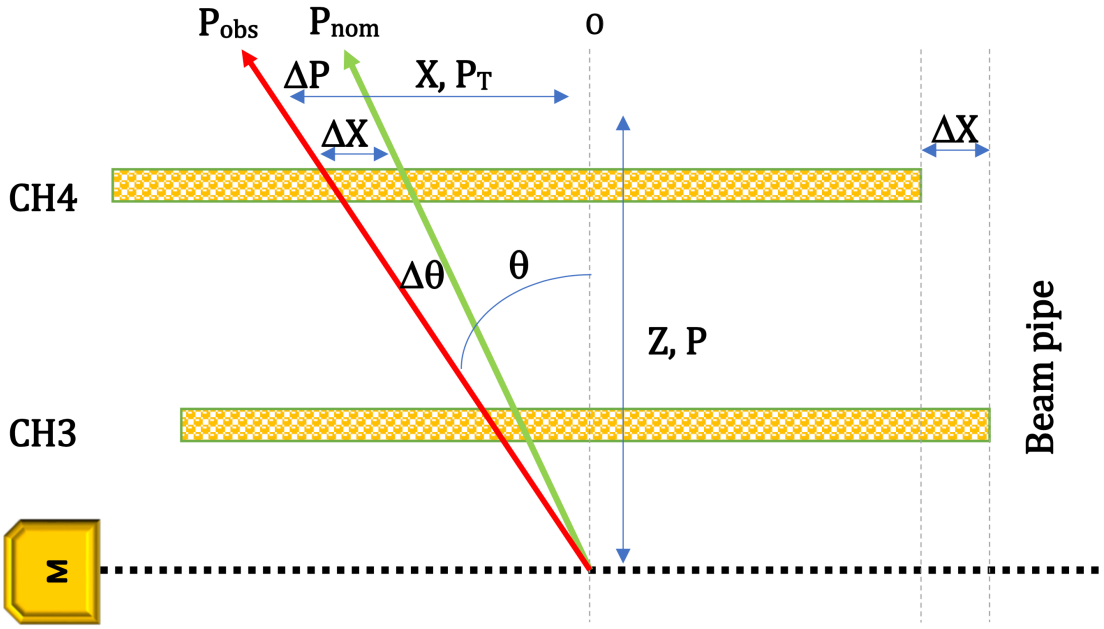

Figure 5.1: A diagram to estimate the size of calibration parameter α, by considering a shift ΔX of the final spectrometer chamber in the X-direction relative to the nominal position; 'M' is the MNP33 magnet.

In Figure 5.1, the observed track with momentum P_{obs} is deviated from the true-track with momentum P_{nom} because of the ΔX misalignment, where $P_{nom} = P_{obs} + \Delta P$. The misalignment also leads to a small deviation in the angle θ, which can be used to estimate ΔP based on,

$$\theta = \frac{P_T}{P_{obs}} = \frac{X}{Z}. \tag{5.2}$$

where P_T is the transverse kick of the MNP33 magnet equal to 270 MeV/c, X is the transverse distance from the origin O and Z is the longitudinal distance between

the magnet centre and chamber four. Using a Taylor expansion for Equation 5.2, the expression for $\Delta\theta$ follows naturally,

$$\Delta\theta = -\frac{P_T \Delta P}{P_{obs}^2} = \frac{\Delta X}{Z}. \tag{5.3}$$

Finally, rearranging the second half of Equation 5.3 for ΔP leads to the definition of α,

$$\Delta P = -\left(\frac{\Delta X}{Z P_T}\right) P_{obs}^2 = \alpha P_{obs}^2. \tag{5.4}$$

This is the origin of the α dependent term in the correction model as $P_{nom} = P_{obs} + \Delta P = P_{obs}(1 + \alpha q P_{obs})$, with q used to handle the sign of the track charge. For example, a misalignment of ΔX = 1 mm corresponds to a prediction of,

$$\alpha = \frac{\Delta X}{P_T Z} \approx \frac{1\ \mathrm{mm}}{5.7 \times 10^6\ \mathrm{MeVc^{-1}mm}} \approx 1.8 \times 10^{-7}\ \mathrm{MeV/c^{-1}}. \tag{5.5}$$

In principle, the real origin of the magnitude of α is far more complicated, but the spectrometer reconstruction has built in spatial alignment for both individual STRAW tubes and chambers [75]. Therefore, we expect to observe values of α far smaller than the prediction in Equation 5.5, as the alignment is typically better than $100\ \mu$m. Additionally, as α is in units of momentum, the effect of the calibration results in a shape change in the momentum spectra.

5.2.2 The β parameter

The calibration parameter β is designed to correct for any miscalibration of the total magnetic field integral. As seen in Chapter 4, the precision of the field integral is directly related to the track momentum. Therefore, β is defined as,

$$\beta = \frac{\Delta B}{B} = \frac{\Delta P}{P} \approx 10^{-3}, \tag{5.6}$$

where the expected size of β is the maximum permitted systematic uncertainty in the total MNP33 field integral provided by Ref. [67]. Unlike the 'shape-changing' α, β is unitless and not dependent on the track charge, expected to alter only the magnitude of momenta.

5.3 Calibration Procedure

5.3.1 Exploiting $K_{3\pi}$ decays

In order to obtain the calibration parameters (α, β), a data driven approach is essential. The clear experimental signature of the three-track decay $K^+ \to \pi^+\pi^+\pi^-$ $(K_{3\pi})$ is a perfect channel for multiple reasons; the decay is not only abundant, but also contains three observable tracks. As the pion four-vectors are directly accessible, the kaon invariant mass can be calculated accurately. Therefore, the calibration procedure can exploit $K_{3\pi}$ to find (α, β) parameters which tune the momentum such that the $K_{3\pi}$ invariant mass closely matches the PDG combined fit value of $M_{K^+} = 493.677$ MeV/c^2, a value that has been measured extensively in numerous experiments [55].

The selection used to collect $K_{3\pi}$ candidates is implemented into NA62FW as the general analyzer `K3piSelection` [66]. The analyzer is used by multiple analysis tools to perform several tasks, such as,

- Calculation of the beam-parameters (Momentum, slope, position).
- Calculation of kaon flux and number protons on target (POT).
- Determination of efficiencies for three-track trigger topologies.

In order to remain consistent with the beam-parameters calculation, the standard selection was adopted, which requires at least one good three-track vertex consistent with the $K_{3\pi}$ hypothesis of the kaon mass. Vertices are reconstructed using a five-dimensional fit based on track parameters (slopes, positions and momentum) at the first STRAW chamber. The fit corrects for residual magnetic fields (using a Kalman filter) and multiple scattering [66] [76]. The $K_{3\pi}$ selection is provided below, requiring exactly one good three-track vertex built in the event, defined as:

- The vertex charge is Q = +1.
- The vertex fit χ^2 is less than 25.
- The vertex longitudinal position (Z-Vertex) within (102; 180) m

- The vertex total momentum (P-Vertex) within (72; 78) GeV/c.

For the tracks in the three-track vertex:

- Within the geometric acceptance of the four STRAW chambers and NewCHOD.
- At least one or more tracks with a geometrically associated CHOD candidate, which has excellent timing precision. Up to three candidates are used to build a vertex time (one per track). The vertex time must be within 10 ns of the trigger time responsible for collecting the event.

Finally, the invariant mass of the three tracks in the $K_{3\pi}$ hypothesis lies in the range of $M_{3\pi} - M_{K^+} = (490; 497)$ MeV/c^2.

Additionally, the tool will only read data that has been pre-selected to contain three-track decays. Using the `FilterRestrictedThreeTrackVertex` tool, the time taken to read the any data sample can be dramatically reduced by building a more compacted data set containing only suitable decays [66]. The filter reduces the raw data size by a factor of ≈30, and applies a looser version of all vertex related cuts above [77]. Figure 5.2 displays the $K_{3\pi}$ invariant mass spectra for the full 2016A filtered data set, compared to signal MC. For this data set, the mean invariant mass

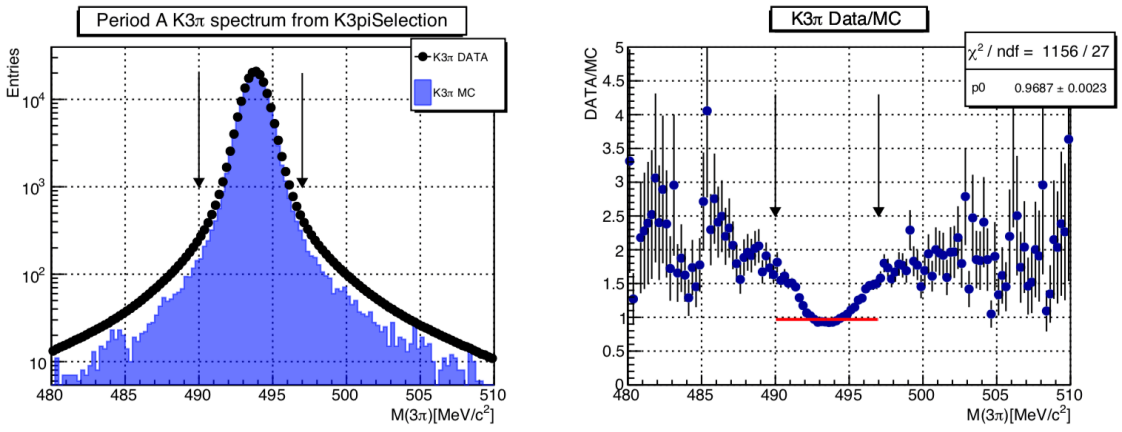

Figure 5.2: Left: The $K_{3\pi}$ invariant mass spectrum for the full 2016 Period A data set, with the SR denoted by the arrows. Right: The data/MC ratio, with flat line fit in the SR.

is 493.807 MeV/c^2 with resolution $\sigma_M = 0.870$ MeV/c^2. In principle, the application of a suitable (α,β) correction will improve the ≈0.2 MeV/c^2 discrepancy between the data and nominal value. In general, the data/MC agreement is reasonable within

the SR, whereas the mass side-bands suffer due to the lack of coincidental kaon decays in the MC. Agreement in this region can be improved with a more stringent three-track selection (see Chapter 6).

5.4 Calibration algorithm

To determine calibration constants (α, β), a suitable algorithm is required. The nature of the task leads to two logical stages:

Stage A: The event level, "DATA MODE"

1. Collect $K_{3\pi}$ candidates by calling `K3piSelection`.
2. Calculate the pion four-vectors for $n_\alpha \times n_\beta$ trial values of (α, β).
3. Reconstruct the kaon mass at each trial, saving the results in histograms in $n_{P_{\pi^-}}$ bins of the negative pion momentum P_{π^-}.

Stage B: The end of run level, "HISTOGRAM MODE"

1. Process a large number of events via Stage A.
2. Fit the invariant mass distribution for each trial $(\alpha, \beta, P_{\pi^-})$ with a Gaussian curve and extract the fit parameters.
3. Build a test-statistic χ^2 described in Equation 5.7 and create a (α, β) vs. χ^2 distribution from the parameter scan.
4. Fit the distribution using a two-dimensional polynomial, extracting the ideal calibration constants at the coordinates of the minima of the fit.

For an NA62Analysis analyzer, Stage A will be run first with the reconstructed data to obtain the result of the scanning procedure in the form of histograms. Stage B will then use the histogram output to perform the calibration calculation. Stage B can process the histogram-output from events collected from a burst, or more ordinarily, a data-taking run (typically 10^3 bursts).

As an alternative to saving $\approx 10^6$ histograms from Stage A, the information is condensed into a single 2D histogram, with a Y-axis corresponding to three-dimensional index for each $(\alpha, \beta, P_{\pi^-})$ trial and the X-axis as the invariant mass of the $K_{3\pi}$ candidates. Table 5.1 contains the chosen configuration for the scan in the calibration parameters. The scan range is slightly larger than the predictions made Sections 5.2.1 and 5.2.2 and the binning is different in each dimension due to the varied sensitivities of the parameters (See Figure 5.4). The number of histograms needed ordinarily

Table 5.1: Details of the scan configuration for the $(\alpha, \beta, P_{\pi^-})$ computation, motivated by the estimation in Sections 5.2.1 and 5.2.2

Parameter	Range	Step Size	Number of Bins
α [MeV/c]$^{-1}$	$\pm\, 2 \times 10^{-7}$	4×10^{-9}	101
β	$\pm\, 6 \times 10^{-3}$	2×10^{-4}	61
P_{π^-}[GeV]	$10, 45$	2	18

is $N_H = n_\alpha \times n_\beta \times n_{P_{\pi^-}} = 110898$, which instead denotes the number of bins needed in the Y-dimension. The histogram is filled in a three-dimensional loop over the scan parameters, where Figure 5.3 displays an example of the output from each stage of the algorithm. Due to the vast size of the scan histogram, a reduced range is shown

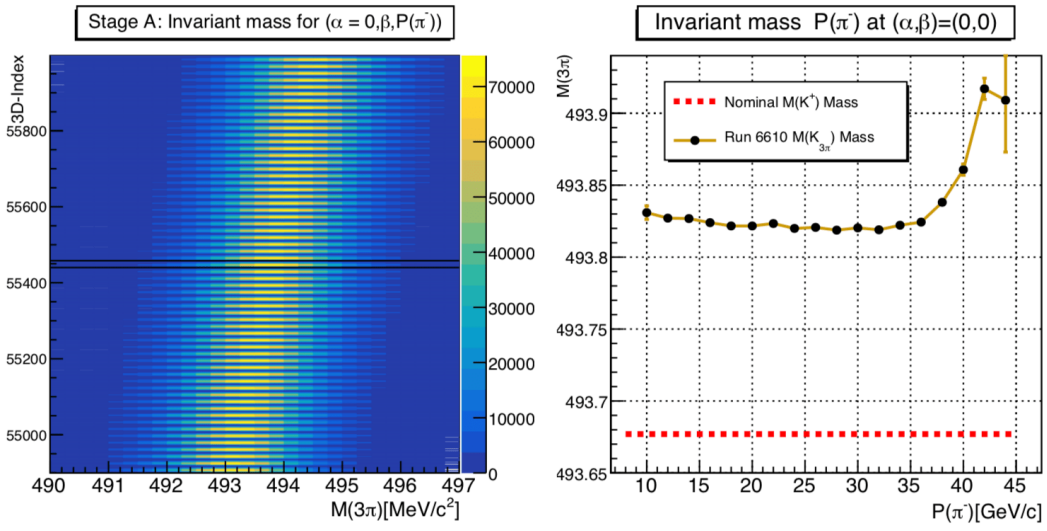

Figure 5.3: Left: A reduced-range example of the histogram output from Stage A for Run 6610; black lines denote the invariant mass distributions vs momentum for $(\alpha, \beta) = (0, 0)$. Right: Comparing the invariant mass vs. momentum distributions for $(\alpha, \beta) = (0, 0)$ compared to nominal.

for only $(\alpha = 0, \beta, P_{\pi^-})$, containing $N_H/n_\alpha = 1098$ bins. The black-lines denote a region with $n_{P_{\pi^-}}$ bins where $(\alpha, \beta) = (0, 0)$ as an example. Stage B is initiated by

extracting and fitting each P_{π^-} slice with a Gaussian, used to create a mass versus momentum graph for each (α, β) trial, displayed in the right-hand plot in Figure 5.3. This leads to the creation of $n_\alpha \times n_\beta = 6161$ graphs in total, where each is used to build a χ^2 test-statistic, defined as,

$$\chi^2 = \sum_{i=1}^{n_{P_{\pi^-}}} \frac{(M_{3\pi,i} - M_{K^+}^{PDG})^2}{(\sigma_{3\pi,i})^2}, \tag{5.7}$$

where $M_{3\pi,i}$ is the fitted invariant mass and $\sigma_{3\pi,i}$ is the uncertainty at momentum bin i for some trial (α, β). In principle, the calibration parameters which correct the raw distribution to the nominal case (denoted by the dashed red line) will minimise the statistic. As α is momentum dependent, it is expected to distort the shape of the distribution and β to control the overall scale. To obtain the constants, the creation of an (α, β) against χ^2 distribution can be used to find the minima, by fitting with a two-dimensional polynomial with cross-term (in case of parameter correlation),

$$\chi^2(\alpha, \beta) = p_0 + p_1\lambda\alpha + p_2\beta + p_3\lambda^2\alpha^2 + p_5\beta^2 + p_6\lambda\alpha\beta. \tag{5.8}$$

Here, $p_{1;6}$ are fitting constants and $\lambda \approx (\beta/\alpha)_{est} = 10^4$ is a scale factor based on the estimates of the (α, β) parameters from Section 5.2. It is used for alpha terms so that each component of Equation 5.8 is the same order of magnitude; this allows the fit to converge to sensible answers first time without any prior configuration. Figure 5.4 displays the χ^2 distribution for an arbitrary run in 2016. The χ^2 distribution has been normalised by the number of degrees of freedom (NDF) at each (α, β) bin; as the NDF is flat, the effect only changes the rate of increase of the Z-axis and not the position of the minima. The change in χ^2/NDF is more drastic in the β-dimension than in α, motivating the choice of the different number of step sizes in each axis. The right-hand plot is the effect of several (α, β) parameters on the mass against momentum distribution, including the found minimal case. The best result shifts the spectrum toward the nominal kaon mass at the most populated region of the plot (between 20-35 GeV), but with a notable change in shape. It is also clear from the $(\alpha, \beta) = (0, \beta_{min})$ distribution that a trivial β correction could have just been applied instead of a two-dimensional approach. However, by additionally obtaining α con-

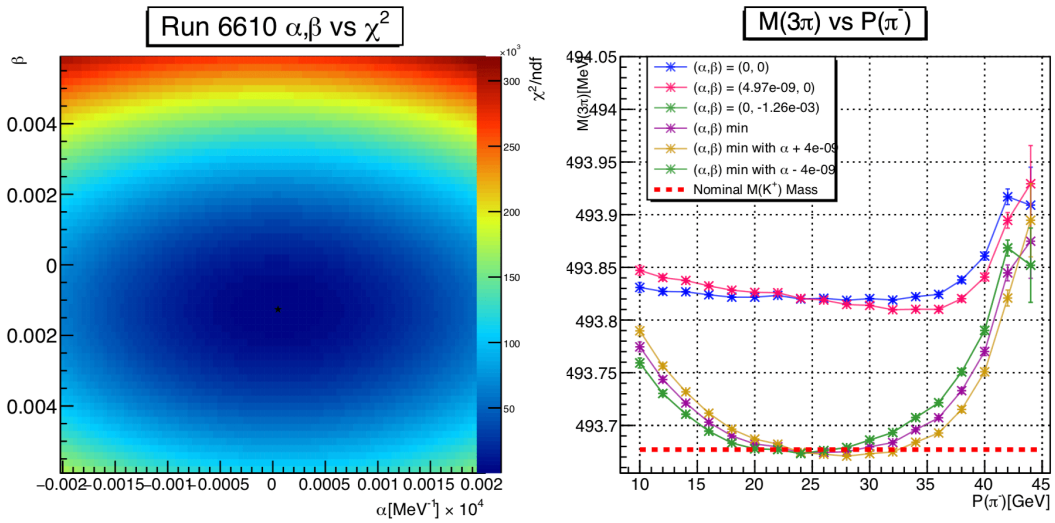

Figure 5.4: Left: (α, β) vs. χ^2/NDF distribution, with polynomial minima is denoted by the star. Right: the resulting mass vs. momentum distributions from the correction with several examples for comparison, such as the minimum $\pm$ a step in α.

stants, we can both fine-tune the momentum determination and also obtain some knowledge of the chamber misalignment for each run. The distributions which are the $(\alpha_{min} \pm \alpha_{step}, \beta_{min})$ show that α only slightly modifies the standard distribution; it is clear that there is no solution with this simple model that can shift the blue line to the nominal kaon mass without a shape distortion. Notably, the distribution which is just to set $(\alpha, \beta) = (0, \beta_{min})$ also results in a shape change; β does not just scale the distribution, but also affects the shape.

5.4.1 Tuning the fit

The description previously focused on building an algorithm to determine calibration constants. In order to guarantee the effectiveness of the algorithm, the fitting performance at each stage requires special attention. The top-down view of Figure 5.4 provides only limited information; for a more complete picture, Figure 5.5 contains one-dimension projections to show the agreement side on. As the (α, β) fit is performed with the weights in each bin set to unity (as statistical bin errors are meaningless for the test-statistic), the case of an unconstrained fit is dominated by the large χ^2/NDF bins. The minimum is approximately in the correct place, but the shape is not well described. This can be improved either by cutting bins of large magnitude or reducing the fit to within a smaller range around the minimum bin.

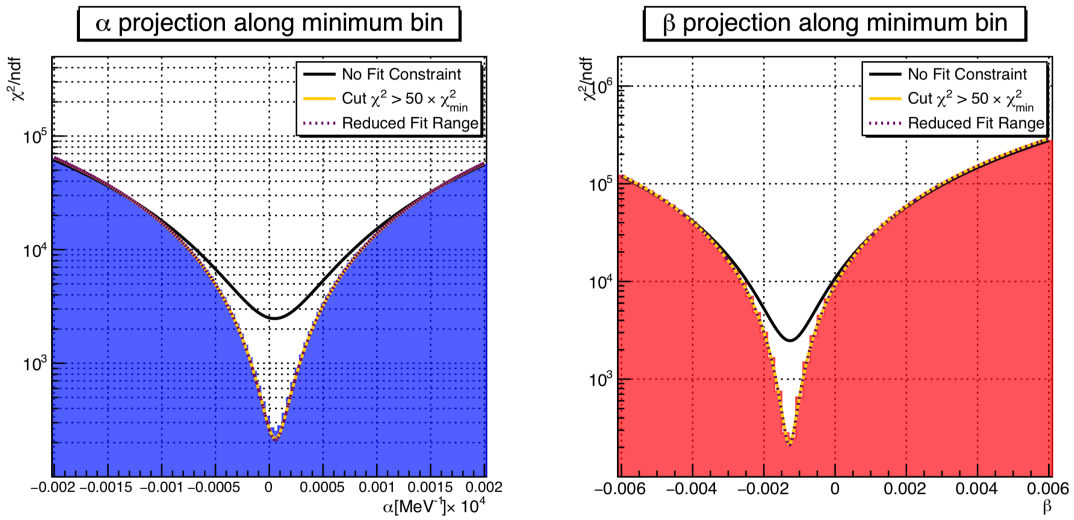

Figure 5.5: One-dimensional projections of the fit with left: α and right: β. The black line denotes the standard fit, whereas the orange and magenta lines show where (a) χ^2 bins larger than the $50 \times \chi^2_{min}$ have been removed and (b) the fit was reduced in range to $\pm$ 10(5) $\alpha(\beta)$ scan steps around the minimum bin.

This results in a drastic improvement to the shape agreement, summarised in Table 5.2, where the errors assigned to (α, β) are computed by finding where the χ^2 distribution increases by 2.3 from χ^2_{min} [78]. The standard approach returns (α, β)

Table 5.2: Summary of the (α, β) results for several tuned χ^2/NDF fits. Without some constraint on the minima, the standard approach returns an answer deviated from the tuned cases by more than 1σ for both parameters.

Method	α [MeV/c^{-1}] (10^{-8})	β (10^{-3})	(α, β) fit χ^2/NDF [10^3]
Standard (No constraint)	0.50 $\pm$ 0.03	-1.26 $\pm$ 0.01	2999.5
Cut $\chi^2 > 50 \times \chi^2_{min}$	0.56 $\pm$ 0.03	-1.28 $\pm$ 0.01	0.3
Reduced Fit Range	0.56 $\pm$ 0.03	-1.28 $\pm$ 0.01	0.1

which are deviated by $\approx 2\sigma$ from the fits which performed well. For this reason, the χ^2 cut approach was adopted as it is automatically tuned to the minimum of the distribution. In addition to the final-stage fitting improvements, the mass spectra used to build the components of the test-statistic require additional scrutiny. By fitting the invariant mass spectra at each momentum bin, the χ^2/NDF distribution is highly dependent on the mass fit quality. During the invariant-mass building Stage A, improvements could be considered:

- Requesting trigger information to remove events which intrinsically distort the spectrum.

- Include cuts to remove beam-related background.
- Increase the granularity of the (α, β) scan.

An example of a distortion would be from the dimuon trigger line which requires two MUV3 candidates in the final state. For $K_{3\pi}$ to fire such a condition requires two secondary pion decays, which if occurring in the spectrometer volume would affect the invariant mass. Cuts to remove beam-related background would improve the tails in Figure 5.2 by increasing the purity of the sample. However, both approaches would deviate from `K3piSelection`. The final point, which is to increase the scan granularity is also undesirable as it will increase both the CPU time required and the memory size of the output files that are stored during reprocessing.

Regardless, the actual Gaussian mass fits are free to be tuned appropriately. In the default case, the centre of the maximum bin b^c_{max} is found for each mass spectra and used to define a fit range based on the mass resolution σ_M,

$$(b^c_{max} \pm n\sigma_M) \tag{5.9}$$

where n is an integer between (1; 5) and rounded $\sigma_M = 0.90$ MeV/c^2. Table 5.3 displays the response of both the mass and (α, β) fits with n. For $n = 1$, only

Table 5.3: Comparing the goodness of fit versus the size of the mass-range in the Gaussian fit. This is limited to $n = 4$ by the size of the mass-window in the selection.

n	Gaussian fit χ^2/ndf	(α, β) fit χ^2/ndf (10^3)	α[MeV/c^{-1}] (10^{-8})	$\beta(10^{-3})$
1	1.3	3.4	0.41 $\pm$ 0.05	-1.20 $\pm$ 0.01
2	112.5	8.3	0.50 $\pm$ 0.03	-1.28 $\pm$ 0.01
3	356.4	1.3	0.55 $\pm$ 0.03	-1.28 $\pm$ 0.00
4	529.3	0.2	0.56 $\pm$ 0.03	-1.28 $\pm$ 0.00

the core of the distribution is fitted, whilst $n = 4$ accounts for the full selection window. As the mass fit extends in range and the goodness of fit worsens, the (α, β) fit improves and the parameters stabilise. This can be seen in Figure 5.6. The shape of the (α, β) vs. χ^2/NDF becomes less fluctuated as the tails of the distribution enter into the mass fit. As we rely purely on a good calibration result, $n = 4$ is the optimal solution.

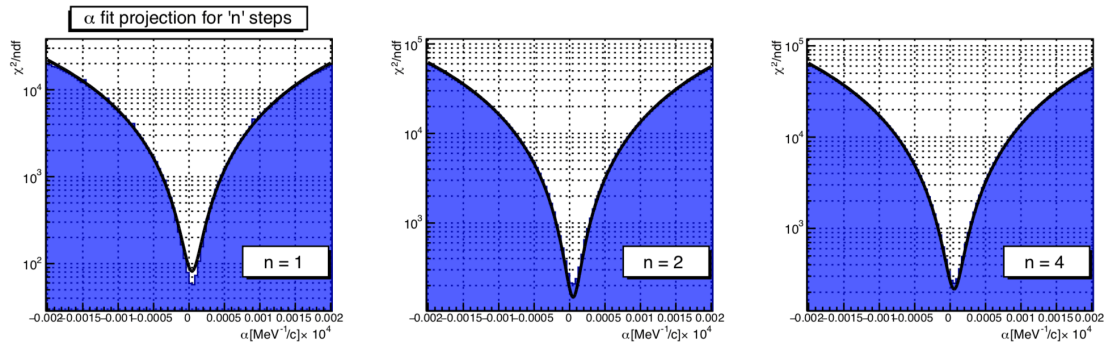

Figure 5.6: Response of the fit shown in one-dimension for α with a mass-window where left: $n = 1$, centre: $n = 2$, and right: $n = 4$. The first case has a less stable shape in the distribution and overestimates the minimum, whereas the centre case underestimates. By $n = 4$, the minima is adequately described.

5.5 Results

The analyzer `AlphaBetaComputation` was implemented into NA62 Framework (NA62FW), designed to be used at the initial stage of the data processing [66]. In ideal operation, the computation is used in two stages to mirror Stage A and B described previously. The analyzer is used directly after the event filtering stage to produce the scanning histograms, and then again (on the output of the first stage) to find the optimal (α, β) parameters. As the reprocessing is performed run-by-run, the calibration parameters are determined and subsequently used in all standard analysis tools during the later stages of reprocessing. In this section, the results of the computation are presented for both the 2016A and 2017A data sets. In addition to the final parameters, the effect of the correction to the measured kaon mass is provided. Finally, a study exploring the response of the calibration for deliberately miscalibrated MC is presented to understand the effectiveness of the tool.

5.5.1 In 2016

The 2016A data set corresponds to the sample recorded after the full commissioning of the NA62 detector between September and November 2016 (see Section 6.2). The full sample is equivalent to 169 runs ($\approx 8\times10^4$ SPS bursts) which successfully passed the full reconstruction and data-reprocessing procedure. For each run, a set of calibration constants were determined. Figure 5.7 displays that for the lat-

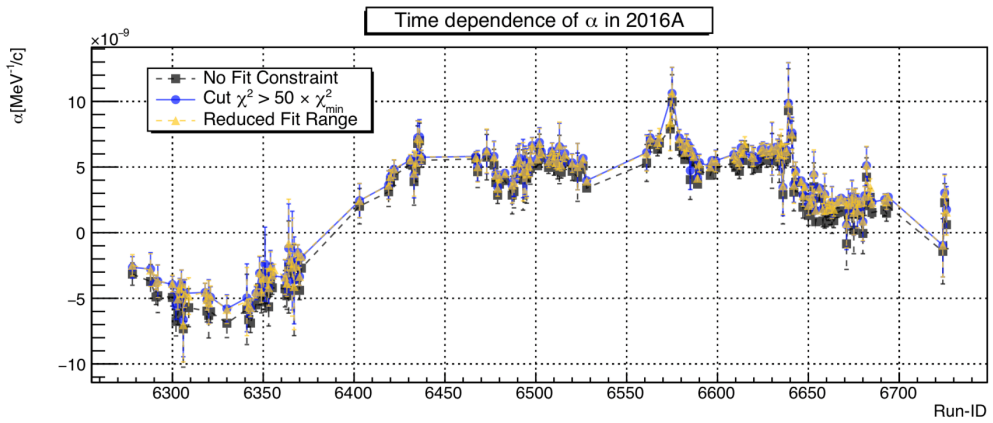

Figure 5.7: Time-dependence of α in 2016A. The blue dots correspond to the chosen fit technique.

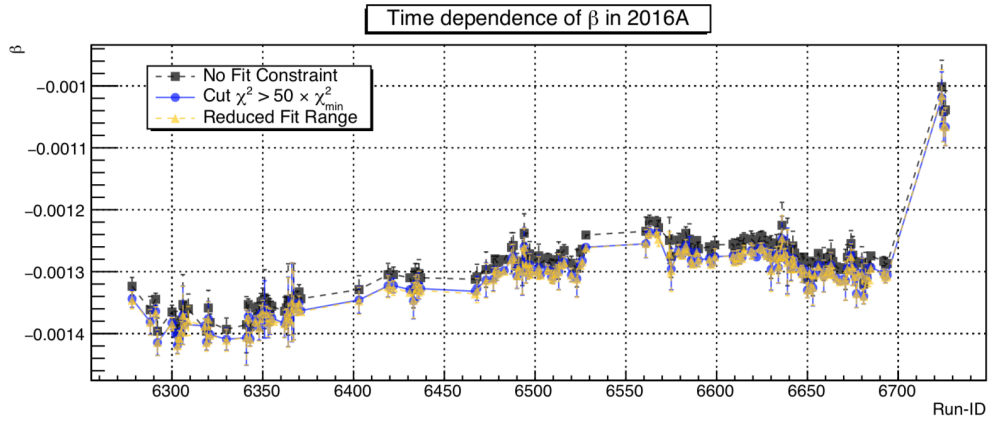

Figure 5.8: Time-dependence of β in 2016A. The blue dots correspond to the chosen fit technique.

ter stages of 2016, α was stable at $\approx 5 \times 10^{-9}$ MeV/c^{-1} after transitioning from $\approx -5 \times 10^{-9}$ MeV/c^{-1} early part of the run. Using the conversion from Equation 5.5, this corresponds to $\approx$10 μm in misalignment. A possible reason for the transition could be temperature related. For example, the $\Delta\alpha$ in 2016 is equivalent to $\approx 10^{-8}$ MeV/c^{-1} which corresponds to a 57 μm change in the misalignment. For a metre long polyethylene STRAW tube, the temperature change required to achieve such an expansion is of the $\mathcal{O}(10$ K), which is entirely feasible in a high-radiation environment.

The parameter β shown in Figure 5.8 is even more stable at $\approx -1.35 \times 10^{-3}$, only becoming slightly smaller over time. The only significant feature can be found at the end of 2016, where β jumps by $\approx 0.5 \times 10^{-3}$. The jump is understood to be a residual effect of the MNP33 magnet being deactivated so that a series of non-K^+

runs could be measured for the exotic programme. The final three runs correspond to the return of the standard K^+ beam operation. The only difference between the constrained and unconstrained fit approaches appears to be a systematic shift by less than a step-size of the scan for both (α, β) parameters, which was observed previously in Table 5.2.

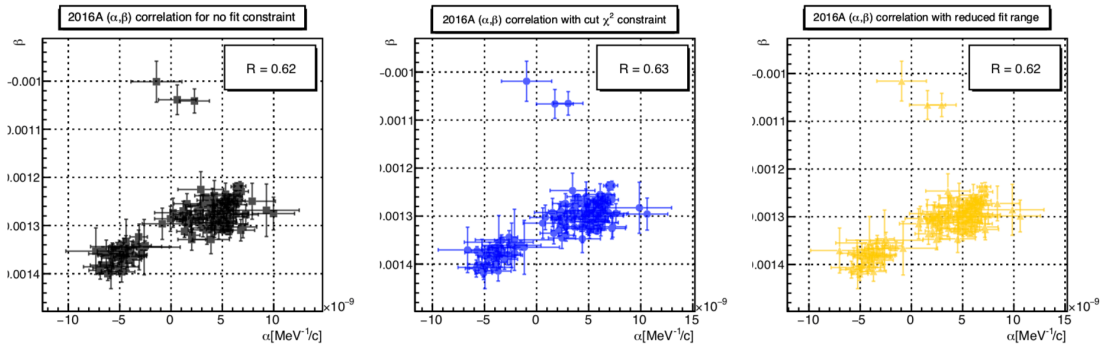

Figure 5.9: Correlation between (α, β) parameters in 2016A for Left: no fit constraint, Centre: with a χ^2/NDF cut and Right: the reduced fit range. R is the correlation factor i.e Pearson's regression.

Additionally, Figure 5.9 contains the regression R between the calibration parameters in 2016A for the three fit approaches. Each method is consistent, suggesting that both parameters are moderately correlated, yielding $R \approx 0.6$. However, the stable conditions do not yield dramatic changes in the parameters. For example, the three largely deviated points correspond to the final three runs where β was expected to change. Finally, the effect of the correction on the $K_{3\pi}$ mass is presented in Figure 5.10. While the mass resolution remains the same after the correction ($\sigma_M \approx 0.86$

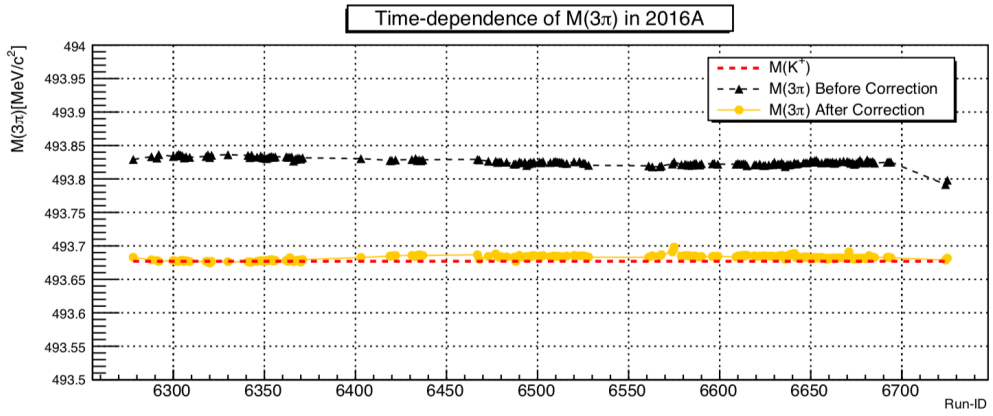

Figure 5.10: Comparison of the time-dependence of the $K_{3\pi}$ mass post (α, β) corrections in 2016A.

MeV/c^2), the invariant mass displays a large improvement, having shifted the invariant mass by -0.14 MeV/c^2 to leave the systematic discrepancy between $M_{3\pi}$ and M_{K^+} at ≈+6 KeV/c^2. In addition, the corrected values remain remarkably stable over the full period, providing evidence that the computation is extremely consistent regardless of the starting values.

5.5.2 In 2017

The 2017A data set corresponds to the sample recorded between September and October 2017 (see Section 6.2). The full sample corresponds to 79 runs (8× 10^4 SPS bursts) and is a similar size to 2016A. Again, a set of calibration constants were extracted for each run. Figure 5.11 displays that α was an order of magnitude larger

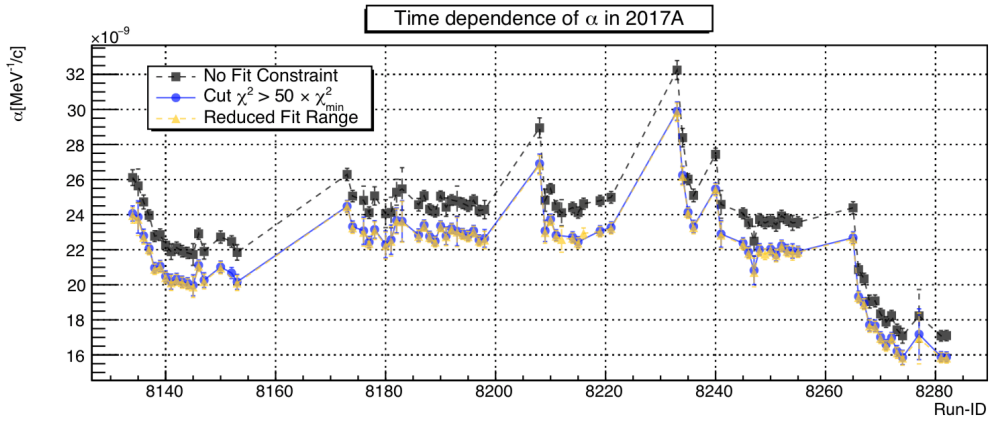

Figure 5.11: Time-dependence of α in 2017A. The blue dots correspond to the chosen fit technique.

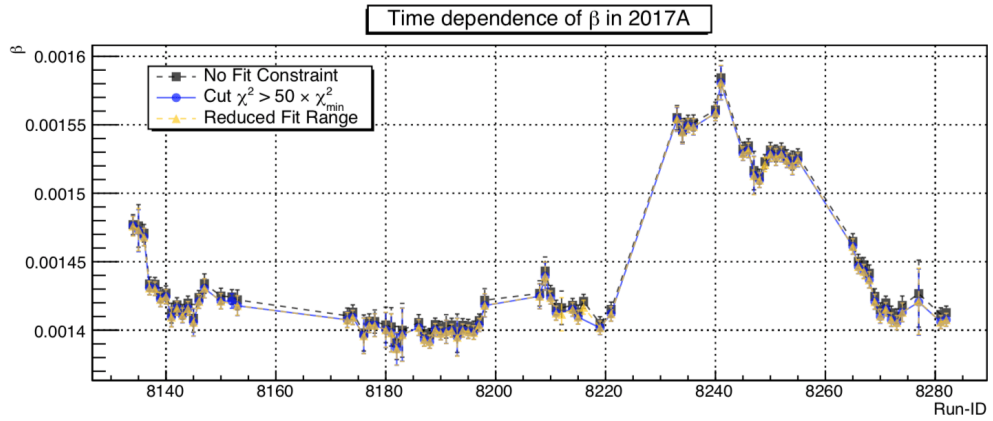

Figure 5.12: Time-dependence of β in 2017A. The blue dots correspond to the chosen fit technique.

in 2017, suggesting misalignment of the order ≈100 μm. In general, α is stable ex-

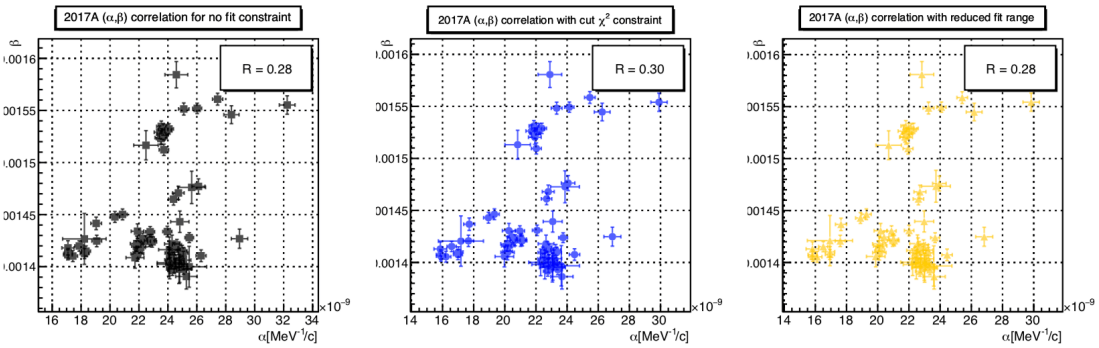

Figure 5.13: Correlation between (α, β) parameters in 2017A for Left: no fit constraint, Centre: with a χ^2/NDF cut and Right: the reduced fit range. R is the correlation factor i.e Pearson's regression.

cept from the start and end of the run-period, with some 'spikes' at certain runs in between. In Figure 5.11, the parameter β is perhaps more interesting due to frequent MNP33 magnet trips that were a notable feature during the data-taking process. The issues are reflected by +15% change in β between Runs (8220; 8270), before returning to values similar with those from before the start of the issues. The peak β value occurs after the MNP33 was turned off altogether, which was seen similarly in 2016. As seen previously, constraining the fit systematically shifts the parameters found by the computation by a fixed value within a step-size of (α, β).

Again, both α and β were plotted in order to determine the regression. Unlike 2016, the typical regression $R = 0.28$ suggests that the parameters are even less correlated. This suggests that the magnet miscalibration only dramatically affects β and not α, as the points where the MNP33 is known to have tripped resides in a similar area of the plot to the 2016 cases where the MNP33 had changed current. As ≈20% the data experienced this issue, it is likely the R is smaller as a result as the magnetic field changes are not reflected in α. Like 2016, the effect of the correction on the $K_{3\pi}$ is presented in Figure 5.14. In general, the invariant mass before correction is different in 2017 compared to 2016. Table 5.4 contains the main differences between the two samples and the magnitude of the corrections. As in 2016, the mass resolution

Table 5.4: Comparing the result of the correction for 2016A and 2017A. The values are in MeV/c^2

Data set	$M_{3\pi}$ Initial	$M_{3\pi}$ post-correction	$\Delta M_{3\pi}$	Difference from Nominal	σ_M
2016A	493.825	493.683	-0.142	+0.006	0.860
2017A	493.522	493.696	+0.174	+0.018	0.881

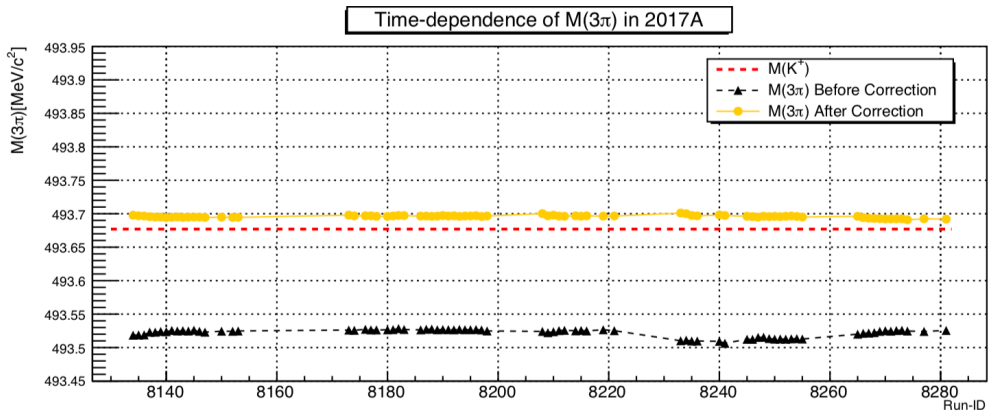

Figure 5.14: Comparison of the time-dependence of the $K_{3\pi}$ mass post (α, β) corrections in 2017A.

remains the same post correction (at $\sigma_M \approx 0.88$ MeV/c^2), with the invariant mass displaying a large improvement, shifting on average by +0.174 MeV/c^2 to leave the systematic discrepancy between the $M_{3\pi}$ and M_{K^+} at ≈+18 KeV/c^2 for 2017A. The difference here is ≈ 10 KeV/c^2 larger than for 2016, but the result of the procedure is highly dependent on the initial data-taking conditions. For example, the (α, β) correction to the momentum re-aligns the invariant mass in different directions for the two data sets, suggesting that the response in the spectrometer is fundamentally different in 2017 than it was in 2016.

5.5.3 Simulation

In addition to producing (α, β) constants in data, the tool can be applied to signal MC. This can provide verification that the computation behaves as expected; NA62MC and NA62Reco can be modified to apply the effects that the tool is designed to correct for. For example,

- In NA62Reco, deliberately misalign a spectrometer chamber by shifting the alignment constants to find a response in α.
- In NA62MC, change the field scale factor $M_{sf} = B/B_{nom}$ of the MNP33 to study the response in β.

To understand the response of the computation, 10^5 signal MC $K_{3\pi}$ were generated, corresponding to ≈ 10^4 Monte Carlo (MC) candidates post-selection.

5.5.3.1 Misalignment in the spectrometer

For this study, the spectrometer reconstruction was modified to include the alignment procedure. In standard operation, the alignment is only performed for real data where the positions of the spectrometer chambers may not be nominal. By allowing the simulation to use the alignment, systematic chambers shifts can be applied. The alignment is performed by offsetting the four (U, V, X, Y) coordinates of each STRAW chamber with constants determined using a muon run, where the hit positions of the STRAW were very accurately known. By allowing the simulation to use the alignment procedure, a shift can be applied in any direction by simply changing the alignment file. Only the X-dimension of the fourth chamber was misaligned in order to compare with the simplistic case outlined in Section 5.2.1. Figure 5.15 displays the change in the α result when shifting away from nominal alignment values.

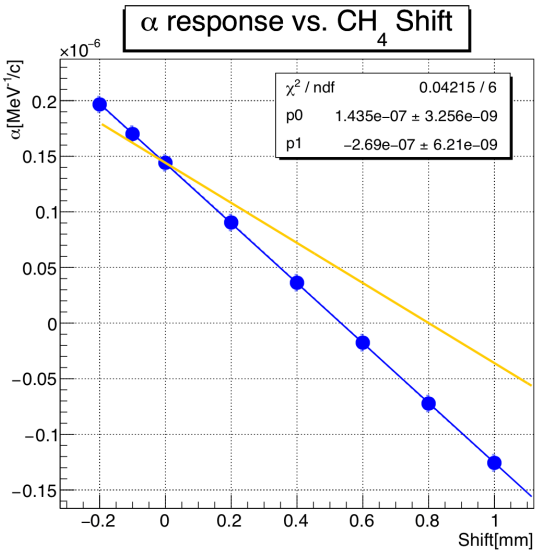

Figure 5.15: Response in α after the deliberate misalignment of spectrometer chamber 4. The $X-$axis is the shift from the nominal constant. The orange line depicts the simplistic expectation.

The effect is large and strongly linear for α, where a 1 mm misalignment almost covers the full α scan range. Clearly the response, whilst slightly different from the simplistic expectation, shows the a linear trend as expected for the computation to correct for the effect.

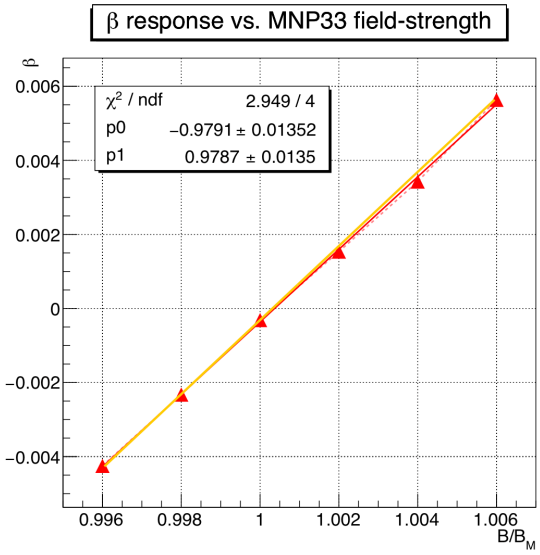

Figure 5.16: Response inβ after the re-scaling of the MNP33 magnet. The $X-$axis is the ratio of the field to the nominal value.The orange line depicts the simplistic expectation.

5.5.3.2 Scaling the MNP33 field

In the case of β, alternative sets of MC samples were generated for several M_{sf} values between (0.996; 1.006) and reconstructed with the default chamber alignment constants. Figure 5.16 displays the change in the β for each of these samples.With respect to first test, magnetic field scaling is the more simple of the two mechanisms; as track momenta relies on the measurement of the precise kick of the MNP33 field, the relationship between the field and β is linear, precisely what is demonstrated. Again, the algorithm handles the discrepancy of a miscalibration in the field integral in the appropriate manner. Additionally, this reinforces what is seen in 2017A for runs with particular magnetic field problems; a significant change in β.

5.5.4 Monitoring

So that the data processing experts at NA62 can monitor the spectrometer-calibration performance, a set of histograms were produced in the form of a post-processing graphical report, created at the end of Stage B for each run. Figure 5.17 displays a typical post-processing graphical report, using an arbitrary run in 2016. The top left-hand corner is the print-out information of the Run number, $(\alpha \pm \sigma\alpha, \beta \pm \sigma\beta)$ and the goodness of fit χ^2/NDF. The remaining two plots on the top column are

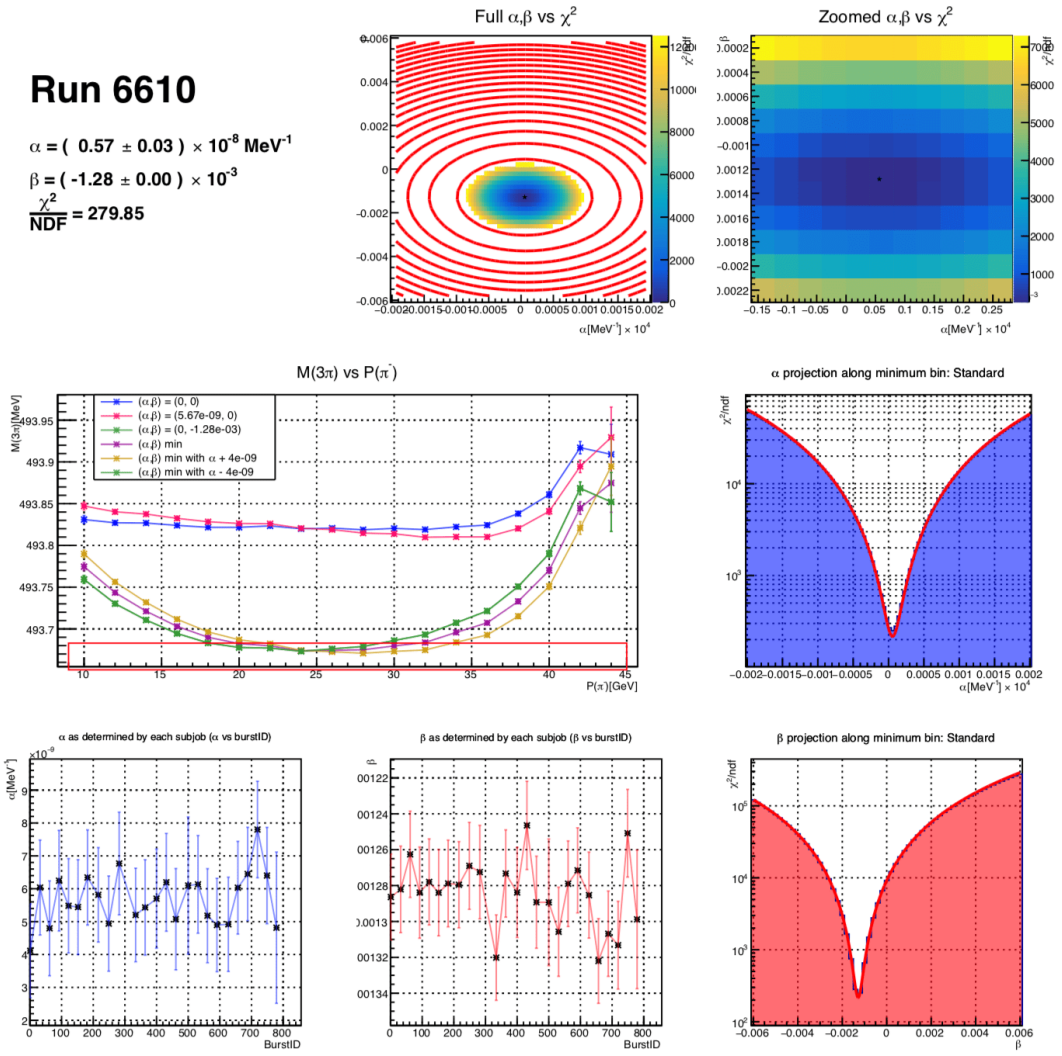

Figure 5.17: Data-processing graphical report from 2016 Run 6610.

the standard (α, β) vs. χ^2/NDF plot, along with a version which is focused on a few bins around the minimum. This row is intended to provide immediate information about the fit minima. The central graph is the invariant mass plotted against the negative pion momentum for before and after the correction, including a few interesting cases. The blue and red plots to the right of the canvas, as displayed previously in this thesis, are the one-dimensional projections of the fit, used to check for clear disagreement between the fit and the data. The final plots at the bottom are used to check the stability during a run. Typically, the runs are split into smaller groups of bursts to be submitted as parallel jobs on the lxplus batch service. As explained in Section 5.4, the Stage B can also determine constants for a group of bursts. The results of each smaller job enter directly into this plot to show the change in the

parameters during the run. Naturally, as the statistics are smaller in each job, the precision is worse than for the overall run which leads to larger errors for bursts. Regardless, the stability can be useful especially for runs with interesting features, such as a magnet trip, as β will ramp up or down. In the past, the computation aided understanding of runs which were missing the spectrometer alignment constants in reconstruction, observable via a large shift in α.

6

Event selection

In this chapter, the development of a selection for the rare $K^+ \to \pi^+\mu^+\mu^-$ ($K_{\pi\mu\mu}$) decay is presented. As described in Chapter 2, the current largest sample of $K_{\pi\mu\mu}$ decays ($N_{\pi\mu\mu} = 3120$) was collected by the NA48/2 experiment between 2003 and 2004. However, the sample is contaminated to the level of $(3.3 \pm 0.7)\%$ due to the tails of the irreducible $K_{3\pi}$ background [48]. Using data recorded in 2016 by the new NA62 detector, the selection developed below is used to collect a sample of decays where the background contribution is suppressed to a negligible level. In addition to the signal, a selection to collect a sample of normalisation $K^+ \to \pi^+\pi^+\pi^-$ ($K_{3\pi}$) decays is described, developed by extracting the relevant criteria of the final $K_{\pi\mu\mu}$ selection. This is to maximise the symmetry between the two samples. As presented in the later chapters, the sample of decays collected here is used to reconstruct the $d\Gamma/dz$ spectrum which is utilised to extract the model-independent branching fraction and form factor LECs.

6.1 Strategy

The main motivation to collect a background-free sample of $K_{\pi\mu\mu}$ decays is the suppression of the associated systematics effects. In this analysis, the spectrum of the kinematic variable $z_{\mu\mu} = (M_{\pi\mu\mu}/M_{K^+})^2$ is used to extract both the branching fraction and the LECs of the form factor. If a large background component is present in the sample and corresponds to a spectrum that is difficult to predict, the associated sys-

tematic effects will be hard to estimate accurately and will subsequently reduce the precision of the analysis. At NA62, the experimental setup offers the possibility to collect a $K_{\pi\mu\mu}$ sample with a negligible background. In the previous measurements, the dominant background was $K_{3\pi}$ decays where two of the pions decayed in flight to muons, mimicking the signal final-state. In the NA48/2 measurement, the corresponding uncertainties were the largest systematic terms in the analysis [48].

The similarity of the two decays is both useful and a difficulty. For example, the $K_{\pi\mu\mu}$ decay is characterised by one beam-originating three-track vertex, from which two reconstructed opposite sign muons and one positively charged pion originate. Similarly, the abundant $K_{3\pi}$ decay is characterised by many of the same features with the exclusion of two final-state muons. This allows for the collection of a large normalisation sample with many similar features to the signal, but at the cost that $K_{3\pi}$ can contribute as background in the SR if the pions decay in flight. Only with a highly-tuned selection which exploits the unique features of NA62 can a sensible balance be achieved.

The collection of both a $K_{\pi\mu\mu}$ signal sample with negligible background and a well-symmetrised normalisation $K_{3\pi}$ sample involves exploiting the following types of criteria:

- Vertex and track criteria, relating to kinematics and topology.
- Particle identification, relating to unique sub-detector responses.
- Precision timing between sub-detector signals.

Firstly, using the data and MC samples described in Section 6.2, a base-line NA48/2-like selection was implemented in order to compare the performance of NA62 with the previous experiment and is provided in Section 6.3. The $K_{\pi\mu\mu}$ selection was finalised by maximising the number of observed signal candidates whilst rejecting the high-mass sideband events in 2016A, which was achieved by exploiting unique features of the NA62 design. The final selections (signal, normalisation) are presented in Section 6.5 including the invariant mass spectra for both signal $K_{\pi\mu\mu}$ and

normalisation $K_{3\pi}$. Both selections are applied equally to both data and MC samples in the analysis.

6.2 Data samples

6.2.1 Recorded data samples

The selection was developed using a data-driven approach, using the very first data set produced by the NA62 experiment after the full detector commissioning in September 2016. At the time of this thesis, two samples were available for analysis, corresponding to data taken in the fall of 2016 and 2017. Both samples were reprocessed and reconstructed using the same NA62FW revision, and their features are summarised in Table 6.1. The main focus of this thesis is on the 2016A data set.

Table 6.1: Summary of the current NA62 data samples for 2016 and 2017, including some key features of the data-acquisition [79].

Sample	N_{Runs}	N_{Bursts}	Sample Features
2016A	169	89482	- Minimum bias stream: Control trigger. - $K_{3\pi}$ Normalisation: 2016A Multi-track trigger - $K_{\pi\mu\mu}$ Signal: 2016A Dimuon trigger.
2017A	79	82510	- Minimum bias stream: Control trigger. - $K_{3\pi}$ Normalisation: 2017A Multi-track trigger - $K_{\pi\mu\mu}$ Signal: 2017A Dimuon trigger.

The label 'A' is used to denote the period of data taking where both the conditions of the TDAQ were consistent over time and the sub-detector systems were performing nominally. Additional samples are expected to be available from summer 2018, which will increase the statistics in 2016 by a factor ≈ 2 and 2017 by a factor ≈ 5. The two samples were collected with different trigger configurations, presented in Table 6.2. For 2016A, both the signal and normalisation trigger streams were very similar, different by only the L_0 condition MO_2 used for collecting a Dimuon sample. The strategy changed for 2017A based on the data quality observed in 2016, where large inefficiencies were observed due to both the Q_X primitive and !LAV algorithm, as discussed in detail in Chapter 7. In 2017A, the Q_X issue was fixed and the !LAV

Table 6.2: The trigger streams for normalisation $K_{3\pi}$ and signal $K_{\pi\mu\mu}$ in 2016 and 2017. The label D denotes the downscale on the trigger, and the primitives and algorithms below are described at the end of Chapter 3.

Sample	Decay	L_0 Primitive	L_1 Algorithm	D
2016A	$K_{3\pi}$	RICH $\cdot$ Q_X	KTAG $\rightarrow$!LAV $\rightarrow$ STRAW$_e$	(25; 150)
	$K_{\pi\mu\mu}$	RICH $\cdot$ Q_X $\cdot$ MO$_2$	KTAG $\rightarrow$!LAV $\rightarrow$ STRAW$_e$	1
2017A	$K_{3\pi}$	RICH $\cdot$ Q_X	KTAG $\rightarrow$ STRAW$_e$	100
	$K_{\pi\mu\mu}$	RICH $\cdot$ Q_X $\cdot$ MO$_2$	STRAW$_e$	2

removed all together from both streams. Additionally, the KTAG condition was removed from the Dimuon trigger so that exotic (forbidden) decays could be studied using the same stream. Apart from the differences in the trigger configurations, the 2017A data set was recorded at higher instantaneous beam intensity with respect to 2016A which directly affects the TDAQ performance. Figure 6.1 displays the relative intensity spectra for the samples as recorded by events collected with the Dimuon trigger. A detailed discussion of the 2017A data set is the topic of Chapter 9.

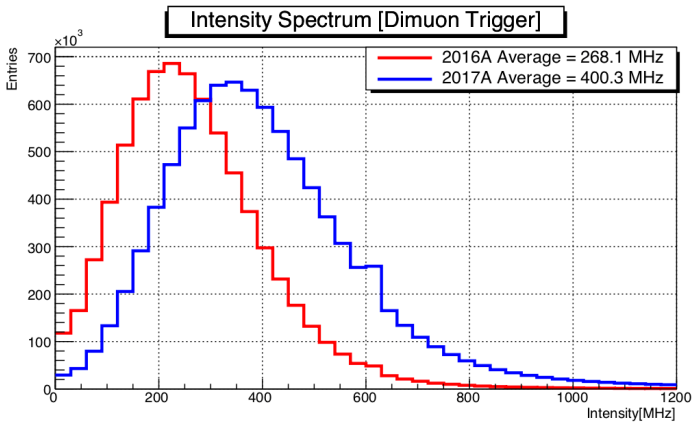

Figure 6.1: Comparison of the instantaneous intensity spectrum for 2016A and 2017A as observed by Dimuon triggered events. The average intensity is $\approx$ 130 MHz larger in 2017.

After the processing of both data sets, the filter `FilterDimuonThreeTrackVertex` was used to select only events that are considered significant for the analysis, so that the time taken to read the full data set is drastically reduced [66]. The tool is based on filter used by the computation of (α, β) described in Section 5.3 and offers a reduction factor of $\approx$ 190. The selection is designed to collect both normalisation and signal, depending on the trigger fired for the event. The criteria is summarised be-

low, and again focuses on finding at least one good three-track vertex:

- Event must have fired either the Control, Multi-track or Dimuon trigger.
- At least one good three-track vertex built in the event, defined as:
  - The vertex fit χ^2 is less than 40.
  - The vertex longitudinal position (Z-Vertex) is greater than 102 m.
  - The vertex total momentum (P-Vertex) is less than 90 GeV/c
  - All tracks in the vertex within the geometric acceptance of the four STRAW chambers.
- **For Dimuon triggered events only:** At least two vertex tracks with a spatially associated MUV3 candidate.

All conditions used in the filter are implemented again in the selection but with tighter constraints. Additionally, bursts or events with low trigger counts or with sub-detector responses systematically shifted from the expectation are removed automatically by the standard bad burst mechanism, where all trigger related detectors are checked for issues [66].

6.2.2 MC samples

Large generations of MC events were generated specifically for this analysis. The two signal MC samples for $K_{3\pi}$ and $K_{\pi\mu\mu}$ are generated in the standard fiducial volume, between 102.425 $<$ Z $<$ 180 m downstream of the target. The $K_{\pi\mu\mu}$ generator uses χPT form factor described in Section 2.2.3 for the transition, using LECs $(a_+, b_+) = (-0.575, -0.700)$ which are the average of the B865 and NA48/2 $K_{\pi\mu\mu}$ measurements [55]. Additionally, the effect of the Coulomb interaction term Ω_C between the final state particles is simulated for both signal and normalisation samples. Figure 6.2 contains Ω_C for both $K_{\pi\mu\mu}$ and $K_{3\pi}$; the size is dependent only on the invariant masses of the pairs of daughters in the decay. Whilst the average Ω_C is close to unity in both cases, hot-spots occur corresponding to where the daughter pair is at rest, such that the Coulomb interaction becomes involved by either attracting or repelling the particles in the pair. For $K_{\pi\mu\mu}$, the largest effect is for where the

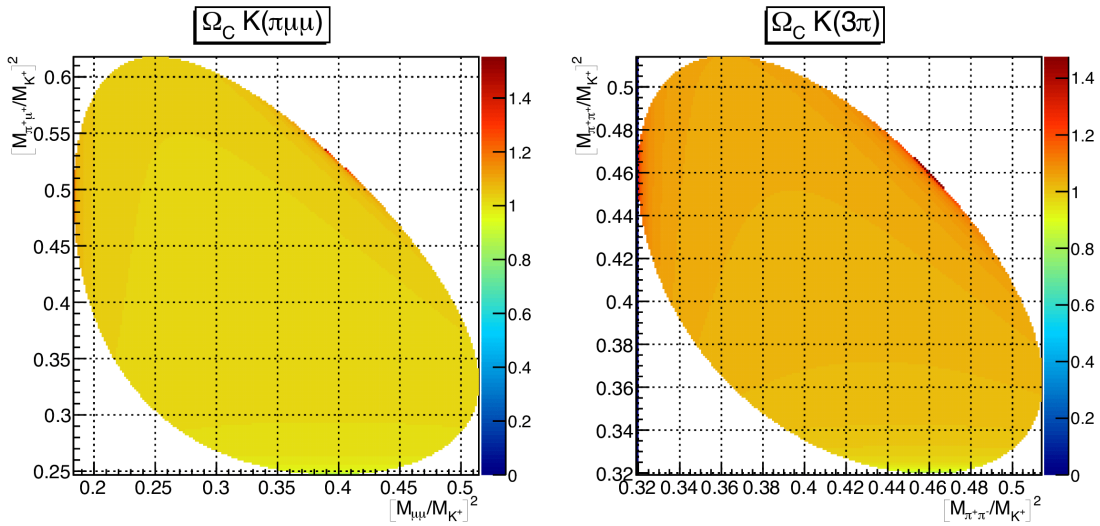

Figure 6.2: Magnitude of Ω_C in Dalitz-space for $K_{\pi\mu\mu}$ and $K_{3\pi}$. The term is on average is ≈ 1.03 for both decays, though the Dalitz space is symmetric in the case of $K_{3\pi}$. Three hot-spots are present which deviate largely from the average. The X-axis in right corresponds to the kinematic variable $z_{\mu\mu}$.

dimuon pair is at rest (i.e $z_{\mu\mu} = 4r_\mu^2$), where Q_C rapidly increases. However, the hot-spots corresponding to the where $\pi^+\mu^+$ or $\pi^+\mu^-$ are at rest occur approximately at the same point in $z_{\mu\mu}$, cancelling the effect when observing only the one-dimensional $z_{\mu\mu}$-spectrum. The $K_{3\pi}$ case displays the exact same features, but the Dalitz space is symmetric as all three daughters have the same mass.

Samples corresponding to processes that could contribute as backgrounds were also generated. The uncommon semi-leptonic $K^+ \to \pi^+\pi^-\mu^+\nu_\mu$ ($K_{\mu 4}$) decay with a branching fraction of $(1.4 \pm 0.9) \times 10^{-5}$, can contribute via decay-in-flight of the π^- track. In addition, $K_{3\pi}$ decays occurring in the TRIM5 magnet of the GTK are expected to be important as the magnet distorts the invariant mass of an already known low-mass background. A summary of the generated samples used in the analysis can be found in Table 6.3, including the statistics and the volume downstream of the target used.

6.2.3 Tuning the MC

Aside from the standard tuning to the beam applied at the generation level, further efforts were made to ensure that the simulation is as close to real-life data-taking

Table 6.3: Summary of the generated NA62MC samples. The generated volume is with respect to the distance to the target, with N_{Gen} corresponding to the number generated.

MC Sample	N_{Gen}	Generated volume downstream
$K_{3\pi}$	2.6×10^7	(102.425; 180.000) m
$K_{\pi\mu\mu}$	10^7	(102.425; 180.000) m
$K_{\mu 4}$	2×10^7	(102.425, 180.000) m
$K_{3\pi}^{\mathrm{TRIM5}}$	10^8	(96.950; 102.425) m

conditions as possible. Firstly, the efficiencies of important sub-detectors were measured in data and included in the analysis framework. The second consideration is to measure the differences in the three-track reconstruction efficiency between data and simulation. Below, the extraction and implementation of these efficiencies is described.

6.2.3.1 Sub-detector efficiency

In this analysis, sub-detector efficiencies must be understood to produce a trustworthy acceptance measurement for both signal and normalisation. Although the bad-burst mechanism removes bursts and events based on expected detector responses, the detector inefficiency is expected to be a subtle yet systematic effect in all data sets. Fortunately, only a small number of sub-detector systems are used extensively in the analysis. In order of importance,

- STRAW: Track and vertex reconstruction.
- MUV3: $\mu^{\pm}$ particle-identification.
- NewCHOD : precision timing.

The STRAW spectrometer is naturally the most important for all charged-track analyses, and is the subject of Section 6.2.3.2. The MUV3 detector is used for muon identification; the efficiency of the detector directly affects the $K_{\pi\mu\mu}$ signal acceptance but not $K_{3\pi}$ normalisation. The NewCHOD efficiency is important for both samples, as it is present in the trigger and is also used for precision timing.

Two standard tools, `MUV3Efficiency` and `NewCHODEfficiency` [66], were implemented to determine both the MUV3 and NewCHOD detector efficiencies. Their methodologies are discussed below:

- **MUV3 Efficiency**: the analyzer selects a sample of halo muons using spectrometer and MUV 1/2 energy information. Halo muons are typically at large Closest-Distance of Approach (CDA) with respect to the beam and illuminate the full MUV3 face unlike K^+ decays. By direct extrapolation of the selected tracks to the MUV3, the tool uses the standard MUV3 spatial search-radii to find whether a candidate was reconstructed as expected. The tool provides the tile-by-tile efficiencies.

- **NewCHOD Efficiency**: this analyzer uses all available one-track candidates to ensure a complete NewCHOD illumination. Like the MUV3 version, tracks are extrapolated and the standard NewCHOD spatial search-radii is used to find whether a hit was reconstructed as expected. Again, the tile-by-tile efficiencies are returned.

As both analyzers are designed to use minimum bias data, the efficiencies for both detectors were measured using the 2016A samples filtered for control-triggered events [66]. Figure 6.3 contains the tile-by-tile efficiency for both detectors, On average, the tile-

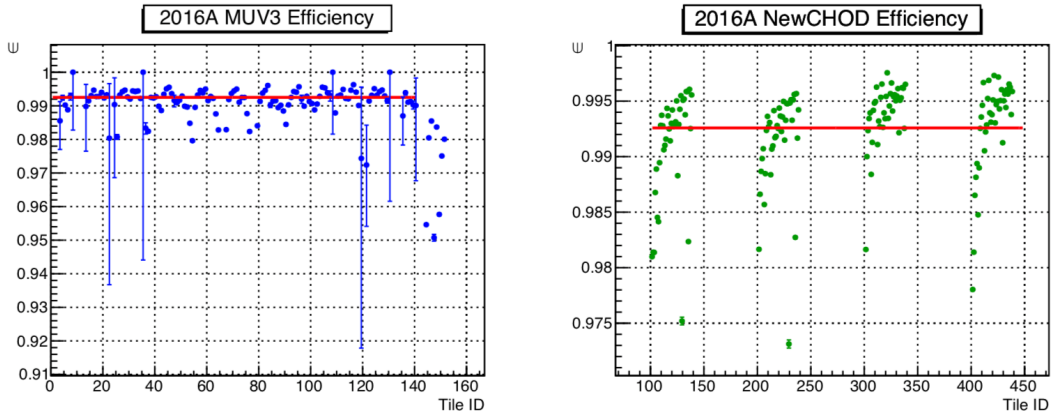

Figure 6.3: The MUV3 and NewCHOD detector efficiencies in 2016A, versus Tile-ID. Tiles with ID >140 are the inner MUV3 tiles, whilst the lower efficiency tiles at the start of each NewCHOD 'block' are also closest to the beam-line. The red lines denote the 'average' efficiencies overall, which are very similar (note the different Y-scales).

efficiency for both sub-detectors is very high at $\approx 99.3\%$. The MUV3 tiles with large errors all appear at the far edges of the detector where the particle rate is extremely low. Additionally, the lowest efficiency tiles all originate from regions closest to the beam-line for both sub-detectors. The numbering scheme of the MUV3 means that

the last nine tiles are the inner pads, whilst the first tiles at the start of each New-CHOD quadrant (four regions are clear in the plot) correspond to the inner-most regions. This is expected as the rate in these regions is the highest, which can to unavoidable losses because of radiation-related failures of the TDAQ.

6.2.3.2 Three-track reconstruction efficiency

The spectrometer track reconstruction efficiency is the most important detector-related efficiency to consider, as tracks are used for all kinematic calculations and sub-detector associations. If there is a fundamental difference in the reconstruction performance for data and MC, then the simulation is not a good description of real-life. Any residual differences must be taken into account.

A dedicated analyzer was developed based upon a similar study for single-track decays [80]. The procedure is to measure the efficiency using $K_{3\pi}$ decays in a completely unbiased way, as follows,

- Build all two-track vertices using `SpectrometerVertexBuilder`.
- Assign $\pi^{\pm}$ masses to the vertex tracks, and build a probe-track based on the missing four-momentum between the nominal kaon and the two-track vertex.
- Select events where the probe-track is consistent with the $\pi^{\pm}$ hypothesis to within 10 MeV/c.
- Apply vertex and track-quality cuts based upon the $K_{\pi\mu\mu}$ selection.
- Search for a real non-vertex reconstructed track consistent with the probe-track.

An event is considered efficient if a $K_{3\pi}$ candidate can be fully reconstructed. This requires the probe-track to have a reconstructed match that was not used to build the vertex. The vertex and track-quality cuts used match those described in the selection development in Section 6.5.1, in order to measure reconstruction efficiencies that are the most relevant to the $K_{\pi\mu\mu}$ analysis. In this preliminary tool, the beam-parameter determined kaon is used to build the probe track. In principle, this definition of the kaon is fixed per run and the precision could be improved by using matching GTK

candidates to measure the kaon properties on an event-by-event basis.

The analyzer is designed to be used identically for both data and MC in order to perform a direct comparison. Using the min-bias control-filtered data and the standard $K_{3\pi}$ MC samples, the reconstruction efficiency can be plotted versus multiple variables. A directly relevant example is probe-momentum, as seen in Figure 6.4. The agreement in (a) for data and MC is excellent, with only a small divergence

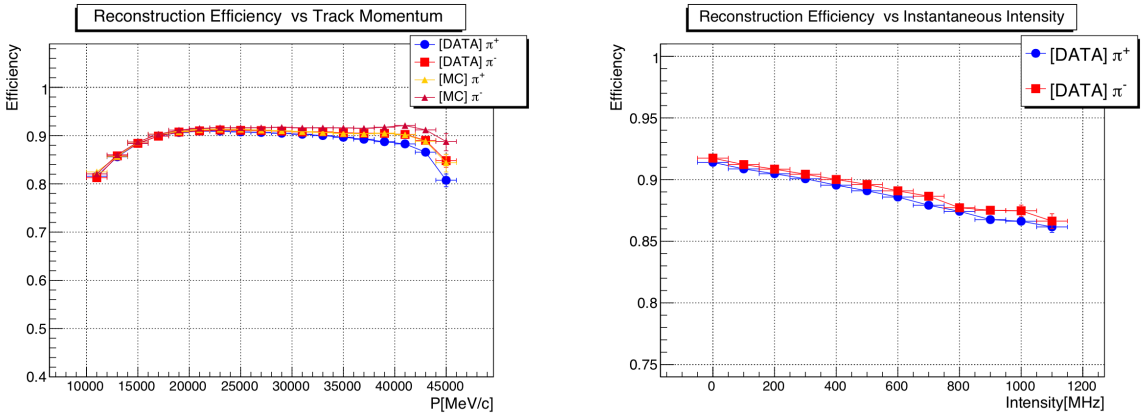

(a) (b)

Figure 6.4: Three-track reconstruction efficiency versus (a) track-momentum for both data and MC and (b) for data versus instantaneous beam intensity. The first case shows excellent agreement but with a small divergence at high momentum. The reconstruction is also intensity-dependent, with a small difference between the efficiency as determined by the charge of the probe-track.

at high-momentum. The efficiency is also slightly dependent in (b) on the instantaneous beam-intensity, with a small but notable difference between the efficiency for three-track events depending on the charge of the probe that is created. This is quantified by Figure 6.5, which is the reconstruction efficiency versus (X, Y) at the first STRAW chamber. The larger inefficiency occurs around the beam-hole and the outermost edges. Tracks in the inner regions are often reconstructed in fewer views than those at intermediate (X, Y), whereas those which occur close to the beam-line or the outer-edges are prone to acceptance related effects. The radius of the illumination is under half the diameter of a STRAW chamber, where positive-probe tracks (π^+) illuminate the chamber relatively evenly. Ultimately, by the fourth chamber, tracks on the outer edges can be swept out of acceptance as a result. In the case of negative probes (π^-), a low-efficiency tail is evident to the left of the beam-

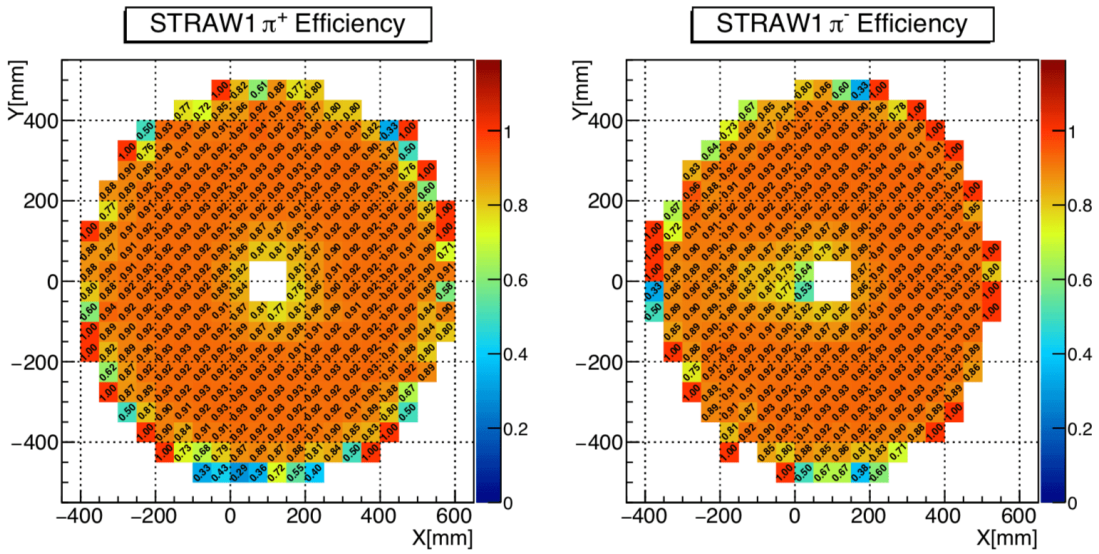

Figure 6.5: Three-track reconstruction efficiency at the first STRAW chamber, for left: the positive probe and right: the negative probe. The lower-efficiency of negative tracks can be seen to the left of the chamber hole, as they are swept by the MNP33 magnet towards the hole of the chambers downstream, whereas the effect for positive tracks is most dramatic on the outer edges. Overall, the negative case is of a slightly higher efficiency.

hole where the MNP33 magnet sweeps tracks inside of the beam-hole in the later chambers. The overall efficiency for both types of probe is essentially equivalent, at $\approx 91\%$. Despite the preliminary nature of this measurement, the analysis is in agreement with similar studies performed based on MC-only methods. In Ref. [81], an alternative MC Truth-Reco matching is performed, recording efficiencies for $K_{3\pi}$ events of $\approx 89\%$. By loosening the $K_{\pi\mu\mu}$ tuning, the method described here provides efficiencies which are an excellent agreement.

6.2.3.3 Applying detector efficiencies

A pre-analyzer `ApplyDetectorEfficiency` was developed to remove reconstructed candidates based upon the detector and track-reconstruction efficiencies for simulated samples. This is used before the stage of selection, so that both data and MC are as close to equivalent as possible before the proper analysis. In the case of the track-reconstruction, it is the ratio between the data and MC response that is important. Using the ratio, the MC simulation can be artificially corrected to match the real data distribution. The additional complication is that the data response is intensity dependent. To handle all of the above, the following method is

implemented:

- **MUV3, NewCHOD** : Tile-by-tile efficiencies are read by the pre-analyzer. The MC MUV3/NewCHOD candidates, which each have an associated tile, are removed if a flat random number generation between (0; 1) is greater than the corresponding tile-efficiency as measured in data.
- **Track reconstruction**: the momentum-dependent reconstruction efficiencies are read by the pre-analyzer for both data and MC samples. The ratio of the data and MC efficiency is created with respect to the track momentum. Simulated track candidates with momentum p are removed if a flat random number generation between (0; 1) is greater than the data/MC efficiency ratio distribution at the corresponding momentum bin. Additionally, the ratio can be produced for any intensity between $\mathcal{I}$ = (0; 1200) MHz based on the response in data.

The signal and normalisation acceptances which are determined using MC samples are therefore intensity-dependent, and must be combined using weighted averages based on the residual intensity spectrum.

6.3 Base-line selection

The NA62 experiment is designed to be technically superior with respect to the previous NA48/2 experiment. The more sophisticated tracking system has an improved design resolution, allowing for smaller Signal Regions (SRs). Additionally, the implementation of a larger magnet current is expected to increase separation between signal and the dominant irreducible background from $K_{3\pi}$ decays observed in the previous analysis. In order to observe the situation for NA62 in comparison, a NA48/2-like base-line selection was adopted, after tuning specific kinematic cuts to suit the NA62 experimental setup.

6.3.1 Base-line vertex and track requirements

Require exactly one good three-track vertex present in the event, defined as:

- The vertex charge is Q = +1.

- The vertex fit χ^2 is less than 20.
- The vertex longitudinal position (Z-Vertex) within (102; 180) m
- The vertex total momentum (P-Vertex) within (73; 77) GeV/c.
- The vertex transverse momentum P_T is less than 30 MeV/c.
- The vertex-beam CDA less than 50 mm.

For the tracks in the three-track vertex:

- Within the geometric acceptance of the four STRAW chambers, NewCHOD, LKr and MUV3.
- Tracks separated from one another by at least 20 cm at the LKr face.
- At least two or greater tracks with a spatially associated NewCHOD candidate. Up to three candidates are used to build an average vertex time. The candidate times must be self-consistent to within 10 ns, and also within 10 ns of the trigger time.

The selection searches for good quality (low χ^2), beam-originating three-track vertices. The cut in longitudinal Z-Vertex corresponds to the fiducial decay volume defined by the geometrical region of the vacuum tank, whilst P-Vertex, P_T and CDA assures consistency with the K^+ beam momenta and position. The requirement for the tracks to be in the acceptance of multiple sub-detectors is for several reasons,

- STRAW: Improves the track quality and momenta.
- NewCHOD : Improve vertex time by increasing association likelihood.
- LKr: Improves the E/P calculation.
- MUV3: Requirement for even the pion track reduces the chance of mis-identification.

The association of tracks to detector candidates is performed spatially using search-radii along the line of the extrapolation. Search-radii are required due to multiple scattering in the STRAW tubes. In general, the radii are different at each sub-detector and are inversely dependent on track momenta. For the NewCHOD case, the radius

is defined by the width of the truth-reconstructed residual of extrapolated track positions for a $K_{\mu 2}$ sample, where the resolution is $\sigma_{x,y} = (0.07 + 47.3\mathrm{GeV}/p)$ mm [66].

Timing is only requested to check consistency with the trigger. NewCHOD candidates are used to build the vertex time as the CHOD is unreliable for the current available version of the data set. Whilst the CHOD has the best time resolution, hits in the top half of the detector experienced a flaw which applied the T0 timing corrections multiple times depending on the number of hits in coincidental horizontal counters [82]. With the next revision, CHOD candidates could be re-adopted.

6.3.2 Base-line particle identification

Build a particle-identification (PID) defined as:

- Exactly two vertex tracks with at least one spatially associated MUV3 candidate (μ identification) and one with none (π identification.)
- μ tracks must have a LKr E/P less than 0.2.
- π tracks must have a LKr E/P less than 0.9.

Requiring two tracks to have a spatially associated MUV3 candidate is the simplest form of $K_{\pi\mu\mu}$ identification. The spatial association radii for LKr and MUV3 are slightly different compared to the NewCHOD[66],

- LKr uses a search radius of $(50 + 5)$ mm around track extrapolations to handle residual misalignment.
- MUV3 uses a similar definition to the NewCHOD , where the resolution was determined to be $\sigma_{x,y} = (2120\ \mathrm{GeV}/p)$ mm.

The LKr E/P criteria was inspired by a study performed for the search for the Lepton Number Violating (LNV) decay $K^{\pm} \to \pi^{\mp}\mu^{\pm}\mu^{\pm}$ at NA48/2 [72], where the same LKr detector was in operation. By collecting a pure data sample of $\pi^{\pm}, \mu^{\pm}$ and $e^{\pm}$ in data, the probability to have muons with $E/P < 0.2$ was found to be (99.74 $\pm$ 0.01)%, whilst electrons can be suppressed by $\approx 10^2$ using $E/P < 0.9$.

6.3.3 Base-line spectra

The base-line spectrum is built with dimuon-triggered candidates that survived the full base-line selection. Normalisation candidates are collected from multi-track-trigger events which pass only the vertex and track requirements. The $K_{\pi\mu\mu}$ invariant mass spectra is displayed in Figure 6.6, including the MC overlays of the main contributions for the 2016A data sample. For comparison, the distributions from the NA48/2 paper are displayed in Figure 6.7.

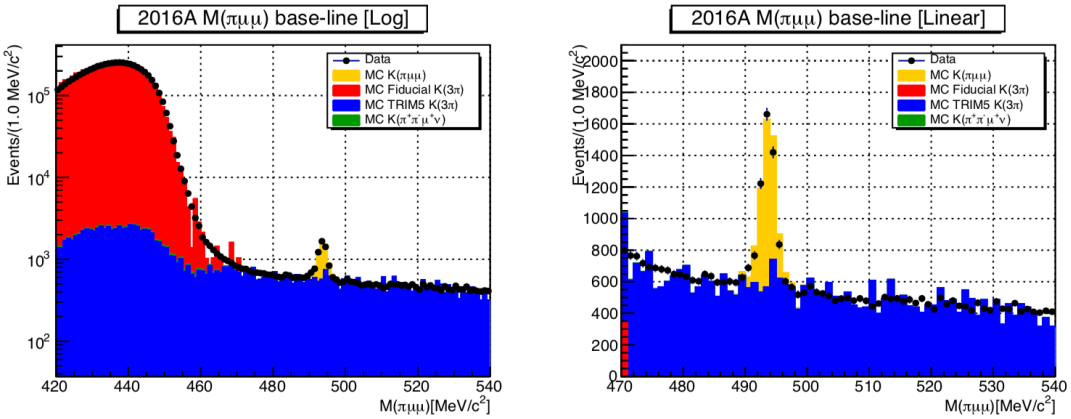

Figure 6.6: The $K_{\pi\mu\mu}$ invariant mass distribution in 2016A for the base-line selection with right: with log-scale and left, linear in the region near M_{K^+}. Orange denotes the $K_{\pi\mu\mu}$ MC expectation.

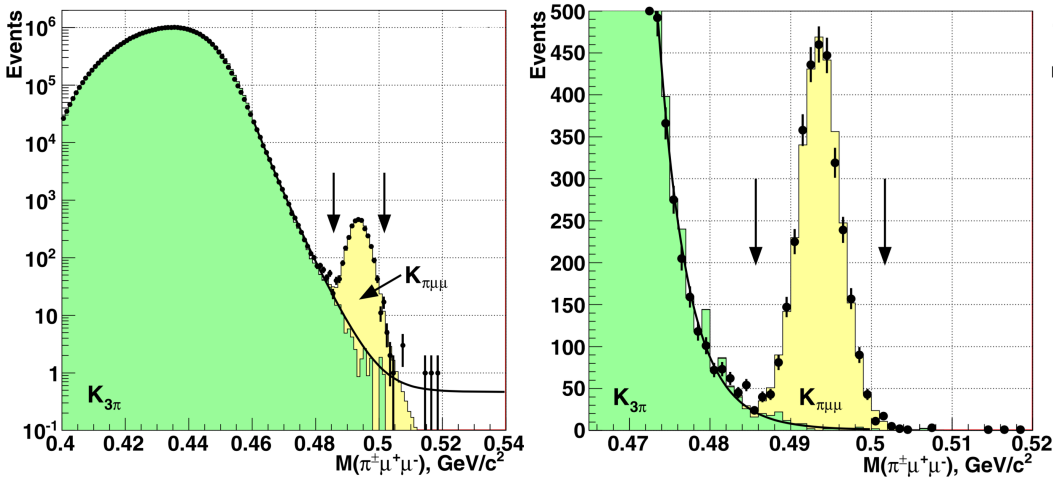

(a) (b)

Figure 6.7: The $K_{\pi\mu\mu}$ invariant mass distribution from the NA48/2 analysis. (a) is in log-scale and (b) in linear. The fiducial $K_{3\pi}$ background tails directly into the SR (denoted by arrows) and the $K_{pi\mu\mu}$ mass resolution σ_M is equal to 2.5 MeV/c^2 [48].

The spectrum contains a number of interesting features, indicating some obvious differences between the two data samples collected at the NA48/2 and NA62 experiments:

- **Separation:** A clear separation for NA62 data between the signal $K_{\pi\mu\mu}$ (orange) and the low-mass backgrounds $K_{3\pi}$ (red) and $K_{\mu 4}$ (green). Both backgrounds enter due to secondary in-flight pion decays to muons, or via accidental in-time MUV3 associations.
- **Resolution:** Improved signal resolution $\sigma_M \approx 1.1$ MeV/c^2, over a factor two smaller than NA48/2.
- **Tail:** Significant exponential tail above 480 MeV/c^2 for NA62 data which was not observed at NA48/2. Hypothesised to be upstream $K_{3\pi}$ decays.

The first two points are the expected as a consequence of a more sophisticated tracking system. The better σ_M resolution allows for a smaller SR definition, which is also not as tight with respect to NA48/2 in terms of the number of standard deviations. The SR for both signal and normalisation is defined as,

$$|M_{\pi\mu\mu,3\pi} - M_{K^+}| \leqslant 5 \text{ MeV/c}^2. \tag{6.1}$$

which is approximately five standard deviations for both cases. Despite the improvements, a large-exponential tail can be seen, a feature not observed by NA48/2. This component is well-described by the $K_{3\pi}^{\text{TRIM5}}$ simulation represented by the blue-distribution, where $K_{3\pi}$ candidates have been forced to decay upstream (Z = 102 m) in the TRIM5 magnet region equivalent to $\approx$ 0.5% of the fiducial decay volume. The acceptance for these decays is ≈ 4 times greater than for the fiducial counterparts, as tracks are less likely to escape down the beam-pipe as they originate upstream. The TRIM5 steering magnet has the additional affect of distorting track momentum, leading to $K_{3\pi}$ candidates with two secondary pion decays appearing in the long tails into and beyond the SR. To achieve the aim of a negligible background component, a selection which fully suppresses the TRIM5 component is required.

6.4 Developing the NA62 selection

In this section, the development of a more stringent $K_{\pi\mu\mu}$ selection is described. A data-driven approach was used to obtain a final selection that removes all background candidates N_B in the high-mass sideband of the $K_{\pi\mu\mu}$ SR, defined as $M_{\pi\mu\mu} > 505$ MeV/c^2.

6.4.1 Tuning vertex and track criteria

The observation that the long exponential background is well described by TRIM5 $K_{3\pi}$ MC provides a hint on how it can be suppressed. Firstly, TRIM5 decays occur 'upstream' of the usual fiducial volume, and secondly the track momenta of the daughters is expected to be distorted as the decay happens during the beam-steering. In data, the invariant mass spectra $M_{\pi\mu\mu}$ can be plotted against vertex/track-related variables as seen in Figure 6.8. The left-hand distribution displays that the

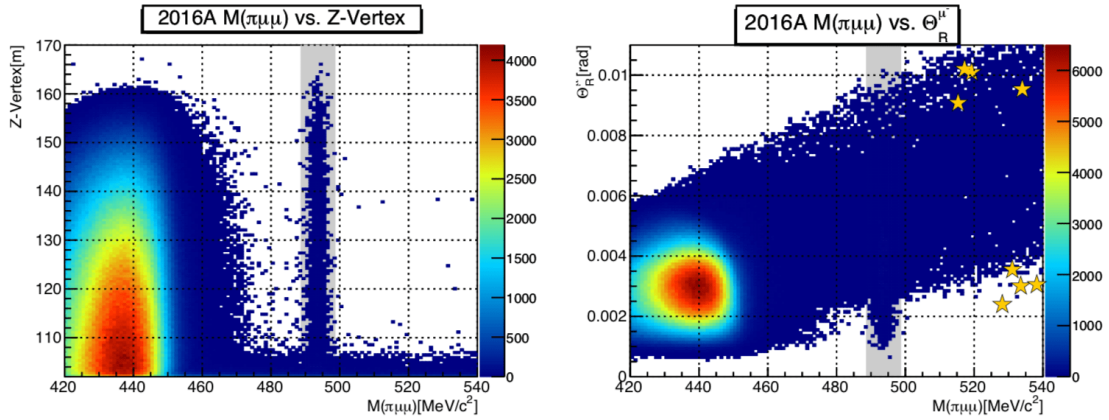

Figure 6.8: The 2016A invariant mass distributions plotted against left, Z-Vertex and right, the μ^- opening angle Θ_R with respect to the lab frame. The SR is in grey and unconstrained in either Y-dimension, and the stars correspond to candidates surviving the selection after a Z-Vertex >110 m cut is applied.

vast majority of sideband events occur at low Z-Vertex, strengthening the TRIM5 hypothesis. Though the TRIM5 magnet is only 40 cm long and centred at 102 m, distortion of all three vertex tracks can modify the determined decay coordinate, boosting the Z-Vertex well into the fiducial volume.

Additionally, the steering distortion can be observed using the lab-frame opening

angles Θ_R of the daughter tracks. The range of opening angles available to each daughter track is fixed kinematically depending on the available phase-space and daughter mass. Pions in $K_{3\pi}$ are limited to smaller opening angles compared to the products in $K_{\pi\mu\mu}$ as a consequence. The right-hand-side of Figure 6.8 displays that low-mass candidates (mostly $K_{3\pi}$ background) are at smaller opening angles, whilst the tail has a distinctive shape. The orange stars correspond to candidates surviving the selection after cutting away events with a Z-Vertex below 110 m, motivating an additional criteria based on Θ_R. Figure 6.9 contains the opening angles for the relevant processes for both positive and negative tracks. The fiducial MC generations

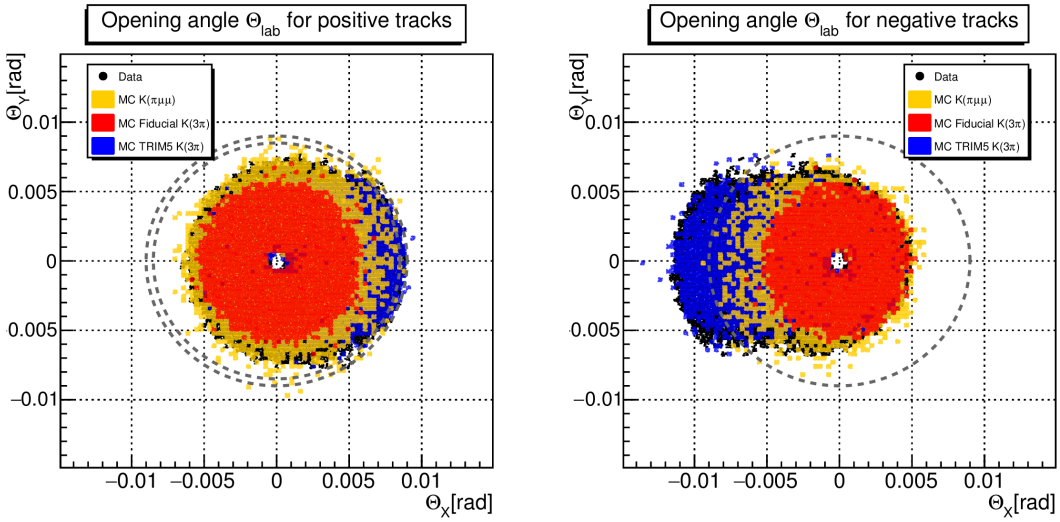

Figure 6.9: Comparison of opening angles for positive and negative tracks for the data set, fiducial MC $K_{3\pi}$, TRIM5 $K_{3\pi}$ and $K_{\pi\mu\mu}$. Each of the MC samples are scaled to match the expected entries. The selection criterion for each track is displays by the dashed circles, with the smaller radii case in the left-hand-side for the π^+ track.

show circular distributions, where $K_{3\pi}$ sits inside of the available opening angles for $K_{\pi\mu\mu}$. The most indicative effect of the TRIM5 distortion is seen in the negative track distribution, where tracks follow an oval shape, spraying into the negative X-dimension beyond the $K_{\pi\mu\mu}$ tails. The large difference with respect to positive tracks is because the steering is tuned for the positively charged kaon, so the positive products are steered similarly, whilst the negative tracks are deflected more dramatically.

The strategy to suppress the majority of the background is straightforward:

- The vertex longitudinal position (Z-Vertex) within (110; 165) m

- The lab-frame opening angle Θ_R for each track in the vertex must be:
  - for μ tracks less than 9.0 mrad.
  - for π tracks less than 8.5 mrad.

Where the choice of opening angle cut is displayed on both sides of Figure 6.9, and applied to all three tracks for symmetry. Figure 6.10 displays the change in the invariant mass spectra after applying the new cuts. The TRIM5 component predicted

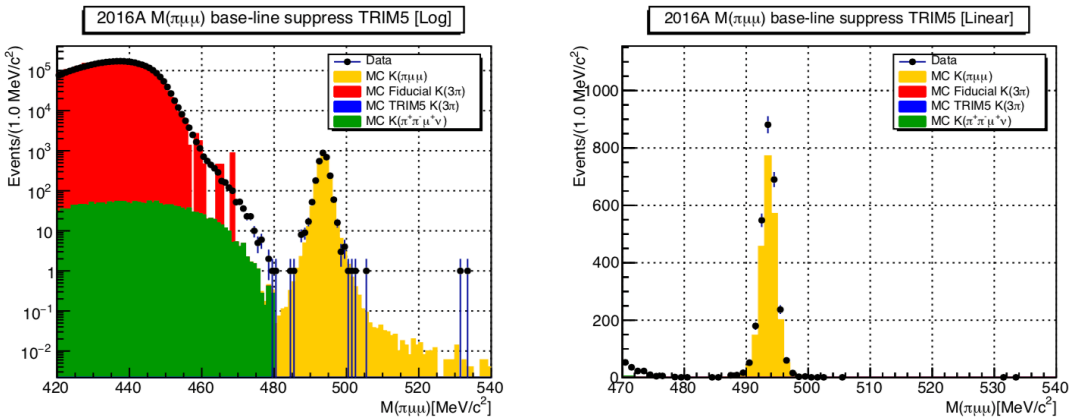

Figure 6.10: Invariant mass distribution in 2016A for base-line selection after including TRIM5 suppression cuts. Left, log-scale and right, high-mass linear. The majority of high-mass sideband candidates have been suppressed.

using $N_{3\pi}$ and the MC generation is now fully suppressed, leaving only two unrelated candidates in the high-mass sideband. The linear scale shows that the prediction of the number of $K_{\pi\mu\mu}$ candidates is $\approx 10\%$ lower than the number observed. There are a number of possible reasons, such as a disagreement between data and MC or that the trigger criteria respond differently depending on the decay entering the plot.

6.4.2 Tuning PID and including precision timing

To achieve a truly negligible background contribution, a more stringent particle identification is required to suppress the various components observed in Figure 6.10. Each possible background is discussed below,

- $K^+ \to \pi^+\pi^+\pi^- \to \pi^+\mu^+\mu^-$: Whilst the mass-separation from $K_{\pi\mu\mu}$ is vastly improved with respect to NA48/2, $K_{3\pi}$ with two secondary pion decays in-flight is an extremely large component. Here, pions are assigned muon masses,

appearing in the $M_{\pi\mu\mu}$ spectrum at low values. Unfortunately, the lack of MC statistics for this process make it difficult to compare with data in the region $470 < M_{\pi\mu\mu} < 485$ MeV/c^2.

- $K^+ \to \pi^+\pi^-\mu^+\nu_\mu \to \pi^+\mu^+\mu^-\nu_\mu$: Whilst occurring at a rate $\approx 10^3$ lower than $K_{3\pi}$, only one secondary pion decay in-flight is required to enter as background. As the decay is four-body and a real muon is present in the intermediate stage, a broader invariant mass spectrum that approaches the $K_{\pi\mu\mu}$ peak is predicted in MC. An additional complication is due to the possible $\pi^+\mu^+$ 'swaps', where the pion is mis-identified as the muon and vice-versa.

- $K^+ \to \mu^+\pi^+\mu^- \to \pi^+\mu^+\mu^-$: The signal process $K_{\pi\mu\mu}$ can appear as a background to itself due to the possible $\pi^+\mu^+$ swaps which also affect $K_{\mu4}$. Assigning the wrong mass hypothesis to the tracks results in the prediction of flat tails around the peak in the MC, contributing at the level of 10^{-2} in the spectrum.

- Accidentals: The high-intensity environment of NA62 leads to a significant number of accidental candidates in the downstream sub-detectors. With more possible associations for vertex tracks, the probability for mis-identification is larger than that predicted in the MC. Therefore, the $\pi^+\mu^+$ swapping mechanism could be far larger in reality.

Therefore, a more stringent set of particle-identification criteria were introduced based upon the identification of the dimuon pair $\mu^+\mu^-$. The requirement of exactly two tracks with at least one spatially associated MUV3 candidate is expanded, including the following conditions:

- The μ tracks are opposite sign ($\mu^+\mu^-$).

- Both μ tracks are associated to at least one outer MUV3 tile.

- Neither μ track can be associated to the same MUV3 candidate, provided that both tracks have only one association.

- Both μ tracks are associated to MUV3 candidates within 5 ns of the vertex time.

The first condition assures that only a SM-allowed sample is collected. This requirement also suppresses the contribution of secondary decays in-flight of $K^+ \to$

$\pi^+\pi^+\pi^- \rightarrow \mu^+\mu^+\pi^-$, which will enter directly into the spectrum provided there is no requirement on the muon charge configuration. Additionally, accidentals for this process are easy to obtain due to the beam-halo and the dominant $K_{\mu 2}$ rate. The requirement for outer MUV3 associations is to align with the trigger logic MO_2, which requires two outer MUV3 pads to be fired within 10 ns. As a consequence, both criteria ensure a larger separation of the muon pair at the MUV3 face. The final criteria are motivated by Figure 6.11. The $\pi^+\mu^+$ swaps can occur where the real μ^+

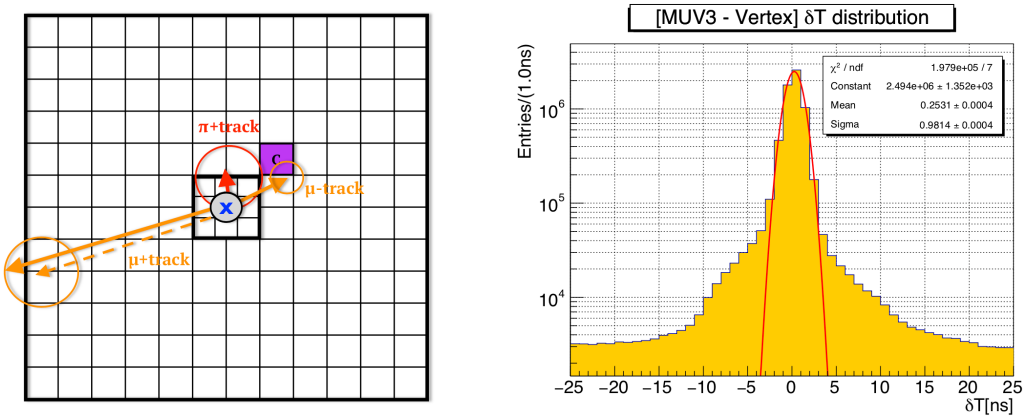

(a) (b)

Figure 6.11: Supporting diagrams for the MUV3 related logic. a) A schematic of a $K_{\pi\mu\mu}$ decay originating upstream from the beam 'X', where the real μ^+ misses the detector and the π^+ is accidentally associated to the same candidate as the μ^- . b) the timing resolution between vertex tracks and MUV3 candidates for a $K_{\pi\mu\mu}$-like selection.

track misses the detector and the π^+ is associated spatially to the same candidate as the μ^- track. The example shows that even a single candidate can appear as $K_{\pi\mu\mu}$. Accidental rate also contributes to mis-identification. By applying a precise timing constraint, most of the accidental associations can be suppressed. The right-hand plot shows the timing residual between the vertex times and associated MUV3 candidates, which has a 1 ns resolution.

The final advantage unique to NA62 is the KTAG detector. The KTAG time-stamps K^+ candidates with a resolution to better than a few hundred ps. As both $K_{\pi\mu\mu}$ and $K_{3\pi}$ originate from kaon decays, checking if the three-track vertex has a KTAG candidate consistent in time is definitive advantage over the previous analyses. We can introduce a requirement to find at least one good KTAG candidate consistent

with the signal decay, defined as,

- At least four KTAG sectors fired,
- Candidate time within 10 ns of the trigger time,
- Candidate time within 10 ns of the vertex time.

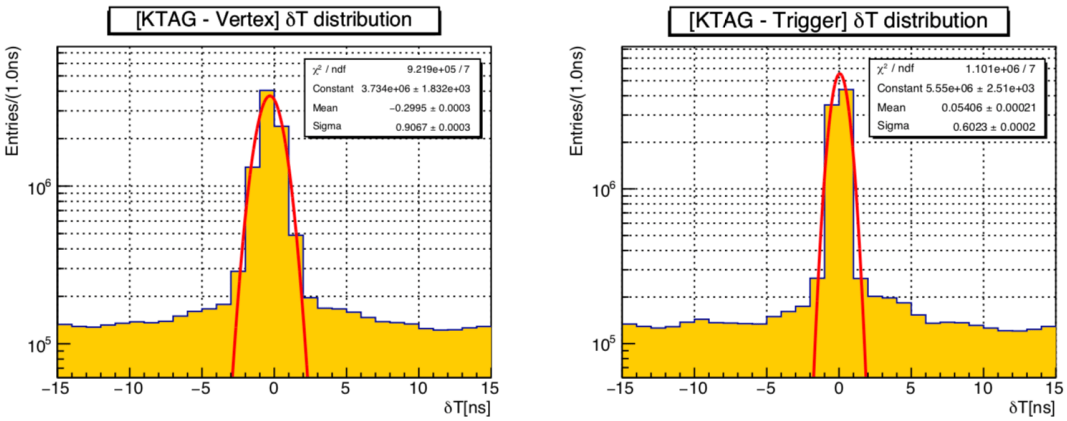

Figure 6.12: The timing residuals of left, KTAG candidates to three-track vertex times, and right, to the Dimuon trigger time. The resolution of both distributions is below 1 ns.

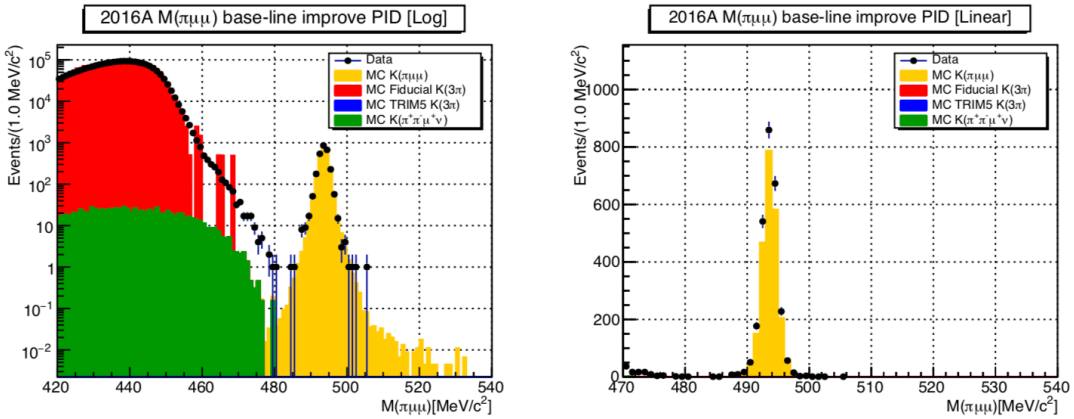

Figure 6.13: Invariant mass distribution in 2016A for base-line selection after TRIM5 suppression and the improved PID criteria. Left, log-scale and right, high-mass linear. All sideband candidates have been suppressed, with an improved separation between low-mass and the signal peak.

The choice of criteria is inspired by the L_1 trigger algorithm which is present both dimuon and multi-track trigger streams. The 10 ns time window is relatively broad with respect to the 1 ns resolution observed in the residuals, as displayed in Figure 6.12. By requesting a good KTAG candidate time-consistent with the vertex, accidental contributions at the MUV3 stage are also improved as three detectors are

required to be in timing coincidence. The invariant mass spectrum after including the new PID criteria is contained in Figure 6.13, where all high-mass candidates have been successfully removed and the signal and background separation is optimal.

6.5 The final selection

The selection was finalised by maximising the number of observed $K_{\pi\mu\mu}$ candidates N_S whilst fully suppressing the sideband components N_B. A simplistic iteration procedure was used,

1. Remove each cut independently, and build a selection of the criteria which increase N_B when removed.
2. Continue to reintroduce cuts until $N_B = 0$, starting with the conditions which decrease N_S the least.

Resulting in the removal of a small number of cuts, specifically the E/P requirement for muons and the separation of the tracks at the LKr. The procedure was also used to rule out the implementation of the other photon-vetoes in the analysis, based on the large amount of signal that would be lost due to accidental activity.

The final selection is used to collect both normalisation $K_{3\pi}$ and signal $K_{\pi\mu\mu}$, by requiring vertex quality requirements and kaon identification for both signal and normalisation, then $\mu^{\pm}$ identification for $K_{\pi\mu\mu}$ signal alone. The use of extremely similar selections is to assure a high-level of symmetry between the two samples in order to cancel the selection-related systematic effects to first order. In addition to the criteria discussed previously, a track-momentum cut was included because the track-reconstruction efficiency could only be probed in the region between $8 < P < 48$ GeV/c.

6.5.1 Track and vertex requirements

Exactly one good three-track vertex built in the event, defined as:

- The vertex charge is Q = +1.

- The vertex χ^2 fit is less than 20.
- The vertex longitudinal position (Z-Vertex) within (110; 165) m
- The vertex total momentum (P-Vertex) within (73; 77) GeV/c
- The vertex transverse momentum $P_T <$ 30 MeV/c
- The vertex-beam CDA < 50 mm.

For each track in the three-track vertex:

- Within the geometric acceptance of the four STRAW chambers, NewCHOD, LKr and MUV3.
- At least two or greater tracks with a geometrically associated NewCHOD candidate. Up to three candidates are used to build an average vertex time. The candidate times must be self-consistent to within 10 ns, and also within 10 ns of the trigger time.
- Within (8; 48) GeV/c, for higher trigger and reconstruction efficiency, discussed in Chapter 7 and Section 8.2.2.

6.5.2 Kaon identification

At least one good KTAG candidate, defined as

- At least four KTAG sectors fired,
- Candidate time within 10 ns of the trigger time,
- Candidate time within 10 ns of the vertex time.

6.5.3 Decay identification

For events collected with the dimuon trigger only, $(\mu^+\mu^-)$ identification is applied, defined as:

- Exactly two tracks in the vertex with at least one geometrically associated MUV3 candidate.
- Require μ tracks to be opposite sign.

- Require lab-frame opening angle Θ_R for μ tracks to be less than 9.0 mrad.
- Require μ tracks to be associated to at least one outer MUV3 pad.
- Require associated MUV3 candidate time to be within 5 ns of vertex.
- Require for no repeated MUV3 pad associations for μ track pairs that have only one association each.

Pion (π^+) identification, defined as:

- Exactly one track with no MUV3 candidate.
- Require lab-frame opening angle Θ_R for π track to be less than 8.5 mrad.

Electron ($e^\pm$) rejection, defined as:

- $E/P < 0.9$.

All Dimuon triggered events surviving the selection are saved, as the candidates outside the signal region are used to estimate the background level in the signal region.

Independently, the following is applied for the Multi-track triggered events,

- At least one π^+ track with no spatially associated MUV3 candidates.

The cut above is to symmetrise with the π^+ identification in the $K_{\pi\mu\mu}$ selection and drastically reduce any effects of accidental MUV3 association on the acceptance calculation.

6.5.4 The final spectra

The final $K_{3\pi}$ normalisation spectrum is contained in Figure 6.14, The sample is very clean, with a background contamination of $(0.0010 \pm 0.0001_{\text{stat}} \pm 0.0007_{\text{syst}})$%, where the error is dominated by the systematic uncertainty on $\mathcal{B}(K_{\mu 4})$. The final $K_{\pi\mu\mu}$ spectrum is contained in Figure 6.15. where the contribution from high-mass candidates has been suppressed and the separation between the low-mass tail and the $K_{\pi\mu\mu}$ is notable to below 10^{-1}. Unlike $K_{3\pi}$, the number of background candidates has been estimated using RooFit to be below one, as explained in more detail of Section 8.2.1

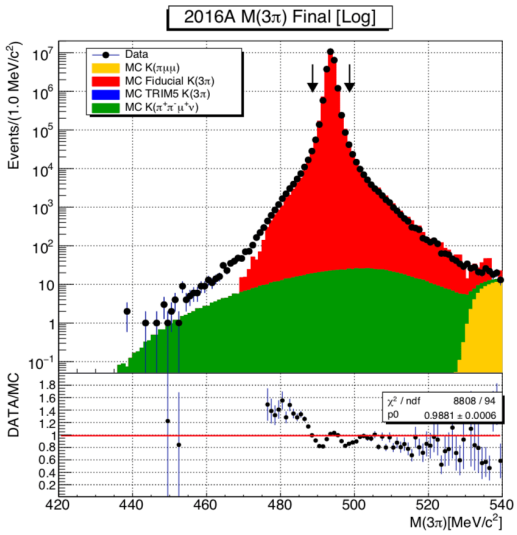

Figure 6.14: The final normalisation $K_{3\pi}$ spectrum for 2016A. The signal region is denoted by arrows, using a ± 5 MeV window around the nominal kaon mass, and the bottom distribution is the data sample divided by the MC sample to show agreement.

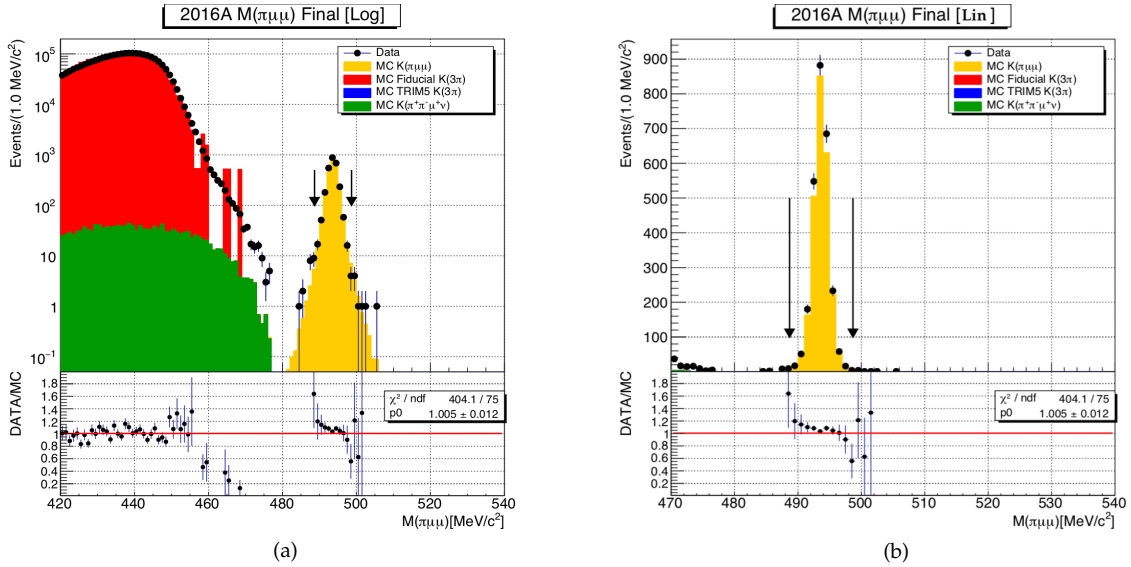

(a) (b)

Figure 6.15: The $K_{\pi\mu\mu}$ spectra for 2016A in (a) log-scale and (b) linear. The signal regions are denoted by arrows, using a ± 5 MeV window around the nominal kaon mass, and the bottom distributions is the data sample divided by the MC sample to show agreement.

in analysis Chapter 8. The data-MC discrepancy is reduced by a few percent in the final selection, and is explored further in the $d\Gamma/dz$ reconstruction procedure.

Finally, a data-MC comparison procedure was performed for both the $K_{3\pi}$ and $K_{\pi\mu\mu}$ samples. Multiple distributions can be found in Appendix A for the most important cuts implemented in the analysis. The only large shape-discrepancy is for the description of the vertex momentum, but as the disagreement is present for both normalisation and signal, the effect is expected to cancel out to first order with the normalisation procedure.

7

Measuring trigger efficiency

In this chapter, the trigger efficiencies for the $K_{3\pi}$ normalisation and $K_{\pi\mu\mu}$ signal samples are measured. The samples were collected using the following trigger streams:

- $\boldsymbol{K_{3\pi}}$: RICH·Q_X →KTAG→!LAV→STRAW$_e$ (Multi-track trigger)
- $\boldsymbol{K_{\pi\mu\mu}}$: RICH·$Q_X$·$MO_2$ →KTAG→!LAV→STRAW$_e$ (Dimuon trigger)

The similarity of the streams is deliberate, so that any systematic effects of the data acquisition process will cancel via a normalisation procedure. For the data recorded in 2016, a series of flaws were discovered with several aspects of the TDAQ, imposing the need for an extreme level of care when determining the efficiencies. As the flaws relate to both signal kinematics and beam intensity, a complete cancellation of the systematic components is highly implausible. Additionally, the abundance of $K_{3\pi}$ decays means that each normalisation efficiency component can be easily measured using minimum-bias streams, but as the ratio $\mathcal{B}(K_{\pi\mu\mu})/\mathcal{B}(K_{3\pi}) \approx 10^{-6}$, alternative approaches must be developed to obtain high-precision efficiency measurements for $K_{\pi\mu\mu}$. The final and most important requirement for the $K_{\pi\mu\mu}$ efficiency measurement is that it must be performed in bins of $z_{\mu\mu} = (M_{\mu\mu}/M_{K^+})^2$; the extraction of both the branching fraction and form factor LECs relies on an accurate reconstruction of the underlying $d\Gamma/dz$ versus $z_{\mu\mu}$ spectrum. The strategy to perform these measurements is explained in Section 7.1, with the computation for each common trigger component provided in order of difficulty between Section 7.2 - 7.6,

and followed by the MO_2 calculation unique to the Dimuon trigger in Section 7.7. The final trigger efficiencies are provided in Section 7.8.

7.1 Strategy

For the complicated TDAQ implemented at NA62, it is important to measure the trigger efficiencies with respect to multiple quantities, in order to determine whether the data acquisition biases the collected data in any particular fashion. For example,

- The stability of the trigger-efficiency with respect to time.
- Kinematic dependence, observed with respect to track momentum P, the ratio of the variable $z_{\pi^+\pi^-} = (M_{\pi^+\pi^-}/M_{K^+})^2$ for $K_{3\pi}$ or the equivalent $z_{\mu\mu} = (M_{\mu\mu}/M_{K^+})^2$ for $K_{\pi\mu\mu}$.
- The affect of variable beam-intensity on performance.

The number of observed candidates in any given physics analysis must be corrected for the trigger efficiency to infer the true number of candidates that were present in the detector. If the trigger is kinematically dependent, the $z_{\mu\mu}$ spectrum of the collected $K_{\pi\mu\mu}$ sample could be distorted compared the true distribution. Variable beam intensity is also expected to affect the trigger performance as increased rate leads to more accidental candidates alongside the signal. To account for any of these effects accordingly, the following strategy was adopted to determine the normalisation efficiencies $\epsilon_{3\pi}$, and from that obtain the required signal efficiency spectrum $\epsilon_{\pi\mu\mu}(z_{\mu\mu})$.

- Determine the normalisation efficiencies $\epsilon_{3\pi}$ for each primitive/algorithm using a sample of $K_{3\pi}$ from either,
  - L_0: Minimum-bias control trigger.
  - L_1: Autopassed from Multi-track trigger (2% of L_1 yield)

  The dependence of the efficiency is measured with respect to time, a relevant kinematic variable (P, $z_{\pi^+\pi^-}$) and the instantaneous beam intensity.

- For components which display no clear discrepancies with expectation, the normalisation efficiency $\epsilon_{3\pi}$ can be converted to a binned-distribution of $\epsilon_{\pi\mu\mu}(z_{\mu\mu})$ using the following formula,

$$\epsilon^{\mathrm{DATA}}_{\pi\mu\mu}(z_{\mu\mu}) = \epsilon^{\mathrm{DATA}}_{3\pi}\left(\frac{\epsilon^{\mathrm{MC}}_{\pi\mu\mu}(z_{\mu\mu})}{\epsilon^{\mathrm{MC}}_{3\pi}}\right), \tag{7.1}$$

  where the MC values are extracted from a "simple" emulation of the trigger-component response in simulation for $K_{3\pi}$ and $K_{\pi\mu\mu}$.

- For components with known flaws, a series of trigger emulators were developed which replicate the L_0 firmware or L_1 algorithm. The $\epsilon_{\pi\mu\mu}(z_{\mu\mu})$ is then obtained by measuring the efficiency directly using MC samples, after injecting accidentals into the simulation as extracted from data. This MC + Accidentals (MCA) method is verified after tuning the procedure using the result for $K_{3\pi}$ compared to the online primitive or algorithm.

The selection used to collect the $K_{3\pi}$ and $K_{\pi\mu\mu}$ samples is extracted from the final version described in Chapter 6. The idea is to use the accurately measured normalisation efficiencies from the data and convert them using the response in MC. After the full 2016 data set was collect, both the Q_X and !LAV components of the trigger were discovered to be flawed. This is the motivation for the final bullet point above; the flaws were found to be both kinematically and intensity-dependent. Therefore, the MCA approach was implemented to tackle these measurements, especially as neither issue is truly factorisable. The MO_2 criteria is unique to the Dimuon trigger and the strategy is slightly different. The $z_{\mu\mu}$ dependence is extracted directly from data using a sample of the low mass background $K^+ \to \pi^+\pi^+\pi^- \to \pi^+\mu^+\mu^-$, where two of the pions decayed in-flight.

7.2 KTAG

The L_1 KTAG algorithm is designed to positively identify a beam-kaon candidate consistent with the L_0 event time. The algorithm is considered the simplest to handle because the efficiency depends purely on the presence of the kaon and not the

decay products downstream. Therefore, the efficiency is considered to be identical for normalisation $K_{3\pi}$ and signal $K_{\pi\mu\mu}$ and will completely cancel in the ratio when normalising. Regardless, the efficiency is expected to be high for kaon decays, and the time-stability and beam-intensity dependence of the KTAG algorithm is displayed in Figure 7.1, measured directly using the Multi-track autopassed $K_{3\pi}$.

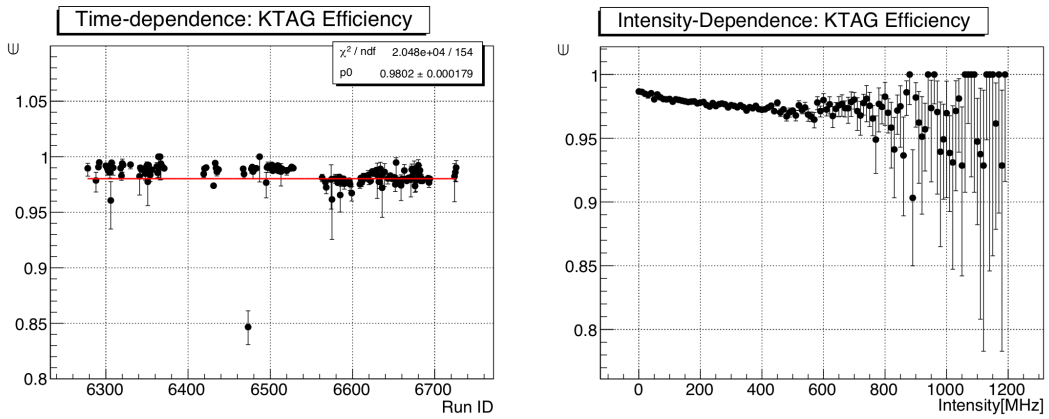

(a) (b)

Figure 7.1: The KTAG algorithm efficiency (a) with respect to time and (b) versus beam-intensity. The red-line in (a) is the average efficiency across the period, stable except for one low-statistics run with ID = 6470.

As the KTAG algorithm is close to identical to the criteria implemented in the particle-identification of the selection, "simple" emulation yields an expected MC efficiency of $1.0000 \pm 0.0000_{\text{stat}}$ for both samples. The equivalent measurement in data is,

$$\epsilon_{3\pi}^{\text{KTAG}} = \epsilon_{\pi\mu\mu}^{\text{KTAG}} = 0.9802 \pm 0.0002_{\text{stat}}, \tag{7.2}$$

where the value is the overall average extracted from (a) of Figure 7.1 and $\epsilon_{\pi\mu\mu}^{\text{KTAG}}$ is assumed to be flat with respect to $z_{\mu\mu}$. The statistical error corresponds to the full 2016A data sample and is therefore small. The left-hand side of Figure 7.1 displays some variation in the efficiency with respect to Run ID. This is a consequence of the beam intensity which was constantly changing during the data acquisition process. Overall, the KTAG algorithm depends fairly loosely on the beam-intensity (as seen in the right-hand side of Figure 7.1) decreasing by $\approx 1\%$ across the full spectrum. The average overall efficiency is a reflection of this relationship.

7.3 RICH

The L_0 RICH primitive is implemented to collect events with signals in at least two RICH PMT supercells. As $K_{3\pi}$ and $K_{\pi\mu\mu}$ contain three charged tracks, the high beam momentum guarantees that at least one track is above the Cherenkov threshold required to generate hits in the RICH. Figure 7.2 contains the RICH efficiency with respect to time and track momentum P for $K_{3\pi}$ minimum bias candidates. The efficiency is stable in-time aside from $\approx$ 10 low efficiency runs which have limited statistics. The distribution also displays little-to-no momentum dependence as is expected for a three-track process. The RICH normalisation efficiency provided by the flat-line in (a) is measured to be,

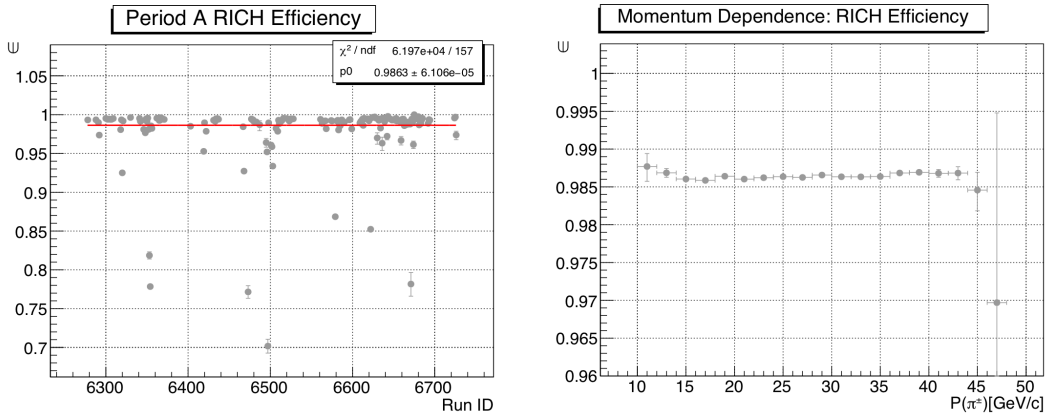

(a) (b)

Figure 7.2: The RICH primitive efficiency (a) with respect to time and (b) versus π momentum. The red-line in (a) is the average efficiency across the period and is in general stable, except for $\approx$ 10 lower efficiency runs. The momentum dependence is generally weak across the available phase-space.

$$\epsilon_{3\pi}^{\mathrm{RICH}} = 0.9863 \pm 0.0001_{\mathrm{stat}}, \tag{7.3}$$

where the small statistical error reflects the size of the 2016A data set. As explained in the strategy, to determine the $\epsilon_{\pi\mu\mu}^{\mathrm{RICH}}$ efficiency, $\epsilon_{3\pi}^{\mathrm{RICH}}$ is converted using the MC ratio method provided by Equation 7.1. To determine the MC components for both $K_{3\pi}$ and $K_{\pi\mu\mu}$ required by the ratio, the L_0 RICH emulator was used which replicates the online primitive generation at the analysis level offline [66]. The emulator is fully flexible and can be used for both data and MC, with the former useful to

test the emulator performance. Figure 7.3 compares the online-primitive intensity-dependence with the emulated efficiency for $K_{3\pi}$ minimum-bias data. The RICH

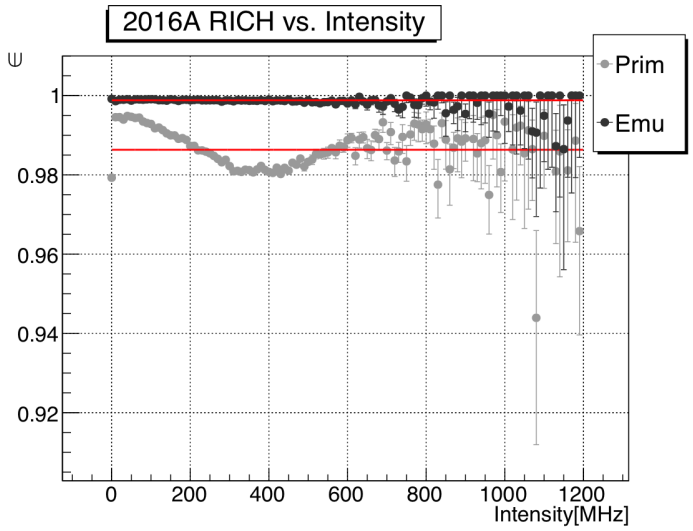

Figure 7.3: Comparing online and emulated RICH primitive efficiency in 2016A for $K_{3\pi}$. The online distribution displays a distinct shape-deviation near 300 MHz not reproduced by the emulator. The red-line is the overall average for the primitive efficiency.

emulator measures the efficiency a few percent higher than the online primitive, without the distinct shape distortion in the region of intensity $\mathcal{I}$ = 300 MHz. The small number of low-efficiency runs that were observed in (a) of Figure 7.2 are expected to contribute to this shape. Though an obvious discrepancy with the emulator, the same behaviour is expected for the $K_{\pi\mu\mu}$ efficiency and is therefore contained in the value of $\epsilon_{3\pi}^{\mathrm{RICH}}$ when converting. The final $\epsilon_{\pi\mu\mu}^{\mathrm{RICH}}(z_{\mu\mu})$ is the result of the procedure, presented in Figure 7.4. The response of the emulator returns as almost 100% efficient for both MC samples and the measurement is dominated by the actual $K_{3\pi}$ efficiency. The average $K_{\pi\mu\mu}$ RICH efficiency is determined to be,

$$\epsilon_{\pi\mu\mu}^{\mathrm{RICH}} = 0.9864 \pm 0.0000_{\mathrm{stat}} \pm 0.0060_{\mathrm{syst}}. \tag{7.4}$$

The accuracy of this approach relies on the performance of the emulator with respect to the instantaneous beam-intensity compared with the primitive dependence. The statistical term reflects the size of the MC sample used, whereas the systematic error corresponds to the difference between the mean efficiency denoted by the red line in Figure 7.3 and the efficiency of the primitives at the average intensity at $\mathcal{I} \approx 300$

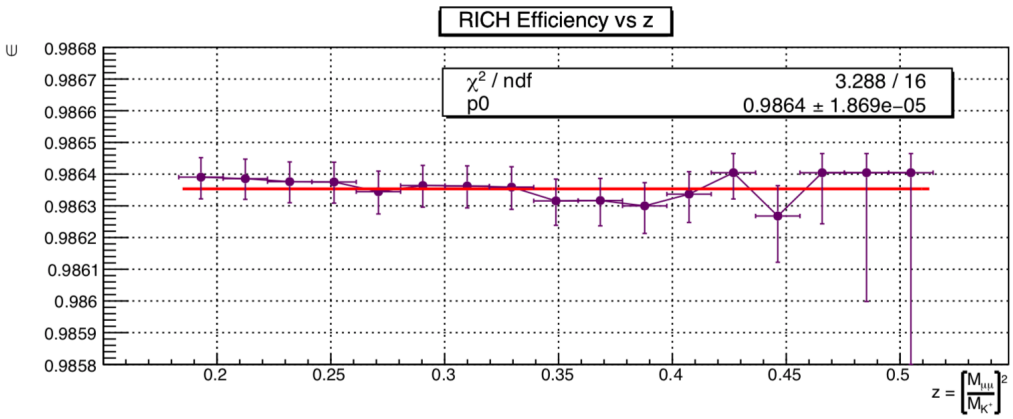

Figure 7.4: The RICH Efficiency vs z in 2016A. The essentially-flat shape is because the emulator returns efficiency 1.0 for almost all bins in both MC samples, where the actual scale is set by the value of $\epsilon_{3\pi}^{\mathrm{DATA}}$. The red-line denotes the average efficiency.

MHz, equivalent to $\approx 0.6\%$.

7.4 STRAW$_e$

The L$_1$ STRAW$_e$ algorithm uses a fast-reconstruction to search for events containing negative tracks. The algorithm is implemented in both streams as $K_{3\pi}$ and $K_{\pi\mu\mu}$ contain either a π^- or μ^-. Figure 7.5 contains the time and intensity dependence of the algorithm. The efficiency is stable with time, with a slow intensity fall-off

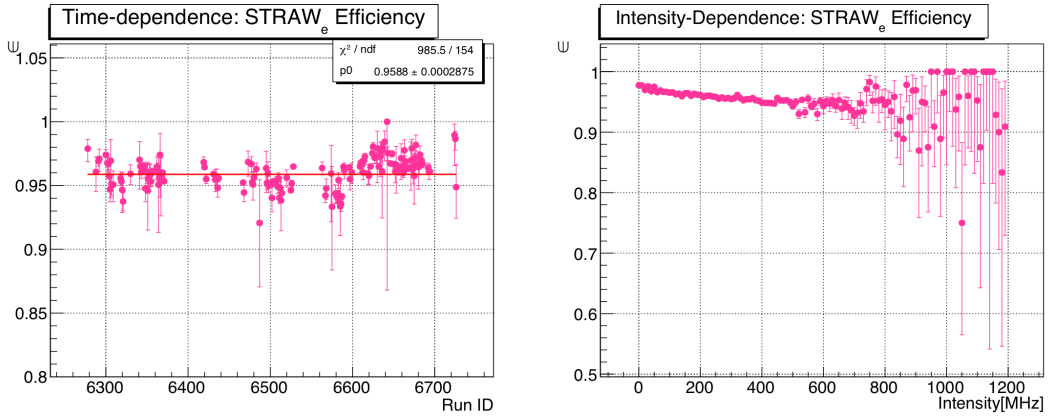

(a) (b)

Figure 7.5: The STRAW$_e$ algorithm efficiency (a) with respect to time and (b) versus intensity. The red-line in (a) is the average efficiency across the period and is in general stable. The algorithm also displays a gentle intensity dependence, decreasing by 1% across the spectrum.

across the spectrum. The normalisation efficiency provided by the flat line in (a) is

measured to be,

$$\epsilon_{3\pi}^{\mathrm{STRAW_e}} = 0.9588 \pm 0.0003_{\mathrm{stat}}. \tag{7.5}$$

To determine the $\epsilon_{\pi\mu\mu}^{\mathrm{STRAW_e}}$ efficiency, the $\epsilon_{3\pi}^{\mathrm{STRAW_e}}$ is converted using the MC ratio approach used by the RICH. However, the STRAW$_e$ algorithm has no suitable emulation method to apply in the simulation as the algorithm uses digitised hits before the reconstruction level. Naturally, all events collected by the selection contain a negative track and so the ratio can only be unity for MC. Instead, Figure 7.6 contains the π^- momentum dependence of the algorithm for autopass $K_{3\pi}$ candidates. Fitting the distribution with a first-order polynomial, the momentum-dependence

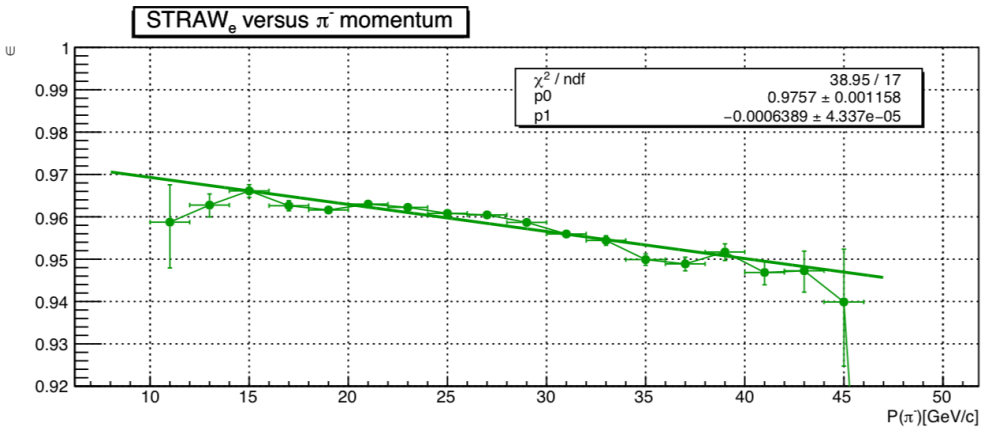

Figure 7.6: The STRAW$_e$ momentum dependence in 2016A, measured using autopass $K_{3\pi}$ candidates. The fit corresponds is a first-order polynomial, which decreases with π^- momentum.

function is determined to be,

$$\epsilon_{3\pi}^{\mathrm{STRAW_e}}(P_{\pi^-}) = \epsilon_0 + \epsilon_1 P_{\pi^-} = 0.9757 - 0.0006 P_{\pi^-}, \tag{7.6}$$

which is the simplest polynomial that can adequately model the dependence. As both the signal $K_{\pi\mu\mu}$ and normalisation $K_{3\pi}$ have intrinsically different track-momentum spectra, the efficiency $\epsilon_{\pi\mu\mu}^{\mathrm{STRAW_e}}$ cannot be taken to be equivalent to the $K_{3\pi}$ case. We assume that the functional form of Equation 7.6 is the algorithm's universal negative track momentum dependence, as previous studies suggest that the reconstruction efficiency for pions and muons is equivalent [83]. The overall efficiency in data $\epsilon_{3\pi}^{\mathrm{STRAW_e}}$ is then converted to a $\epsilon_{\pi\mu\mu}^{\mathrm{STRAW_e}}(z_{\mu\mu})$ distribution using the usual conver-

sion method of Equation 7.1. The MC ratio is instead determined by evaluating the momentum-dependence of Equation 7.6 for MC events, based on the negative track momentum for each event. Figure 7.7 contains the final STRAW$_e$ $z_{\mu\mu}$-distribution for $K_{\pi\mu\mu}$. The slope falls almost linearly, with the red line providing the average

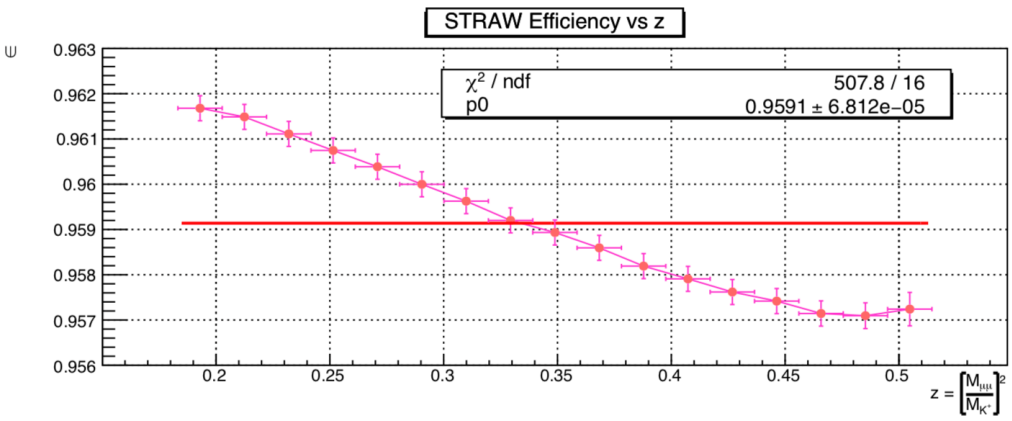

Figure 7.7: The STRAW$_e$ Efficiency vs z in 2016A. The slope falls linearly across the phase-space, decreasing by $\approx 0.5\%$ from start to finish. The red-line is to denote the overall average of the efficiency.

efficiency across the full phase-space,

$$\epsilon_{\pi\mu\mu}^{\mathrm{STRAW_e}} = 0.9591 \pm 0.0001_{\mathrm{stat}} \pm 0.0050_{\mathrm{syst}}, \tag{7.7}$$

but with only a small decrease from start to finish of $\approx 0.5\%$. The precision of the approach relies on the accuracy of the momentum-efficiency model. The χ^2/NDF fit to determine Equation 7.6 is ≈ 2.5, meaning that the model could be optimised. Without a proper physics motivation to do so, we take a systematic error based on the maximum significant deviation from the line of 0.5% at $P(\pi^-)$ = 35 GeV/c. In addition, other contributions to the systematic term are considered, such as:

- **Fit error:** The effect of evaluating Equation 7.6 with a Gaussian smear on the fit parameters ϵ_0 and ϵ_1 based on their precision is included in the estimate.
- **Fit extrapolation:** Additionally, the momentum-spectra for $K_{3\pi}$ is not as broad as $K_{\pi\mu\mu}$, and so the efficiency for candidates with momentum outside of ($10 \leqslant P^- \leqslant 46$) GeV/c is inferred from extrapolation. As the form is unknown outside of this region, the effect of using a flat extrapolation is considered instead, with the variation taken as a systematic.

However, both errors are negligible with respect to the model-dependent systematic.

7.5 Q_X (NewCHOD)

The Q_X condition is one of two components of the trigger which were found to be flawed. At L_0, Q_X is designed to collect events with hits in at least two diagonally opposed NewCHOD quadrants. The primitive is implemented in both trigger streams as $K_{3\pi}$ and $K_{\pi\mu\mu}$ both contain three-charged tracks. By requesting NewCHOD quadrants to satisfy Q_X for MC events yields an efficiency $\epsilon_{\mathrm{MC}}^{\mathrm{Q_X}} \approx 0.9990$ for both samples, despite the fact that the illumination of the detector is different as displayed in the channel map of Figure 7.8. The presence of two lighter final-state

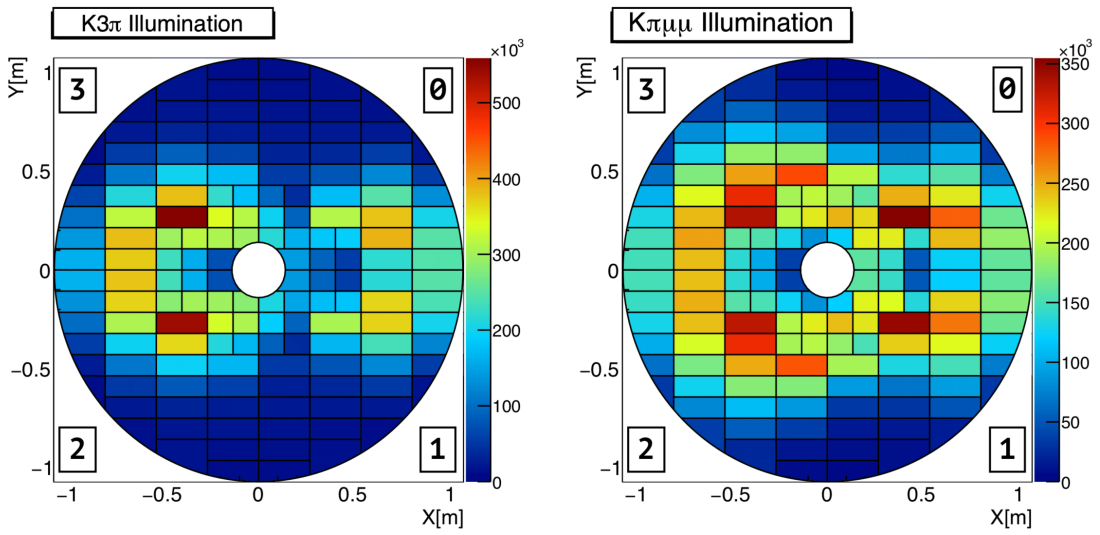

Figure 7.8: The normalised NewCHOD Illumination for $K_{3\pi}$ and $K_{\pi\mu\mu}$ MC. The difference is purely kinematic as the opening angles for $K_{3\pi}$ is limited with respect to $K_{\pi\mu\mu}$ due to the difference in phase-space. The numbered corners refer to the quadrant number in the readout.

muons can result in larger opening angles of the daughters in the lab-frame, leading to a wider spread of hits at the NewCHOD. Figure 7.9 contains the probability of firing each NewCHOD quadrant for both $K_{3\pi}$ and $K_{\pi\mu\mu}$ MC, different on account of the contrasting illumination. In general, $K_{\pi\mu\mu}$ is more likely to fire quadrants on the right-side of the detector, while $K_{3\pi}$ the left. The Q_X condition can be split into three exclusive parts, such that $Q_X = (Q_{02}^{EX} \vee Q_{13}^{EX}) \vee Q_4$. Table 7.1 displays the "simple" emulated MC efficiencies for each component. In general, the larger opening angles

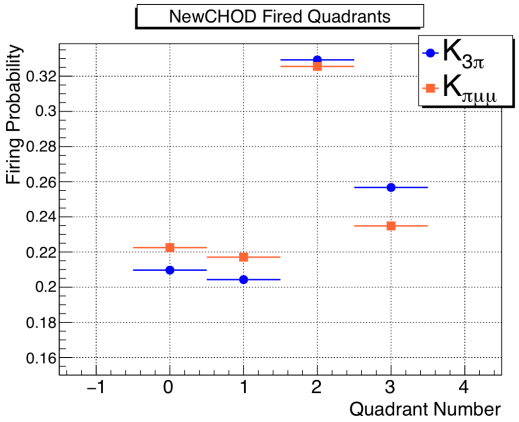

	$\epsilon(K_{3\pi})$	$\epsilon(K_{\pi\mu\mu})$
Q_X	0.9989 ± 0.0001	0.9983 ± 0.0001
Q_{02}^{EX}	0.4596 ± 0.0015	0.4798 ± 0.0014
Q_{13}^{EX}	0.4519 ± 0.0015	0.4751 ± 0.0014
Q_4	0.0879 ± 0.009	0.0435 ± 0.0006

Figure 7.9 & Table 7.1: The firing probability of NewCHOD quadrants for $K_{3\pi}$ and $K_{\pi\mu\mu}$ MC, accompanied by the exclusive component efficiencies of Q_X in tabular form. The difference in illumination of the samples lead to contrasting quadrant probabilities. The result is a set of trigger-components that are distinct, but which sum to similar Q_X efficiencies overall. The errors are statistical only.

of $K_{\pi\mu\mu}$ leads to ≈4% higher likelihood for the exclusively diagonal components of Q_X to fire, whereas $K_{3\pi}$ is twice as likely to fire all four quadrants Q_4 compared with $K_{\pi\mu\mu}$. Despite this kinematic dependence, the components sum to the same Q_X efficiencies overall.

Figure 7.10 contains the time and intensity dependence of the primitive measured with minimum bias $K_{3\pi}$ decays. Relatively stable with time, the normalisation effi-

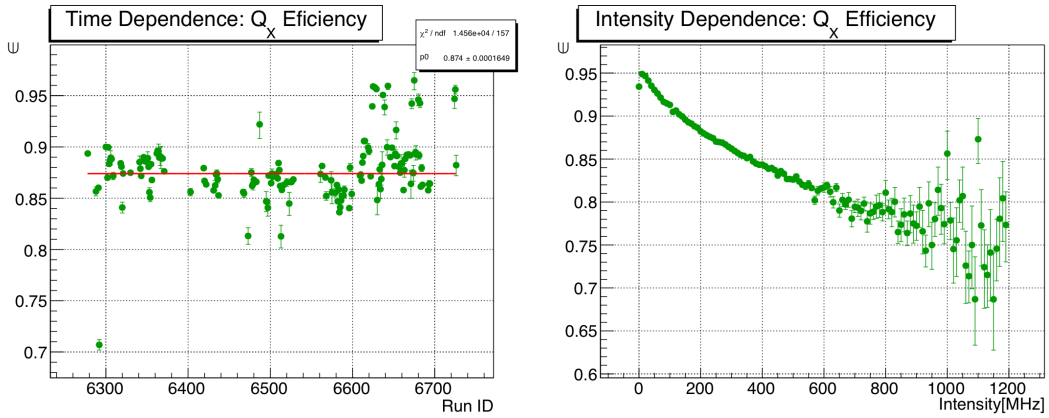

(a) (b)

Figure 7.10: The Q_X primitive efficiency (a) with respect to time and (b) versus intensity. The red-line in (a) is the average efficiency across the period. The primitive displays a large intensity dependence, decreasing by $\approx 20\%$ across the spectrum. Some runs with ID > 6600 display a higher-efficiency than average, all of which correspond to a lower beam-intensity.

ciency provided by the flat-line in (a) is measured to be,

$$\epsilon_{3\pi}^{\mathrm{Qx}} = 0.8740 \pm 0.0002_{\mathrm{stat}}, \tag{7.8}$$

which is low in comparison to expectation, indicating the presence of a flaw. The primitive is also highly dependent on the beam-intensity, decreasing by $\approx 20\%$ across the available range. A clear indication of the effect can be seen as some runs with ID > 6600 are known to be at low-intensity. All examples of this have an efficiency substantially better than the average at $\approx 95\%$.

7.5.1 Flaw in the NewCHOD firmware

After discussion with TDAQ experts, the flaw was discovered with the NewCHOD primitive-generating firmware. The flaw occurs at the time-cluster merging stage, and can be understood using the flow-diagram presented in Figure 7.11. The flow is,

- Hits from the readout are sent to an array of buffers in the sorting modules. Each buffer, or 'split', contains hits related to a 100 ns time interval, with the earliest hits in the first split and the latest in the final. The hits in each split are all within 100 ns of each other, but are random and remain unsorted with respect to time.
- Each split is read from first-to-last to begin the clustering process. The very first hit is converted into the cluster format (containing all useful information) and passed to the distributor module.
- As the second hit is read and converted to a cluster, it is compared to the distributor cluster. The following can happen:
  - If the time of the two clusters is consistent, the clusters are merged in the distributor module and remain to be compared with the next hit.
  - If the time is not consistent but the second hit is later in time, the distributor cluster is sent to the clustering array and the second hit becomes the distributor cluster used for the next comparison.

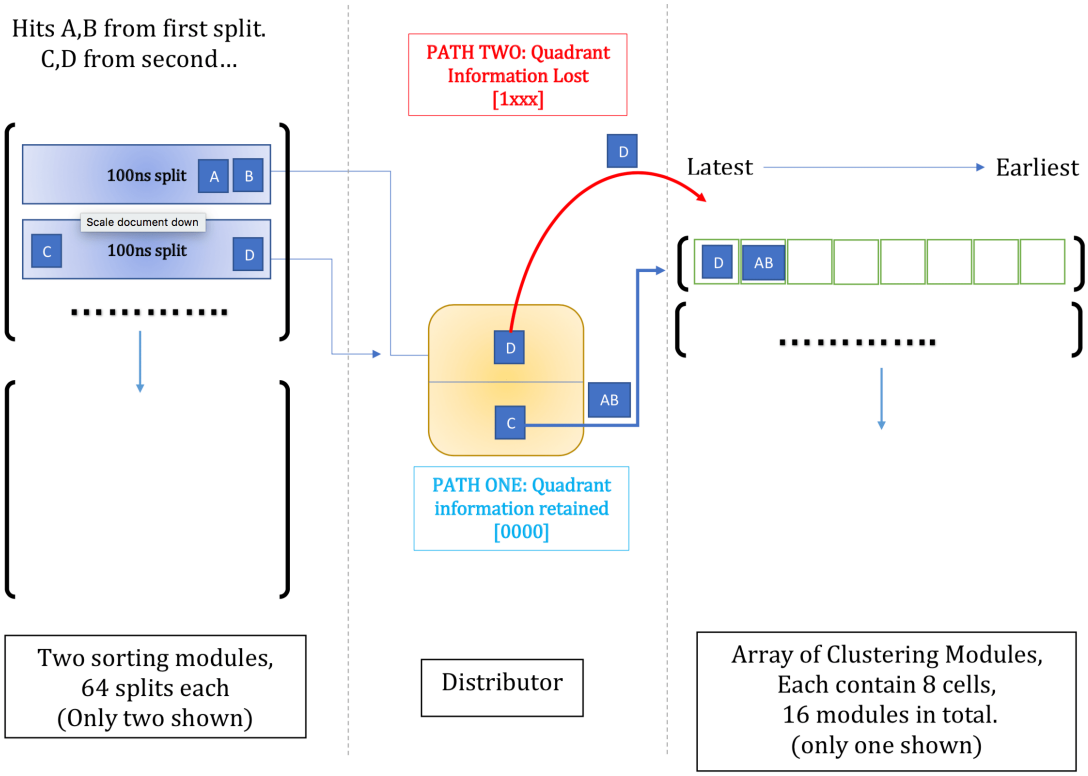

Figure 7.11: A flow diagram of the NewCHOD firmware flaw. Here hits A and B are from the first split and are time-consistent, so are merged at the distributor. Following this, the first hit read from the second split C actually has the largest time of the hits in the buffer. All other hits read from this split, such as D, jump straight to the clustering module and the quadrant information for the hit is lost.

– Otherwise if later, the hit is converted to a cluster and pushed directly to the clustering array leaving the distributor cluster untouched.

In Figure 7.11, a specific example is shown using four hits A, B, C and D. Hit A has the largest time in the first split, and resides at the distributor as the second hit B arrives. Here, the hits are consistent in time and are merged to form cluster AB. As the second split is read, the first hit C is found to be later than cluster AB and so AB is pushed to the clustering module via path one, and C now resides at the distributor. In the case that hit C has the latest time in the second split, all subsequent hits such as D are earlier and pushed directly into the clustering module via path two. The flaw enters for this type of flow. In this path, the information for quadrants 1→3 is lost and Q_X cannot be satisfied.

As the information for certain quadrants is dropped, the kinematic difference between $K_{3\pi}$ and $K_{\pi\mu\mu}$ becomes a bigger problem as the inefficiency depends on the NewCHOD illumination for each event. The randomised nature of the hits also becomes problematic with higher beam-intensity as an increased number of hits can enter each split, and the quadrant information is lost any time the distributor cluster is later than the hit being read. A simple conversion from $K_{3\pi}$ is not a possibility as the two issues are not factorisable.

7.5.2 Q_X emulator

In order to handle the complicated nature of the inefficiency, a L_0 trigger emulator was developed which attempts to replicate the behaviour of the NewCHOD primitive generating firmware, including any flaws present [66]. The emulator can be used at the analysis level to compare the performance with the online primitives. Figure 7.12 contains the emulator and online efficiencies with respect to time and intensity. The excellent agreement is a result of a tuning procedure. As the ineffi-

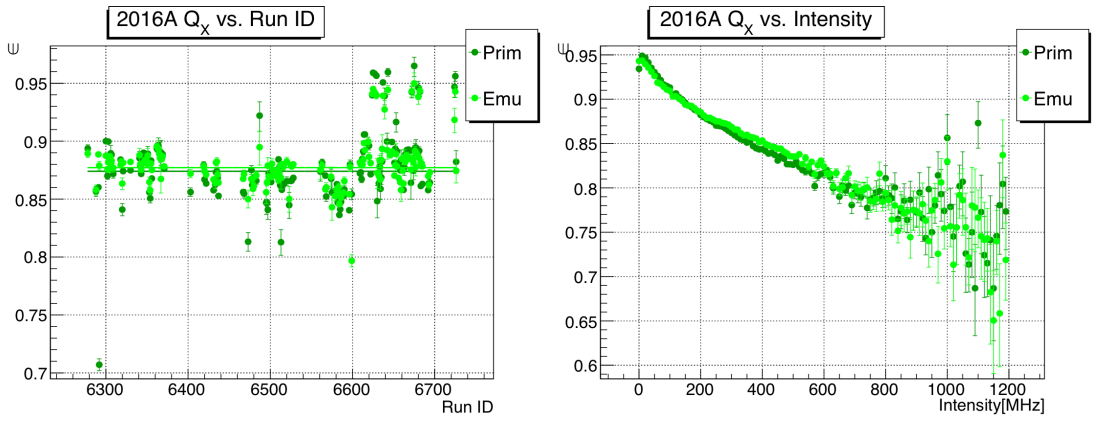

(a) (b)

Figure 7.12: Comparing primitive and emulated L_0 efficiencies for Q_X in 2016A, with (a) against time and (b) versus intensity. The emulator was tuned so that the result agrees excellently with the online primitive efficiency.

ciency depends largely on the random hit ordering in the 100 ns splits, the behaviour was replicated by adding a partial-hit-randomisation algorithm. The effect is controllable by the variable `L0NewCHODEmulator::ShuffleFraction`, a fraction defined between (0; 1). If the fraction is zero, the hits are completely time-ordered

and the flaw is not present (all hits in the splits follow the uncorrupted path one), leading to extremely high efficiencies. Likewise, a fraction of one corresponds to maximal randomness, using a Mersenne twister to shuffle the hits. The optimal fraction was found to be 0.73, a value representing a partial ordering. On average, primitive and emulated efficiencies agree to better than 0.1% overall.

7.5.3 Determining $K_{\pi\mu\mu}$ Q_X efficiency

As the flaw leads to a geometric dependence caused by time-ordering of hits, a simple conversion from $K_{3\pi}$ using MC ratios to get the $K_{\pi\mu\mu}$ Q_X efficiency as a function of $z_{\mu\mu}$ is unreliable. Instead, a MC + Accidentals (MCA) approach is adopted, where the Q_X efficiency is extracted directly from the simulation. To inject accidentals into the simulation, the number of accidental NewCHOD hits were obtained using the following method:

- Take number of NewCHOD hits in the lower timing side-band of the δT = $T_{\mathrm{trig}} - T_{\mathrm{NewCHOD}}$ distribution. An offset region $+74$ ns of T_{trig} is used, with a window of 28 ns, a region where the distribution is flat and best represents the accidental rate.
- The number of accidental hits of this region is sampled in bins of 4 ns, and plotted versus the instantaneous beam-intensity from the GTK between (0; 1200) MHz. The choice of many bins is to sample NewCHOD hits more smoothly.
- The information is fed to the `L0NewCHODEmulator`, so that the correct number of accidental hits are added to the algorithm for any given intensity.

with accidentals added, the emulator can be used at any intensity. To obtain the actual overall efficiency as measured by the MCA method, the results at each intensity must be combined using a weighted-average, where the weights are the number of entries at each intensity bin observed in the residual intensity spectrum.

To verify that the approach provides sensible results, both the $\epsilon^{\mathrm{Q_X}}_{\pi\mu\mu}(z_{\mu\mu})$ and $\epsilon^{\mathrm{Q_X}}_{3\pi}(z_{\pi^+\pi^-})$ spectra are created, as the latter can be measured directly in data to compare. To handle the effects of both intensity and kinematic dependence, a two-dimensional grid

is constructed of z versus intensity, with the $K_{3\pi}$ example displayed in Figure 7.13. The average Q_X efficiency is calculated at each z-bin by constructing the weighted-

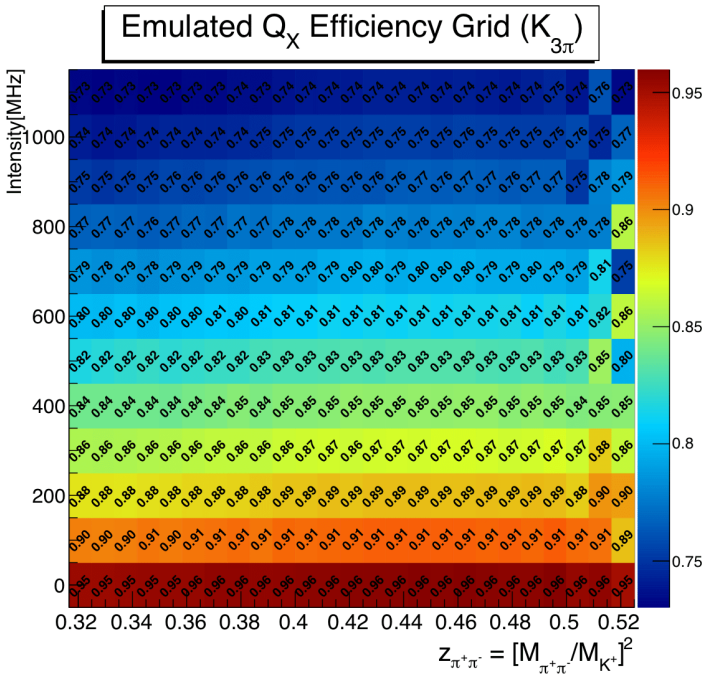

Figure 7.13: The two-dimensional MCA Q_X grid for $K_{3\pi}$ decays. The diagonal labels correspond to the ϵ_{Q_X} at each bin

average over the twelve 100 MHz intensity bins used in the grid,

$$\epsilon_z^{Q_X} = \sum_{\mathcal{I}=0}^{12} \frac{w_{\mathcal{I}} \epsilon_{z,\mathcal{I}}^{Q_X}}{w_{\mathcal{I}}}, \tag{7.9}$$

where $\mathcal{I}$ in the intensity-bin index, $\epsilon_{z,\mathcal{I}}^{Q_X}$ is the emulated Q_X efficiency at the $(z, \mathcal{I})$ bin and $w_{\mathcal{I}}$ is the number of candidates in the $\mathcal{I}^{\text{th}}$ bin of the intensity-spectrum. Finally, the weighted-average at each z-bin can be plotted in one dimension. This is displayed in (a) of Figure 7.14 where a direct comparison to the online primitive efficiency can be made, whereas (b) corresponds to the MCA reconstructed $\epsilon_{\pi\mu\mu}^{Q_X}(z_{\mu\mu})$ spectrum which is used in the analysis to reconstruct $d\Gamma/dz$. The MCA and online primitive efficiencies in (a) agree to within 0.1% on average, after re-tuning the shuffle fraction to get a close agreement. The new shuffle fraction is 0.62, corresponding to increased time-ordering with respect to previously. The requirement to re-tune is unsurprising, as the overall efficiency depends on the time ordering of the hits; the emulator generates hits which are fundamentally different to the online coun-

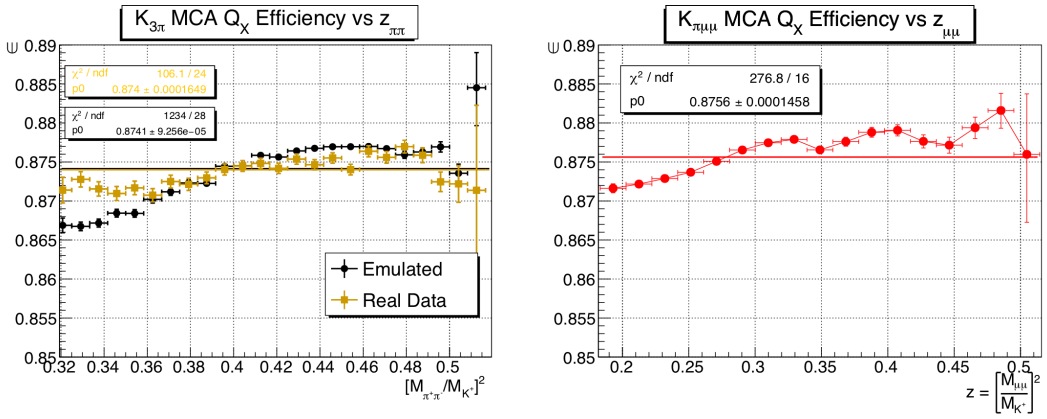

(a) (b)

Figure 7.14: Reconstructing the MCA Q_X efficiency for (a) $K_{3\pi}$ versus $z_{\pi^+\pi^-}$ where it can be compared directly to the online primitive distribution, and (b) $K_{\pi\mu\mu}$ versus $z_{\mu\mu}$ which is used directly in the analysis.

terpart. The shape of the efficiency spectrum for $K_{3\pi}$ is flatter with $z_{\pi^+\pi^-}$ compared to the reconstructed MCA approach. A systematic error of 0.5% is assigned to the $K_{\pi\mu\mu}$ efficiency that can only be measured using this approach, corresponding to the deviation at low $z_{\pi^+\pi^-}$ bins. The average $K_{\pi\mu\mu}$ is therefore measured to be,

$$\epsilon^{\mathrm{Qx}}_{\pi\mu\mu} = 0.8756 \pm 0.0001_{\mathrm{stat}} \pm 0.0050_{\mathrm{syst}}, \tag{7.10}$$

extracted from the flat-line in (b) of Figure 7.14. The shape is roughly the same for $K_{\pi\mu\mu}$ as $K_{3\pi}$, but 0.2% higher on average.

7.6 !LAV

The second component found to be flawed is the L_1 !LAV algorithm, designed to veto events containing at least two LAV hits with leading and trailing edges that are consistent to within 10 ns of the L_0 trigger time. The algorithm is applied in both trigger streams to veto soft-photons from the large accidental $K_{2\pi}$ background. As the algorithm criteria can easily be reproduced at the analysis level, simulating !LAV

for MC yields two very different efficiencies for $K_{3\pi}$ and $K_{\pi\mu\mu}$,

$$\epsilon^{\text{!LAV}}_{\text{MC}_{3\pi}} = 0.9026 \pm 0.0001_{\text{stat}}, \tag{7.11}$$

$$\epsilon^{\text{!LAV}}_{\text{MC}_{\pi\mu\mu}} = 0.9562 \pm 0.0001_{\text{stat}}. \tag{7.12}$$

For comparison, the MC $K_{3\pi}$ value can be compared directly to the data. Figure 7.15 contain the time and intensity-dependence of the algorithm for autopass $K_{3\pi}$ candidates. The normalisation efficiency provided by the flat-line in (a) is measured to

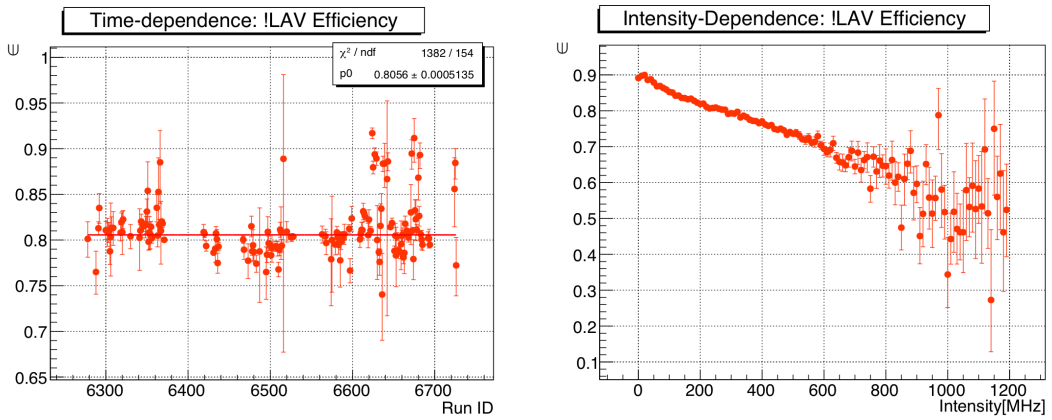

(a) (b)

Figure 7.15: The !LAV algorithm efficiency (a) with respect to time and (b) versus intensity. The red-line in (a) is the average efficiency across the period. Like Q_X, the algorithm displays a large intensity dependence, decreasing by $\approx 40\%$ across the spectrum. Some runs at low-intensity with ID > 6600 display a far higher efficiency than average.

be,

$$\epsilon^{\text{!LAV}}_{3\pi} = 0.8056 \pm 0.0005_{\text{stat}}, \tag{7.13}$$

which is 10% lower than the MC prediction and highlights the presence of a flaw. The inefficiency is also driven by accidentals at higher beam intensity. As was observed with Q_X, the low-intensity runs present at run ID > 6600 display a $\approx 10\%$ higher-efficiency compared with the average.

7.6.1 Flaw with !LAV algorithm

Unlike Q_X, there is no technical limitation creating the inefficiency for the signal. The !LAV algorithm works exactly as intended, but the flaw is that the algorithm is

unsuitable for collecting unbiased samples of three-track decays. This because the inefficiency has three components:

- A self-component, due to inelastic collisions and hadronic interactions with material from the daughters in the decay.
- Accidental component, due to in-time large-angle photons or other non-decay originating pions interacting with material.
- Combinatorial component, where hits from the self or accidental component combine to fire !LAV if neither mechanism generated enough hits individually.

The self-component is dependent on the decay composition. Hadrons like pions have a chance to interact in-elastically with material in the downstream of the detector, leading to a high flux of particles at large opening angles. A study performed using MC displayed that the dense RICH mirror is a hot-spot for inelastic pion collisions, in which the subsequent hadronic shower creates hits in the LAV12 station, causing !LAV to fail and the event to be vetoed [84]. This component can be described by the GEANT4 simulation of hadronic showers in NA62MC, which leads to the difference of prediction of the MC efficiencies in Equations 7.11 and 7.12. For $K_{3\pi}$ decays, the self-component is maximal whereas $K_{\pi\mu\mu}$ contains only one pion, and so the self-component is ≈ 2.2 times smaller in comparison.

The intensity-dependent accidental component is of a similar size to the $K_{3\pi}$ self-component based upon the magnitude average normalisation efficiency. This component enters due to hadronic showers of accidental beam pions and the large rate of $K_{2\pi}$ decays, but importantly, it will enter with an identical magnitude for both normalisation $K_{3\pi}$ and signal $K_{\pi\mu\mu}$. The added complication is the combinatorial component. Though expected to be small, the magnitude depends on the number of hits in the tail due to the self-component, for cases where neither the self or accidental components could veto !LAV individually. As both of the final two components are absent from simulation, a simple MC conversion from $K_{3\pi}$ is unreliable and a similar MCA approach to Q_X must be adopted.

7.6.2 !LAV emulation

Unlike Q_X, the !LAV algorithm is software-based and can be simply reproduced offline at the analysis stage. The offline algorithm can therefore be used on data to get a comparison with the online efficiency. Figure 7.16 compares the emulated and online algorithm efficiencies with respect to time and intensity as measured with autopass $K_{3\pi}$ candidates. As there is no hit ordering dependence, the agreement

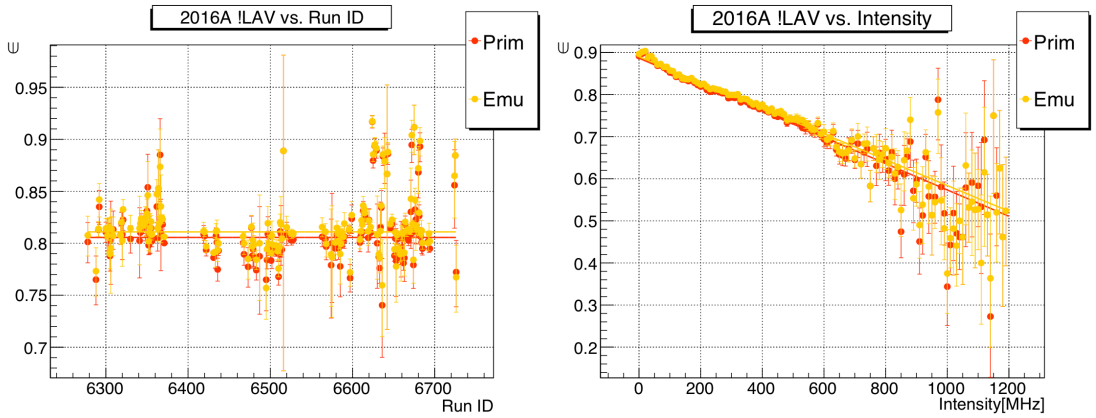

(a) (b)

Figure 7.16: Comparing !LAV algorithm and emulated L_1 efficiencies in 2016A, where (a) is with respect to Run ID and (b) is versus intensity. The offline emulation provides excellent agreement.

cannot be tuned. However, the agreement is excellent overall, with the emulated efficiency entering as $\approx 0.5\%$ higher than the online-algorithm, but with very similar responses for both time and intensity distributions.

7.6.3 Determining $K_{\pi\mu\mu}$!LAV efficiency

In order to measure the $K_{\pi\mu\mu}$ adequately, all three components of the inefficiency need to be accounted for properly. The simplest approach is identical to the Q_X strategy; perform a MCA measurement. To do this and account for all components, accidentals must be extracted from data and injected accordingly. Figure 7.17 contains the $\delta T = T_{\text{trig}} - T_{\text{LAV}}$ spectrum for LAV12, containing only hits with both leading and trailing edges. The peak at zero corresponds to the self-component with flat accidental component sitting beneath, with two regions indicated for accidental extraction as they are flat. The method, similar to Q_X, follows as,

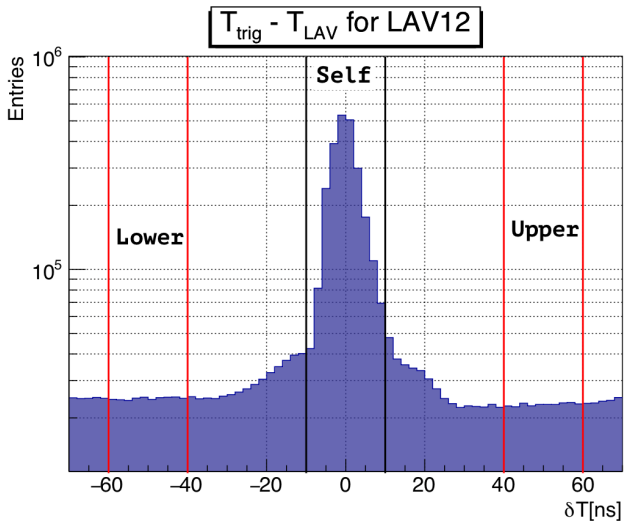

Figure 7.17: The δT distribution for LAV12. The large peak corresponds to the self-interactions, residing on top of the flat-background component. Two regions for accidental extraction are labelled, whereas the self region corresponds to the online window.

- Take the number of LAV hits in the lower timing side-band of the $\delta T = T_{\rm trig} - T_{\rm LAV}$ distribution, defined as offset by +50 ns with a $\pm$ 10 ns window.
- The number of accidental hits in this region is plotted versus the instantaneous beam-intensity from the GTK between (0; 1200) MHz.
- The information is fed into the modified !LAV algorithm emulator, and a number of accidentals are extracted at random for any given intensity.

The emulated !LAV algorithm returns an efficiency based on all three components at any intensity. As was performed for Q_X, both the $\epsilon_{3\pi}^{\rm !LAV}(z_{\pi^+\pi^-})$ and $\epsilon_{\pi\mu\mu}^{\rm !LAV}(z_{\mu\mu})$ distributions were created using a two dimensional grid, and collapsed into one-dimension by calculating the weighted-average at each z-bin. The first case is used to verify the technique as the same spectrum can be extracted directly in data, whereas the second is used directly to reconstruct $d\Gamma/dz$. Both distributions are contained in Figure 7.18. On average, the emulated efficiency using the MCA approach for $K_{3\pi}$ is 0.6% lower than for the observed value in data. As the shape agreement is excellent, this value is taken as a systematic for the $K_{\pi\mu\mu}$ measurement. As the accidentals enter at the correct level in MC, the hadronic interactions appear to be over-predicted for events containing three pions. The simulation is therefore expected to be even better for $K_{\pi\mu\mu}$ as only one pion is in the event, as the systematic effect could be up

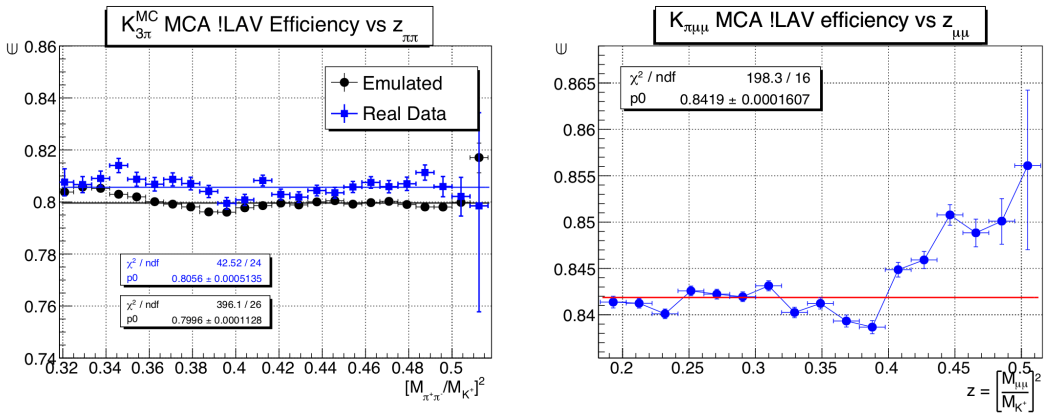

(a) (b)

Figure 7.18: Reconstructing the MCA !LAV efficiency for (a) $K_{3\pi}$ versus $z_{\pi^+\pi^-}$ where it can be compared directly to the online algorithm distribution, and (b) $K_{\pi\mu\mu}$ versus $z_{\mu\mu}$ which is used directly in the analysis.

to three times smaller. The average $K_{\pi\mu\mu}$ is therefore measured to be,

$$\epsilon_{\pi\mu\mu}^{\text{!LAV}} = 0.8419 \pm 0.0002_{\text{stat}} \pm 0.0060_{\text{syst}}, \tag{7.14}$$

extracted from the flat-line in (b) of Figure 7.18. The shape is fairly different in comparison to $K_{3\pi}$, especially at high $z_{\mu\mu}$ bins where the efficiency appears to increase linearly. Candidates in this region contain π^+ with transverse momentum P_T typically close to zero, unlike elsewhere in the phase-space. This reduces the chance for direct π^+ interaction, leading to !LAV being less likely to be fired. The behaviour is not observed for $K_{3\pi}$ because all three daughters are pions.

7.7 MO_2 (MUV3)

The MO_2 component is unique to the Dimuon trigger, requiring at least two MUV3 outer pads to be within a 10 ns coincidence. The primitive is used to collect candidates with two final state muons, a process which is relatively rare at NA62 except for accidental pile-up of decays containing muons. As $K_{3\pi}$ is unsuitable, a different process was used. Based on the low-mass background observed in the final dimuon spectrum of Chapter 6, a sample of minimum-bias $K^+ \to \pi^+\pi^+\pi^- \to \pi^+\mu^+\mu^-$ decays were collected using the following criteria:

- Passes the final NA62-like $K_{\pi\mu\mu}$ selection,
- Collected with the minimum bias control trigger,
- Candidate consistent within SR: $|M_{3\pi} - M_{K^+}| \leqslant 5$ MeV/c.

The $K_{3\pi}$ candidates surviving the $K_{\pi\mu\mu}$ selection provide an ideal handle to measure the MO_2 component. Figure 7.19 compares the normalised MUV3 illuminations for $K_{3\pi\to\pi\mu\mu}$ measured in data compared to $K_{\pi\mu\mu}$ MC. Provided there is no geometric-

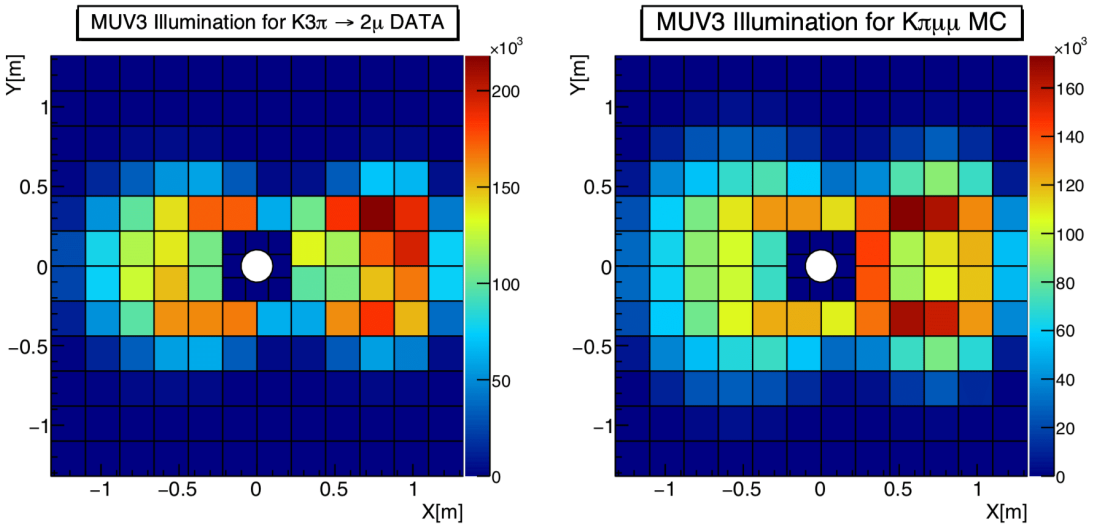

Figure 7.19: The MUV3 Illumination for left, $K_{3\pi\to\pi\mu\mu}$ data and right $K_{\pi\mu\mu}$ in MC. Like the New-CHOD, the first case is fundamentally $K_{3\pi}$, with relatively lower opening angles. The absence of candidates in the inner pads is an artefact of the selection, as candidates with only in-time outer pad associations are selected, reducing the probability of association in this region.

based inefficiency, the illuminations in data are expected to be relatively similar. The sacrifice for using such a natural equivalent to the signal is statistics, where only $\approx 10^4$ decays appear for control-triggered events in 2016A, whereas closer to 10^7 candidates were available for $K_{3\pi}$ measurements. Figure 7.20 contain the time and intensity dependence of the efficiency for these candidates, re-binned with respect to previous distributions. The average MO_2 efficiency for these decays as measured by the red line in (a) is,

$$\epsilon^{\mathrm{MO_2}}_{K_{3\pi\to\pi\mu\mu}} = 0.9710 \pm 0.0019_{\mathrm{stat}}. \tag{7.15}$$

To improve the precision of this measurement, the MO_2 efficiency can instead be measured using the Multi-track trigger sample. As the Multi-track is identical to

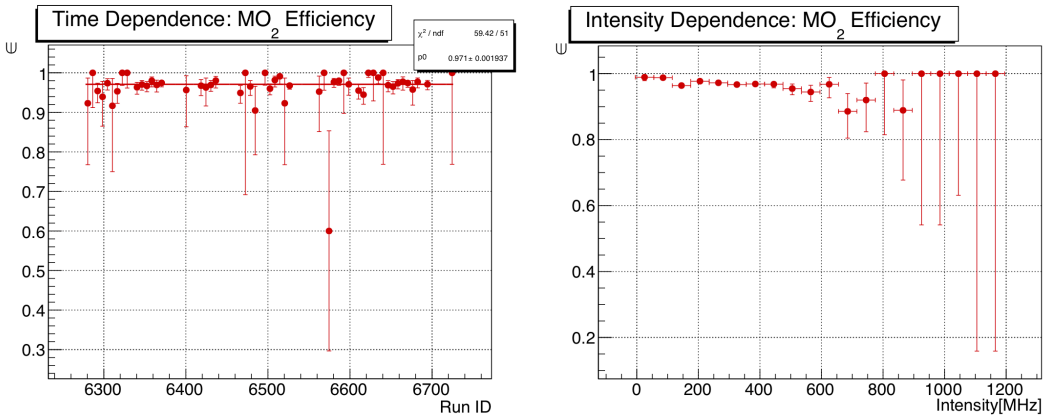

(a) (b)

Figure 7.20: The MO_2 primitive efficiency (a) with respect to time and (b) versus intensity for $K_{3\pi} \to \pi^+\mu^-\mu^-$ minimum bias decays. The red-line in (a) is the average efficiency across the period. The primitive displays a gentle intensity dependence which is limited by low-statistics.

the Dimuon trigger but without MO_2, the decays collected are far more suitable. Measuring the component using this stream also removes the double counting of inefficiency. For example, if events are inefficient for RICH or Q_X, they could be similarly inefficient for MO_2. However, the inefficiency would be counted twice when combining the results as the L_0 criteria are not applied sequentially like L_1. Therefore, the Multi-track MO_2 efficiency is expected to be higher and more likely to reflect the real $K_{\pi\mu\mu}$ dependence. Additionally, the gain in statistics compared to minimum bias is a factor of $\approx$ 10. Using this sample, the $z_{\mu\mu}$ dependence can be plotted directly, as seen in Figure 7.21. The bins between the dashed grey lines

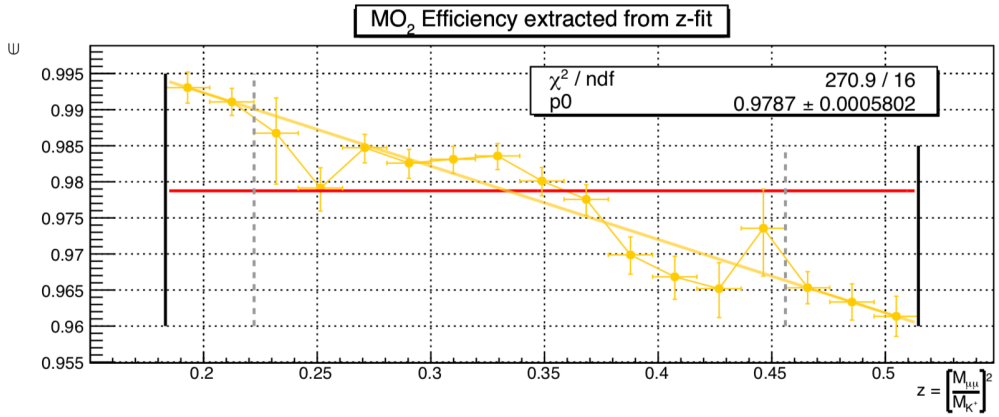

Figure 7.21: The MO_2 Efficiency vs z in 2016A. The shape between the grey dashed lines represent the measurement in data, which is then extrapolated using a linear fit to the full phase-space. The variation across the region is $\approx$ 3%.

represent the data measurements, which do not occupy the full $K_{\pi\mu\mu}$ phase-space denoted by the black lines. To extend the measurements for the full region, the data points were fitted with a first order polynomial and extrapolated as denoted by the orange line. This provides a measurement for the first two and last five bins. The errors assigned to the bins are based on the errors on the gradient, taken at a 68.3% C.L. As we are effectively blind to the true efficiencies in this region, the variation of the chosen bins here (for example, a flat extrapolation) is considered as a systematic error. The red-line denotes the average efficiency across the full phase-space, measuring the MO_2 efficiency for $K_{\pi\mu\mu}$ decays as.

$$\epsilon_{\pi\mu\mu}^{\mathrm{MO}_2} = 0.9787 \pm 0.0006_{\mathrm{stat}} \pm 0.0010_{\mathrm{syst}}, \tag{7.16}$$

which is almost 1% higher than for the control trigger minimum-bias sample and with an error three times smaller. No clear shape change was observed with respect to $z_{\mu\mu}$ between using minimum bias and Multi-track samples.

7.8 Full trigger efficiencies

The full trigger efficiency for $K_{3\pi}$ Multi-track and $K_{\pi\mu\mu}$ Dimuon events is obtained by calculating the product of each trigger component for each stream. Therefore, a single Dimuon efficiency distribution in terms of $z_{\mu\mu}$ is produced using the components, as shown in Figure 7.22. The scale of the trigger efficiency is dominated by both Q_X and !LAV, whereas the shape is mostly due to the change in MO_2 efficiency across the phase-space. The KTAG efficiency is included, taken as flat across the phase-space and extracted directly from the $K_{3\pi}$ measurement. Table 7.2 contains the trigger efficiencies for each component of the Dimuon and Multi-track triggers for $K_{\pi\mu\mu}$ signal and $K_{3\pi}$ normalisation. The errors for $K_{3\pi}$ are purely statistical are their magnitude reflects the large size of the sample. The same value is used for the KTAG in both.

The flat line in the $K_{\pi\mu\mu}$ efficiency spectrum provides the overall signal trigger efficiency, whereas $K_{3\pi}$ is extracted from the products in Table 7.2 with the final values

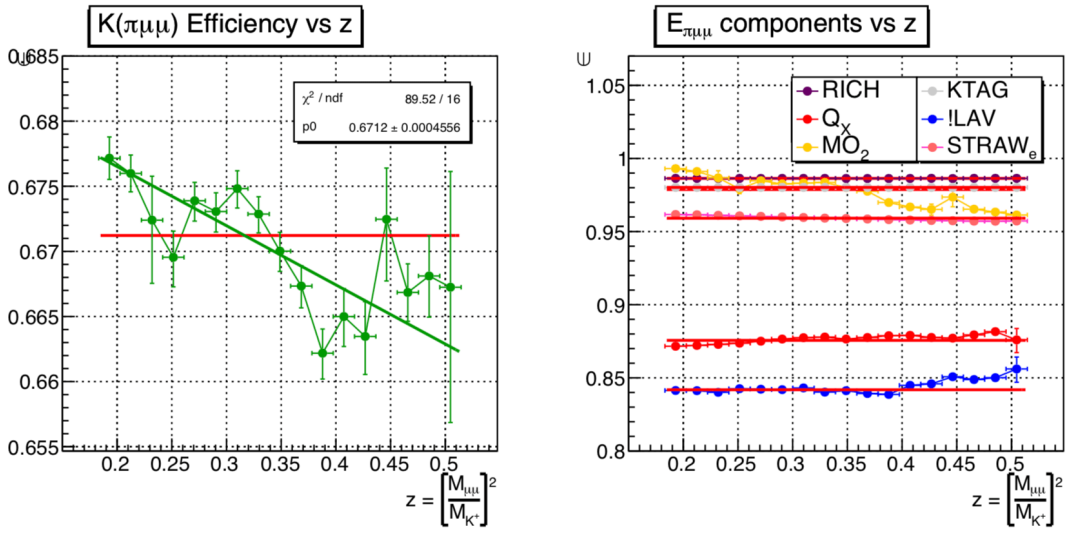

Figure 7.22: The overall $K_{\pi\mu\mu}$ efficiency spectra vs z in 2016A. Left, the combined efficiencies and right, the individual components. The scale is dominated by Q_X and !LAV, decreasing linearly mostly due to the MO_2 efficiency.

Table 7.2: Comparison of the trigger efficiency components for $K_{3\pi}$ and $K_{\pi\mu\mu}$ in 2016A. The MO_2 mask is only present for the $K_{\pi\mu\mu}$ signal and the largest magnitude difference is for the !LAV algorithm.

Component	$K_{3\pi}$	$K_{\pi\mu\mu}$
RICH	$0.9863 \pm 0.0001_{\text{stat}}$	$0.9864 \pm 0.0000_{\text{stat}} \pm 0.0060_{\text{syst}}$
Q_X	$0.8740 \pm 0.0002_{\text{stat}}$	$0.8756 \pm 0.0001_{\text{stat}} \pm 0.0050_{\text{syst}}$
MO_2	-	$0.9787 \pm 0.0006_{\text{stat}} \pm 0.0010_{\text{syst}}$
KTAG	$0.9802 \pm 0.0002_{\text{stat}}$	$0.9802 \pm 0.0002_{\text{stat}}$
!LAV	$0.8056 \pm 0.0005_{\text{stat}}$	$0.8419 \pm 0.0002_{\text{stat}} \pm 0.0060_{\text{syst}}$
STRAW_e	$0.9587 \pm 0.0003_{\text{stat}}$	$0.9591 \pm 0.0001_{\text{stat}} \pm 0.0050_{\text{syst}}$

as,

$$\epsilon^{\mathcal{F}}_{\pi\mu\mu} = 0.6712 \pm 0.0005_{\text{stat}} \pm 0.0137_{\text{syst}}, \tag{7.17}$$

$$\epsilon^{\mathcal{F}}_{3\pi} = 0.6526 \pm 0.0005_{\text{stat}} \pm 0.0080_{\text{syst}}. \tag{7.18}$$

The combination of the trigger efficiency components by multiplication introduces an additional systematic due to double-counting of inefficiency. As L_1 is sequential, and MO_2 for $K_{\pi\mu\mu}$ measured using Multi-track events, the double-counting occurs only when combining the RICH and Q_X efficiencies at L_0. A discrepancy of 0.8% was found when comparing the product RICH $\cdot$ Q_X with the direct measurement of the overall L_0 Multi-track efficiency using events which positive CHOD primitives. However, as the systematic error is present with the same magnitude for both signal

and normalisation, it cancels directly in the ratio when normalising. With these final measurements (Figure 7.22, Table 7.2), the trigger efficiencies can be fully accounted for when reconstructing the $d\Gamma/dz$ spectrum in bins of $z_{\pi\mu\mu}$ as presented in Chapter 8.

8

The $K^+ \to \pi^+\mu^+\mu^-$ analysis

In this chapter, the measurement of the $K^+ \to \pi^+\mu^+\mu^-$ ($K_{\pi\mu\mu}$) decay is presented. By reconstructing the $d\Gamma/dz$ spectrum, both the model-independent branching fraction and the Low-Energy Constants (LECs) of the form factor are extracted from the 2016A NA62 data set. As discussed in Chapter 2, both of the measurements have been performed previously by the NA48/2 experiment, measuring $\mathcal{B}(K^+ \to \pi^+\mu^+\mu^-)$ = (9.62 $\pm$ 0.25) $\times$ 10^{-8} and (a_+, b_+) = (-0.575 $\pm$ 0.039, -0.813 $\pm$ 0.145). In general, the errors are dominated by low-statistics and the contribution from the irreducible $K_{3\pi}$ background [48]. The analysis performed here uses the sample of decays collected using the selection from Chapter 6 where the contribution from background is suppressed to a negligible level, taking in to consideration the study performed on the trigger efficiency in Chapter 7. A discussion of the resulting systematics effects is also provided.

8.1 Analysis strategy

In theory, the decay is described as a single virtual photon exchange where the shape and magnitude of the spectra of variable $z_{\mu\mu} = (M_{\mu\mu}/M_{K^+})^2$ is dependent on the transition form factor $W(z_{\mu\mu})$. Therefore, the partial decay-rate is described in terms of $z_{\mu\mu}$, as

$$\frac{d\Gamma_{\pi\mu\mu}}{dz} = \Omega_C \frac{\alpha^2 M_{K^+}}{12\pi(4\pi)^4}\lambda^{3/2}(1, z_{\mu\mu}, r_\pi^2)\sqrt{1-4\frac{r_\mu^2}{z_{\mu\mu}}}\left(1+2\frac{r_\mu^2}{z_{\mu\mu}}\right)|W(z_{\mu\mu})|^2. \tag{8.1}$$

where Ω_C is the Coulomb interaction term, $r_{\pi,\mu} = M_{\pi,\mu}/M_{K^+}$ and $\lambda(a,b,c) = a^2 + b^2 + c^2 - 2ab - 2ac - 2bc$. In χPT, the form factor $W(z_{\mu\mu})$ is described as,

$$W(z_{\mu\mu}) = G_F M_{K^+}^2 (a_+ + b_+ z_{\mu\mu}) + W^{\pi\pi}(z_{\mu\mu}), \tag{8.2}$$

where $W^{\pi\pi}(z_{\mu\mu})$ is a dispersion term corresponding to the pion loop and form factor parameters (a_+, b_+) are free low energy constants (LECs) which characterise all of the other possible transition loops [42][44]. In order to extract the LECs using experimental data, the partial decay-rate $d\Gamma/dz$ must be reconstructed. The strategy of the analysis is therefore:

- Develop a $K_{\pi\mu\mu}$ selection to collect candidates with a negligible contribution from all known backgrounds.
- Use a highly-symmetrical selection to collect an abundant normalisation sample which has similar properties to the signal decay.
- Tune the MC simulation to account for important detector and track-reconstruction effects observed in the data.
- Compute the efficiencies and the effects of the trigger logic on both signal and normalisation samples.
- Compute $d\Gamma/dz$ based on the acceptances, trigger efficiencies and the number of observed candidates for both signal and normalisation and extract both the branching fraction and low-energy constants.

The first four points of the strategy were already addressed in previous chapters. The development of a background-free selection for $K_{\pi\mu\mu}$ was presented in Chapter 6, suppressing the systematic contribution of a large background $z_{\mu\mu}$ spectrum. A highly symmetric selection for normalisation $K_{3\pi}$ is also described, including the tuning of the simulation to improve the agreement with reality. The trigger efficiencies were studied and measured extensively in Chapter 7 in order to obtain a $K_{\pi\mu\mu}$ efficiency spectrum with respect to $z_{\mu\mu}$ and also the overall normalisation efficiency for $K_{3\pi}$.

The final piece of the strategy is to combine all of the information from previous chapters to reconstruct the $d\Gamma/dz$ spectrum. The candidates collected from the selections are counted and presented in Section 8.2.1, including an estimate into the level of neglibility of background in the $K_{\pi\mu\mu}$ sample. The signal acceptances, calculated with the newly tuned simulation, are presented in Section 8.2.2 and includes a comparison of the shape with respect to $z_{\mu\mu}$ without the tuning. Finally, the $d\Gamma/dz$ spectrum was reconstructed. The model-independent branching fraction was extracted by direct integration and the LECs were obtained by fitting the distribution with Equation 8.1, after correcting for the effects of the Coulomb interaction term Ω_C and the non-linearity of the candidates in each bin. The propagation of systematic errors to both measurements is also performed, and the details are provided in Section 8.2.3.

8.2 Reconstructing $d\Gamma/dz$

In this section, the reconstruction of the $d\Gamma/dz$ spectrum with respect to $z_{\mu\mu}$ is described. The spectrum can be calculated in i bins of z following,

$$\left(\frac{d\Gamma_{\pi\mu\mu}}{dz}\right)_i = \left(\frac{N_i - N_i^B}{N_{3\pi}}\right) \cdot \left(\frac{A_{3\pi}}{A_i}\right) \cdot \left(\frac{\epsilon_{3\pi}}{\epsilon_i}\right) \cdot \left(\frac{1}{\Delta z_i}\right) \cdot \left(\frac{\hbar}{\tau_K}\right) \cdot \mathcal{B}(K_{3\pi)}. \tag{8.3}$$

Each bracket is a combination of measurable quantities which must be known, with three major components,

- **Number of candidates:** N_i and N_i^B are the number of $K_{\pi\mu\mu}$ and background candidates at the ith $z_{\mu\mu}$-bin. $N_{3\pi}$ is the total number of collected $K_{3\pi}$ normalisation candidates. This is calculated in Section 8.2.1 using the events passing the selection developed in Chapter 6.

- **Acceptances:** A_i is the $K_{\pi\mu\mu}$ acceptance at the ith $z_{\mu\mu}$-bin, whereas $A_{3\pi}$ is the total $K_{3\pi}$ normalisation acceptance. This is calculated in Section 8.2.2 after the MC tuning described in Chapter 6.

- **Trigger Efficiencies:** ϵ_i is the $K_{\pi\mu\mu}$ trigger efficiency at ith $z_{\mu\mu}$-bin, whereas $\epsilon_{3\pi}$ is the total normalisation trigger efficiency. Both components were calculated fully in Chapter 7 and are used here.

The final parameters are independent of the measured samples. The bin-width Δz_i is fixed to be the same size across the full decay phase-space, limited to $4r_\mu^2 \leqslant z_{\mu\mu} \leqslant (1-r_\pi)^2$. The measurement also requires two external inputs, both the $K_{3\pi}$ branching fraction and K^+ life-time [55].

8.2.1 Number of candidates

The number of candidates enter in three places in Equation 8.3. Two quantities, N_i and N_i^B depend on the number of observed $K_{\pi\mu\mu}$ candidates and expected background in the SR at each z-bin. The quantity $N_{3\pi}$ is the integrated amount of $K_{3\pi}$ decays in the full sample collected using the normalisation trigger. Whilst the $K_{3\pi}$ sample statistically consistent with background-free at this sensitivity, a data-driven approach was performed to define a more reasonable $K_{\pi\mu\mu}$ SR and predict the amount of background candidates present in each $z_{\mu\mu}$-bin.

8.2.1.1 N_i and N_i^B

To measure both N_i and predict N_i^B, the definition of the SR used to collect the $K_{\pi\mu\mu}$ signal was tuned directly for the spectrum. The RooFit package was used to build both a signal and background Probability Density Function (PDF) with four components, two for signal and background respectively [85],

- A core Gaussian, to describe the $K_{\pi\mu\mu}$ signal near M_{K^+}.
- A second wider Gaussian, to pick up the non-Gaussian tails of the signal.
- An exponential slope, measured directly on the tail-end of the low-mass events above 460 MeV.
- A second exponential, hypothesised as the contribution from TRIM5 upstream background.

The first component provides a measurement of M_{K^+} as determined by the $K_{\pi\mu\mu}$ candidates, useful for defining the SR, whilst the second is designed to better describe the non-Gaussian tails for the signal. The final two components, relating to the background, are used to determine the amount of background in the newly defined SR. The shape of the first exponential can be inferred directly by RooFit, but

the second requires examination of the invariant mass spectra for TRIM5 decays, which was suppressed in the selection development (see Section 6.4.1). As observed in the left-hand-side of Figure 8.1, a second exponential is the natural choice for these decays, instead of a generic flat component which was used by NA48/2 in this region. To determine the value of the slope to be inputted into RooFit, the Z-Vertex criteria for the selection was turned off and the region between (510; 540) MeV was fitted with an exponential curve. In order to check that the shape of surviving events did not change with respect to the cut on Z-Vertex, the criteria was re-added in steps of 1 m between (102; 110) m and the shape re-fitted, as described by the right-hand-side of Figure 8.1. As the linear slope of Figure 8.1 is consistent

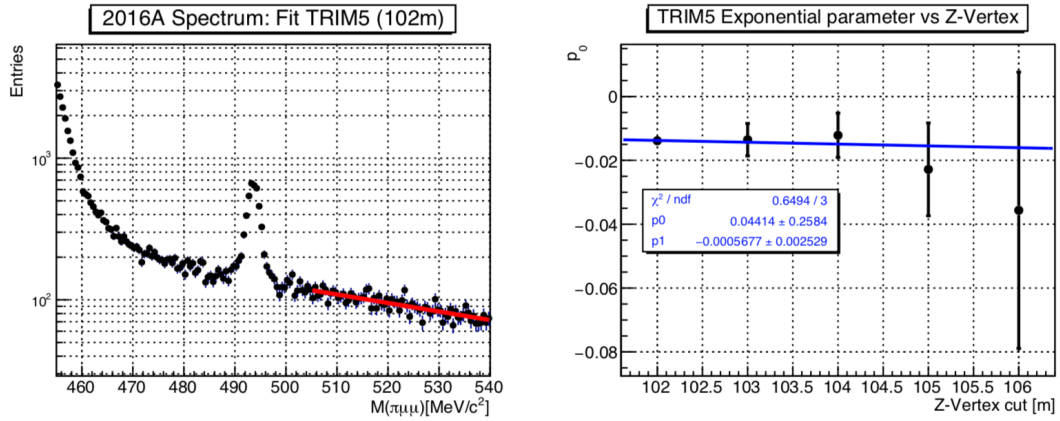

Figure 8.1: Fitting TRIM5 background to extract the overall slope. Left: The $K_{\pi\mu\mu}$ invariant-mass spectra with a Z-Vertex cut at 102m (from Filter); the red line corresponds to the exponential fit across the high-mass region. Right: the TRIM5 slope parameter p_0 after subsequently harder Z-Vertex cuts. Statistics begin to suffer, but the slope is consistent with being flat as the gradient of the first-order-polynomial fit is within one standard-deviation of zero. Only the points with adequate statistics are included.

to within a standard-deviation of being flat across the Z-Vertex cut space, the parameter was fixed and added into the background PDF. As TRIM5 is a hypothesis, the scale is free and is decided automatically by the number of candidates in the upper sideband of the signal PDF. The final result can be seen in Figure 8.2, where an extended maximum-likelihood fit has been performed [86]. The fit provides a number of useful measurements with respect to invariant mass, summarised in the first block of Table 8.1. The determined resolution σ_M is roughly unchanged, but the region is shifted to use the central value found by RooFit. Equation 6.1 is modified

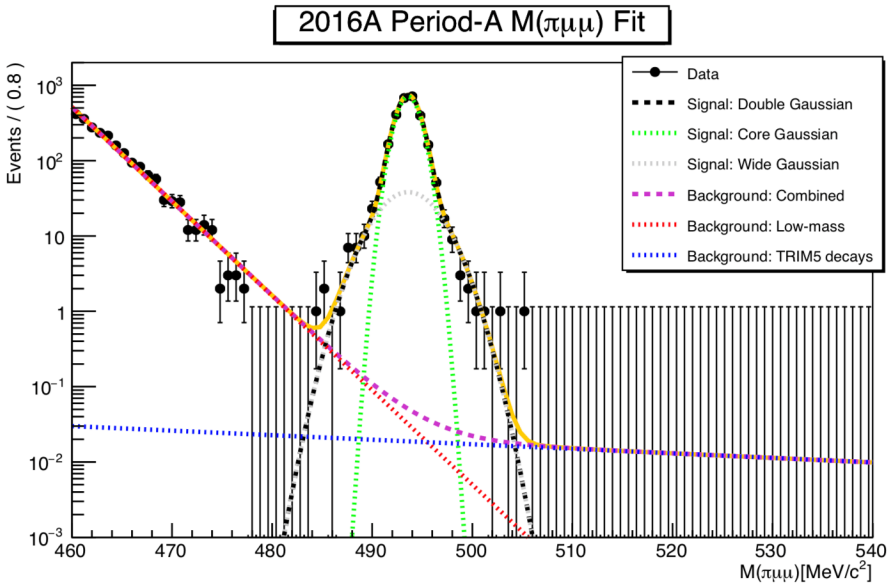

Figure 8.2: The RooFit PDF spectrum. The black-dots correspond to the data-set, whereas the full PDF is the combination of the four individual signal region and background functions. Only the shape of the TRIM5 component is inferred indirectly, and its scale is dependent on the observation of one event at ≈ 505 MeV/c^2.

to become,

$$|M_{\pi\mu\mu} - 493.599| \leqslant 5 \text{ MeV/c}^2, \tag{8.4}$$

and is used to compute the number of signal candidates and expected background, contained in the second block. The fit expects $N^S_{\pi\mu\mu} = 2676.98$ candidates, compared to 2676 actual candidates observed. The largest background contribution is expected to be from the low-mass tail events, which is approximately twice the size of the TRIM5 contribution in the signal region. Regardless, less than one back-

Table 8.1: The RooFit summary. The signal mass $M_{\pi\mu\mu}$ and resolution σ_M are determined and used to define the modified SR in Equation 8.4. Using the modified SR, the number of signal N_S and expected background candidates N_B is determined. The largest background contribution is from the low-mass tail, with less than one background event expected in the SR in total.

Quantity	Value
$M_{\pi\mu\mu}$	(493.599 ± 0.023) MeV/c^2
σ_M	(1.081 ± 0.032) MeV/c^2
$N^S_{\pi\mu\mu}$	2676.98 ± 51.47
$N^B_{\text{Low-mass}}$	0.54 ± 0.01
N^B_{TRIM5}	0.24 ± 0.01
N^B_{Total}	0.78 ± 0.02

ground event is expected in total such that the signal to background ratio S/B is $\approx 3 \times 10^3$. The lack of background is a significant improvement with respect to the NA48/2 analysis, where ≈ 52 background candidates were observed corresponding to a S/B of ≈ 60. The improvement is mostly because of the implementation of a larger MNP33 current, increasing the separation between low-mass candidates and the signal region.

With the number of signal and an estimate of the number of background candidates determined, the $z_{\mu\mu}$-spectra can be produced. Whilst the number of background is now predicted, the shape in $z_{\mu\mu}$ is unknown. For the low-mass component, the $z_{\mu\mu}$-spectra was observed directly, taking the shape from the distribution between $(460; 475)$ MeV/c^2. The TRIM5 component, in addition to making mass-spectra plots, is extracted as the $z_{\mu\mu}$-spectrum from candidates between $(505; 540)$ MeV/c^2 after a Z-Vertex cut of 102 m. Both spectra are appropriately scaled, and can be seen in Figure 8.3. In general, the background components are only visible in log-

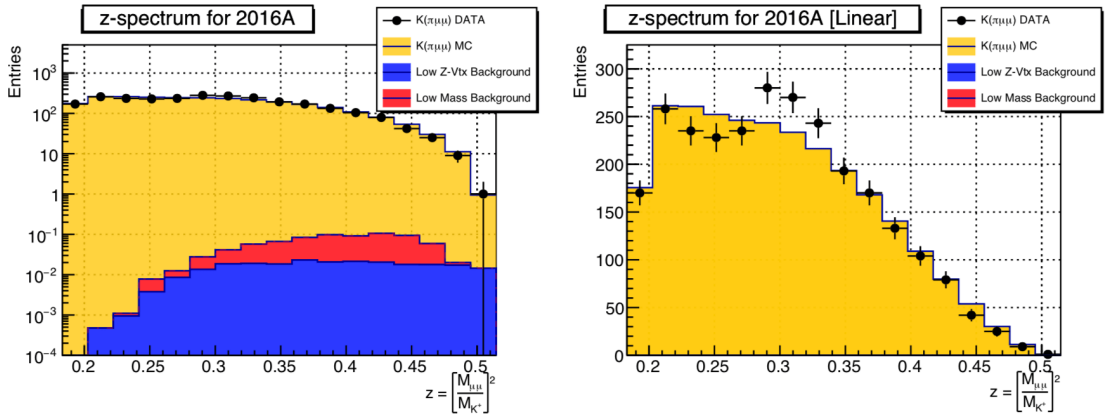

Figure 8.3: The 2016A z-spectra in left, log-scale and right, linear. The background contributes maximally for higher $z_{\mu\mu}$-values but many orders of magnitude below the signal. The linear-scale shows some discrepancy between MC and data for the six bins between $0.21 \leqslant z_{\mu\mu} \leqslant 0.34$.

scale and are typically four orders of magnitude below the signal in each bin. The linear scale exposes a shape-discrepancy between MC and data for the six central bins between $0.21 \leqslant z_{\mu\mu} \leqslant 0.34$. The first three bins in this region sit approximately one standard-deviation below the MC expectation, whereas the next three are closer to two standard-deviations above expectation. Whilst the number of bins deviated roughly in expectation for reasonable statistical fluctuations points, the proximity

of the bins with respect to each other is suspicious. Two possible causes are due to kinematic dependences,

- Distortion via the trigger stream.
- Differences between data-MC reconstruction efficiency.

However, the trigger efficiency varies by less than 2% across the sample as observed in Figure 7.22, and the reconstruction effects do not drastically alter the acceptance shape as observed in Figure 8.7. Without a valid explanation, the residual difference must be taken as a systematic effect and propagated into the error analysis.

The choice of bin size is the result of dividing the full phase-space equally by seventeen, leading to Δz_i = 0.0195. The bins are large with respect to the resolution $\sigma_{z_{\mu\mu}} = 0.0011$, determined using the 10^7 $K_{\pi\mu\mu}$ MC sample after fitting the residual of truth and reconstructed Z-Vertex with a Gaussian. The resolution is stable across the phase-space, as seen in right-hand-side of Figure 8.4. One of the striking fea-

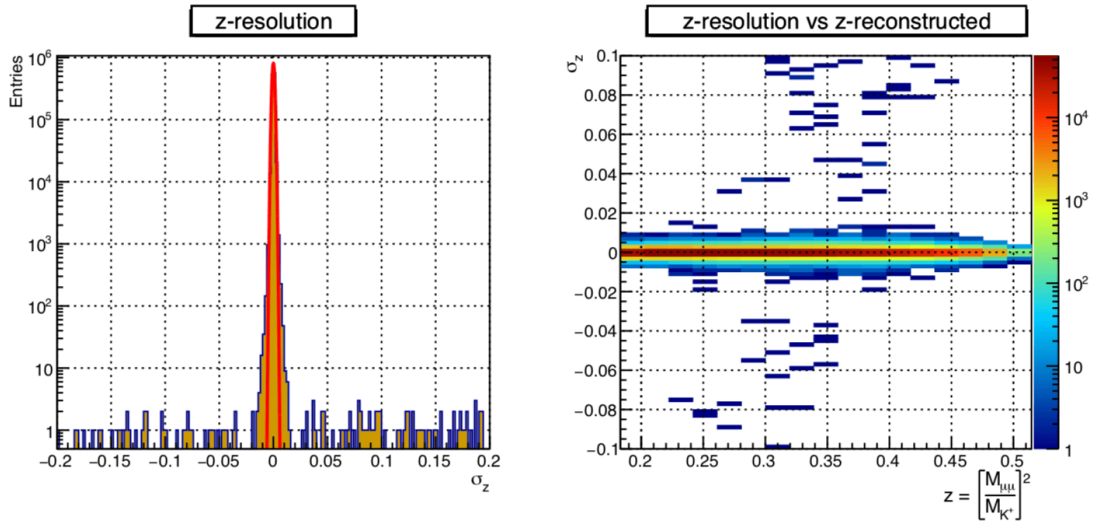

Figure 8.4: The $z_{\mu\mu}$-resolution for $K_{\pi\mu\mu}$ MC. Left, the residual between truth and reconstructed values, where the resolution is extracted via a Gaussian fit. Right, the resolution plotted with respect to the reconstructed z.

ture of both distributions is a flat-component where the residual difference between truth and reconstructed $z_{\mu\mu}$ large. The effect, though altering only a small number of candidates, is due to the $\pi^+\mu^+$ swaps (mis-identification of the π^+ as μ^+), described

previously. The swap-probability can be calculated using the spectrum, defined as:

$$P_{\text{swap}} = \frac{N(\text{Candidates } \geqslant \pm 5\sigma_z)}{N(\text{Total})} = 0.0026 \pm 0.0001. \tag{8.5}$$

The effect of the swaps is expected to be larger in data due to accidental rate. As the $z_{\mu\mu}$-spectrum is distorted as a result, it must be considered as a systematic source.

8.2.1.2 $N_{3\pi}$

Unlike $K_{\pi\mu\mu}$, only the integrated number of $K_{3\pi}$ candidates recorded in 2016A is required. The caveat is the observed number does not reflect the total number as the normalisation sample is recorded with a downscaled trigger. The $K_{3\pi}$ SR is defined as,

$$|M_{3\pi} - M_{K^+}| \leqslant 5\ \text{MeV/c}^2. \tag{8.6}$$

used to count events surviving the $K_{3\pi}$ selection from the Multi-track trigger. Figure 8.5 contains the number of $K_{3\pi}$ across the full 2016A period, before and after correcting for the trigger downscale. The raw number of $K_{3\pi}$ is found to be ,

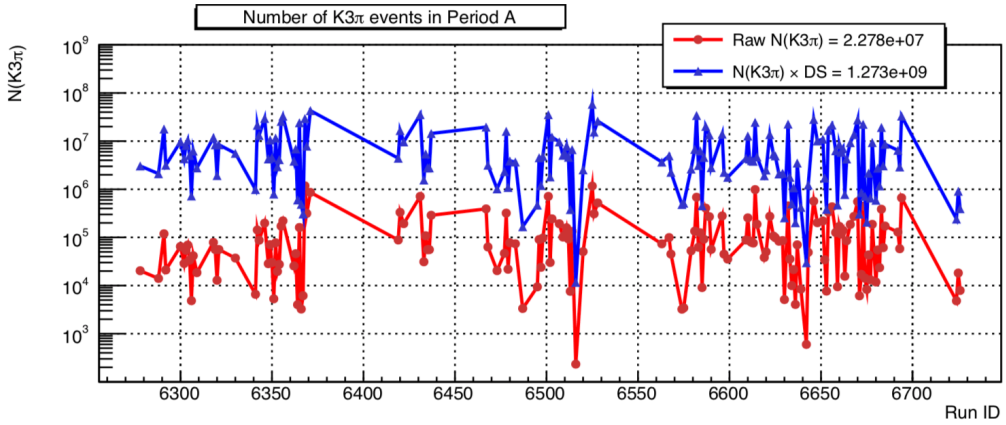

Figure 8.5: The number of observed normalisation $K_{3\pi}$ across 2016A. The red distribution accounts for the raw observed numbers, and the blue is after correcting for the normalisation trigger downscale.

$$N_{3\pi}^{\text{Raw}} = (2.278 \pm 0.001) \times 10^7 \tag{8.7}$$

and the average downscale equates to a factor of 56. The final inferred number of $K_{3\pi}$ is,

$$N_{3\pi}^{\times \mathrm{D}} = (1.273 \pm 0.001) \times 10^{9} \tag{8.8}$$

where the error is dominated by statistics.

8.2.2 Acceptances

The acceptance is a ratio defined as,

$$A = \frac{N(\text{Candidates passing selection})}{N(\text{Candidates originating in fiducial volume})}. \tag{8.9}$$

The ratio is the fraction of decays which originated in the fiducial volume between (102; 180) m that subsequently survived the full selection. It corresponds to the fraction of candidates that we can expect to observe. As acceptance can only be calculated using MC samples, the simulation was tuned in Chapter 6 to match as many of the data-taking conditions as possible, including sub-detector and intensity-dependent reconstruction effects. Additionally, a data-MC comparison has been performed in Appendix A which displays similarly good agreement for both $K_{\pi\mu\mu}$ and $K_{3\pi}$ samples.

As the acceptance for each sample depends on the residual intensity spectrum, the acceptance is calculated using a similar weighted-average technique as the trigger efficiencies in Chapter 7. A two-dimensional grid is reconstructed of $z_{\mu\mu}$ against intensity, as displayed in Figure 8.6, where each bin corresponds to the acceptance at ($z_{\mu\mu}$, $\mathcal{I}$). The acceptance is then determined at each $z_{\mu\mu}$-bin by constructing the weighted average of the twelve 100 MHz intensity bins used in the grid,

$$A_{z_{\mu\mu}} = \sum_{\mathcal{I}=0}^{12} \frac{w_{\mathcal{I}} A_{z_{\mu\mu},\mathcal{I}}}{w_{\mathcal{I}}}, \tag{8.10}$$

where $\mathcal{I}$ in the intensity-bin index, $A_{z_{\mu\mu},\mathcal{I}}$ is the acceptance at the ($z_{\mu\mu}$, $\mathcal{I}$) bin and $w_{\mathcal{I}}$ is the number of candidates in the $\mathcal{I}^{\text{th}}$ bin of the intensity-spectrum. Using the weighted average approach across the full grid results in Figure 8.7, containing A_i,

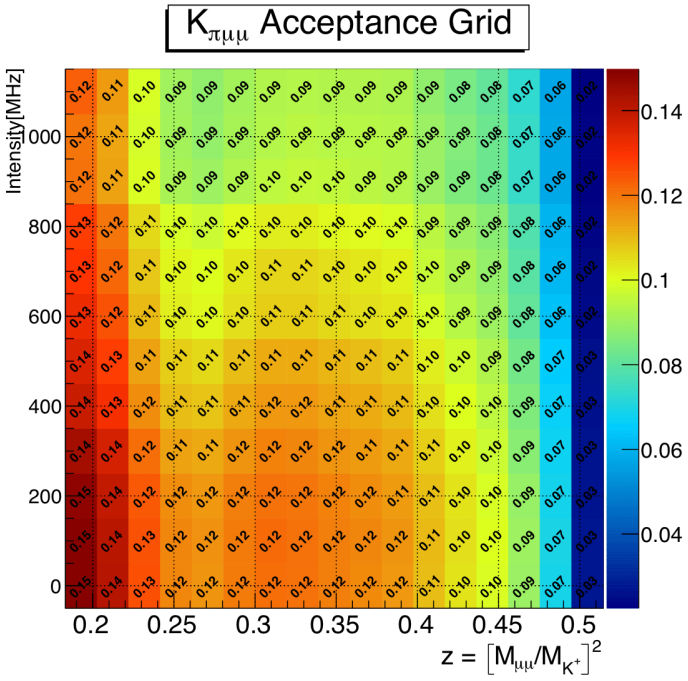

Figure 8.6: The two-dimensional $K_{\pi\mu\mu}$ acceptance grid. The diagonal labels correspond to the acceptance at each bin.

and the evolution of the $K_{\pi\mu\mu}$ acceptance from before the detector and reconstruction efficiencies were accounted for. The final corrected acceptances $A^{\mathcal{FC}}$ are:

$$A^{\mathcal{FC}}_{\pi\mu\mu} = (11.607 \pm 0.005)\%, \tag{8.11}$$

$$A^{\mathcal{FC}}_{3\pi} = (10.847 \pm 0.003)\%, \tag{8.12}$$

where $A^{\mathcal{FC}}_{\pi\mu\mu}$ is the integrated value of A_i across the full phase-space, and $A^{\mathcal{FC}}_{3\pi}$ is determined using the same weighted averaged approach but without the binning of a kinematic variable. The signal acceptance is largest at the first $z_{\mu\mu}$-bin at $\approx 15\%$, but falls off dramatically for high $z_{\mu\mu}$. The effect of the modifications due to the detector and reconstruction efficiencies is larger for $K_{\pi\mu\mu}$, as the stringent $\mu^{\pm}$ particle-identification criteria leads to a sensitivity towards the MUV3 detector efficiency, decreasing the acceptance by $\approx 0.3\%$ overall. The NewCHOD efficiency changes the acceptance in both cases by less than 0.01%. The effect of the reconstruction efficiency, decreases both acceptances by a similar magnitude to the MUV3 case, by $\approx 0.4\%$. Importantly, adding detector and reconstruction efficiencies does not dramatically change the acceptance shape with respect to $z_{\mu\mu}$; the distortion of the

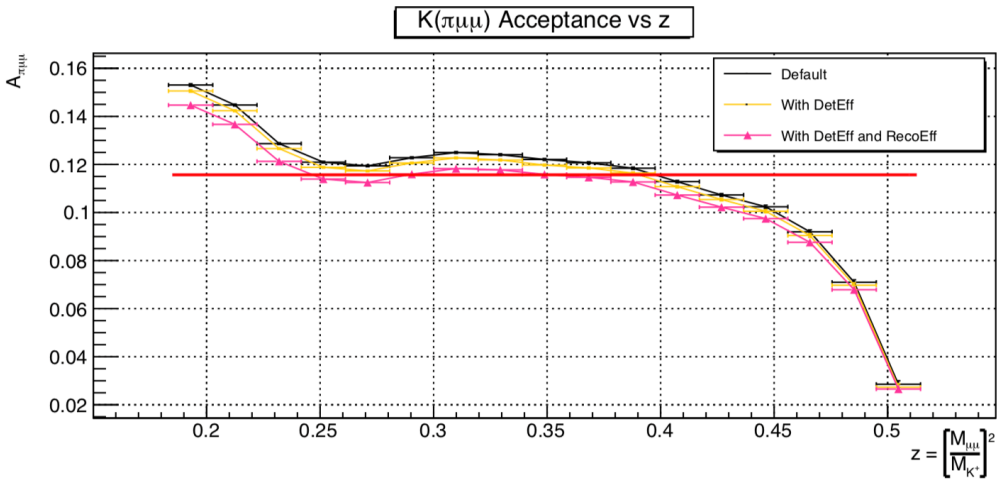

Figure 8.7: The evolution of the $K_{\pi\mu\mu}$ acceptance plotted in bins of $z_{\mu\mu}$. The black line is the acceptance measured directly from the MC sample, the orange after adding the NewCHOD and MUV3 efficiencies and the pink is the final result after adding in the reconstruction efficiency and performing the weighted average approach. No change in shape is observed.

spectrum between $0.21 \leqslant z_{\mu\mu} \leqslant 0.34$ observed in Figure 8.3 appears to be an independent effect.

8.2.3 Results

8.2.3.1 Extracting the LECs

The reconstructed $d\Gamma/dz$ against $z_{\mu\mu}$ spectrum is presented in Figure 8.8. Both distributions are identical aside from the curves, which are the result of fitting with the theoretical $d\Gamma/dz$ shape provided in Equation 8.1. The left-hand plot corresponds to positive LECs whilst the right-hand are negative, as the form factor enters into the partial rate as $|W(z)^2|$. The spectrum has been corrected for the Coulomb factor Ω_C, shifting the distribution down by approximately 3% across the phase-space, but most dramatically in the first $z_{\mu\mu}$-bin. Additionally, the effective z_i values where $d\Gamma/dz$ is evaluated has been corrected to account for the effects of using large bin-widths. As the underlying PDF has a shape that can vary rapidly within a large bin, instead of placing z_i at the bin-centre or bin barycentre, we evaluate for each bin,

$$\mathcal{F}(z_{lw}) = \frac{1}{\Delta z}\int_{z_1}^{z_2} \mathcal{F}(z_i)dz, \tag{8.13}$$

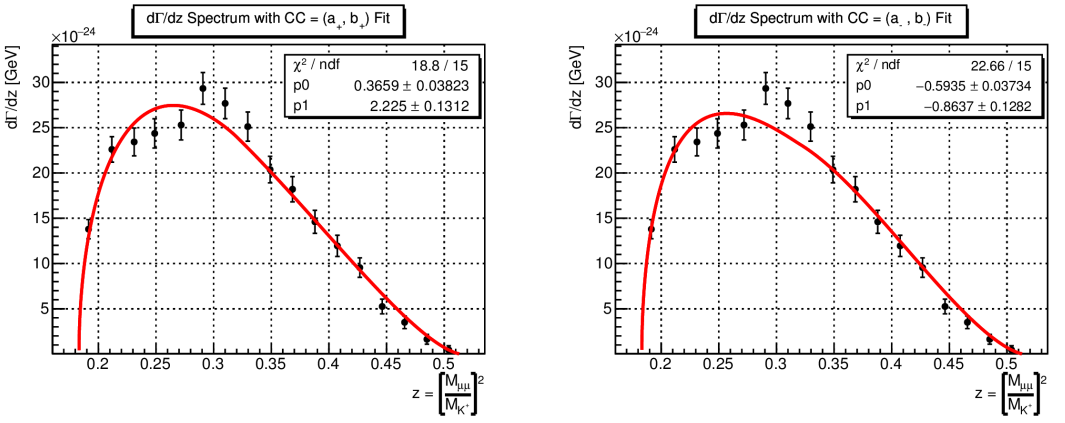

Figure 8.8: The reconstructed $d\Gamma/dz$ vs. $z_{\mu\mu}$ spectrum for 2016A. Left, the positive form factor solution and right, the negative form factor solution. The positive case is preferred according to the fit χ^2.

where $\mathcal{F}(z)$ is the prediction of the underlying PDF based on the NA48/2 measurement (i.e $d\Gamma/dz$), Δz is the bin-width, $z_{1,2}$ are the lower and upper bin edges and z_{lw} is the true data-point position for bins of large-width [87]. To extract the model-independent branching fraction, the $d\Gamma/dz$ spectrum is integrated directly and normalised to the K^+ decay width ($\hbar/\tau_{K^+}$) without the Coulomb correction applied,

$$\mathcal{B}(K^+ \to \pi^+\mu^-\mu^-) = (10.429 \pm 0.203_{\text{stat}} \pm 0.192_{\text{syst}} \pm 0.045_{\text{ext}}) \times 10^{-8}, \qquad (8.14)$$

which is $\approx 2\sigma$ larger than the NA48/2 and PDG-combined measurement. Despite an improved statistical error due to the suppression of the background component, the systematic error is almost twice the size of the previous measurement, dominated by the $z_{\mu\mu}$-spectrum distortion. This is discussed further in Section 8.2.4.

To extract the LECs, the result can be presented in two-dimensional (a_+, b_+) space versus the fit χ^2, as displayed in Figure 8.9. Here, the minima are represented by the yellow and grey stars, where yellow has the lowest χ^2. Contours are displayed for both, representing three standard-deviations. This leads to two sets of LECs presented in Table 8.2, where the positive solution is preferred by $\Delta\chi^2 = 3.9$. The systematic errors dominate over the statistical, again largely due to the $z_{\mu\mu}-$distortion. Whilst the positive solution is preferred, only the negative can be compared with NA48/2 where the NA62 measurement is in agreement to one standard-deviation

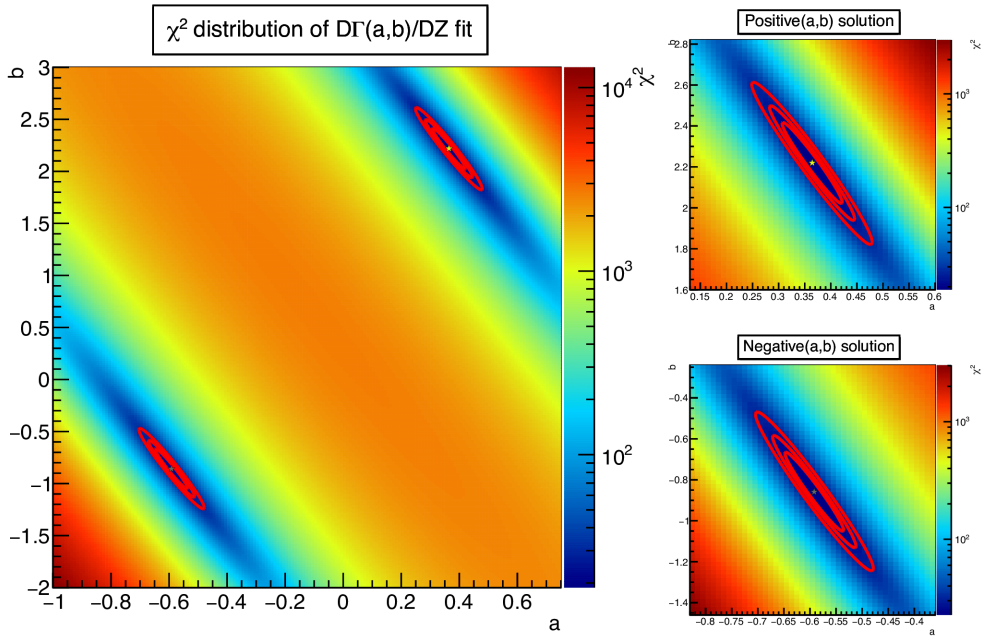

Figure 8.9: The two-dimensional representation of the form factor extraction of (a_+, b_+) versus fit χ^2. The yellow and grey stars represent the minima, with the yellow case being the lowest χ^2. The contours represent the first three standard-deviations from the minima.

Table 8.2: The LECs in 2016A, included statistical, systematic and external errors. The positive solution is statistically preferred by $\Delta\chi^2$ = 3.9.

Sign	LEC	Value	χ^2/NDF
Positive	a_+	$0.366 \pm 0.038_{\text{stat}} \pm 0.050_{\text{syst}} \pm 0.001_{\text{ext}}$	18.8/15
	b_+	$2.220 \pm 0.131_{\text{stat}} \pm 0.184_{\text{syst}} \pm 0.004_{\text{ext}}$	
Negative	a_+	$-0.594 \pm 0.037_{\text{stat}} \pm 0.048_{\text{syst}} \pm 0.001_{\text{ext}}$	22.7/15
	b_+	$-0.864 \pm 0.128_{\text{stat}} \pm 0.175_{\text{syst}} \pm 0.004_{\text{ext}}$	

for both parameters.

8.2.4 Systematics

To compare the measurement with previous analyses, a detailed study of the systematic effects has been undertaken. The systematic and external errors presented in the final measurement above are described here. Any variable that enters into the reconstruction of $d\Gamma/dz$ can be considered a source of systematic error and therefore, we break down the type of systematic into categories:

- Trigger Efficiency: As discussed in Chapter 7, the method used to obtain the $K_{\pi\mu\mu}$ efficiencies lead to systematic terms,

- RICH: The largest effect here is the disagreement between the primitive and emulator efficiency. The systematic is taken from the maximum shape fluctuation of the primitive efficiency from the average.
- Q_X: The systematic difference between the measured primitive efficiency and the MCA emulated weighted-average approach was estimated by comparing the efficiency versus the $z_{\pi^+\pi^-}$ spectra for $K_{3\pi}$ candidates.
- MO_2: As the efficiency versus $z_{\mu\mu}$ distribution is extracted from $K_{3\pi\to\pi\mu\mu}$ decays, the efficiency distribution covers a small phase-space region than for signal $K_{\pi\mu\mu}$. The systematic is estimated by determining how different models of extrapolation (flat, linear) affect the final measurements.
- !LAV: Similarly to Q_X, The systematic difference between the measured primitive efficiency and the MCA emulated weighted-average approach was estimated by comparing the efficiency versus the $z_{\pi^+\pi^-}$ spectra for $K_{3\pi}$ candidates. Note that hadronic simulations are the largest issue, and are expected to be a smaller effect for $K_{\pi\mu\mu}$ than for $K_{3\pi}$.
- $STRAW_e$: The only non-negligible contribution is due to the limitation of the momentum-efficiency model. The systematic is taken from the maximum deviation between the data and fit at $P(\pi^-)$ = 35 GeV/c.

- Acceptances also have a number of sources,
  - The distortion observed in the $z_{\mu\mu}$-spectrum between $0.21 \leqslant z_{\mu\mu} \leqslant 0.34$ was not explained by reconstruction, detector or trigger-efficiency effects and so is taken as a systematic. The effect is estimated by deliberately pulling the $K_{\pi\mu\mu}$ acceptance distribution, estimated using the shape-difference between the data spectrum and trigger-corrected MC distribution, where the latter is scaled to match the number of data events. The expected number is not used to avoid bias, as the error would therefore account for any differences between the final values obtained between NA48/2 and NA62. This is the largest systematic in the analysis.
  - The statistical error of the $K_{3\pi}$ acceptance is treated as a systematic.
  - The errors on the detector tile-efficiencies and data/MC reconstruction ratio enter as a systematic effect, estimated by comparing the standard accep-

tance with one where the efficiencies were Gaussian-smeared based on the statistical error at each tile or momentum bin.

- Systematics due to background,
  - RooFit provides the error in the expected number of background.
  - Additionally, as the background shape inferred and not reliably known, we also estimate the effect of a completely flat-background contribution set at the scale of N_B instead of the prediction based on TRIM5 or low-mass tail events.
- Systematics due to bin properties,
  - The non-negligible resolution on the $z_{\mu\mu}$ variable means that bin-migration is possible. The effect of this is simulated by Gaussian smearing the data sample by the resolution to calculate the systematic difference.
  - The effect of μ^+ mis-identification is also considered, which appear as $\pi^+\mu^+$ swaps in the data sample. The swap-probability was determined based on the resolution spectrum (Equation 8.5), and scaled to match data by estimating the ratio of in-time MUV3 associations for three-track events between data and MC, found to a 10% effect. Approximately 7 mis-identified candidates are predicted for this data sample. The effect was estimated by randomly selecting candidates (using the swap-probability) and assigning a random $z_{\mu\mu}$ value instead of the measurement anywhere in the available phase-space. The difference observed in the calculation is taken as the systematic error.
- The effect of external measurements,
  - The measurement of the $K_{3\pi}$ branching fraction is an external parameter. The error in this measurement has decreased by 3% since the NA48/2 analysis.
  - Form factor only: the K^+ lifetime cancels for the branching fraction calculation (as the integral is divided by $\hbar/\tau_{K^+}$), but not for the form factor fit. The precision of the lifetime is $\approx 0.2\%$.

– Form factor only: the chosen data-point position in $z_{\mu\mu}$, corrected for the effect of large bin-widths, takes input from the NA48/2 measurement. The error in the position is taken from the overall error in those parameters and is only available for one sign of solution, as the previous measurement omits the positive LECs.

The size of the systematic contribution to the branching fraction due each source is presented in Table 8.3. The largest systematic effect is due to the estimation of the $z_{\mu\mu}$-spectrum distortion, followed by the trigger efficiency systematics and the external measurement of the $K_{3\pi}$ branching fraction. For the form factor, the systematic contributions to the positive solution LECs are presented in Table 8.4, and the negative solution in Table 8.5. Like for the branching fraction, the $z_{\mu\mu}$-distortion effect is the largest term and as it drastically affects the shape of the spectrum, it is the dominant error term overall. The effect is therefore likely to be the determining factor in which sign of solution is statistically preffered. Additionally, the positive solutions have slightly larger error terms due to the nature of the χ^2 shape, which increases more slowly than for the negative case.

Table 8.3: Systematic contributions to the 2016A $K_{\pi\mu\mu}$ model-independent branching fraction measurement. The errors are split into categories and are factors of 10^{-8}.

Type	Systematic	$\sigma\mathcal{B}_{\text{syst}}$ $[10^{-8}]$ up	down
Trigger	RICH	0.063	-0.064
	Q_X	0.059	-0.060
	MO_2	0.005	-0.005
	!LAV	0.074	-0.075
	$STRAW_e$	0.054	-0.054
Acceptance	$A_{\pi\mu\mu}$ distortion	0.141	-0.141
	$A_{3\pi}$	0.003	-0.003
	Detector efficiency	0.033	-0.033
Background	N_B	0.000	0.000
	N_B shape	0.000	0.000
Binning	Resolution (z)	0.003	-0.0003
	$\pi^+\mu^+$ swap	0.000	0.000
External	$\mathcal{B}(K_{3\pi})$	0.045	-0.045
Total		0.192	-0.192

Table 8.4: Systematic contributions to the 2016A positive solution. The errors are split into categories and measured for their effect on the measurement both up and down.

Type	Systematic	σa_{syst}		σb_{syst}	
		up	down	up	down
Trigger	RICH	0.0015	-0.0015	0.0047	-0.0047
	Q_X	0.0014	-0.0014	0.0044	-0.0044
	MO_2	0.0031	-0.0031	-0.0096	0.0096
	!LAV	0.0017	-0.0017	0.0055	-0.0055
	$STRAW_e$	0.0012	-0.0012	0.0041	-0.0041
Acceptance	$A_{\pi\mu\mu}$ distortion	0.0491	-0.0491	-0.1818	0.1818
	$A_{3\pi}$	0.0000	0.0000	0.0002	-0.0002
	Detector efficiency	0.0023	-0.0023	-0.0029	0.0029
Background	N_B	0.0000	0.0000	0.0001	0.0001
	N_B shape	0.0003	-0.0003	-0.0012	0.0012
Binning	Resolution (z)	0.0065	-0.0065	-0.0211	0.0211
	$\pi^+\mu^+$ swap	0.0045	-0.0045	-0.0153	0.0153
External	K^+ Lifetime	0.0004	-0.0004	0.0013	-0.0013
	$\boldsymbol{\mathcal{B}}(K_{3\pi})$	0.0010	-0.0010	0.0033	-0.0033
	Data point position	0.0005	-0.0005	0.0023	-0.0012
Total		0.0500	-0.0500	0.1840	-0.1840

Table 8.5: Systematic contributions to the 2016A negative solution. The errors are split into categories and measured for their effect on the measurement both up and down.

Type	Systematic	σa_{syst}		σb_{syst}	
		up	down	up	down
Trigger	RICH	0.0015	-0.0015	0.0047	-0.0047
	Q_X	0.0014	-0.0014	0.0043	-0.0043
	MO_2	0.0030	-0.0030	-0.0094	0.0094
	!LAV	0.0017	-0.0017	0.0055	-0.0054
	$STRAW_e$	-0.0012	0.0012	0.0041	-0.0041
Acceptance	$A_{\pi\mu\mu}$ distortion	0.0465	-0.0465	-0.1721	0.1721
	$A_{3\pi}$	0.0000	0.0000	0.0002	-0.0002
	Detector efficiency	0.0023	-0.0023	-0.0029	0.0029
Background	N_B	0.0000	0.0000	0.0000	0.0000
	N_B shape	0.0003	-0.0003	-0.0011	0.0011
Binning	Resolution (z)	0.0062	-0.0062	-0.0203	0.0203
	$\pi^+\mu^+$ swap	0.0046	-0.0046	-0.0161	0.0161
External	K^+ Lifetime	0.0004	-0.0004	0.0013	-0.0013
	$\boldsymbol{\mathcal{B}}(K_{3\pi})$	0.0010	-0.0010	0.0033	-0.0033
	Data point position	0.0004	-0.0004	0.0011	-0.0009
Total		0.0475	-0.0475	0.1750	-0.1750

9

Future prospects

In this chapter, the future prospects of the $K^+ \to \pi^+\mu^+\mu^-(K_{\pi\mu\mu})$ analysis at NA62 are explored. As explained in Chapter 7, a number of flaws were discovered in the Trigger and Data Acquisition (TDAQ) in the 2016 data. As a result, a number of large systematic errors reduced the precision of the measurements. With efforts made by experts to rectify these issues, both the form factor and branching fraction of the $K_{\pi\mu\mu}$ decay are measured for 2017A, using an identical analysis approach to 2016A. By comparing the difference in the systematic effects, the prospects of performing the world's most precise measurement of the $K_{\pi\mu\mu}$ are described below.

9.1 Strategy

In order to probe the future prospects of the $K_{\pi\mu\mu}$ measurement, the analysis must be repeated using the 2017A data set. In general, the 2017A data set can provide an insight to how the current selection strategy handles more challenging beam conditions, and how changes to the TDAQ relative to 2016A can reduce systematic errors. There are three important aspects to consider:

- **Signal to background:** the average instantaneous intensity for 2017 is 400.3 MHz, almost 130 MHz larger than the average for the 2016A data set. As a result, the accidentals contribution is expected to be larger, possibly leading to a non-negligible background component for the $K_{\pi\mu\mu}$ sample.
- **Spectrum distortion:** A systematic distortion of six bins of kinematic $z_{\mu\mu}$ spec-

trum in the region $0.21 \leqslant z_{\mu\mu} \leqslant 0.34$ lead to the largest systematic error in the whole of the 2016 analysis. The spectrum for 2017A must also be investigated.

- **Trigger efficiency:** Another large systematic contribution, much of the 2016A trigger was found to be flawed for the $K_{\pi\mu\mu}$ analysis. In 2017A, many of the inefficiencies have been rectified and the impact of the improvements must be assessed.

Below, each of the three aspects is explored in detail. Section 9.2 contains the 2017A $K_{\pi\mu\mu}$ and $K_{3\pi}$ samples, including an estimate of the 2017A background contamination and an investigation of the $z_{\mu\mu}$ spectrum. The trigger efficiency is evaluated in Section 9.3 and compared to 2016A values. Finally, the branching fraction and form factor LECs for the 2017A data set is provided in Section 9.5, focusing specifically on the same systematic errors that were relevant for the previous year.

9.2 Event sample

As described in Section 6.2, the 2017A sample is roughly the same size as 2016A, with $\approx$ 83000 reconstructed bursts available for analysis. The size of the sample is expected to increase by a factor $\approx$ 5 by the end of summer 2018 after the full data reprocessing is complete. The normalisation ($K_{3\pi}$) and signal ($K_{\pi\mu\mu}$) samples were collected with two different trigger streams that were reconfigured with respect to 2016:

- **Multi-track trigger (2017A):** RICH$\cdot$ $Q_X \rightarrow$ KTAG $\rightarrow$ STRAW$_e$,
- **Dimuon trigger (2017A):** RICH$\cdot$ $Q_X \cdot$ MO$_2 \rightarrow$ STRAW$_e$.

At L$_0$, all primitive generating firmware was improved, including a fix for the quadrant-dependent flaw in the NewCHOD described in Chapter 7. At L$_1$, the !LAV algorithm was removed from both triggers, and the KTAG algorithm removed from just the dimuon trigger so that exotic decays could be collected through the same stream. Due to the data-acquisition rates in 2017, the Multi-track trigger used a fixed $D = 100$ for all runs, whilst the Dimuon trigger was downscaled by a factor $D = 2$. Of the available $\approx$ 83,000 bursts, only $\approx$ 68,000 are used in this study, cho-

sen for where both the Multi-track and Dimuon triggers were performing nominally.

Using the final selection as presented in Section 6.5, the 2017A signal and normalisation spectra are displayed in Figure 9.1 For normalisation $K_{3\pi}$, the distribution is

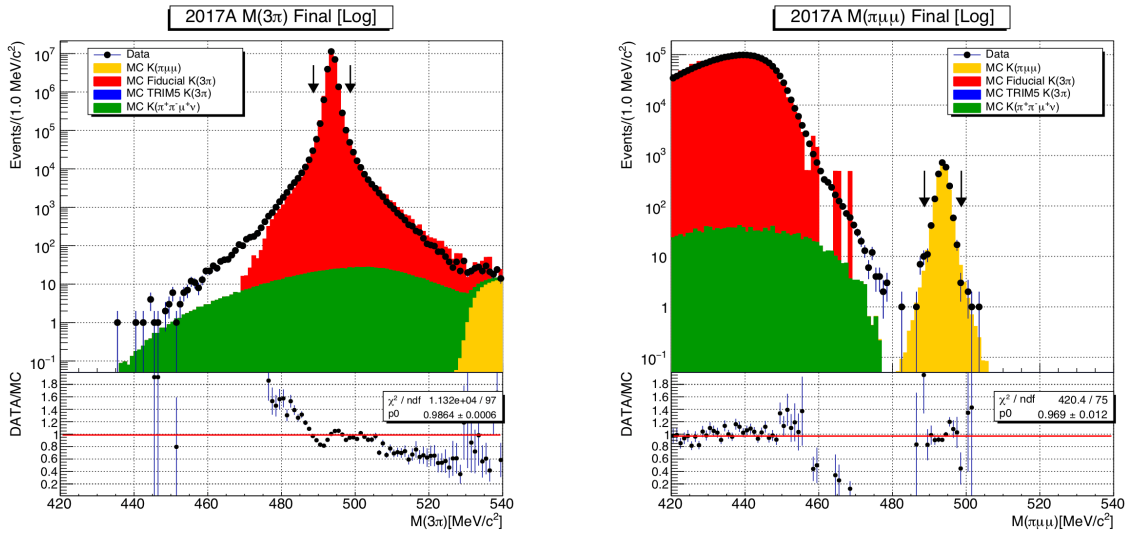

(a) (b)

Figure 9.1: The (a) $K_{3\pi}$ and (b) $K_{\pi\mu\mu}$ spectra for 2017A in log-scale, with the SRs. The bottom pad shows the data-MC agreement based on the expected yields.

similarly as clean as 2016 (with background contamination $\approx 0.1\%$), with excellent MC agreement within the SR. The size of the sample is equivalent to:

$$N_{3\pi}^{2017} = (2.433 \pm 0.001) \times 10^7 \tag{9.1}$$

which corresponds to 2.433×10^9 $K_{3\pi}$ decays when accounting for the downscaling. The $K_{\pi\mu\mu}$ sample is equally as promising, with no candidates in the upper mass sidebands and a reasonably well-separated signal to background peak. Using the RooFit package in an identical fashion to the 2016A analysis (see Section 8.2.1), (a) of Figure 9.2 displays the total PDF describing the spectrum. The total number of candidates collected in a SR defined as $|M_{\pi\mu\mu} - 493.705| \leqslant 5\,\mathrm{MeV/c^2}$ is,

$$N_{\pi\mu\mu}^{2017} = 2260. \tag{9.2}$$

Which is equivalent to 4520 candidates when accounting for the downscale. Notably, the 2017A PDF is missing a high-mass component which was used in 2016

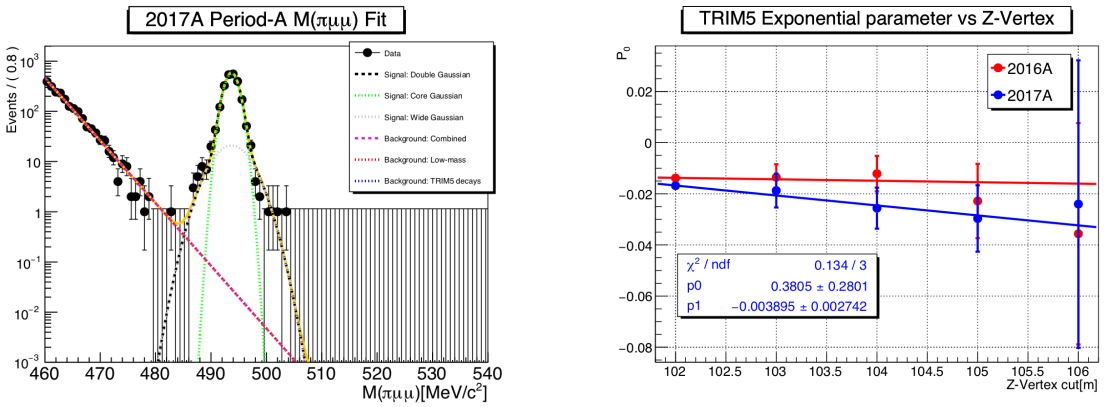

(a) (b)

Figure 9.2: The 2017A RooFit PDF in (a) for the $M_{\pi\mu\mu}$ spectrum and in (b), a comparison of the TRIM5 slope extraction between 2016 and 2017.

to describe the contribution from upstream decays. This component is predicted in RooFit to be entering at the $\mathcal{O}(10^{-5})$, which is four orders of magnitude smaller compared to the previous year. This is mostly due to the smaller statistics, but also because the slope which is extracted from the data with relaxed Z-Vertex cuts is steeper. In (b) of Figure 9.2, the slope parameter p_0 of this component versus increasing Z-Vertex cuts is presented for 2017A, with the 2016A data-points displayed for comparison. The 2017A slope is not consistent with zero, such that RooFit does not find a suitable solution for this level of statistics with the gradient at Z-Vertex = 110 m.

The largest systematic error in 2016 was attributed to the apparent distortion of the kinematic $z_{\mu\mu}$ variable of six bins between $0.21 \leqslant z_{\mu\mu} \leqslant 0.34$. Figure 9.3 displays the 2017A $z_{\mu\mu}$ spectrum including a comparison to the MC expectation. Of the seventeen bins, six are deviated by 1σ and one by 2σ which is within expectation of statistical fluctuation. Importantly, the deviations are not in neighbouring bins, suggesting that this sample does not suffer from the effect seen in the previous year. However, this must be verified in the future by analysing the full 2017 data set when the reconstructed data is available.

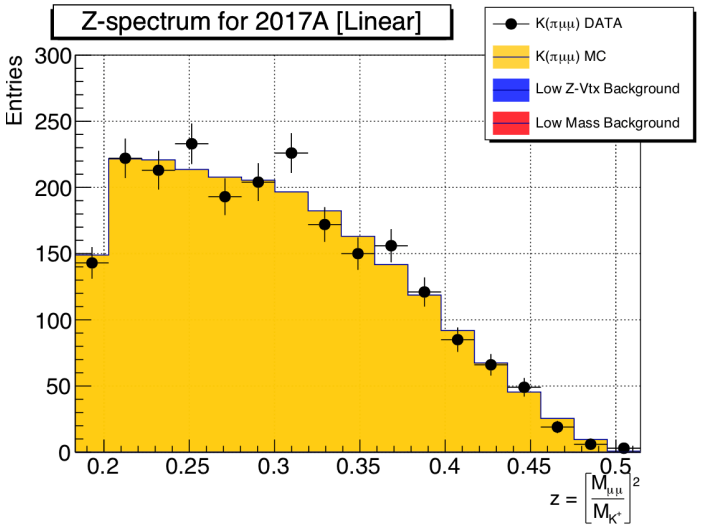

Figure 9.3: The 2017A reconstructed $z_{\mu\mu}$ spectra compared to MC expectation.

9.3 Trigger efficiency

9.4 Comparison to 2016

In 2017, the NA62 TDAQ was re-optimised for multi-track decays. The improvements lead to the observation of higher trigger efficiencies with respect to 2016. The difference is summarised quantitatively in Table 9.1 for $K_{3\pi}$ decays, whilst Figure 9.4 displays the 2017A efficiencies with respect to time and instantaneous intensity. The

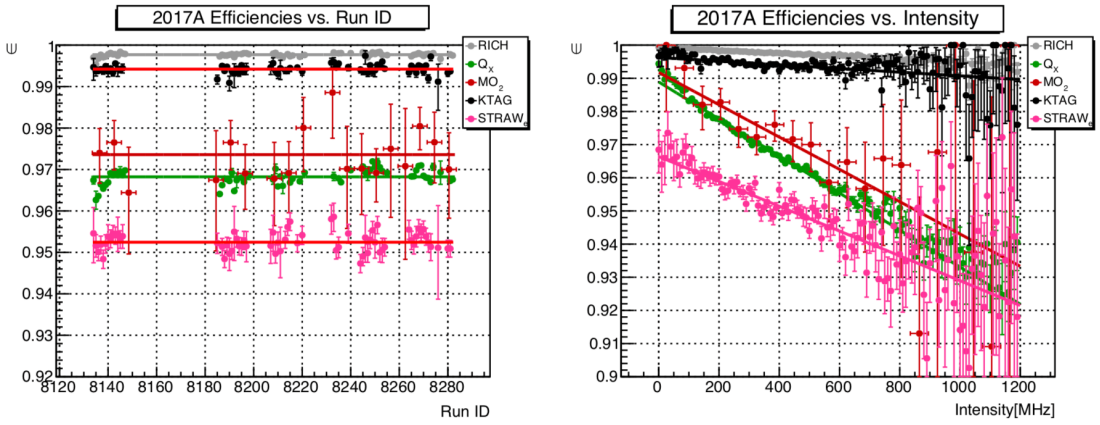

Figure 9.4: The L_0 and L_1 trigger efficiencies in 2017, with left with respect to time and right versus intensity. L_0 are determined using the min-bias control trigger $K_{3\pi}$ and L_1 using multi-track autopass. The MO_2 primitive measurement uses $K_{3\pi} \to \pi^+\mu^+\mu^-$ as an equivalent to $K_{\pi\mu\mu}$ signal.

most obvious improvement is the absence of !LAV, increasing the overall efficiency

Table 9.1: Comparing 2016 and 2017 L_0 and L_1 efficiencies using $K_{3\pi}$ decays. The MO_2 primitive uses $K_{3\pi} \to \pi^+\mu^+\mu^-$ as an equivalent to $K_{\pi\mu\mu}$ signal. The Q_X efficiency has increased by almost 10%, while the !LAV is no longer present. The errors are statistical only; the magnitude reflects the large size of the 2017A sample.

Primitive/Algorithm	2016A	2017A
RICH	$0.9863 \pm 0.0002_{\text{stat}}$	$0.9977 \pm 0.0000_{\text{stat}}$
Q_X	$0.8740 \pm 0.0005_{\text{stat}}$	$0.9682 \pm 0.0001_{\text{stat}}$
MO_2	$0.9787 \pm 0.0006_{\text{stat}}$	$0.9850 \pm 0.0005_{\text{stat}}$
KTAG	$0.9802 \pm 0.0002_{\text{stat}}$	$0.9942 \pm 0.0002_{\text{stat}}$
!LAV	$0.8056 \pm 0.0005_{\text{stat}}$	-
$STRAW_e$	$0.9587 \pm 0.0003_{\text{stat}}$	$0.9525 \pm 0.0002_{\text{stat}}$

by 20%. The Q_X improvement is also large, with a 10% improvement. In general, each other trigger component (except $STRAW_e$) is more efficient by $\approx 1\%$. Overall, for multi-track $K_{3\pi}$, the overall efficiency $\epsilon_{3\pi}$ increases from $\approx 65.9\%$ to 91.5% from 2016 to 2017.

9.4.1 Emulator performance

In terms of the measurement of $K_{\pi\mu\mu}$, both the RICH and Q_X trigger emulators are needed to convert the efficiency from $K_{3\pi}$ decays. Figure 9.5 displays the difference between the emulated and the online primitive efficiencies for $K_{3\pi}$ data for both trigger components. The RICH in (a) displays a vast improvement relatively from

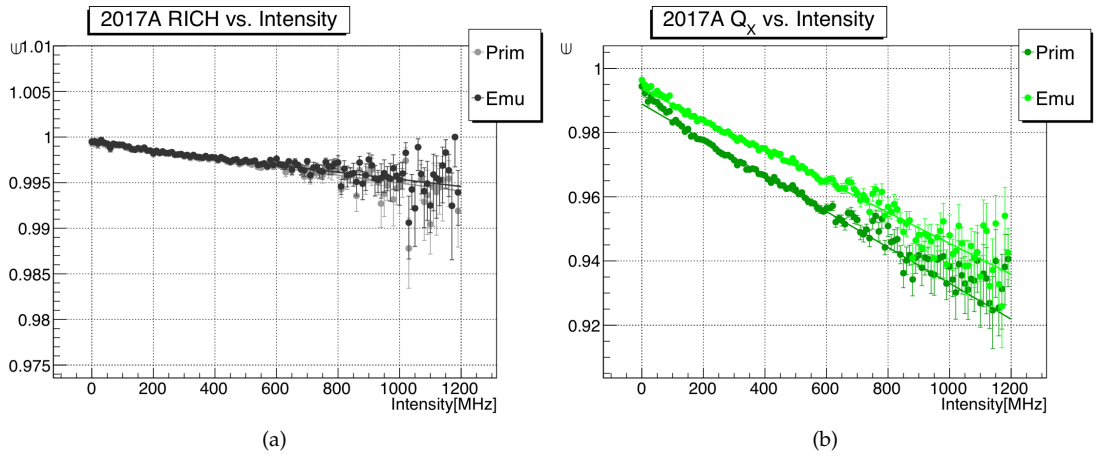

(a) (b)

Figure 9.5: Comparing 2017A RICH and Q_X primitive and emulated efficiencies; (a) is for RICH and (b) for Q_X, where the latter shows an $\approx$1% disagreement.

2016. As the RICH firmware was more refined in 2017, the intensity distortion that was observed in the previous year is absent, leading to an excellent agreement be-

tween the online and emulated efficiencies. For Q_X, the largest geometric-related component of the inefficiency was fixed. However, $\approx 1\%$ discrepancy is observed between the online and emulated primitives in (b). As the efficiency is no longer dependent on the hit-ordering, the emulator hits cannot be reshuffled as they were in 2016. From other studies, it is understood that the discrepancy is present for any primitive which requires more than one NewCHOD hit [88]. As a result, the MCA approach remains the most suitable for the $K_{\pi\mu\mu}$ determination of Q_X. Figure 9.6 contains two distributions; (a) contains the validity of the approach, with the Q_X efficiency plotted versus kinematic $z_{\pi_+\pi_-}$ for both the MCA approach and the online primitives. In (b), is the $K_{\pi\mu\mu}$ equivalent, with the MCA efficiency versus $z_{\mu\mu}$ which is used directly in the $d\Gamma/dz$ reconstruction. The kinematic dependence of the on-

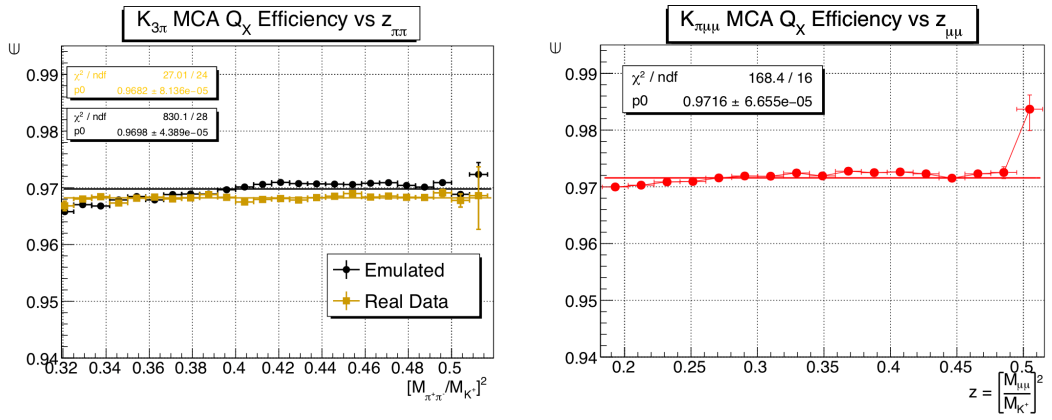

(a) (b)

Figure 9.6: Reconstructing the 2017A MCA Q_X efficiency for (a) $K_{3\pi}$ versus $z_{\pi^+\pi^-}$ where it can be compared directly to the online primitive distribution, and (b) $K_{\pi\mu\mu}$ versus $z_{\mu\mu}$ which is used directly in the analysis. The overall efficiency is $\approx 10\%$ higher with respect to 2016.

line primitive is flatter than the emulator. Despite the emulator disagreeing by $\approx 1\%$ when used on the data, the MCA efficiency agrees to within 0.1%. As this is similar to 2016, a systematic of 0.5% is adopted. Additionally, the two kinematic distributions are very similar, with the $K_{\pi\mu\mu}$ efficiency slightly higher on average than for $K_{3\pi}$.

In summary, the vast improvement in the RICH agreement and the lack of LAV removes or reduces two of the three largest systematic errors relating to the trigger efficiency for the rare-physics analysis, such that the 2017 data can be seen as the

superior data set from the perspective of the TDAQ. The final 2017 $K_{\pi\mu\mu}$ efficiency is presented in the left side of Figure 9.7 in bins of $z_{\mu\mu}$, which is the product the individual components displayed in the right hand side. The scale of the plot is

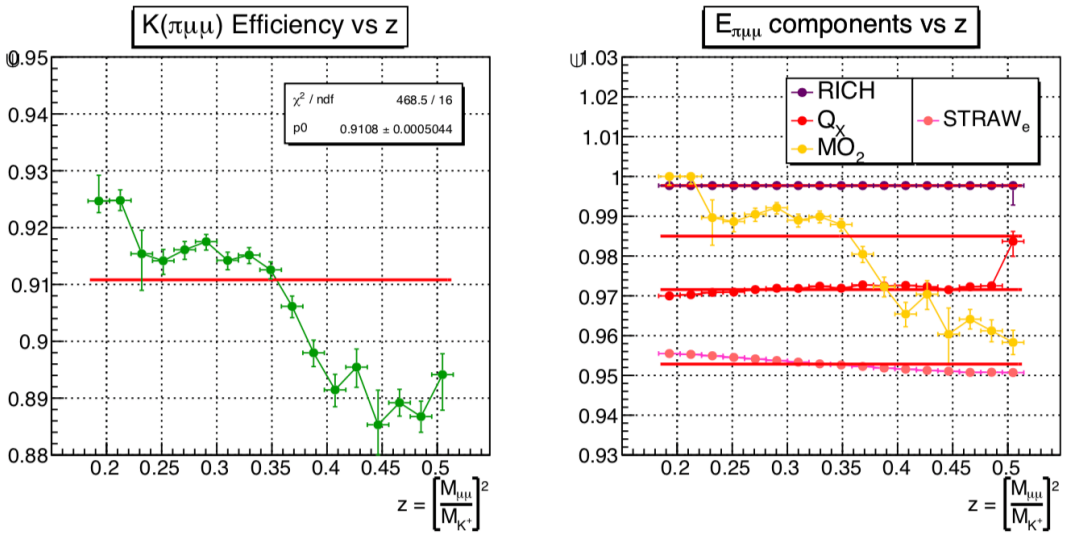

Figure 9.7: The overall $K_{\pi\mu\mu}$ efficiency spectra vs $z_{\mu\mu}$ in 2017A. Left, the combined efficiencies and right, the individual components. The scale is dominated by STRAW$_e$ and the shape is dominated by the MO$_2$ kinematic dependence, the same as observed in 2016.

dominated by the STRAW$_e$ measurement, whilst the shape reflects the kinematic dependence of the MO$_2$ primitive. The trend of the distribution is strikingly similar to 2016, but the average efficiency is $\approx$ 91.1%, which is 24% greater than for the previous year.

9.5 Result

Using the exact same methodology described in Chapter 8, the $d\Gamma/dz$ versus $z_{\mu\mu}$ spectrum was reconstructed and fitted using the theoretical PDF. Figure 9.8 contains the result of the procedure. Again, the model-independent branching fraction is obtained by integrating the spectrum directly in the absence of the Coulomb corrections and normalising to the K^+ decay-width:

$$\mathcal{B} = (9.637 \pm 0.206_{\text{stat}} \pm 0.074_{\text{syst}} \pm 0.041_{\text{ext}}) \times 10^{-8}, \tag{9.3}$$

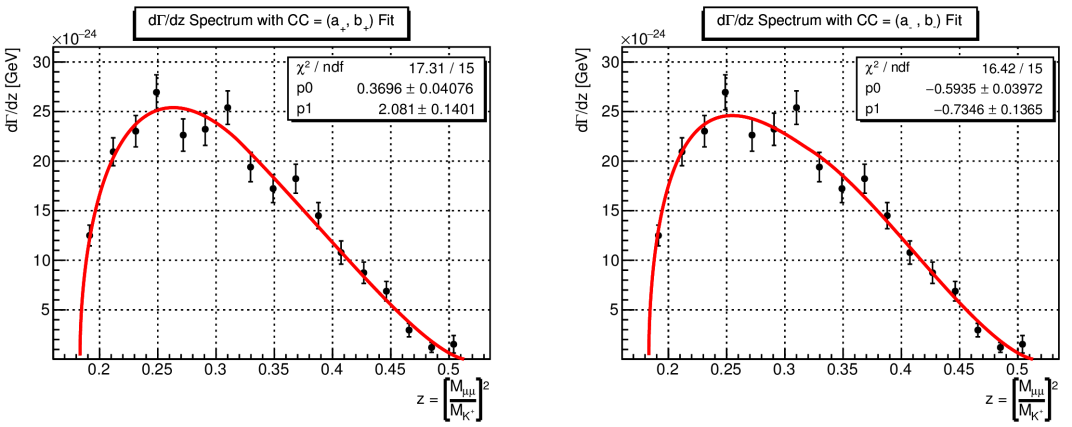

Figure 9.8: The reconstructed $d\Gamma/dz$ vs. $z_{\mu\mu}$ spectrum for 2017A. Left, the positive form factor solution and right, the negative form factor solution. The χ^2/NDF is smaller than for 2016A, with the negative solution preferred by $\Delta\chi^2 = 0.9$.

which is within 1σ of the both the NA48/2 measurement and the global fit [55]. The 2017A LECs are extracted with the coulomb corrected spectra and are contained in Table 9.2: Again, the negative LECs are within 1σ of the previous measurement.

Table 9.2: The LECs in 2017A, included statistical, systematic and external errors. The negative solution is statistically preferred by $\Delta\chi^2 = 0.9$.

Sign	LEC	Value	χ^2/NDF
Positive	a_+	$0.370 \pm 0.041_{\text{stat}} \pm 0.006_{\text{syst}} \pm 0.001_{\text{ext}}$	17.3/15
	b_+	$2.080 \pm 0.140_{\text{stat}} \pm 0.017_{\text{syst}} \pm 0.005_{\text{ext}}$	
Negative	a_+	$-0.593 \pm 0.040_{\text{stat}} \pm 0.006_{\text{syst}} \pm 0.001_{\text{ext}}$	16.4/15
	b_+	$-0.735 \pm 0.137_{\text{stat}} \pm 0.018_{\text{syst}} \pm 0.005_{\text{ext}}$	

In 2017, the difference between the two solutions is far smaller, with the negative solution being preferred by $\Delta\chi^2 = 0.9$. Using the approach outlined in Section 8.2.4 for 2016, the same systematics have been estimated for 2017A to simply compare the effect of the improvements discussed in the above sections. The magnitude of the largest systematics is either drastically reduced or absent with respect to 2016, such that the statistical errors are by far the largest uncertainties in the measurement. Without the flaws in the trigger and the absence of a spectrum distortion, the largest systematic term for both measurements is the MO_2 efficiency extrapolation which will be improved with larger data-set. Whilst a more careful approach is needed in the 2017A analysis because the considered systematics are now small with respect to the statistical error, they are at the correct order of magnitude required to compete

with B-physics if a sample of the $\mathcal{O}(10^5)$ $K_{\pi\mu\mu}$ decays is collected. It is expected that with the full 2017 and 2018 data-sets, the analysis is well-suited to begin to approach these targets.

10

Conclusions

In this thesis, the 2016A data set from the NA62 experiment has been used to measure the branching fraction $\mathcal{B}$ of the $K^+ \to \pi^+\mu^+\mu^-$ decay and extract the low-energy constants (LECs) (a_+, b_+) of the transition form factor $W(z)$. In total, 2676 suitable candidates were collected with a negligible background, obtaining:

$$\mathcal{B} = (10.429 \pm 0.203_{\text{stat}} \pm 0.192_{\text{syst}} \pm 0.045_{\text{ext}}) \times 10^{-8}, \tag{10.1}$$

$$a_+ = 0.366 \pm 0.038_{\text{stat}} \pm 0.050_{\text{syst}} \pm 0.001_{\text{ext}} \tag{10.2}$$

$$b_+ = 2.220 \pm 0.131_{\text{stat}} \pm 0.184_{\text{syst}} \pm 0.004_{\text{ext}} \tag{10.3}$$

where the branching fraction is 10% larger than the previous measurements, but consistent to within two standard deviations. The positive LECs are preferred over the negative solutions by $\Delta\chi^2 = 3.9$. The error in the branching fraction is dominated by limited statistics, but contains a systematic contribution that is a similar order of magnitude. This is mostly because of the notably distorted $z_{\mu\mu}$-spectrum and the complicated nature of the trigger inefficiency. One of the major contributions of this thesis is the understanding of the 2016A trigger inefficiencies and how they can be handled in future analyses. In the case of the LECs, the $z_{\mu\mu}$-distortion is the largest systematic contribution and dominates instead of the statistical term.

In 2017, a new and improved data set was recorded, where most of the dominant systematic errors in the 2016A analysis were either removed or suppressed. In total,

2260 suitable background-free candidates were collected, obtaining:

$$\mathcal{B} = (9.637 \pm 0.206_{\text{stat}} \pm 0.074_{\text{syst}} \pm 0.041_{\text{ext}}) \times 10^{-8}, \tag{10.4}$$

$$a_+ = -0.593 \pm 0.040_{\text{stat}} \pm 0.006_{\text{syst}} \pm 0.001_{\text{ext}} \tag{10.5}$$

$$b_+ = -0.735 \pm 0.137_{\text{stat}} \pm 0.018_{\text{syst}} \pm 0.005_{\text{ext}} \tag{10.6}$$

which is consistent to within a standard deviation of previous measurements. In 2017, the negative LECs are the preferred with $\Delta\chi^2 = 0.9$, and with a smaller χ^2/NDF overall. Now, the statistical errors are by far the most dominant and the largest systematic effect is from the extrapolation of the MO_2 efficiency to cover the full phase-space of $z_{\mu\mu}$. It is clear from the difference between the 2016 and 2017 results that the measurement is extremely challenging. In order to truly determine the correct sign of the LECs, all of the available statistics must be used. As a data sample a factor of ≈ 10 larger expected from 2017 and 2018, the most precise measurement of both the branching fraction and LECs will be achieved in the near future, with the aim to begin approaching a precision of the $\mathcal{O}(10)$ better.

To perform precision measurements of processes such as $K^+ \to \pi^+\mu^+\mu^-$ or the ultra-rare $K^+ \to \pi^+\nu\bar{\nu}$, high performance tracking is required. Firstly, the MNP33 fringe field map was modelled and tested for its accuracy. As a result, the propagation of the charged tracks in the simulation is to within a high-level of agreement with reality. A computation which calibrates the spectrometer momentum calculation was also developed. By selecting a sample of $K_{3\pi}$ decays and finding the ideal (α, β) constants to achieve $M_{3\pi} \approx M_K$, the computation improves the stability and accuracy of the momentum determination regardless of the data-taking conditions of the experiment. The computation is used in the data-reprocessing, and is performed for automatically for every new run at NA62. By introducing these two components, the accuracy of the momentum calculation in both simulation and data has increased, improving the prospects for nearly all future rare K^+ analyses at NA62.

Bibliography

[1] **ATLAS** Collaboration, G. Aad *et al.*, "Observation of a new particle in the search for the Standard Model Higgs boson with the ATLAS detector at the LHC," *Phys. Lett.* **B716** (2012) 1–29, arXiv:1207.7214 [hep-ex].

[2] **CMS** Collaboration, S. Chatrchyan *et al.*, "Observation of a new boson at a mass of 125 GeV with the CMS experiment at the LHC," *Phys. Lett.* **B716** (2012) 30–61, arXiv:1207.7235 [hep-ex].

[3] J. H. Christenson, J. W. Cronin, V. L. Fitch, and R. Turlay, "Evidence for the 2π Decay of the K_2^0 Meson," *Phys. Rev. Lett.* **13** (Jul, 1964) 138–140. https://link.aps.org/doi/10.1103/PhysRevLett.13.138.

[4] **NA48** Collaboration, A. Lai *et al.*, "A Precise measurement of the direct CP violation parameter Re(ϵ'/ϵ)," *Eur. Phys. J.* **C22** (2001) 231–254, arXiv:hep-ex/0110019 [hep-ex].

[5] D. Griffiths, *Introduction to elementary particles*. Wiley-VCH, 2012.

[6] G. D. Rochester and C. C. Butler, "Evidence for the Existence of New Unstable Elementary Particles," *Nature* **160** (1947) 855–857.

[7] K. Nishijima, "Charge Independence Theory of V Particles," *Progress of Theoretical Physics* **13** (Mar., 1955) 285–304.

[8] M. Gell-Mann, "The interpretation of the new particles as displaced charge multiplets," *Il Nuovo Cimento* **4** (Apr., 1956) 848–866.

[9] Z. Xing, "Wolfenstein parametrization reexamined," *Phys. Rev. D* **51** (Apr, 1995) 3958–3959. https://link.aps.org/doi/10.1103/PhysRevD.51.3958.

[10] S. Descotes-Genon and P. Koppenburg, "The CKM Parameters," *Ann. Rev. Nucl. Part. Sci.* **67** (2017) 97–127, arXiv:1702.08834 [hep-ex].

[11] C. Jarlskog, "Commutator of the Quark Mass Matrices in the Standard Electroweak Model and a Measure of Maximal CP Nonconservation," *Phys. Rev. Lett.* **55** (Sep, 1985) 1039–1042. https://link.aps.org/doi/10.1103/PhysRevLett.55.1039.

[12] **LHCb** Collaboration, B. Aaij *et al.*, "Precision measurement of CP violation in $B_s^0 \to J/\psi K^+ K^-$ decays," *Phys. Rev. Lett.* **114** no. 4, (2015) 041801, arXiv:1411.3104 [hep-ex].

[13] **Particle Data Group** Collaboration, C. Patrignani *et al.*, "Review of Particle Physics," *Chin. Phys.* **C40** no. 10, (2016) 100001.

[14] J. C. Hardy and I. S. Towner, "Superallowed $0^+ \to 0^+$ nuclear β decays: 2014 critical survey, with precise results for V_{ud} and CKM unitarity," *Phys. Rev.* **C91** no. 2, (2015) 025501, arXiv:1411.5987 [nucl-ex].

[15] J. J. Aubert *et al.*, "Experimental observation of a heavy particle J," *Phys. Rev. Lett.* **33** (Dec, 1974) 1404–1406. https://link.aps.org/doi/10.1103/PhysRevLett.33.1404.

[16] J. E. Augustin *et al.*, "Discovery of a Narrow Resonance in e^+e^- Annihilation," *Phys. Rev. Lett.* **33** (Dec, 1974) 1406–1408. https://link.aps.org/doi/10.1103/PhysRevLett.33.1406.

[17] L. Maiani, "The GIM Mechanism: origin, predictions and recent uses," in *Proceedings, 48th Rencontres de Moriond on Electroweak Interactions and Unified Theories: La Thuile, Italy, March 2-9, 2013*, pp. 3–16. 2013. arXiv:1303.6154 [hep-ph].

[18] V. Cirigliano *et al.*, "Kaon Decays in the Standard Model," *Rev. Mod. Phys.* **84** (2012) 399, arXiv:1107.6001 [hep-ph].

[19] G. Buchalla, J. Buras, A, and M. E. Lautenbacher, "Weak decays beyond leading logarithms," *Rev. Mod. Phys.* **68** (1996) 1125–1144, arXiv:hep-ph/9512380 [hep-ph].

[20] F. Mescia and C. Smith, "Improved estimates of rare K decay matrix-elements from $K_{\ell 3}$ decays," *Phys. Rev.* **D76** (2007) 034017, arXiv:0705.2025 [hep-ph].

[21] A. J. Buras, D. Buttazzo, J. Girrbach-Noe, and R. Knegjens, "$K^+ \to \pi^+ \nu\bar{\nu}$ and $K_L \to \pi^0 \nu\bar{\nu}$ in the Standard Model: status and perspectives," *JHEP* **11** (2015) 033, arXiv:1503.02693 [hep-ph].

[22] **KOTO** Collaboration, K. Shiomi, "Search for the rare decay of $K_L \to \pi^0 \nu\bar{\nu}$ at J-PARC," *XXXIX International Conference on High Energy Physics* (2018) . https://indico.cern.ch/event/686555/.

[23] T. Masuda *et al.*, "Long-lived neutral-kaon flux measurement for the KOTO experiment," *PTEP* **2016** no. 1, (2016) 013C03, arXiv:1509.03386 [physics.ins-det].

[24] **E949** Collaboration, A. V. Artamonov *et al.*, "New measurement of the $K^+ \to \pi^+ \nu\bar{\nu}$ branching ratio," *Phys. Rev. Lett.* **101** (2008) 191802, arXiv:0808.2459 [hep-ex].

[25] **E949** Collaboration, S. Adler and et al, "Measurement of the $K^+ \to \pi^+ \nu\bar{\nu}$ branching ratio," *Phys. Rev. D* **77** (Mar, 2008) 052003. https://link.aps.org/doi/10.1103/PhysRevD.77.052003.

[26] **NA62** Collaboration, R. Marchevski, "$K^+ \to \pi^+ \nu\bar{\nu}$: first NA62 results," *53rd Recontres de Moriond* (2018) . https://indico.in2p3.fr/event/16579/.

[27] A. Crivellin, G. D'Ambrosio, M. Hoferichter, and L. C. Tunstall, "Violation of lepton flavor and lepton flavor universality in rare kaon decays," *Phys. Rev.* **D93** no. 7, (2016) 074038, arXiv:1601.00970 [hep-ph].

[28] S. Descotes-Genon *et al.*, "Optimizing the basis of B $\to K^* \ell^+ \ell^-$ observables in the full kinematic range," *Journal of High Energy Physics* **2013** no. 5, (May, 2013) 137. https://doi.org/10.1007/JHEP05(2013)137.

[29] W. Altmannshofer and D. M. Straub, "New physics in $b \to s$ transitions after LHC run 1," *Eur. Phys. J.* **C75** no. 8, (2015) 382, arXiv:1411.3161 [hep-ph].

[30] S. Descotes-Genon *et al.*, "On the impact of power corrections in the prediction of $B \to K^* \mu^+ \mu^-$ observables," *JHEP* **12** (2014) 125, arXiv:1407.8526 [hep-ph].

[31] R. R. Horgan *et al.*, "Calculation of $B^0 \to K^{*0} \mu^+ \mu^-$ and $B_s^0 \to \phi \mu^+ \mu^-$ observables using form factors from lattice QCD," *Phys. Rev. Lett.* **112** (2014) 212003, arXiv:1310.3887 [hep-ph].

[32] **LHCb** Collaboration, R. Aaij *et al.*, "Differential branching fraction and angular analysis of the decay $B_s^0 \to \phi \mu^+ \mu^-$," *JHEP* **07** (2013) 084, arXiv:1305.2168 [hep-ex].

[33] **CDF** Collaboration, T. Aaltonen *et al.*, "Measurement of the Forward-Backward Asymmetry in the $B \to K^{(*)} \mu^+ \mu^-$ Decay and First Observation of the $B_s^0 \to \phi \mu^+ \mu^-$ Decay," *Phys. Rev. Lett.* **106** (2011) 161801, arXiv:1101.1028 [hep-ex].

[34] **LHCb** Collaboration, R. Aaij *et al.*, "Test of lepton universality using $B^+ \to K^+ \ell^+ \ell^-$ decays," *Phys. Rev. Lett.* **113** (2014) 151601, arXiv:1406.6482 [hep-ex].

[35] C. Bobeth *et al.*, "Angular distributions of $\bar{B} \to \bar{K} \ell^+ \ell^-$ decays," *JHEP* **12** (2007) 040, arXiv:0709.4174 [hep-ph].

[36] **LHCb Collaboration** Collaboration, R. e. a. Aaij, "Measurement of the ratio of branching fractions $\mathcal{B}(\bar{b}^0 \to D^{*+} \tau^- \overline{\nu}_\tau)/\mathcal{B}(\bar{b}^0 \to D^{*+} \mu^- \overline{\nu}_\mu)$," *Phys. Rev. Lett.* **115** (Sep, 2015) 111803. https://link.aps.org/doi/10.1103/PhysRevLett.115.111803.

[37] **Heavy Flavor Averaging Group (HFAG)** Collaboration, Y. Amhis *et al.*, "Averages of b-hadron, c-hadron, and τ-lepton properties as of summer 2014," arXiv:1412.7515 [hep-ex].

[38] S. Fajfer, J. F. Kamenik, and I. Nisandzic, "On the $B \to D^* \tau \bar{\nu}_\tau$ Sensitivity to New Physics," *Phys. Rev.* **D85** (2012) 094025, arXiv:1203.2654 [hep-ph].

[39] W. Altmannshofer and D. M. Straub, "Implications of $b \to s$ measurements," in *Proceedings, 50th Rencontres de Moriond Electroweak Interactions and Unified*

Theories: La Thuile, Italy, March 14-21, 2015, pp. 333–338. 2015. arXiv:1503.06199 [hep-ph]. https://inspirehep.net/record/1353682/files/arXiv:1503.06199.pdf.

[40] L. C. Tunstall, A. Crivellin, G. D'Ambrosio, and M. Hoferichter, "Probing lepton flavour (universality) violation at NA62 and future kaon experiments," *J. Phys. Conf. Ser.* **800** no. 1, (2017) 012014, arXiv:1611.00495 [hep-ph].

[41] G. Buchalla, "Kaon and charm physics: Theory," in *Flavor physics for the millennium. Proceedings, Theoretical Advanced Study Institute in elementary particle physics, TASI 2000, Boulder, USA, June 4-30, 2000*, pp. 143–205. 2001. arXiv:hep-ph/0103166 [hep-ph].

[42] G. D'Ambrosio, G. Ecker, G. Isidori, and J. Portoles, "The Decays $K \to \pi\ell^+\ell^-$ beyond Leading Order in the Chiral Expansion," *JHEP* **08** no. hep-ph/9808289. FTUV-98-61. INFN-NA-IV-98-25. UWTHPH-1998-45, (Aug, 1998) 004. 18 p. http://cds.cern.ch/record/362106.

[43] G. Isidori, "Soft-photon corrections in multi-body meson decays," *Eur. Phys. J.* **C53** (2008) 567–571, arXiv:0709.2439 [hep-ph].

[44] G. D'Ambrosio, G. Isidori, A. Pugliese, and N. Paver, "Strong rescattering in $K^+ \to 3\pi$ decays and low-energy meson dynamics," *Phys. Rev.* **D50** (1994) 5767, arXiv:hep-ph/9403235 [hep-ph].

[45] G. Ecker, A. Pich, and E. de Rafael, "$K \to \pi\ell^+\ell^-$ decays in the effective chiral lagrangian of the standard model," *Nuclear Physics B* **291** (1987) 692 – 719. http://www.sciencedirect.com/science/article/pii/0550321387904913.

[46] G. Ecker, J. Kambor, and D. Wyler, "Resonances in the weak chiral lagrangian," *Nuclear Physics B* **394** no. 1, (1993) 101 – 138. http://www.sciencedirect.com/science/article/pii/055032139390103V.

[47] **NA48/2** Collaboration, J. R. Batley *et al.*, "Precise measurement of the $K^+ \to \pi^+ e^+ e^-$," *Phys. Lett.* **B677** (2009) 246–254, arXiv:0903.3130 [hep-ex].

[48] **NA48/2** Collaboration, J. R. Batley., "New measurement of the K^+ to $\pi^+\mu^+\mu^-$ decay," *Physics Letters B* **697** no. 2, (2011) 107 – 115. http://www.sciencedirect.com/science/article/pii/S0370269311000797.

[49] **E865** Collaboration, R. Appel *et al.*, "A New measurement of the properties of the rare decay $K^+ \to \pi^+ e^+ e^-$," *Phys. Rev. Lett.* **83** (1999) 4482–4485, arXiv:hep-ex/9907045 [hep-ex].

[50] **E865** Collaboration, R. Appel *et al.*, "Search for lepton flavor violation in K^+ decays," *Phys. Rev. Lett.* **85** (2000) 2877–2880, arXiv:hep-ex/0006003 [hep-ex].

[51] **NA48/2** Collaboration, J. R. Batley *et al.*, "Search for direct CP violation in the decays $K_{3\pi}$," *Phys. Lett.* **B634** (2006) 474–482, arXiv:hep-ex/0602014 [hep-ex].

[52] G. Anelli *et al.*, "Proposal to Measure the Rare Decay $K^+ \to \pi^+ \nu\bar{\nu}$ at the CERN SPS," Tech. Rep. CERN-SPSC-2005-013. SPSC-P-326, CERN, Geneva, Apr, 2005. http://cds.cern.ch/record/832885.

[53] **NA62** Collaboration, E. Cortina Gil *et al.*, "The Beam and detector of the NA62 experiment at CERN," *JINST* **12** no. 05, (2017) P05025, arXiv:1703.08501 [physics.ins-det].

[54] **NA62** Collaboration, F. Hahn, "NA62: Technical Design Document," Tech. Rep. NA62-10-07, CERN, Geneva, Dec, 2010. https://cds.cern.ch/record/1404985.

[55] **Particle Data Group** Collaboration, K. A. Olive *et al.*, "Review of Particle Physics," *Chin. Phys.* **C38** (2014) 090001.

[56] **NA62** Collaboration, V. Palladino, "First results from the NA62 STRAW spectrometer," *PoS* **EPS-HEP2015** (2015) 250.

[57] D. Moraes *et al.*, "The CARIOCA Front End Chip for the LHCb muon chambers," Tech. Rep. LHCb-2003-009, CERN, Geneva, Jan, 2003. http://cds.cern.ch/record/691709.

[58] E. Goudzovski *et al.*, "Development of the kaon tagging system for the NA62 experiment at CERN," *Nucl. Instrum. Meth.* **A801** (2015) 86–94, arXiv:1509.03773 [physics.ins-det].

[59] **NA62** Collaboration, S. Kholodenko, "NA62 Charged Particle Hodoscope. Design and performance in 2016 run," *JINST* **12** no. 06, (2017) C06042, arXiv:1705.05093 [physics.ins-det].

[60] B. Angelucci, E. Pedreschi, M. Sozzi, and F. Spinella, "TEL62: an integrated trigger and data acquisition board," *Journal of Instrumentation* **7** no. 02, (2012) C02046. http://stacks.iop.org/1748-0221/7/i=02/a=C02046.

[61] F. Ambrosino, "The Large Angle Photon Veto System for the NA62 Experiment at CERN," *Physics Procedia* **37** (2012) 293–300, arXiv:1111.4075 [physics.ins-det].

[62] **NA62** Collaboration, "2016 NA62 Status Report to the CERN SPSC," Tech. Rep. CERN-SPSC-2016-016. SPSC-SR-183, CERN, Geneva, Apr, 2016. https://cds.cern.ch/record/2143208.

[63] M. Sozzi *et al.*, "The integrated low-level trigger and readout system of the CERN NA62 experiment," *Submitted to Nuclear Inst. and Methods in Physics Research, A* (2017) .

[64] J. Pinzino, "Studies of a STRAW Tracker L1 trigger for $K^+ \to \pi^+ \nu\bar{\nu}$ and exotic decays," *Internal NA62 Documentation* (May, 2017) . NA62-17-05.

[65] N. C. for Environmental Information, "International Geomagnetic Reference Field," 2018. https://www.ngdc.noaa.gov/geomag-web/#igrfwmm.

[66] **NA62** Collaboration, "NA62 Software,". https://na62-sw.web.cern.ch.

[67] J. R. Fry, G. Ruggiero, and F. Bergsma, "Precision magnetic field mapping for CERN experiment NA62," *Journal of Physics G: Nuclear and Particle Physics* **43**

no. 12, (2016) 125004.
http://stacks.iop.org/0954-3899/43/i=12/a=125004.

[68] J. C. Maxwell, "A dynamical theory of the electromagnetic field," *Phil. Trans. R. Soc. Lond* **155** (1865) 459–512.

[69] A. Chappuis and E. Goudzovski, "Magnetic field in the decay volume: simulation and tracking tool," *Internal NA62 Documentation* (Jul, 2015) . NA62-15-06.

[70] J. R. Fry and G. Ruggiero, "The magnetic field of the NA62 dipole magnet," *Internal NA62 Documentation* (Oct, 2014) . NA62-14-09.

[71] V. Duk, "Fast NA62MC simulation," *Internal NA62 Communication* (2018) . Lepton Flavour WG, NA62 Collaboration Meeting.

[72] K. Massri, *Kaon identification and Search for Lepton Number Violation in $K^{\pm}$ decay-in-flight experiments at CERN*. PhD thesis, University of Birmingham, 2015. https://cds.cern.ch/record/2299436.

[73] **NA48** Collaboration, V. Fanti *et al.*, "The beam and detector for the NA48 neutral kaon CP violation experiment at CERN," *Nuclear Instruments and Methods in Physics Research Section A: Accelerators, Spectrometers, Detectors and Associated Equipment* **574** no. 3, (2007) 433 – 471. http://www.sciencedirect.com/science/article/pii/S0168900207002719.

[74] B. Bloch-Devaux, "Alpha and Beta correction for NA48/2," *Internal NA48/2 Documentation* (May, 2005) . NA48-05-05.

[75] R. Skogeby, *Resolution Improvements and Physical Modelling of a Straw Tracker*. PhD thesis, Umeå Universitet, 2017.

[76] R. Frühwirth, "Application of Kalman filtering to track and vertex fitting," *Nuclear Instruments and Methods in Physics Research Section A: Accelerators, Spectrometers, Detectors and Associated Equipment* **262** no. 2, (1987) 444 – 450. http://www.sciencedirect.com/science/article/pii/0168900287908874.

[77] E. Goudzovski, "Lepton Flavour WG: Filtering 06/04/2017," *Internal NA62 Communication* (April, 2017) . Lepton Flavour WG.

[78] K. Pearson, "X. on the criterion that a given system of deviations from the probable in the case of a correlated system of variables is such that it can be reasonably supposed to have arisen from random sampling," *The London, Edinburgh, and Dublin Philosophical Magazine and Journal of Science* **50** no. 302, (1900) 157–175.

[79] E. Goudzovski, "Lepton flavour WG 07/02/2018," *Internal NA62 Communication* (Feb, 2018) . Lepton Flavour WG.

[80] M. Koval, "Straw Spectrometer Status," *Internal NA62 Communication* (2016) . Straw WG, NA62 Collaboration Meeting Washington.

[81] M. Koval, "Spectrometer reconstruction efficiency for three track events," *Internal NA62 Communication* (2018) . Lepton Flavour WG, NA62 Collaboration Meeting.

[82] R. Lollini, "CHOD Data Quality," *Internal NA62 Communication* (2018) . Data Quality and Processing WG.

[83] E. Maurice and J. R. Fry, "Spectrometer efficiency measurement in 2015 minimum bias data," *Internal NA62 Documentation* (August, 2016) . NA62-16-08.

[84] C. Parkinson, "Why do $K_{3\pi}$ events fail L1LAV?," *Internal NA62 Communication* (2017) . Lepton Flavour WG, NA62 Collaboration Meeting.

[85] W. Verkerke and D. Kirkby, "The RooFit toolkit for data modeling," *ArXiv Physics e-prints* (June, 2003) , `physics/0306116`.

[86] R. J. Barlow, "Extended maximum likelihood," *Nucl. Instrum. Meth.* **A297** (1990) 496–506.

[87] G. Lafferty and T. Wyatt, "Where to stick your data points: The treatment of measurements within wide bins," *Nuclear Instruments and Methods in Physics Research Section A: Accelerators, Spectrometers, Detectors and Associated*

Equipment **355** no. 2, (1995) 541 – 547. http://www.sciencedirect.com/science/article/pii/0168900294011125.

[88] C. Parkinson, A. Sturgess, *et al.*, "Status of the $\pi\mu\mu$ analysis," *Internal NA62 Communication* (2018) . Lepton Flavour WG, NA62 Collaboration Meeting.

Appendix A

$K_{3\pi}$, $K_{\pi\mu\mu}$ data-MC comparison

The data/MC agreement is presented for $K_{3\pi}$ (red) and $K_{\pi\mu\mu}$ (orange) candidates collected with the final selection described in Chapter 6. The comparison is performed for vertex and track related variables.

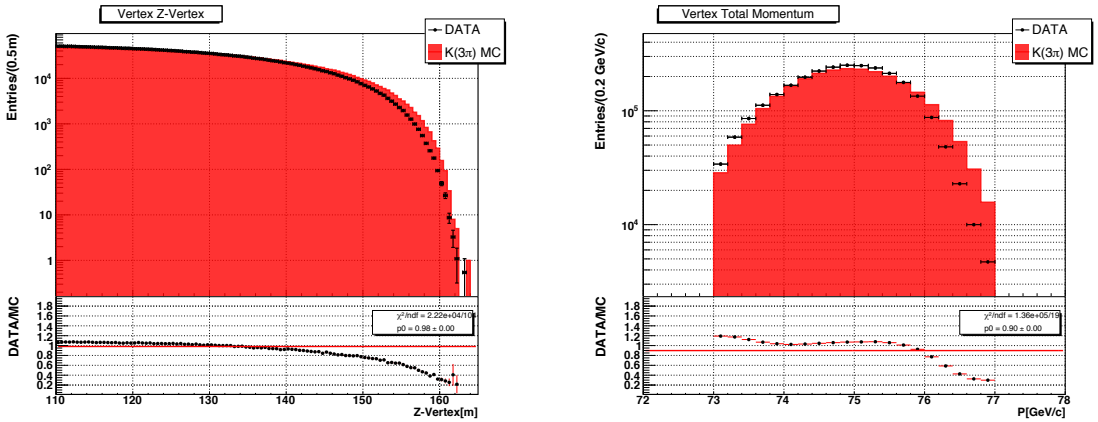

(a) (b)

Figure A.1: Distributions of (a) the reconstructed longitudinal vertex position Z-Vertex and (b) the reconstructed vertex momentum $P-$Vertex for $K_{3\pi}$ signal and MC. Cuts are applied between (110; 165)m for (a), and between (73; 77) GeV/c for (b). The largest discrepancy enters in (b), but is expected to cancel via normalisation with the $K_{\pi\mu\mu}$ sample.

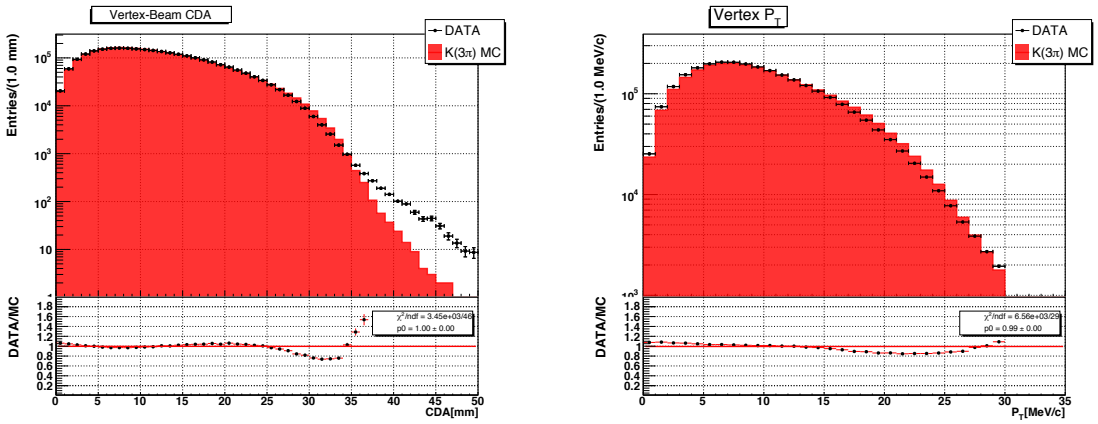

(a) (b)

Figure A.2: Distributions of (a) the reconstructed vertex-nominal-beam CDA and(b) the reconstructed vertex transverse momentum P_T for $K_{3\pi}$ signal and MC. Cuts are applied as <50 mm for (a), and <30 MeV/c for (b).

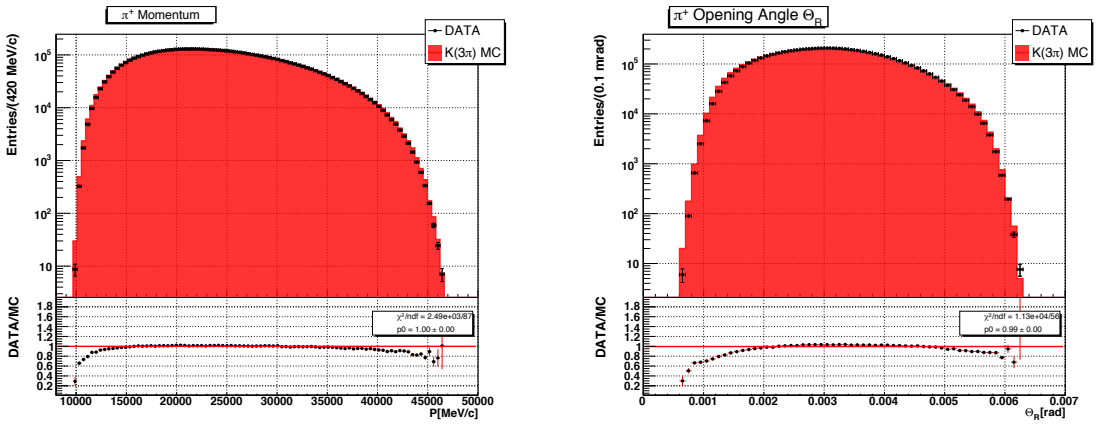

(a) (b)

Figure A.3: Distributions of (a) the reconstructed π^+ track momentum and (b) the reconstructed π^+ opening angle Θ_R for $K_{3\pi}$ signal and MC. Cuts are applied between (8; 48) GeV/c for (a), while Θ_R is used by the $K_{\pi\mu\mu}$ PID only.

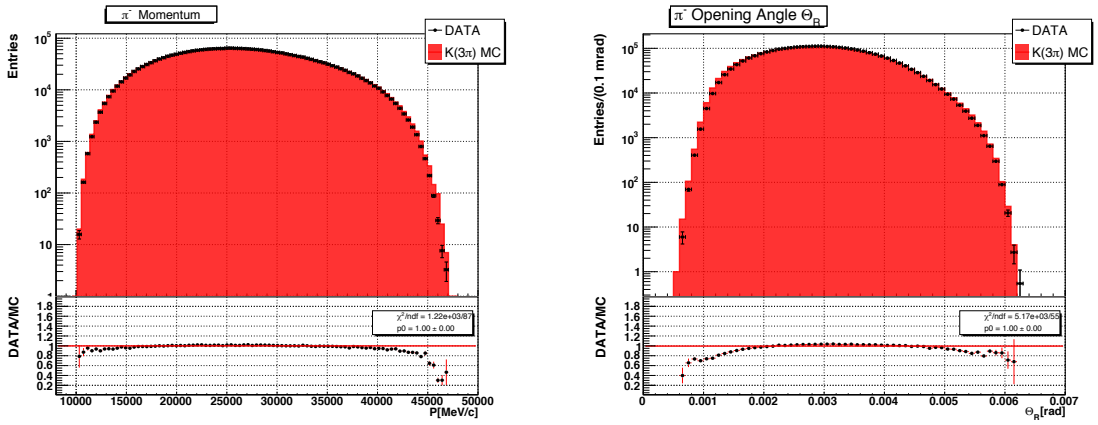

(a) (b)

Figure A.4: Distributions of (a) the reconstructed π^- track momentum and (b) the reconstructed π^- opening angle Θ_R for $K_{3\pi}$ signal and MC. Cuts are applied between (8; 48) GeV/c for (a), while Θ_R is used by the $K_{\pi\mu\mu}$ PID only.

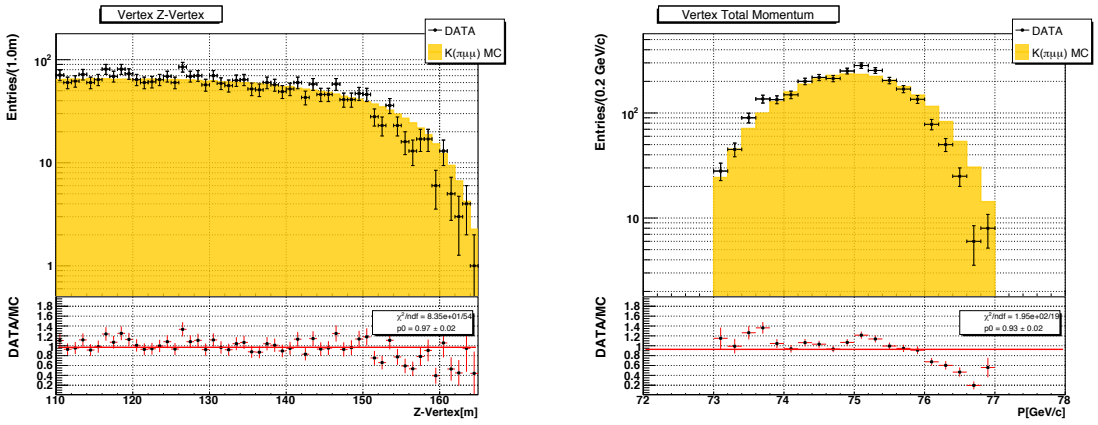

(a) (b)

Figure A.5: Distributions of (a) the reconstructed longitudinal vertex position Z-Vertex and (b) the reconstructed vertex momentum $P-$Vertex for $K_{\pi\mu\mu}$ signal and MC. Cuts are applied between (110; 165)m for (a), and between (73; 77) GeV/c for (b). The largest discrepancy enters in (b), but the shape is very similar to the normalisation sample in Figure A.1.

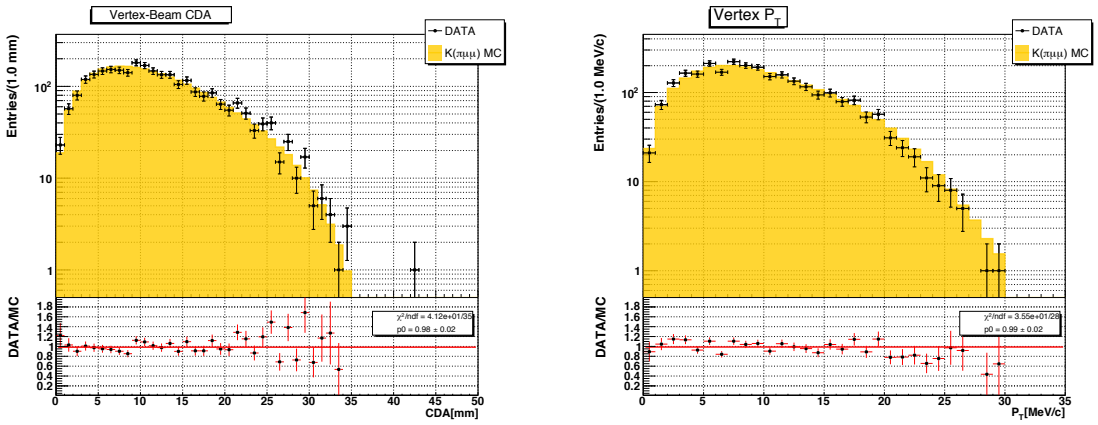

(a) (b)

Figure A.6: Distributions of (a) the reconstructed vertex-nominal-beam CDA and(b) the reconstructed vertex transverse momentum P_T for $K_{\pi\mu\mu}$ signal and MC. Cuts are applied as <50 mm for (a), and <30 MeV/c for (b).

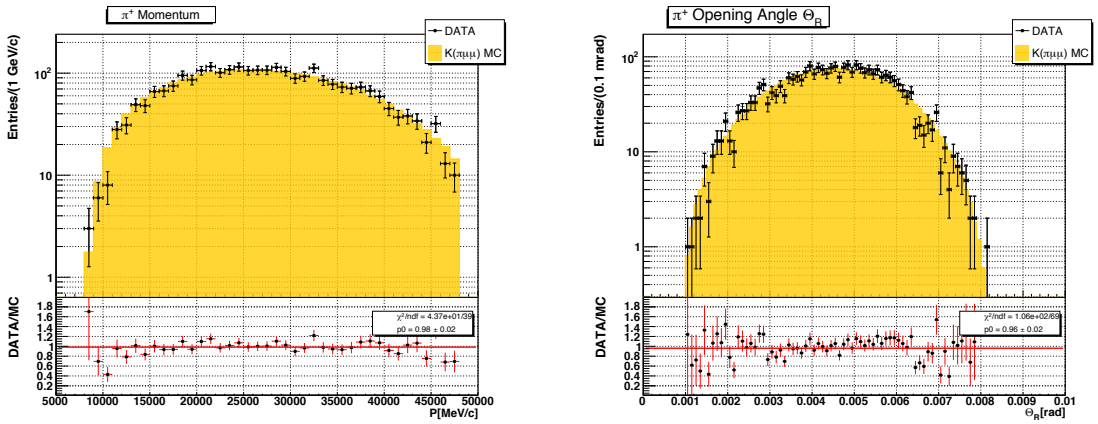

(a) (b)

Figure A.7: Distributions of (a) the reconstructed π^+ track momentum and (b) the reconstructed π^+ opening angle Θ_R for $K_{\pi\mu\mu}$ signal and MC. Cuts are applied due between (8; 48) GeV/c for (a), and <8.5 mrad for (b).

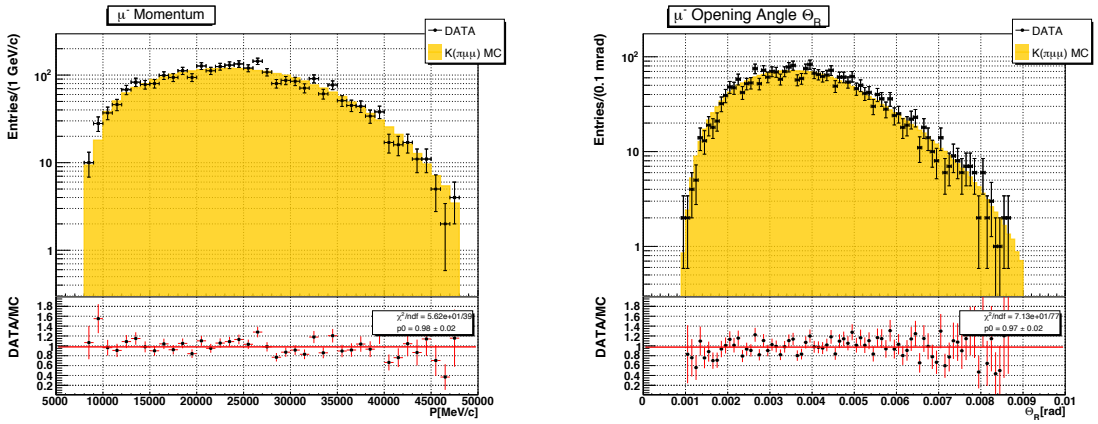

(a) (b)

Figure A.8: Distributions of (a) the reconstructed μ^- track momentum and (b) the reconstructed μ^- opening angle Θ_R for $K_{\pi\mu\mu}$ signal and MC. Cuts are applied between (8; 48) GeV/c for (a), and <9.0 mrad for (b).